THE THERMOELASTIC PROPERTIES OF POST-PEROVSKITE ANALOGUE PHASES

Thesis submitted for Doctor of Philosophy

by

Alexander Lindsay-Scott

Department of Earth Sciences

University College London

November 2011

I, Alexander Lindsay-Scott, confirm that the work presented in this thesis is my own. Where information has been derived from other sources, I confirm that this has been indicated in the thesis.

Abstract

Post-perovskite $MgSiO_3$ is a major component of the D'' zone at the base of the lower mantle, so knowledge of its physical properties is essential to understanding mantle dynamics. Unfortunately, $MgSiO_3$ post-perovskite is stable only at Mbar pressures. This difficulty can be addressed by combining computer simulations with experiments on analogue post-perovskite ABX_3 phases, stable at ambient pressure and temperature. In this project, the properties of $MgSiO_3$ and other oxide and fluoride post-perovskites were simulated using both athermal and molecular dynamics *ab initio* methods. Correspondence with experiment was generally good, although better in compression than when heated. Because few ABO_3 oxides with this structure are known, an empirical approach was developed to predict whether post-perovskite phases would occur for given A, B and X elements, and to estimate the stabilisation pressures required. Only $CaIrO_3$ forms at ambient pressure; single crystals were prepared for structural measurements, but the extremely high absorption made X-ray diffraction unreliable. Powdered $CaPtO_3$ was synthesised at high-pressure and its thermoelastic properties and structure determined at high-pressure and from low to high-temperature by neutron powder diffraction; its isothermal equation of state was determined by X-ray powder diffraction. $CaPtO_3$ (and $CaIrO_3$ as measured previously) have the same axial compression sequence ($\kappa_c > \kappa_a > \kappa_b$) as $MgSiO_3$, but all show different axial expansion at high-temperature. Across D'' significant changes in the physical properties of $MgSiO_3$ post-perovskite are likely to arise from changes in temperature as well as from changes in pressure; the differences in axial expansion therefore suggest that $CaPtO_3$ and $CaIrO_3$ may not be suitable analogues. Computer simulations suggest that ABF_3 compounds may provide better analogues for $MgSiO_3$ post-perovskite. A new post-perovskite $NaNiF_3$ has been synthesised at 15 GPa and its unit cell parameters determined; further experiments on these fluorides are the subject of ongoing work.

Acknowledgements

I would like to express my thanks for the expertise and unfailing support provided by my Ph.D. supervisors Dr. Ian Wood, Professor David Dobson, Professor Lidunka Vočadlo and Professor John Brodholt. I have thoroughly enjoyed working with them. Dr. Kevin Knight, Dr. Matt Tucker and Mr. Christopher Barry at ISIS, and Dr. Wilson Crichton at ESRF all gave me important assistance with my experiments. Dr. Stephen Stackhouse provided advice on VASP and data from molecular dynamics simulations, and Dr. Alexander Côté also provided advice on VASP. Dr. Dominic Fortes assisted with pressure calibration, and Dr. Takashi Taniguchi carried out large-volume sample synthesis. I would also like to thank Professor David Price for identifying research as a possible outcome at my interview for a first degree, and Dr. Wendy Kirk for encouraging my application to UCL. Special thanks are due to my wife Carole and to my sons Jon and Peter for their encouragement and support during eight years of study.

My research has been funded by a postgraduate studentship from the Natural Environment Research Council. HECToR, the UK national high-performance computing service which I have used for *ab initio* simulation, is provided by UoE HPCx Ltd at the University of Edinburgh, Cray Inc. and NAG Ltd, and funded by the Office of Science and Technology through the Engineering and Physical Research Council's High-End Computing Programme.

Contents

1 Introduction

My objective is to determine the thermoelastic properties of analogues of post-perovskite-structured $MgSiO_3$ by combining an experimental study of low-pressure ABX_3 analogue phases with *ab initio* simulations, and to compare these properties with those of post-perovskite $MgSiO_3$.

1.1 Post-perovskite

Until 2004 it was thought that there were two major phases present throughout the whole of the Earth's lower mantle: perovskite-structured $MgSiO_3$ and NaCl-structured magnesio-wüstite, (Mg,Fe)O. However, in 2004 it was discovered, from laser-heated diamond-anvil cell experiments, that perovskite-structured $MgSiO_3$ transforms to an orthorhombic $CaIrO_3$-structured "post-perovskite" phase at around 120 GPa (Murakami *et al.*, 2004; Oganov and Ono, 2004). This pressure is equivalent to a depth within the Earth of ~2600 km, just above the core-mantle boundary. This led to the suggestion that post-perovskite $MgSiO_3$ might be the majority phase in the thin D" zone of the Earth that extends into the mantle up to ~300 km from the core-mantle boundary. If this is the case, then the physical and chemical properties of post-perovskite are likely to dominate the dynamics of much of the core–mantle boundary region. The interpretation of seismic data for D" and modelling of the heat flow in this region will then depend critically on physical properties of post-perovskite $MgSiO_3$ such as its elastic moduli, the Clapeyron slope of the perovskite-post-perovskite phase boundary, the degree of crystal alignment, and its transport properties - diffusion, viscosity and thermal conductivity (Trønnes, 2010).

The atomic arrangement in the post-perovskite phase of $MgSiO_3$ differs greatly from that found in perovskite $MgSiO_3$, and it is likely that the physical properties of the two phases will also differ appreciably. The perovskite phase contains the 3-dimensional network of corner-linked octahedra found in all perovskites; in contrast, the orthorhombic crystal structure of ABO_3 post-perovskites contains both corner-sharing and edge-sharing octahedra (see Section 1.4).

1.2 Analogues of post-perovskite

The probable importance of $MgSiO_3$ in the core-mantle boundary region of the Earth implies that determination of its physical properties is essential for interpretation by deep-Earth geoscientists of the seismic observations of this region, and for modelling heat flow and magnetic fields in this region. These properties are very difficult to measure, because post-perovskite $MgSiO_3$ is stable only at pressures of ~100 GPa and cannot be quenched to ambient conditions. It is therefore more practical to obtain some of the experimental results required for comparison with computer simulations of post-perovskite $MgSiO_3$ from studies of isostructural analogues, whose thermoelastic and rheological properties at lower temperature and pressure such as compressive and thermal structural distortion, expansivity, bulk and shear incompressibility, thermal conductivity and viscosity might be similar to those of $MgSiO_3$ under D" conditions. Ideally, such analogues should either form at atmospheric pressure, or should be recoverable to atmospheric pressure following high-pressure synthesis. If high-pressure is required to form the material, it is preferable that the formation pressure should not exceed ~20 GPa, as samples of around a few mm^3 in size may then be prepared using multi-anvil presses.

Post-perovskite $MgSiO_3$ and its analogues have been extensively studied since 2004, both experimentally and using *ab initio* methods. Previous publications will be referred to in detail at the appropriate point in the present work; a summary of the more recent studies which are relevant to the subject of this thesis is given in the following tables.

Compound	References
$CaGeO_3$	Fang and Ahuja, 2006 (simulation)
$CaIrO_3$	Hirose and Fujita, 2005
	Cheng *et al*., 2010
$CaSnO_3$	Tateno *et al*., 2010
$CdGeO_3$	Fang and Ahuja, 2006 (simulation)
$CaPtO_3$	Matar *et al*., 2008 (simulation)
$CdTiO_3$	Fang and Ahuja, 2006 (simulation)
$MgGeO_3$	Tsuchiya and Tsuchiya, 2007a
$MgSiO_3$	Catalli *et al*., 2009
	Tateno *et al*., 2009
$MnGeO_3$	Tateno *et al*., 2006
	Yamazaki *et al*., 2011
$NaMgF_3$	Umemoto *et al*., 2006
$NaCoF_3$	Dobson *et al*., 2011 (also $NaNiF_3$ unit-cell parameters)
$SrRuO_3$	Cai *et al*., 2011 (simulation)

Table 1-1: Studies of the perovskite to post-perovskite transition

Compound	References
Al_2O_3	Ono *et al*., 2006a
$CaIrO_3$	Lindsay-Scott *et al.,* 2007
	Boffa Ballaran *et al*., 2007
	Niwa *et al*., 2010
$CaPtO_3$	Lindsay-Scott *et al*., 2010
$CaRhO_3$	Wang *et al*., 2011
$CdGeO_3$	Tateno *et al*., 2006
$Mg_{0.9}Fe_{0.1}SiO_3$	Nishio-Hamane *et al*., 2009
$Mg_{0.85}Fe_{0.15}Al_{0.15}Si_{0.85}O_3$	
$MgGeO_3$	Hirose *et al*., 2005
	Kubo *et al*., 2006
$MgSiO_3$	Ono *et al*., 2006b
	Guignot *et al*., 2007
	Komabayashi *et al*., 2008
$NaMgF_3$	Hustoft *et al*., 2008 (bulk EOS)
	Martin *et al*., 2006b
$NaZnF_3$	Yakovlev *et al*., 2009

Table 1-2: Studies of unit-cell parameters at several pressures and/or temperatures

Compound	References
$CaIrO_3$	Rodi and Babel, 1965
	Sugahara *et al.*, 2008
	Hirai *et al.*, 2009
$CaIr_{1-x}Pt_xO_3$	Hirai *et al.*, 2011
$CaIr_{0.5}Rh_{0.5}O_3$	
$CaPtO_3$	Inaguma *et al.*, 2008
	Ohgushi *et al.*, 2008
$CaRhO_3$	Shirako *et al.*, 2009
	Yamaura *et al.*, 2009
$CaRuO_3$	Kojitani *et al.*, 2007
	Zhong *et al.*, 2010
$Ca_{1-x}Sr_xIrO_3$	Cheng *et al.*, 2011
Fe_2O_3	Ono and Ohishi, 2005
$MgGeO_3$	Hirose *et al.*, 2005
$MgSiO_3$	Murakami *et al.*, 2004
	Oganov and Ono, 2004
Mn_2O_3	Santillan *et al.*, 2006
$NaIrO_3$	Bremholm *et al.*, 2011
$NaMgF_3$	Martin *et al.*, 2006a
	Martin *et al.*, 2006b
$NaZnF_3$	Yakovlev *et al.*, 2009
	Yakovlev *et al.*, 2009a

Table 1-3: Crystallographic studies of structure at one pressure and temperature

Compound	References
$CaIrO_3$	Martin *et al.*, 2007a
	Martin *et al.*, 2007b
	Martin, 2008
$CaPtO_3$	Lindsay-Scott *et al.*, 2011
$MgSiO_3$	Hirate *et al.*, 2010 (simulation)
$Mg_{0.91}Fe_{0.09}SiO_3$	Shim *et al.*, 2008
$MgGeO_3$	Kubo *et al.*, 2008

Table 1-4: Studies of structure at several pressures and/or temperatures

Compound	References
$CaIrO_3$	Liu *et al*., 2011 (thermal EOS)
$CaIr_{1-x}Pt_xO_3$	Hirai *et al.*, 2011
$CaIr_{0.5}Rh_{0.5}O_3$	
$Ca_{1-x}Na_xIrO_3$	Ohgushi *et al*., 2006
$CaPtO_3$	Ohgushi *et al*., 2008 (C_P)
$CaRhO_3$	Yamaura *et al*., 2009
	Matar *et al*., 2010 (simulation)
	Wang *et al*., 2011 (thermal anisotropy)
$CaRuO_3$	Zhong *et al*., 2010 (simulation)
	Shirako *et al*., 2011
$Ca_{1-x}Sr_xIrO_3$	Cheng *et al*., 2011
$MgSiO_3$	Stackhouse *et al*., 2005a (simulation)
	(thermal anisotropy and elasticity)
	Stackhouse and Brodholt, 2007 (simulation)
	(thermal anisotropy and elasticity)
	Komabayashi *et al*., 2008 (thermal EOS)
	Liu *et al*., 2010 (simulation)
	(thermal EOS, C_V)
$NaIrO_3$	Bremholm *et al*., 2011 (C_P)
$SrRuO_3$	Cai *et al*., 2011 (simulation)

Table 1-5: Studies of magnetic or (where noted) thermal properties

Compound	References
$MgSiO_3$	Stackhouse *et al*., 2005a
	Tsuchiya *et al*., 2004
$CaIrO_3$	Stølen and Trønnes, 2007
Al_2O_3	Stackhouse *et al*., 2005b

Table 1-6: Simulation studies of force constants c_{ij}

The simple oxides Fe_2O_3 (Ono and Ohishi, 2005), Al_2O_3 (Oganov and Ono, 2005; Ono *et* al., 2006a) and Mn_2O_3 (Santillan *et al*., 2006) also form post-perovskites at high-pressure.

It can be seen from these tables that the experimental measurements of post-perovskite $MgSiO_3$ have been limited to determination of its unit-cell parameters and crystallographic structure, and of how these change with changing pressure and temperature. Other properties such as shear incompressibility, thermal conductivity and viscosity are more difficult to determine at the high-pressure and high-temperature at which post-perovskite $MgSiO_3$ is stable. This thesis has therefore used the unit-cell parameters, crystallographic structure, and their changes with changing pressure and temperature as the properties for an initial determination of the suitability of the post-perovskite analogues studied.

1.3 $CaIrO_3$ and $CaPtO_3$ post-perovskite analogues

The analogue phase that has been most studied to date is $CaIrO_3$. However, post-perovskite $CaIrO_3$ has a number of disadvantages as an analogue of $MgSiO_3$. The most obvious disadvantages are that the ratios of the atomic masses are very different, and that $CaIrO_3$ may exhibit structural distortion due to the Jahn-Teller effect. Boffa Ballaran *et al.* (2007) have measured the bulk and axial incompressibilities of $CaIrO_3$ at ambient temperature. Its thermal expansion at both high and low temperatures has been determined by Lindsay-Scott *et al.* (2007)(work that I carried out as a final year undergraduate project). The thermoelastic and structural properties of $CaIrO_3$ have been studied as a function of pressure and temperature by Martin *et al.*, (2007a, 2007b) and by Martin (2008), and the thermoelastic properties at simultaneous high-pressure and high-temperature by Liu *et al.* (2011). $CaIrO_3$ shows unusual behaviour in that, unlike $MgSiO_3$, the response of the structure to heat is not simply the reverse of the response to pressure (see Section 9.4.1 and Figure 9-19). For example, it was found that the *b*-axis, which is the most compressible, expanded most on heating, but that the thermal expansion of the *c*-axis is far larger than that of the *a*-axis, despite the fact that the *c*-axis shortens less under pressure.

There has been very little work on the systematics of changes in the crystal structure of post-perovskite as a result of changes in pressure or temperature (see Table 1-4). Experimental studies have been published which include data on the effect of changes in pressure and temperature on the structure of post-perovskite $(Mg_{0.91}Fe_{0.09})SiO_3$ (Shim *et al.*, 2008) and of the effect of pressure on the structure of post-perovskite $MgGeO_3$ (Kubo *et al.*, 2008). However, because of the difficulties inherent in diamond-anvil cell experiments at high-pressure, these studies did not accurately define the relatively small changes in post-perovskite structure driven by changes in pressure (see, for example, Figure 10-12 and Figure 10-13).

Even with single-crystal methods, it is difficult to obtain accurate coordinates for the oxygen atoms in $CaIrO_3$ using X-ray diffraction because of the presence of Ir, and such studies have only been made at ambient pressure and temperature (Sugahara *et al.*, 2008; Hirai *et al.*, 2009). Investigations of the post-perovskite structure by X-ray powder diffraction have been made at high-temperature (Martin *et al.* 2007a), including a pair-distribution function study (Martin, 2008); general trends in the oxygen coordinates are discernable but their scatter is understandably large. For such

materials, containing both "light" and "heavy" atoms, neutron diffraction commonly offers a better method for the determination of their crystal structure (as discussed in Section 7.2). However, in the particular case of $CaIrO_3$, neutron studies are greatly hampered by the very high absorption cross section of the Ir ions. The available results from the high-pressure (ambient temperature) neutron powder diffraction study by Martin *et al.* (2007b) in the range 0 – 9.7 GPa are therefore quite widely spaced in pressure, and their measurements as a function of temperature at ambient pressure are confined to data collected at 2 K and 293 K. No computer simulation studies have been published of the changes in a post-perovskite structure with temperature, although work has been done on the effect of temperature on the seismic anisotropy of the perovskite and post-perovskite polymorphs of $MgSiO_3$ (Stackhouse *et al.*, 2005a; Stackhouse and Brodholt, 2007).

$CaPtO_3$ is expected to have some advantages over $CaIrO_3$ as a post-perovskite analogue phase, although, like $CaIrO_3$, its ionic mass ratios are very different from those of $MgSiO_3$ and its crystal structure is equally difficult to determine accurately by X-ray diffraction. Unlike $CaIrO_3$, $CaPtO_3$ does not exhibit structural distortion due to the Jahn-Teller effect. It has therefore been suggested that it might provide a better analogue of $MgSiO_3$ (Ohgushi *et al.*, 2008). $CaPtO_3$ is also far more amenable than $CaIrO_3$ to investigation by neutron diffraction, since the thermal neutron absorption cross section of Pt, although not negligible, is over forty times less than that of Ir. The post-perovskite oxides show a variety of magnetic behaviour, as summarised by Shirako *et al.* (2011); $CaRuO_3$ is antiferromagnetic below 270 K, and $CaRhO_3$ and $CaIrO_3$ order with a canted antiferromagnetic structure starting at 90 K and 115 K respectively. In contrast $NaIrO_3$ and $CaPtO_3$ do not order magnetically; $NaIrO_3$ shows Curie-Weiss paramagnetism and $CaPtO_3$ is diamagnetic.

$CaIrO_3$ may be synthesised at atmospheric pressure (see e.g. Lindsay-Scott *et al.*, 2007). Synthesis of $CaPtO_3$ has to date been reported only at high pressures, in the range 4 GPa to 7 GPa (see, for example, Section 6.5.1). $CaPtO_3$ is readily recoverable to atmospheric pressure after synthesis, but high-temperature X-ray powder diffraction measurements made during the present work show that it persists for periods of less than 2 hours, in air, at 850 ^{o}C (Section 6.6). The crystal structure of $CaPtO_3$ has been determined at ambient temperature and pressure using X-ray powder diffraction by Inaguma *et al.* (2008) and by Ohgushi *et al.* (2008).

The present work describes experiments using both $CaIrO_3$ and $CaPtO_3$. I synthesised polycrystalline post-perovskite $CaIrO_3$ during my previous M.Sci. project, and continued in the present work with synthesis of single-crystal $CaIrO_3$. I then synthesised polycrystalline post-perovskite $CaPtO_3$ (with the assistance of Dr. T Taniguchi, in Japan – see Section 6.5.3); this method was used to produce sufficient material for a high-pressure X-ray powder diffraction experiment at the European Synchrotron Radiation Facility (ESRF) and for high-pressure and high-temperature neutron powder diffraction experiments at the ISIS neutron source (STFC Rutherford Appleton Laboratory, UK). I also examined the thermoelastic properties of post-perovskite analogue oxides and fluorides (including $CaPtO_3$) using *ab initio* computer simulation.

The remainder of this thesis describes:

- details of the post-perovskite structure (Section 1.4)
- the basic principles of *ab initio* athermal and molecular dynamics computer simulations (Chapter 2)
- details of computer simulation procedures using the Vienna Ab-initio Simulation Package (VASP) (Chapters 3 and 14)
- computer simulation results for four oxide and three fluoride post-perovskites (Chapter 4)
- an empirical method for predicting ABO_3 post-perovskite stabilisation pressures, based on electronegativity differences between B and O atoms, *t*-factors and perovskite octahedral tilt (Chapter 5)
- synthesis and characterisation of post-perovskites $CaIrO_3$, $CaPtO_3$ and $NaNiF_3$ (not previously reported)(Chapters 6 and 15)
- some aspects of X-ray and neutron diffraction relevant to analysis of post-perovskites (Chapter 7)
- X-ray powder diffraction measurement of the thermoelastic properties of $CaPtO_3$ at high-pressure at the ESRF (Chapter 8)
- time of flight neutron powder diffraction measurements made at ISIS of thermoelastic properties and crystal structure changes of $CaPtO_3$ at high-pressure and at high-temperature (Chapter 9)

- a comparison of experimental and simulation results at high-pressure and at high-temperature (Chapter 10)
- conclusions from the present work, and suggestions for further work (Chapter 11).

Chapters 4, 5, 6, 8 and 9 each conclude with a summary section, and Chapter 10 ends with a discussion. The summary of conclusions is on page 291, followed by a list of further work.

1.4 The post-perovskite structure

The post-perovskite ABO_3 structure is usually described as being composed of BO_6 octahedra, linked by sharing edges into chains that run parallel to [100]. These chains are then linked along [001] by sharing corners, so as to form sheets of octahedra lying parallel to (010); the sheets are separated along [010] by planar interlayers of A-cations. These features are illustrated in Figure 1-1, which shows the crystal structure of post-perovskite $CaPtO_3$ viewed down the *a*-axis. Figure 1-2 shows the octahedra, viewed at 20° to the *a*-axis.

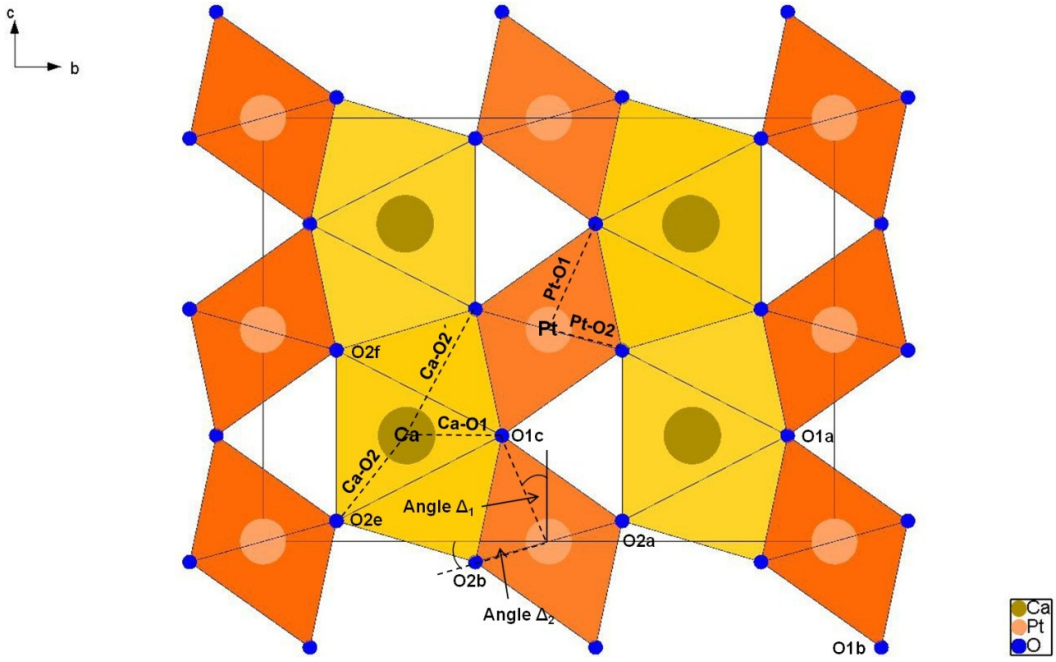

Figure 1-1: The $CaPtO_3$ post-perovskite structure viewed along the *a*-axis. Rods of edge-shared octahedra running parallel to the *a*-axis are linked into corrugated sheets by corner-sharing parallel to the *c*-axis, so as to produce sheets of PtO_6 octahedra lying parallel to (010); these sheets are then separated along the *b*-axis by planar interlayers of Ca ions. The oxygen atoms involved in corner-linking of the octahedra are labelled O1 and the oxygen atoms involved in edge-linking of the octahedra are labelled O2. Bonds and oxygen-oxygen distances referred to in the text are shown as dashed lines. Alternatively, the structure can be pictured in terms of sheets of hendecahedral CaO_8 coordination polyhedra (shown in a lighter colour). These hendecahedra are composed of triangular prisms (with the axis of the prism running parallel to the *a*-axis) capped on two of the three prism faces and linked into sheets (sheet composition CaO_3) by face-sharing along the *a*-axis and by edge-sharing along the *c*-axis. Figure 1-1 to Figure 1-4 use unit cell parameters and atomic coordinates measured for $CaPtO_3$ at 291 K and at ambient pressure using neutron powder diffraction as described in Section 9.2.

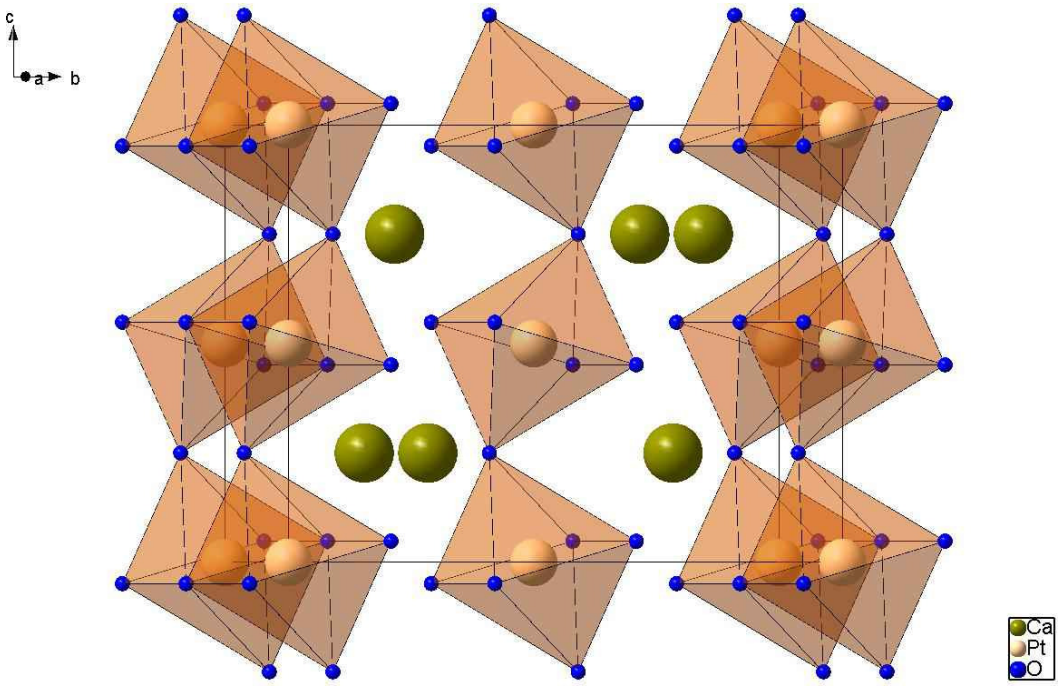

Figure 1-2: The Pt coordination octahedra viewed at an angle of 20° to the *a*-axis.

The space group of the post-perovskite ABO_3 structure is *Cmcm*, with $Z = 4$; the unit-cell parameters of post-perovskite $CaPtO_3$ are: $a \approx 3.13$ Å, $b \approx 9.92$ Å, $c \approx 7.35$ Å, at 291 K. All atoms in the structure are in special positions. The B-cation sits in the 4*a* sites (0, 0, 0) which have site symmetry *2/m* (the *2*-fold axis runs parallel to the *a*-axis of the unit cell). The A-cation and O1 anion sit on 4*c* sites (0, *y*, ¼) which have site symmetry *m2m* (the site-symmetry symbols refer to the *a*, *b*, and *c* axes respectively). For the A-cation, $y \approx 0.25$; for the O1 anion, which corner-links the octahedra along [001], $y \approx 0.92$. The O2 anions, which edge-link the octahedra along [100], sit on 8*f* sites (0, *y*, *z*), with site symmetry *m* (the mirror plane lying perpendicular to the *a*-axis); for O2, $y \approx 0.63$ and $z \approx 0.05$.

The post-perovskite structure is often referred to in terms of the description given on page 19, as by using this approach it is easy to visualise the atomic arrangement and to compare it with the ABO_3 perovskite structure, where the network of BO_6 octahedra is fully corner-linked. However, as pointed out by Sugahara *et al.* (2008), the post-perovskite structure can equally well be viewed as being composed of sheets of

composition AO_3, also lying parallel to (010), formed from linked AO_8 coordination polyhedra (hendecahedra or undecahedra), separated by interlayers of B-cations (see Figure 1-1). The AO_8 hendecahedron is a polygon with 8 vertices and 11 faces, formed from a trigonal prism (with two O1 anions and 4 O2 anions at its vertices), which is capped on two of its prism faces by O2 anions (see Figure 1-3); the axis of the trigonal prism runs parallel to the *a*-axis. These polyhedra are linked parallel to [100] by face-sharing of the basal pinacoids of the trigonal prisms and are linked parallel to [001] by sharing two of the edges in each of the two caps.

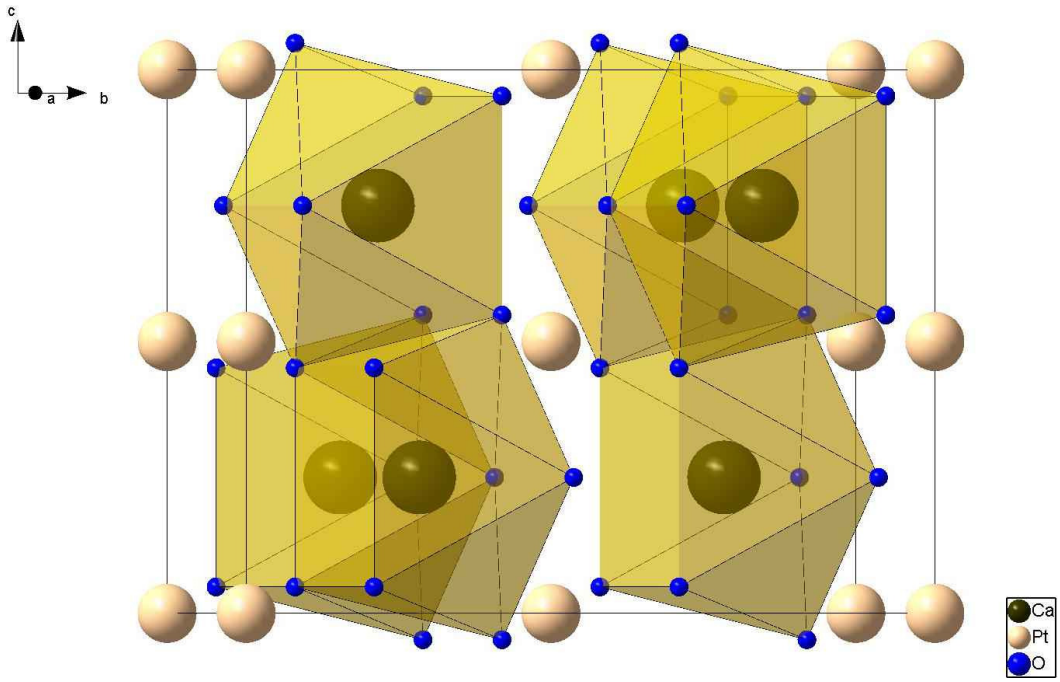

Figure 1-3: The Ca coordination hendecahedra viewed at an angle of 20° to [100]. Void space not occupied by the hendecahedra or the octohedra forms ~37% of the unit cell volume.

Both of the descriptions of the post-perovskite structure given above are correct, but neither provides a complete view of the interactions within the crystal; the same anions form the vertices of both the BO_6 octahedra and the AO_8 hendecahedra, which are closely linked together. In discussing the coordination polyhedron, it should be noted that some previous authors (e.g. Martin *et al.*, 2007a; Bremholm *et al.*, 2011) have assumed that the unit-cell volume is equal to four times the sum of the volumes of the BO_6 octahedra and the AO_8 hendecahedra, but this is not correct; the void space not occupied by the hendecahedra and octahedra forms over one third (~37%) of the unit-cell volume.

It is important to note the restrictions, or lack of them, placed on the cation coordination polyhedra by the crystal symmetry. The point group symmetry of the BO_6 octahedron is *2/m*, with the 2-fold axis running parallel to the *a*-axis; since this point group is centrosymmetric, the B-cation is constrained to lie at the geometric centre of the anion octahedron. The O1 and B ions lie on the mirror plane and the bond distances B-O1a and B-O1b must be equal, with O1a-B-O1b (Figure 1-1) constrained to be linear (in the discussion below, the O1 ions which corner-link the octahedra are referred to as the "*apical anions*"). The four O2 anions which form the remaining vertices of the octahedron (its "*central plane*") are symmetry-related to each other by the 2-fold axis and the mirror plane. The four ions O2a, O2b, O2c, O2d shown in Figure 1-4 are therefore required to be coplanar and are constrained to lie at the corners of a rectangle. The plane defined in this way is required to have indices (*0, k, l*) but *k* and *l* need not be rational (see below).

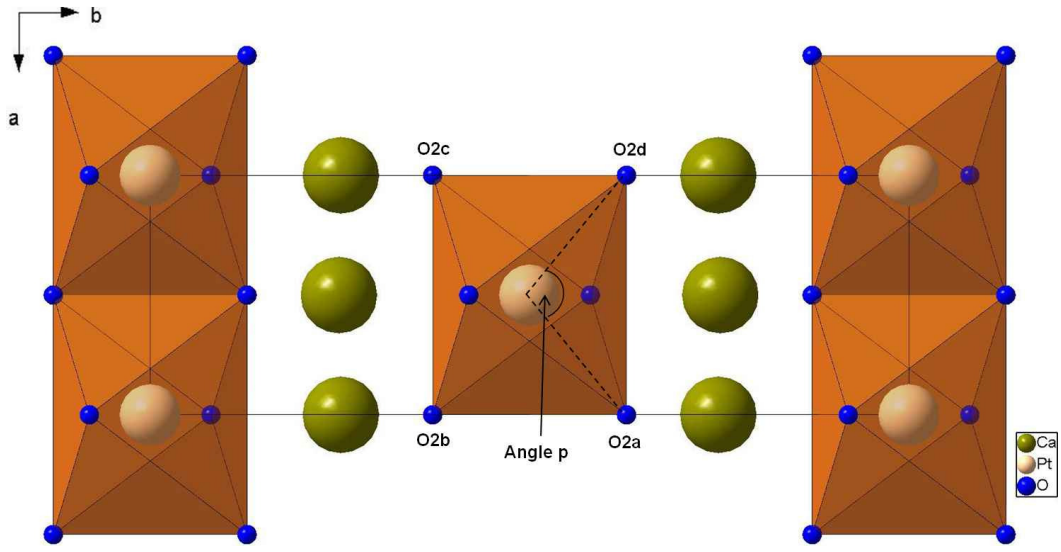

Figure 1-4: The structure viewed along [001] showing the coplanar ions O2a, O2b, O2c and O2d and the angle *p* made by O2a-Pt-O2d. The post-perovskite structure is conventionally defined by the three unit-cell parameters *a*, *b* and *c* and four variable atomic co-ordinates Ca *y*, O1 *y*, O2 *y* and O2 *z*; however, it may also be defined by four bond lengths Pt-O1, Pt-O2, Ca-O1 and Ca-O2 and three inter-atomic angles Δ_1, Δ_2 and *p*, as shown in Figure 1-1 and this Figure.

All four B-O2 bond distances must be equal, but there is no requirement for them to be equal in length to the B-O1 bond. The central plane of the octahedron may be distorted into a rectangle; the angle p = O2a-B-O2d (Figure 1-4) then differs from 90°, with

$$p = 2\tan^{-1}\left(\frac{(a/2))}{\left(((O2y-0.5)b)^2+(O2zc)^2\right)^{1/2}}\right) \quad (1.1)$$

The apices and central plane of the octahedron are crystallographically independent of each other, so two rotation angles

$$\Delta_1 = tan^{-1}\left(\frac{4b(1-O1y)}{c}\right) \quad (1.2)$$

and

$$\Delta_2 = tan^{-1}\left(\frac{cO2z}{b(O2y-0.5)}\right) \quad (1.3)$$

are needed to specify their orientations with respect to the axes of the unit cell (Figure 1-1). Symmetry requires the rotations Δ_1 and Δ_2 to operate about the a-axis (Figure 1-1) but places no other restriction upon them, so the B-O1 bond is not required to be perpendicular to the central plane of the octahedron. The deviation from perpendicularity, defined as the angle q by Kubo *et al.* (2008), is given by $q = \Delta_2 - \Delta_1$; this quantity will be pressure and temperature dependent. Alternatively, instead of using angles Δ_1, Δ_2 and p, the structure may be described using the angles p and q to specify the distortion of the BO_6 octahedron, together with the B-O1-B bond angle, r = $(180 - 2\Delta_1)$°. Note that any description of octahedral rotation must take both Δ_1 and Δ_2 into account; where $\Delta_1 \neq \Delta_2$, the octahedron is not regular but "skewed", even if B-O1 = B-O2.

The point group symmetry of the AO_8 hendecahedron is *m2m*, with the 2-fold axis running parallel to the *b*-axis and the mirror planes lying parallel to (100) and (001). The point group *m2m* is polar and so the *y* coordinate of the hendecahedron (however defined) is not fixed, and there is no requirement that it should be related to the *y* coordinate of the A-cation; the two may move independently of each other along [010]. Along the *a*- and *c*-axes there is, however, no freedom of movement. If the hendecahedron is considered as being formed from a bi-capped trigonal prism, then the

prism axis is constrained to lie parallel to the *a*-axis, with the A-cation constrained to lie half way along the prism. The plane formed by the anions O2e, O2f and O1c (Figure 1-1) must lie parallel to (100), and these three anions must form an isosceles triangle, with the A-cation, when viewed in projection on (100), lying somewhere along the perpendicular bisector of the triangle (Figure 1-1). The two A-O1 bonds in the trigonal prism are therefore required to be equal in length, as are the four A-O2 bonds, but there is no requirement for A-O1 and A-O2 to be equal. The symmetry also requires that the two O2 anions that form the caps of the prism both lie on the mirror plane parallel to (100), exactly half way along the prism axis (Figure 1-1). The length of the A-O2 bond in the trigonal prism and the distance from the A cation to the O2 anions forming the prism caps are not simply proportional to each other, as the former involves the length of the a-axis and the latter does not; the structure may be described in terms of either of these two distances, but the A-O2 bond in the trigonal prism is the shorter of the two and is used here.

The unit-cell parameters may be specified in terms of the four shortest cation–anion bond lengths and the three tilt angles (Δ_1, Δ_2 and p) by the following relationships:

$$a = 2(Pt-O2)\sin\left(\frac{p}{2}\right) \tag{1.4}$$

$$b = 2\left[\begin{array}{l}(Pt-O2)\cos\left(\frac{p}{2}\right)\cos(\Delta_2)+\left\{(Ca-O2)^2-\left(\frac{a}{2}\right)^2-\left[\left(\frac{c}{4}\right)-(Pt-O2)\cos\left(\frac{p}{2}\right)\sin(\Delta_2)\right]^2\right\}^{1/2} \\ +\left\{(Ca-O1)^2-\left(\frac{a}{2}\right)^2\right\}^{1/2}+(Pt-O1)\sin(\Delta_1)\end{array}\right] \tag{1.5}$$

$$c = 4(Pt-O1)\cos(\Delta_1) \tag{1.6}$$

The values of *a* and *c* required in Equation 1.5 are incorporated by substitution of Equations 1.4 and 1.6. This approach, which enables the structural sign of changes in the cell dimensions to be determined, is similar to that used by Knight and Price (2008) for the pyroxene mineral jadeite.

2 *Ab initio* simulation

In this Chapter I describe the background and the general principles of the simulation method which I used, and how they are implemented in the Vienna Ab-initio Simulation Package (VASP) code.

2.1 Theory of a*b initio* simulation

The quantum mechanical computer simulations described in the present work were performed using the VASP computer code (Kresse and Furthmüller, 1996; Kresse *et al.*, 2010). *Ab initio* simulation is well described in Vočadlo and Dobson (1999), Karki *et al.* (2001), Fortes (2004), Gillan *et al.* (2006), Oganov *et al.* (2007) and Stackhouse and Brodholt (2007), and I am indebted to these sources for their inspiration of much of this Chapter.

2.1.1 Schrödinger's equation

Ab initio simulation uses quantum physics with fundamental physical constants such as the mass of the electron to calculate the energy of materials, and hence their properties, such as the equilibrium structure, thermodynamic functions (e.g. enthalpy), equations of state and elastic constants.

Quantum physics resolves the inability of classical electromagnetic theory to explain why the power radiated by an ideal black body is not unlimited at high frequency. Planck proposed that the emitted (or absorbed) electromagnetic energy is quantized, and this led to identification of the wave/particle duality of electromagnetic radiation, as seen in the diffraction of neutrons and X-ray photons. In quantum wave mechanics, the time-independent form of Schrödinger's equation specifies the wave-like character of a system and the eigenvalues of permitted energy states:

$$\hat{H}\Psi_i(\boldsymbol{r}) = E_i\Psi_i(\boldsymbol{r}) \tag{2.1}$$

where Ψ_i is the wavefunction of the ith state of the system at position $\boldsymbol{r}$, and E_i is the energy of this state of the system; $i = 0$ is the ground state configuration of minimum energy. Ψ_i is the eigenfunction and E_i the eigenvalue of the Hamiltonian operator

$$\widehat{H} = -\frac{\hbar^2}{2m}\nabla^2 + V(\boldsymbol{r}) \tag{2.2}$$

where $\hbar = {}^{h}/_{2\pi}$; h is Planck's constant, m is the mass of the particle and $V(\boldsymbol{r})$ is the potential of the particle in the electrostatic field. Schrödinger's equation can be solved exactly for the hydrogen atom (and for single-electron ions) where

$$V(\boldsymbol{r}) = {}^{-e^2}/_{4\pi\epsilon_0 r} \tag{2.3}$$

and r is the distance between the proton and the electron.

In practice, *ab initio* computer simulation techniques do not require empirical parameters, but do require several approximations, which are described below. The principal approximation relates to the exchange-correlation energy.

2.1.2 *Ab initio* simulation for multiple electrons and atoms

Where an atom has more than one electron, or where a system has more than one atom, exact solutions of Schrödinger's equation are not known. The Born-Oppenheimer approximation simplifies the problem by assuming that the atomic nuclei are stationary with respect to the electrons, so that the kinetic energies of the nuclei and electrons can be separated. The ionic motion is then described by classical Newtonian mechanics.

Electrons are fermions with antisymmetric wavefunctions. No two electrons can be in the same quantum state (the Pauli exclusion principle), so electrons with the same spin repel each other. The difference in energy due to this effect is the exchange energy. Because the motion of the electrons is correlated, their wavefunctions are very complicated functions of their positions and so the exchange energy cannot be determined analytically.

In the Hartree approximation the electrons are totally independent and uncorrelated. The approximate wavefunction for an N-electron atom is the product of N one-electron wavefunctions:

$$\Psi_i(\boldsymbol{r}_1, \boldsymbol{r}_2 \ldots \boldsymbol{r}_N,) = \Psi_1(\boldsymbol{r}_1)\Psi_2(\boldsymbol{r}_2) \ldots \Psi_N(\boldsymbol{r}_N) \tag{2.4}$$

The Hartree approximation ignores the effects of exchange energy. The Hartree-Fock approximation takes account of exchange energy, using an antisymmetrised product of N one-electron wavefunctions (spin orbitals) called a Slater determinant.

The energy difference remaining between the energy calculated using the Hartree-Fock approximation and the exact electronic energy calculated using the non-relativistic Schrödinger equation within the Born-Oppenheimer approximation is called the correlation energy. Correlation energy results from the redistribution of electrons due to the contrast between delocalised wave and point charge descriptions. The approximation required in the Hartree-Fock approach is that the wavefunctions can be represented by a Slater determinant, which omits the correlation energy.

The Hartree-Fock approximation works quite well in some cases, but for most materials an alternative approach is required which does take account of the correlation energy.

2.1.3 Density Functional Theory (DFT)

DFT (Hohenberg and Kohn, 1964; Kohn and Sham, 1965) is an *ab initio* approach which takes account of correlation energy. DFT avoids having to calculate wavefunctions for each of the many electrons in a system, because it is based on the electron density. The electron density is a scalar field with only three spatial coordinates regardless of the size of the system. This means that, using DFT, wavefunctions do not need to be calculated for 3N coordinates where N is the number of electrons. DFT is based on the Hohenberg-Kohn theorem (Hohenberg and Kohn, 1964). This states that the electron density uniquely determines the Hamiltonian and hence the ground state energy of the system. The ground state energy of the system is a functional of the electron density. This theorem also states that the energy of the system is the ground state only if the input electron density is the true ground state density.

However, in the Hohenberg-Kohn system the electron-electron energy functionals of the electrons cannot be calculated. The Kohn-Sham approximation (Kohn and Sham, 1965) takes an approach similar to that of Hartree-Fock, by reducing the N electron system to N non-interacting one-electron systems or Kohn-Sham orbitals. The energy

of this synthetic system is the sum of several terms: the kinetic energy of the non-interacting electrons, their energy due to interaction with nuclei, their Coulomb (Hartree) energy, and the exchange-correlation energy. The exchange-correlation energy is not known, so the Kohn-Sham Schrödinger equation must be solved iteratively to obtain a self-consistent electron density. This requires an estimate of the exchange-correlation energy, and this requires a further approximation.

2.1.4 Approximating the exchange-correlation energy: LDA and GGA

Kohn and Sham's approximation for the exchange-correlation energy is that it is the same as that of an electron in an homogenous electron gas with the same electron density as the Kohn-Sham system. It is assumed that the electron density varies only slowly in space. The exchange energy of an homogenous electron gas is known analytically, and its correlation energy has been determined using quantum Monte Carlo calculations (Ceperley and Alder, 1980). This is the local density approximation (LDA). The local spin density approximation (LSDA) relaxes the requirement that spin-up and spin-down electron states be equal, allowing magnetic properties to be simulated. LDA leads to reasonable structural parameters, although bond lengths and unit cell parameters tend to be underestimated relative to experiment. However, it often fails to produce accurate energetic data (Stackhouse and Brodholt, 2007).

The exchange correlation energy in LDA is not dependent on the rapidity of spatial variation of the electron density. In the generalised gradient approximation (GGA) the exchange correlation energy is a function of the gradient of the electron density. The GGA method significantly improves the description of the core electrons, and to some extent that of the valence electrons, compared with LDA. Total energy calculation and the description of magnetic systems are also improved, although GGA overestimates volumes by a few percent and pressures by a few GPa (e.g. Stackhouse *et al.*, 2010; Ammann *et al.*, 2010). An example of the unit-cell volume calculated at different pressures for $MgGeO_3$ using results from GGA, LDA and experiment is shown in Figure 10-1.

2.1.5 Basis set of wavefunctions

The Kohn-Sham orbitals can be implemented for atoms and molecules using a basis set of Gaussian wavefunctions. For solid state crystalline materials the number of wavefunctions required can be reduced by simulating a single unit-cell and considering

it repeated infinitely in all directions. The wavefunctions required can then be expressed as a sum of plane waves whose wave vectors are reciprocal lattice vectors of the crystal. This is known as a basis set. The error inherent in using a plane wave basis set can be reduced by increasing the size of the unit-cell and/or increasing the frequency of Brillouin zone (or $\boldsymbol{k}$-point) sampling of the energy. The (first) Brillouin zone is the primitive cell defined in reciprocal space, whose boundaries are defined by planes related to points on the reciprocal lattice. Waves in a periodic medium can be defined by their behaviour in the Brillouin zone.

2.1.6 Pseudopotentials

The core electrons closest to the nuclei have higher kinetic energy and so require an impractically large number of plane waves. However, these electrons participate less in bonding and have less influence on the properties of the material, which depend almost entirely on the valence electrons. Plane wave pseudopotential theory replaces the wavefunctions of the core electrons with a weaker and more slowly varying pseudopotential (Figure 2-1).

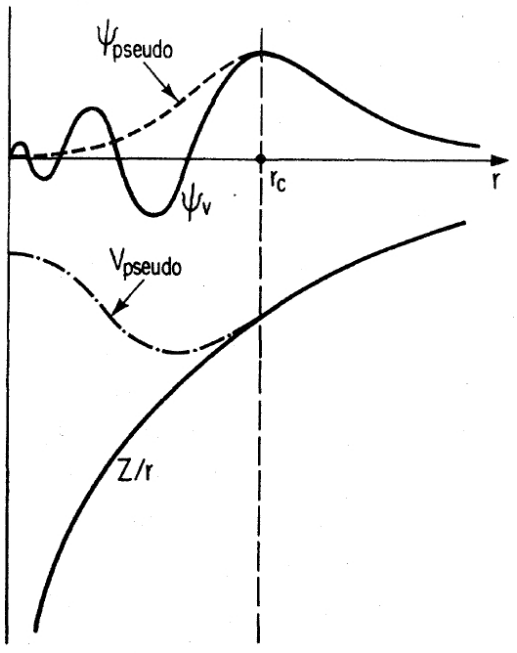

Figure 2-1: Comparison of a wavefunction in the Coulomb potential of the nucleus (solid lines) to the one in the pseudopotential (dashed lines)(Payne *et al.*, 1992). The real and the pseudo wavefunction and potentials match above the cut-off radius r_c.

In the pseudopotential approach, the system is considered to be composed of ionic cores and valence electrons. The force on one ion is the sum of the electrostatic forces due to the other ionic cores, together with the force exerted by valence electrons.

The pseudopotential acts on a set of pseudo-wavefunctions which represent the rapidly oscillating wavefunctions of the valence electrons. The pseudopotential is a frozen core approximation; core orbitals are assumed to be the same in a free atom and in any chemical environment. Using this assumption, the Kohn-Sham equations can then be solved for the valence electrons alone, which interact with the atomic cores via pseudopotentials. I used Projector Augmented Wave (PAW) (Blöchl, 1994; Kresse and Joubert, 1999) pseudopotentials in the present work (Kresse and Furthmüller, 1996; Kresse *et al.*, 2010).

In principle, an infinite basis set of plane waves is required to exactly model the energy. In practice the basis set is truncated at a finite cut-off value of the plane-wave kinetic energy. All plane-waves with a kinetic energy smaller than the cut-off are included in the basis set. The cut-off is chosen so that the properties being modelled converge to an acceptable level of inaccuracy (see Section 3.4).

The GGA gradient function includes a dimensionless enhancement factor, which takes different forms in different GGA pseudopotentials such as those of Perdew and Wang (PW91) (Wang and Perdew, 1991) and Perdew, Burke and Enzerhof (PBE)(Perdew *et al.*, 1996). I used GGA with PW91 with VASP in the present work. I found that using PBE resulted in differences in unit-cell and structural parameters of less than 0.1% when simulating post-perovskite $CaIrO_3$.

More than one GGA PW91 pseudopotential may be available for an element. Non-standard pseudopotentials treat the outer shell core electrons as valence states. These can include the outermost *s*, *s* and *p*, or *s*, *p* and *d* shells. Using these "small core" pseudopotentials with some of the core orbitals treated as valence orbitals gives improved accuracy (Oganov *et al.*, 2007) at high-pressure and for oxides (Hafner *et al.*, 2010: The PAW and US-PP database). This is because under more extreme conditions, more of the core electrons participate in bonding. Harder pseudopotentials require a higher cut-off energy and so are more computationally intensive. I found that the convergence of unit-cell and structural parameters improved significantly using harder

pseudopotentials for some elements, with less improvement for others (see Section 3.5). The DFT results from VASP reported here use harder pseudopotentials (Kresse *et al.*, 2010) in accordance with VASP developer recommendations (Hafner *et al.*, 2010) where they give significant improvements.

2.2 Simulating pressure

VASP simulations may be athermal (effectively at 0 K), or may use molecular dynamics (MD) to simulate higher temperatures. Athermal simulations in the present work simulated the effect of pressure by specifying a constant volume and then relaxing the unit-cell parameters and the positions of the ions, subject to the forces between the ions and electrons, until the ground state minimum energy was achieved. The electron density was calculated iteratively for each set of ionic positions until self-consistency was achieved. This resulted in an external (bulk) pressure and an internal energy of the ion-electron system, both of which depended on the constant volume specified.

I initially set the volume to that at approximately 0 GPa pressure. Then I decreased the volume in steps to produce results at successively higher pressures. The minimum energy E_0 and volume V_0 at 0 K were calculated from the set of simulated volumes and energies by fitting an isothermal equation of state (EOS) to the *E-V* data (see Section 3.9.1). The slope of the *E-V* curve represents the pressure at a particular volume.

I carried out athermal simulations on the post-perovskites $MgSiO_3$, $MgGeO_3$, $CaIrO_3$, $CaPtO_3$, $NaMgF_3$, $NaZnF_3$ and $NaNiF_3$, on the perovskites $MgSiO_3$, $MgGeO_3$, $CaSiO_3$, $NaMgF_3$, $NaZnF_3$ and $NaNiF_3$, and on the compounds Mg_2SiO_4 and $Ca_2Mg_4Si_3O_{12}$ (see section 4.4.1).

2.3 Simulating temperature

DFT can be used for athermal (static) simulations (at 0 K) where there is no kinetic energy from thermal motion, neglecting even zero-point energy. Including zero-point energy would expand unit-cell parameters by about 0.2% (Wu and Cohen, 2006). However, the effect of atomic vibration on thermal pressure and on the post-perovskite structure is important for post-perovskite $MgSiO_3$ at the pressure and temperature of the D" zone, and for laboratory experiments on post-perovskite analogues such as

$CaPtO_3$ and $CaIrO_3$. Simulation techniques for modelling thermal vibration include lattice dynamics (LD) and molecular dynamics.

LD describes a system in terms of a simulation box which contains harmonic oscillators whose frequencies vary with cell volume. It calculates the motions of atoms as wave-like lattice vibrations or phonons using the quasiharmonic approximation. This assumes that atoms vibrate like a quantized harmonic oscillator (see Figure 2-2a). It ignores anharmonic effects from phonon-phonon interactions, which are more significant at higher temperatures, but less significant as pressure increases.

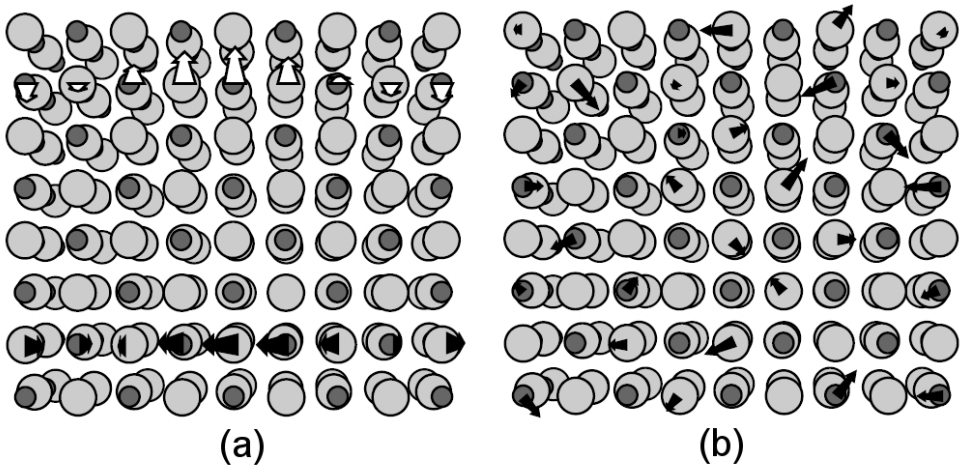

Figure 2-2: Schematic simulation boxes for LD (*a*) and MD (*b*). (*a*) In a lattice-dynamics calculation the motion of the individual particles is treated collectively as a vibrational wave (phonon) in the crystal. (*b*) MD simulations take account of the explicit motion of individual particles in the simulation box (Vočadlo and Dobson, 1999).

Ab initio MD calculates the ionic positions and the electronic energy functional for a time step using DFT. It then calculates the change in the positions and momenta of the nuclei from one time step to the next one using Newton's equations of motion, subject to the electrostatic forces (see Figure 2-2b). These calculations are repeated iteratively for a large number of time steps. MD calculates time averaged structural and thermodynamic properties.

The calculation of electron energies assumes that the electron sub-system is in its ground state, and that the nuclei are completely static at their positions at the end of each time step (the Born-Oppenheimer approximation). It also assumes that the total

energy – the kinetic energy of the nuclei and the ground state electron energy – is conserved. The volume of the unit-cell is fixed. Calculating the motion of the nuclei classically ignores quantum effects, so MD is less accurate at low temperatures. However, this explicit calculation of nuclear motion takes account of anharmonic effects, making it more accurate than LD at high temperatures. In MD the temperature is calculated from the average kinetic energy of the nuclei. The constant-temperature MD calculations in the present work used a statistical sampling Nosé thermostat with an Andersen thermostat (Andersen, 1980; Nosé, 1984; Alfè and Gillan, 2007; Kresse *et al.*, 2010). The pressure or stress is calculated from the time average of the DFT stress tensor.

I carried out MD simulations on the post-perovskites $CaIrO_3$, $CaPtO_3$ and (for calibration with Stackhouse and Brodholt (2007) – see Section 3.2) $MgSiO_3$.

3 Details of the *ab initio* calculations

This Chapter describes how I configured the VASP code for simulation of post-perovskites at high-pressure and high-temperature, and outlines my approach to analysing the results.

3.1 Athermal simulation configuration

For the athermal simulation of post-perovskite and orthorhombic (*Pbnm*) perovskite I used a 20 atom supercell (Z = 4 unit-cells) or simulation box (e.g. Stackhouse *et al.*, 2005a; Stølen and Trønnes, 2007).

3.2 MD simulation configuration

I used MD rather than LD for simulation of thermal motion, because MD is more accurate than LD at high temperatures. The MD simulation method used in the present work was based on that described in Stackhouse and Brodholt (2007), with additional information on VASP parameter selection and the averaging of atomic positions (Stackhouse, 2009).

For MD simulation and for gamma point (Brillouin zone centre) athermal simulations I used a 60 atom supercell which was a 3 x 1 x 1 multiple of the 20 atom athermal simulation unit-cell (Stackhouse *et al.*, 2005a). The 60 atom supercell was required for MD simulation in order to achieve the required accuracy. A larger supercell would improve the accuracy of the simulation by reducing the size of the Brillouin zone in reciprocal space, but this would require more computer processing time.

In MD simulation, the atomic positions were relaxed over a number of time steps, starting with a specified temperature, while the unit-cell parameters *a*, *b* and *c* remained fixed. I carried out simulation runs for post-perovskite $CaIrO_3$ at temperatures between 298 K and 1200 K. My post-perovskite $CaPtO_3$ simulation temperatures between 291 K and 973 K corresponded to the temperatures used in my neutron diffraction study of post-perovskite $CaPtO_3$ at the HRPD ISIS facility (Section 9.2).

The atomic positions for post-perovskite $MgSiO_3$ used in the present work at temperatures between 500 K and 4000 K at an (uncorrected) pressure of 136 GPa were taken from VASP XDATCAR files produced by S. Stackhouse using VASP MD (Stackhouse and Brodholt, 2007). To check for consistency of results, I carried out a simulation of post-perovskite $MgSiO_3$ at 1000 K which produced similar results to those of Stackhouse and Brodholt (2007), with a unit-cell volume 0.39% smaller.

3.3 Athermal simulation parameters used in VASP

The *ab initio* simulation parameters are specified for the VASP code using four input files: POTCAR, POSCAR, KPOINTS and INCAR.

POTCAR file

The POTCAR file contains the pseudopotentials for each element. The POTCAR files for each of the elements which constitute the material to be modelled were concatenated into one file; so for $CaIrO_3$ the POTCAR files for Ca, Ir and O were concatenated. The concatenation sequence must correspond to the sequence of the elements in the POSCAR file.

POSCAR file

The POSCAR file specifies the unit-cell geometry and the ionic positions. For MD, POSCAR also contains starting ionic velocities and predictor-corrector coordinates. Each VASP run produces a file CONTCAR which is an updated version of POSCAR, containing the values of the POSCAR variables at the end of the run. This can be used directly as the POSCAR input file for a subsequent run, since it represents a partially relaxed starting point for the unit-cell geometry and ionic positions at a given volume. For MD, the refined velocities and predictor-corrector coordinates in CONTCAR specify an improved set of lattice vibrations which is nearer equilibrium at a given temperature.

KPOINTS file

The KPOINTS file specifies the $\boldsymbol{k}$-point sampling of the Brillouin zone. In the present work I used automatic $\boldsymbol{k}$-mesh generation with Monkhorst-Pack $\boldsymbol{k}$-point sampling

(Monkhorst and Pack, 1976).

INCAR file

The INCAR file specifies parameters which determine how VASP is to do the simulation. Guidelines on their values are given in the VASP manual (Kresse *et al.*, 2010). The same INCAR parameters were used in the present work for all VASP multiple ***k***-point simulations, and the values used are shown in Appendix A (Chapter 13).

3.4 VASP parameter optimisation for convergence

3.4.1 Convergent properties

The VASP code iteratively improves the plane wave basis set until the electronic groundstate is achieved to within the energy limit specified by the EDIFF parameter, so VASP automatically carries out energy convergence to within the value specified in EDIFF. An accurate result requires that the simulated properties should also converge. Three other simulation parameters affect the convergence of these properties and therefore the accuracy of the simulated structure; these are the number of ***k***-points, the plane wave basis set cut-off energy ENCUT, and the energy cut-off for augmentation charges ENAUG.

Convergence is affected by the number of ***k***-points specified because the error inherent in using a plane wave basis set can be reduced by increasing the frequency of ***k***-point (Brillouin zone) sampling. This error may also be reduced by using a larger supercell (and hence a smaller Brillouin zone), at the expense of larger computer processing time. A higher value of ENCUT increases the number of waves in the plane wave basis set, increasing the accuracy of the simulation. A higher value of ENAUG increases the cut-off for augmentation charges.

The combined effect of the values specified for the number of ***k***-points, EDIFF, ENCUT and ENAUG must together be sufficient to produce the convergence required for the properties being examined. However, larger numbers of ***k***-points and larger values of EDIFF, ENCUT and ENAUG increase simulation run times. Very long run times make MD simulation less feasible. The critical properties in the present work for

which convergence was tested were those defining the post-perovskite structure: the 3 unit-cell parameters and the 4 atomic coordinates, which are together equivalent to the 4 bond lengths and 3 angles needed to specify the structure (see Section 1.4).

3.4.2 Energy convergence using the EDIFF parameter

I used a value for EDIFF of 10^{-4} eV when testing convergence by increasing the number of ***k***-points, and 10^{-6} eV thereafter for athermal simulations (e.g. Stackhouse *et al.*, 2010). An EDIFF value of 10^{-7} eV instead of 10^{-6} eV for post-perovskite $CaIrO_3$ resulted in mean differences in the unit-cell parameters of 0.006% and in the 4 atomic coordinates of 0.008%. I concluded that an EDIFF value of 10^{-6} eV was sufficiently small for the accuracy required for athermal structural simulation in the present work.

3.4.3 Convergence using *k*-points, ENCUT and ENAUG

The ***k***-point sampling of the Brillouin zone, and the values of the plane-wave energy cut-off ENCUT and the augmentation energy ENAUG specified in INCAR, were tested and selected to give acceptable convergence of the internal energy and of the 7 structural parameters.

A commonly published DFT simulation criterion for the convergence of energy between simulations using different sets of parameter values is the difference in the internal energy of the unit cell from one set of simulation parameters to the next, in meV/atom.

In the present work the internal energy was converged to less than 1.4 meV/atom when simulating $MgSiO_3$, $CaPtO_3$, $CaIrO_3$, $MgGeO_3$, $MgHAlO_3$, $NaMgF_3$, $NaNiF_3$ and $NaZnF_3$ (see Table 14-1). Good practice is to converge to less than 5 meV/atom (Côté, 2008); for example, criteria used in previous work include 2.3 meV/atom for $MgGeO_3$ (Kubo *et al.*, 2008) and 1 meV/atom for fayalite (Stackhouse *et al.*, 2010).

The convergence of the internal energy was tested by increasing the number of ***k***-points (using the default POTCAR values for ENCUT and ENAUG, with EDIFF = 10^{-4} eV) from 3x3x3 through 4x4x4, 5x5x5, 6x6x6 to 9x5x5, and measuring the difference in energy per atom. An equally-spaced Brillouin zone Monkhorst-Pack ***k***-mesh (*n*x*n*x*n*) has been used successfully for the post-perovskite structure in previous work (e.g. Stackhouse *et al.*, 2005a). In principle, the mesh dimensions

should be inversely proportional to those of the unit-cell. So for a post-perovskite with a smaller *a*-axis unit-cell dimension, n_1 in an n_1 x n_2 x n_3 mesh should be larger than n_2 or n_3. A 5x5x5 mesh results in 27 irreducible Monkhorst-Pack ***k***-points, while 9x5x5 (Stølen and Trønnes, 2007) results in a denser mesh of 64 irreducible ***k***-points. In practice 5x5x5 was found to be sufficient to produce convergence. The perovskite unit cell has smaller differences between the orthorhombic unit-cell dimensions, so the equally-spaced 5x5x5 ***k***-points mesh was also appropriate for the perovskite structure.

After the ***k***-point convergence had been checked, the ENCUT and ENAUG cut-off energies were increased. I found that a value of 800 eV was sufficient to meet the required convergence criteria for both post-perovskite and perovskite compounds. It is desirable to use the same ***k***-point sampling, ENCUT and ENAUG when comparing internal energy differences between bulk phases with different compositions, for example when examining the transition between perovskite and post-perovskite phases (Kresse *et al.*, 2010).

As a result of convergence checking, the VASP parameters KPOINTS = 555, ENCUT = 800 and ENAUG = 800 with EDIFF = 10^{-6} were used for all VASP athermal simulation of post-perovskites and perovskites.

As an example, Figure 3-1 shows, for $CaPtO_3$, the convergence of the internal energy, the 3 unit-cell parameters and the 4 atomic coordinates by adjusting the ***k***-points, ENCUT and ENAUG parameters, as described below. Appendix B (Chapter 14) shows data on convergence for the other post-perovskites and perovskites simulated in the present work.

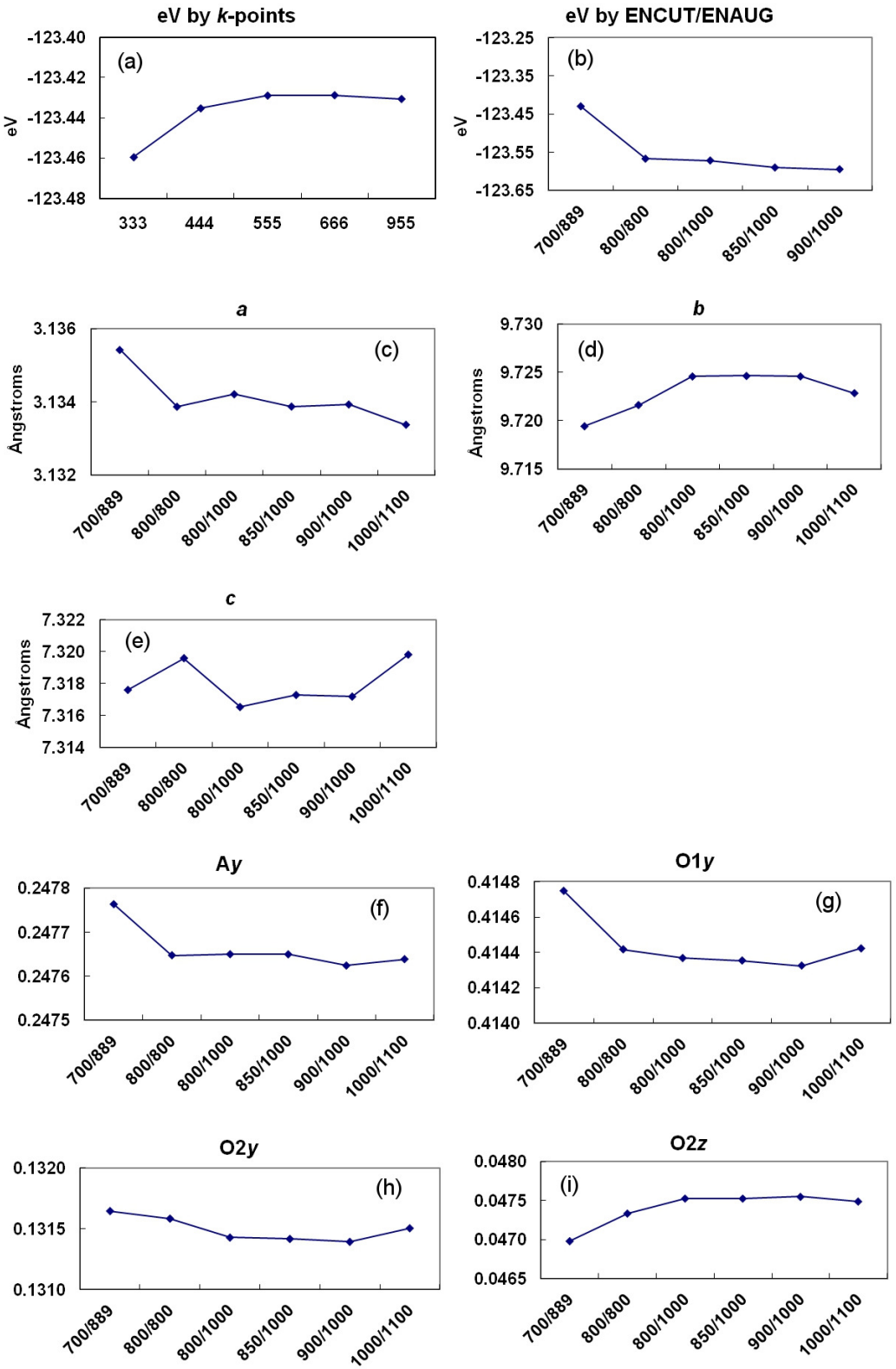

Figure 3-1: Post-perovskite $CaPtO_3$: Convergence of unit-cell (Z = 4) energy and structural parameters. *x*-axis labels *nnn* in (a) represent *nxnxn k*-points, and in (b) to (i) *x*-axis labels *nnn*/*mmm* represent ENCUT/ENAUG values in eV. Numbers of irreducible *k*-points are 8 (333 and 444), 27 (555 and 666) and 45 (955).

3.5 Pseudopotentials used

There may be more than one VASP PAW pseudopotential for any one element (see Section 2.1.6). Initially I used the standard potentials, with the exception of O where the harder pseudopotential was used, but these did not always produce satisfactory results (as discussed here). I calculated the V_0 unit-cell volumes at 0 GPa using a Birch-Murnaghan third order energy-volume (E-V) EOS (see Section 3.9.1). I also calculated V_0 and the $a_0\ b_0\ c_0$ unit-cell parameters at 0 GPa using a Birch-Murnaghan third order pressure-volume (P-V) EOS. I compared the pressures given for the same volumes by the two EOSs and found that they differed significantly for both $CaIrO_3$ and $CaPtO_3$; the V_0 calculated from the P-V EOS was ~5% less than that calculated from the E-V EOS, and the bulk modulus K_0 ~18% more, because the pressure was not as well converged with increasing ENCUT as the other convergence criteria.

The most direct solution was to increase ENCUT to improve pressure convergence. However, warning messages from VASP indicate that the standard Ca pseudopotential is too soft to increase ENCUT beyond 600 eV. The only Ir pseudopotential available is also too soft to increase ENCUT beyond 800 eV. The solution was to use a harder Ca pseudopotential for both $CaIrO_3$ and $CaPtO_3$ with ENCUT=800 eV, which also reduced the difference between the E-V and P-V calculated values of V_0 to less than 2%.

3.6 MD unit-cell relaxation

In MD simulation of post-perovskite $CaPtO_3$ at 869 K, the simulated temperature of the system took about 1000 time steps to equilibriate, so that the atomic thermal velocities recorded in the CONTCAR file approximated to thermal equilibrium phonons. Lower temperature runs equilibriated more slowly.

The temperature, T, during each successive time step varied as the momentum and kinetic energy of the atoms changed. The temperature equilibriation of the system was checked by plotting the time step temperatures against time; Figure 3-2a shows an unequilibriated run for post-perovskite $CaPtO_3$ at a specified temperature of 869 K, and Figure 3-2b shows an equlibriated run at the same temperature. Equilibriated systems displayed more regular temperature oscillations. The standard error (standard

deviation/√number of observations) in the mean temperature over all time steps for equilibriated simulations was typically less than 0.2% of the value of *T*.

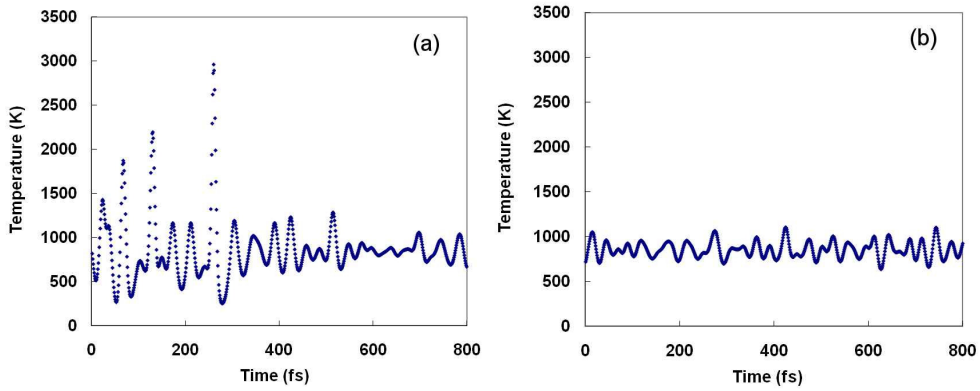

Figure 3-2: MD simulated temperature by time step for post-perovskite $CaPtO_3$ (a) unequilibriated temperature (mean temperature = 870(321) K) (b) equilibriated temperature (mean temperature = 870(90) K). The numbers in parentheses are standard deviations of the samples and refer to the least-significant digits.

The variation in temperature between steps resulted in bulk and axial pressures varying between steps. The standard VASP code did not support constant-pressure MD, so some manual adjustment of the cell parameters was necessary. The objective was to find a combination of unit-cell parameters such that the mean bulk pressure was less than 0.5 GPa from the target pressure, and the mean axial pressures each differed from the mean bulk pressure by less than 0.5 GPa (e.g. Stackhouse and Brodholt, 2007). This was in effect a manual relaxation of the unit-cell parameters for a given temperature. The target pressure was 0 GPa for the MD simulation of $CaIrO_3$ and $CaPtO_3$ post-perovskites, and 136 GPa for the MD simulation of post-perovskite $MgSiO_3$.

The manual relaxation of the unit-cell parameters for each temperature was carried out iteratively, usually using simulation runs of 200 time steps. This number of time steps represented a reasonable compromise between the reproduceability of results, the computer processing time required and the job turnround using the HECToR UK national high-performance computing service. The equilibriation achieved by each run was preserved for further refinement by using the CONTCAR output file (specifying partially relaxed atomic positions and atomic velocities) as the POSCAR input file for

the following run. After refining unit-cell parameters using 200-step runs, a 1000-step run was made for confirmation that the mean bulk and axial pressures were acceptable before committing to an 11 hour production run using 4000 time steps (4 ps). A 4ps run typically used 128 processing cores (4 cores/node) for 8½ to 11 hours, with a resource usage of ~2.5 allocation (computer processing) units/time step. These statistics apply to the HECToR XT4 configuration then in use. This has been upgraded at the time of writing to the new XT6 configuration which uses 24 cores/node. The tradeoff between the number of cores used and the degree of parallelisation (parameter NPAR) to run VASP efficiently is different using XT6, and will need to be optimised for further MD production runs.

The initial values of the unit-cell parameters *a*, *b* and *c* in the POSCAR file for each temperature were based on the ratios *b/a* and *c/a* from experimental values at that temperature. The value of *a* was estimated from experiment and adjusted for the larger value expected as a result of using the GGA approximation. The values of *b/a* and *c/a* were then refined in successive simulations by adjusting the *a*, *b* and *c* values in the POSCAR file.

3.7 MD simulation parameters

Some VASP parameters defined in INCAR have different values for MD compared with those for athermal simulation. Symmetry is switched off (ISYM=0), and IBRION=0 specifies that Newton's equations of (ionic) motion are to be used. ISMEAR is set to -1, specifying that wavefunction partial occupancies are set using Fermi smearing, with SIGMA specifying the width of the smearing in eV. I set SIGMA to k_BT where k_B is the Boltzmann constant and T is the initial MD temperature specified in INCAR parameter TEBEG in K. SIGMA ranges from 0.025 eV at 298 K to 0.344 eV at 4000 K.

When the EDIFF energy convergence target for the plane wave basis set was set to 10^{-5} eV instead of 10^{-4} eV for post-perovskite $CaIrO_3$, it resulted in a mean difference in the 4 atomic coordinates of 0.11%. I concluded that an EDIFF value of 10^{-4} eV was sufficiently small for accurate MD structural simulation (e.g. Stackhouse, 2009).

ENCUT and ENAUG were set to 800 eV as for athermal simulation, except for gamma point simulation of post-perovskite $MgSiO_3$ (see Section 3.8) where ENCUT=500 and

ENAUG=2000 were used for compatibility with previously recorded data (Stackhouse and Brodholt, 2007). This difference in ENCUT and ENAUG produced a difference in volume at 0 GPa of less than 0.02%.

Several INCAR parameters are MD-specific. POTIM = 1 specifies a 1 fs time step (10^{-15} seconds) for ionic motion. NSW specifies the number of ionic relaxation (time) steps. This was set to 4000 (4 ps) for all runs except the post-perovskite $MgSiO_3$ simulations by Stackhouse and Brodholt (2007) at or above 3000 K, where 6000 steps (6 ps) were used. The initial temperature is specified in TEBEG. Because the centre of mass is conserved there are only $3(N_{ions}-1)$ degrees of freedom, so the real simulation temperature T = TEBEG x $N_{ions}/(N_{ions}-1)$. Therefore TEBEG was specified as T x $(N_{ions}-1)/N_{ions}$ where T was the required temperature to be simulated. For post-perovskite $CaPtO_3$, T was chosen to match the experimental temperatures at which structural measurements were made using neutron diffraction at the HRPD ISIS facility. I used the thermostat parameter SMASS=0, which controlled the frequency of the temperature oscillations during the simulation so that they had a period of about 40 time steps (Stackhouse, 2009). The Brillouin zone was sampled at the gamma point only.

3.8 Gamma point simulation

MD simulation is computer-intensive because it calculates the ground state energy not just once but for each of (typically) several thousand time steps. The VASP MD simulation used in the present work therefore sampled the Brillouin zone at the gamma point only, in order to achieve reasonable simulation run times (see e.g. Stackhouse *et al.*, 2005a).

However, sampling the Brillouin zone at the gamma point produced a different unit-cell volume at 0 K compared with sampling at multiple ***k***-points, such as the 27-point irreducible ***k***-point grid (=555) used here for athermal simulations. This difference in cell volume was ~0.05% in post-perovskite $MgSiO_3$ at 136 GPa, and 0.91% in V_0, where V_0 is the volume at 0 K and 0 GPa. The difference in cell volume was 0.67% and 0.01% in V_0 for post-perovskite $CaPtO_3$ and $CaIrO_3$ respectively.

Comparison of the behaviour of different post-perovskite structures as a function of pressure and temperature required the plotting of structural parameters against V/V_0; at 0 K for a range of pressures, and at 0 GPa for a range of temperatures (where for $MgSiO_3$ V_0 is the volume at 0 K and 136 GPa)(see Sections 4.2, 10.4 and 10.5). The difference in V_0 between the gamma point simulation (used for high temperatures) and multiple ***k***-point simulation (used for high-pressures) means that plotting structural parameters from both high-pressure and high-temperature simulations against V/V_0 would result in a step change in the plot at $V=V_0$.

This problem was addressed by using athermal gamma point sampling to simulate post-perovskites at high-pressure as well as at high-temperature. This gamma point athermal simulation used a supercell of 60 atoms, and energy cut-off parameters, which were the same as those used in the MD simulations (see Section 3.7). So where both high-temperature and high-pressure simulation results are plotted against V/V_0, the ***k***-point sampling and other simulation parameters were as far as possible identical for both simulations. The same approach was taken for $CaPtO_3$ and $CaIrO_3$.

3.9 Post processing of VASP output

3.9.1 Calculating the athermal equation of state

An EOS describes how the volume of a compound varies as a function of pressure or temperature. VASP athermal simulation describes the behaviour of a compound under varying pressure at a constant temperature of effectively 0 K. The internal energy *E*, pressure and volume are reported at the end of a simulation run. An isothermal EOS describes the relationship between the volume of the compound at a constant temperature and its internal energy (E-V EOS) or pressure (P-V EOS).

The third order Birch-Murnaghan pressure-volume (P-V) EOS (BM3EOS)(e.g. Poirier, 2000) takes account of finite strain in the material, and of the increase in incompressibility with pressure. It may be written as:

$$P = \frac{3}{2}K_0\left[(x)^{\frac{7}{3}} - (x)^{\frac{5}{3}}\right]\left[1 + \frac{3}{4}\left(K_0' - 4\right)\left((x)^{\frac{2}{3}} - 1\right)\right] \quad (3.1)$$

Where $x = \left(\frac{V_0}{V}\right)$, P is the pressure, K is the incompressibility $-V\frac{dP}{dV}$, K' is the derivative of K with respect to pressure, V is volume of the unit-cell and the subscript *0* denotes a value at 0 GPa.

The integral of PdV defines the energy-volume (E-V) EOS, with E_0 being the internal energy of the unit-cell at 0 GPa and 0 K. This is given by:

$$E = \frac{9}{4}K_0V_0x\left(\frac{1}{2}(x)^{\frac{1}{3}} - (x)^{-\frac{1}{3}}\right) + \frac{9}{16}K_0V_0x\left(K_0' - 4\right)\left(x - 3(x)^{\frac{1}{3}} + 3(x)^{-\frac{1}{3}}\right) + E_0 - \frac{9}{16}K_0V_0\left(K_0' - 6\right) \quad (3.2)$$

In some cases where the values were insufficient for the third order P-V EOS I used a second order Birch-Murnaghan P-V EOS (BM2EOS), where K'_0 is fixed at a value of 4.

I also used a Birch-Murnaghan third order P-V EOS to represent the pressure dependence of the axes of a post-perovskite compound, of its BX_6 octahedra and AX_8

hendecahedra, and of its interatomic bonds. For axes and bonds, $x = \left(\frac{{i_0}^3}{i^3}\right)$ where i is the unit-cell parameter or bond length. For octahedra and hendecahedra, V is the volume of one octahedron or hendecahedron.

The bulk incompressibility K at a given pressure P is given by

$$K = -V_P \frac{dP}{dV} \tag{3.3}$$

where V_p is the volume at pressure P, with $\frac{dP}{dV}$ found by differentiating the P-V EOS with respect to V. This is useful for calculating K at (for instance) 125 GPa for $MgSiO_3$.

E-V and P-V EOSs were calculated from VASP simulation data using the programs BM3EV and BM3PV written by Dr. I.G. Wood, Prof. L. Vočadlo and others at UCL.

P-V EOSs were calculated from experimental data using the EOS-fit program (Angel, 2000, 2001) weighted by errors in volume and pressure, described in Chapters 8 and 9.

3.9.2 Calculating structural data

The VASP output file OUTCAR specifies the relaxed value of the unit-cell parameters a, b and c at a calculated pressure as a result of specifying a fixed volume. It also specifies the positions of the atoms after relaxation within the unit-cell. I constructed a structural spreadsheet template in Excel which calculated interatomic distances, angles, and (for the ABX_3 post-perovskites) the variable atomic coordinates A y, X1y, X2y and X2z, using the unit-cell parameters and atomic positions.

The post-perovskite spreadsheet template also calculated the volumes of the AX_8 hendecahedron and BX_6 octahedron. The hendecahedron volume excludes the void volume which is not part of either the hendecahedra or the octahedra in a unit-cell. The hendecahedron volumes as calculated in Martin *et al.* (2007a) and in Bremholm *et al.* (2011) include void volume and are therefore incorrect; the void volume is typically ~37% of the unit-cell volume (see Figure 4-7f). It should be noted that the approximation to the hendecahedron volume used in Kubo *et al.* (2008) gives a volume

which differs from the exact value by less than 1% of unit-cell volume.

The perovskite version of the spreadsheet similarly calculated interatomic distances and angles (see Section 5.12).

3.9.3 Calculating transition pressures

VASP athermal simulation can be used to predict the pressure at which a polymorphic compound makes the transition from one phase to another. Two phases coexist in thermodynamic equilibrium at a given pressure and temperature when their Gibbs energies *G* are equal. Since

$$G = E + PV - TS \tag{3.4}$$

then at 0 K this condition is equivalent to their enthalpies *H* being equal:

$$H = E + PV \tag{3.5}$$

A phase change can be predicted from VASP athermal simulation (at 0 K) by finding the pressure where the enthalpy of the two polymorphs is the same. This approach may also be used to predict when the enthalpy balance will favour one direction of a chemical reaction. Note, however, that in both cases the activation energy required for the phase change or reaction is not simulated, and that the effect of temperature on the pressure required for a phase change is not simulated either. The additional pressure required at a temperature above 0 K may be estimated by multiplying the temperature by the Clapeyron slope dP/dT, where this can be estimated for the phase transition. Note that the Clapeyron slope dP/dT ($= \Delta S/\Delta T$) is only constant at finite temperatures, since at 0 K $\Delta S = 0$.

3.9.4 Processing MD results

Calculating atomic positions

The temperature and pressure data were extracted from the VASP output files and processed using Excel. These data included external (bulk) pressure and the stresses in the *x, y, z, xy, yz* and *zx* directions for each time step. Once the unit-cell parameters had been adjusted for a specified temperature so that the mean bulk pressure and axial pressures met the required targets, the post-perovskite structure at that temperature was analysed.

The position of each atom in the 60 atom supercell was recorded by VASP for each time step as the *x, y* and *z* fractions of the unit supercell parameters *a, b* and *c* in a file called XDATCAR.

The thermal motion of atoms during MD simulation meant that atoms on or near the boundaries of the supercell might move outside the supercell. In this case VASP recorded their fractional position in the adjacent supercell. I wrote a FORTRAN program MDAVGG to produce mean *x, y* and *z* fractions over all time steps for each of the 60 atomic positions in the supercell for a given temperature, taking account of atomic motions crossing supercell boundaries. The mean 60 atom supercell positions were then reduced to 20 atom cell positions using Excel, and from these the variable atomic coordinates A *y*, O1 *y*, O2 *y* and O2 *z* were calculated.

The positions of the atoms can be visualised using two FORTRAN programs which I wrote to process the VASP XDATCAR file. Program MDPOS extracts the positions of specified atoms over successive MD simulation time steps so that Excel can plot them. Program MDDEN sums atomic densities for atoms between selected fractional atomic coordinates over successive time steps in a 3 dimensional grid so that they can be plotted using gnuplot (see Section 10.7).

Calculating structural data for MD

The structural spreadsheet template (see secton 3.9.2) determined the standard error in the mean for the post-perovskite $CaPtO_3$ and $CaIrO_3$ MD structural parameters. The errors in the unit-cell parameters were estimated by determining the standard error in the mean of the *x, y* and *z* axial stresses over the total number of time steps in the MD simulation. The axial P-V EOSs derived from the VASP athermal simulation were then used to find the change in each unit-cell parameter corresponding to a one standard error change in axial stress. This change in unit-cell parameter was used as an estimate of the standard error in the mean of that parameter. The standard error in each interatomic distance, angle and volume was then calculated by propagating errors in unit-cell parameters and atomic coordinates.

Calculating mean, mode and median bond lengths

The mean, mode (most frequently occurring value) and median (mid-point of the population) bond lengths for MD simulated post-perovskite octahedral bonds were calculated from the VASP XDATCAR file. I wrote a FORTRAN program MDLEN which calculated the bond lengths between specified pairs of atoms in the 60 atom MD supercell, taking account of atomic motions crossing supercell boundaries, and summing the number of occurrences of bond lengths over a specified number of bins. The results were analysed in Excel to find the mean, median and mode for each bond type, and plotted by bond type and compound (see Section 4.3).

4 Simulation results

4.1 Introduction

In this Chapter I describe the structural systematics of post-perovskites calculated in compression and expansion, using DFT athermal simulation and finite temperature MD simulation. This chapter also describes the results of the athermal simulation of phase transitions in some post-perovskite-related materials. Finally I describe the Jahn-Teller effect and its relevance to post-perovskite analogues. The advantage of examining post-perovskite structures using comparator simulations is that results can be calculated consistently over a wide range of pressure.

The range of simulated pressures used in this chapter corresponds to a wide range of V/V_0 values, from 1.0 to 0.7; $V/V_0 = 0.7$ corresponds to ~133 GPa in $MgSiO_3$, ~125 GPa in $CaPtO_3$ and ~51 GPa in $NaZnF_3$, for example. Chapter 10 compares experimental results for post-perovskite oxides over the smaller range of compression available from experiment with the simulated results described in this Chapter, and also compares results from expansion by heating.

The oxide post-perovskites simulated in compression in the present work for comparison with experiment were $MgSiO_3$, $MgGeO_3$, $CaIrO_3$ and $CaPtO_3$. DFT athermal simulation has been used previously to examine both the EOS and the static structure of post-perovskites such as $MgSiO_3$ (Tsuchiya *et al.*, 2004), $MgGeO_3$ (Tsuchiya and Tsuchiya, 2007a), $CaIrO_3$ (Tsuchiya and Tsuchiya, 2007b) and $CaRhO_3$ (Matar *et al.*, 2010). It has also been used to calculate the EOS of $MgSiO_3$ (Oganov and Ono, 2004), $CaIrO_3$ (Stølen and Trønnes, 2007) and of $CaPtO_3$ (Matar *et al.*, 2008).

The only published study which includes simulation of the effect of compression on the post-perovskite atomic structure is that of $MgGeO_3$ by Kubo *et al.* (2008)(see Section 10.5.3).

The fluoride post-perovskites $NaMgF_3$, $NaZnF_3$ and $NaNiF_3$ were also simulated in compression in the present work. Experimental studies of the fluoride post-perovskite $NaMgF_3$ were published prior to the present work (Liu *et al.*, 2005; Hustoft *et al.*, 2008), and an experimental and simulation study of post-perovskite $NaZnF_3$ was

published in the course of the present work (Yakovlev *et al.*, 2009; Yakovlev *et al.*, 2009a), but these studies did not include any examination of structural change at high-pressure or high- temperature. My work on the influence of electronegativity, ionic radii and tilt angles on post-perovskite stabilisation pressure (see Chapter 5) identified $NaZnF_3$ and $NaNiF_3$ perovskites as candidates for transformation to the post-perovskite structure; post-perovskite $NaNiF_3$ was synthesised as part of the present work (Section 6.8.3).

As far as I am aware, no study has been published which simulates the effect of heating on the post-perovskite structure, although Stackhouse and Brodholt (2007) have studied the elastic moduli of $MgSiO_3$ at high temperatures. Chapter 10 describes results from the simulation of thermal expansion carried out in the present work.

I also simulated the effect of compression on the hypothetical hydrous aluminosilicate post-perovskite $MgHAlO_3$, for comparison with post-perovskite $MgSiO_3$. $MgHAlO_3$ is of interest because it is known that even small amounts of water can profoundly affect the physical properties of minerals such as forsterite (e.g. Brodholt and Refson, 2000). The effect of the substitution of AlH for Si in decreasing the transition pressure of $MgSiO_3$ perovskite to post-perovskite has been simulated (Akber-Knutson *et al.*, 2005), but that study did not specify the location of the H atom in the post-perovskite structure. The tetrahedral 4*c* site occupied by Cu atoms in the *Cmcm* $KCuZrQ_3$ (Q= S, Se, Te) chalcogenides (Mansuetto *et al.*, 1992: see also Table 3 in Yang and Ibers, 1999) lies within the "void volume" in the cell that is not part of the BX_6 octahedron or of the AX_8 hendecahedron. This 4*c* site may be a suitable location for the H atom in $MgHAlO_3$ (Figure 4-1: compare with Figure 1-1), and this site has been used in the present work.

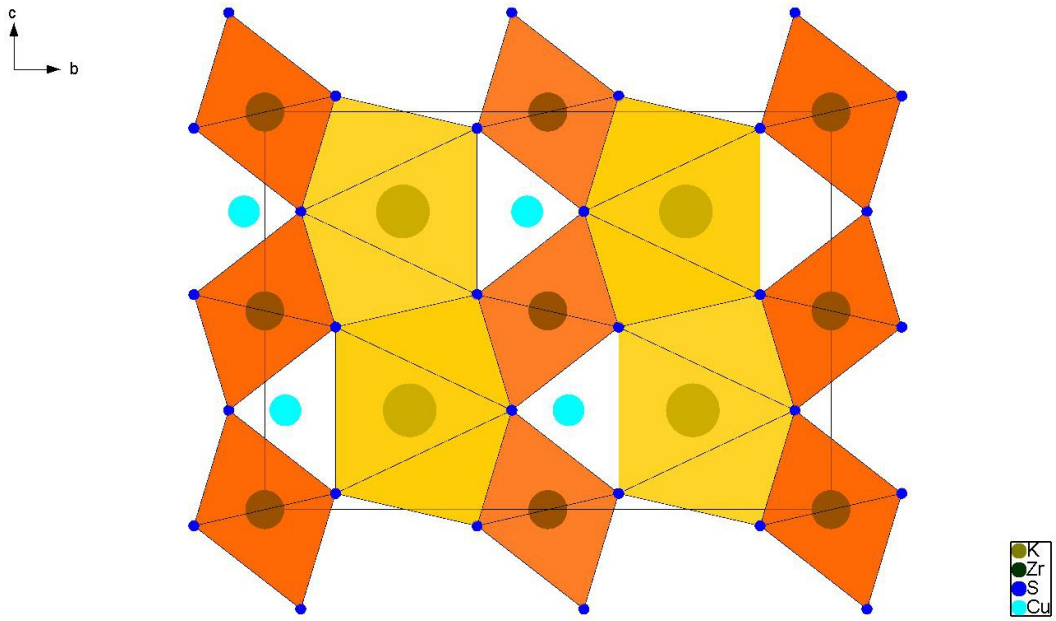

Figure 4-1: View of $KCuZrS_3$ viewed along the *a*-axis (based on Mansuetto *et al.*, 1992). This structure was used for simulation of $MgHAlO_3$ with the substitutions of Mg for K, H for Cu, Al for Zr and O for S.

4.2 Athermal simulation of post-perovskite structures

4.2.1 Volumetric and axial compression

The simulations showed that the oxide post-perovskites are much less compressible than the fluoride post-perovskites, with $MgSiO_3$ being the least compressible of the oxides (Figure 4-2). To enable the ready comparison of the different materials, the volume axis in Figure 4-2 is V/V_0 where V is the unit-cell ($Z = 4$) volume at a given pressure, and V_0 is the volume at 0 GPa derived from a BM3 EOS fitted to the simulated data points; the EOS parameters, including V_0, are shown in Table 4-1.

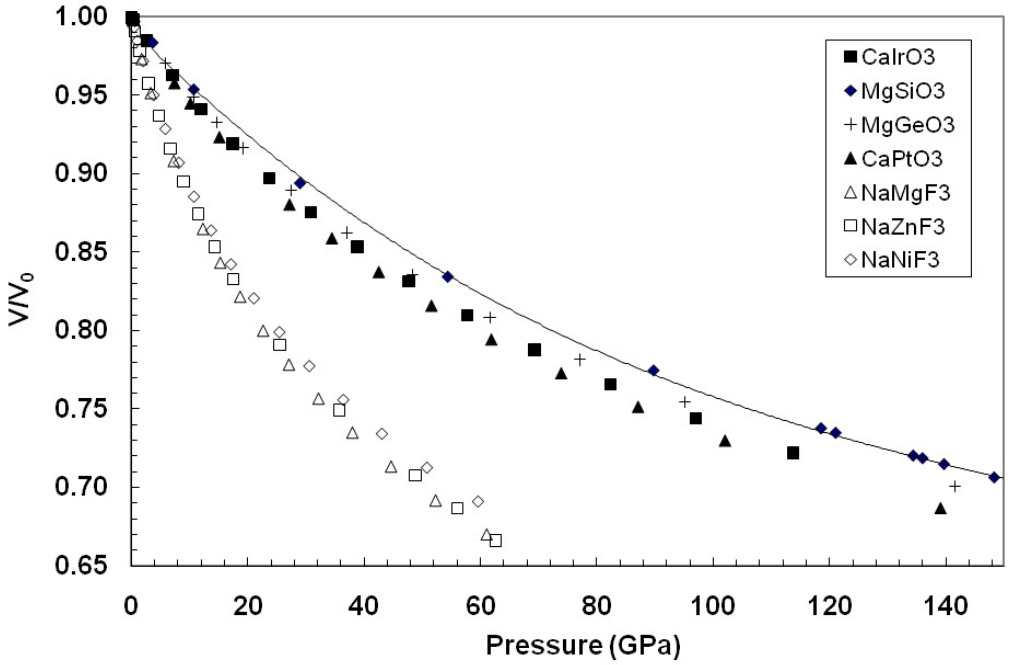

Figure 4-2: Normalised unit-cell volume plotted against pressure for post-perovskite oxides and fluorides. The trend line fitted to $MgSiO_3$ data points is for guidance only.

These athermal simulations calculated volumes for post-perovskite-structured compounds down to 0 GPa at 0 K. However, some of these compounds may in practice transform to the perovskite structure as pressure decreases. $MgSiO_3$ changes phase from perovskite to post-perovskite at 111.1 GPa at 2000 K (Guignot *et al.*, 2007), which is equivalent to 89.2 GPa at 0 K assuming a Clapeyron slope of 13.3 MPa K^{-1} (Tateno *et al.*, 2009). The corresponding transition pressure for $MgGeO_3$ at 0 K is 48.6 GPa (assuming a Clapeyron slope of 8 MPa K^{-1}: Hirose *et al.*, 2005) and for

$NaMgF_3$ is 14.1 GPa (assuming a mean Clapeyron slope of 8 MPa K^{-1}, from the range 6-10 MPa K^{-1}: Hustoft *et al*., 2008).

The unit-cell parameters *a*, *b* and *c* are plotted against V/V_0 in Figure 4-3. The *b*-axis shows the largest variation between different post-perovskites, although this variation decreases under pressure. By contrast the variation in the *c*-axis unit-cell parameter increases with increasing pressure because the Δ_1 octahedral tilts (see Section 1.4) of $CaIrO_3$, $CaPtO_3$ and the fluoride post-perovskites decrease faster than those of $MgSiO_3$ and $MgGeO_3$ (see Figure 4-11a); a decrease in Δ_1 octahedral tilt will increase the *c*-axis length.

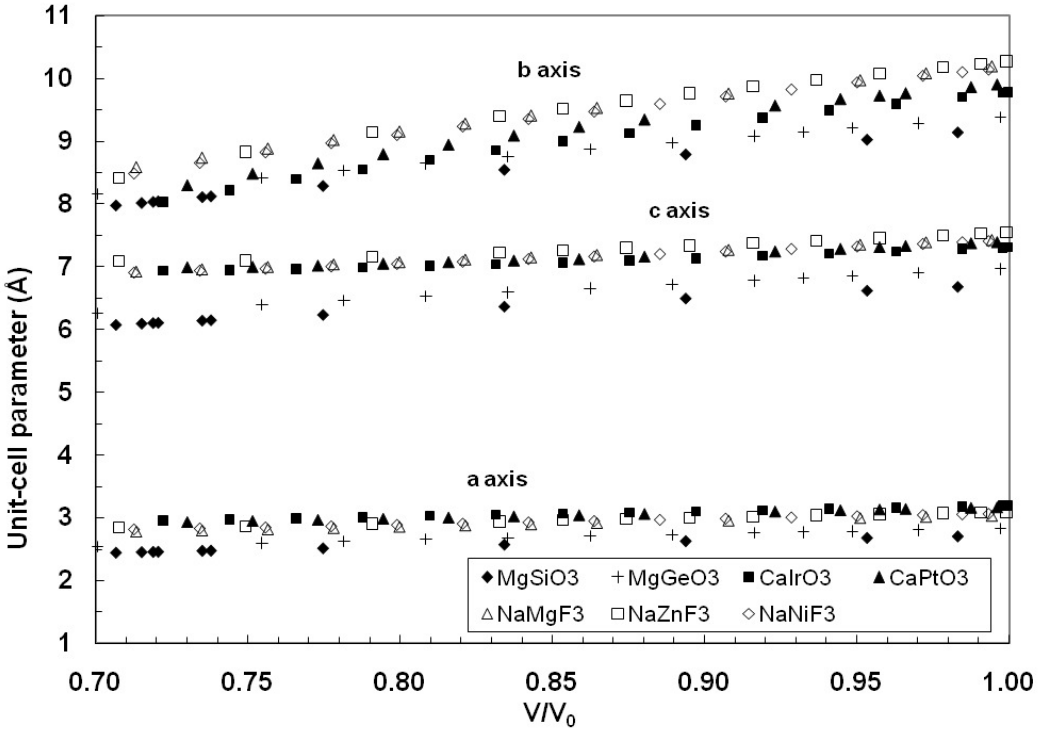

Figure 4-3: Post-perovskite unit-cell parameters in compression.

The anisotropy of the axial incompressibilities of oxide post-perovskites is shown by plotting $(i/i_0)^3$ against V/V_0 where *i* is the *a*, *b* or *c* orthorhombic cell parameter normalised to the corresponding a_0, b_0 or c_0 value (i_0) from each BM3 EOS (Figure 4-4). Points appearing above the isotrope (such as the *a* and *c* axes) are less compressible than the volumetric compressibility, and their EOS has $K'_0 > 4$ (Table 4-1). Those points below the isotrope (the *b* axes) are more compressible than the

volumetric compressibility, and their EOS has $K'_0 < 4$ (Table 4-1). Note that $CaIrO_3$ is more anisotropic than $CaPtO_3$, and both are more anisotropic than $MgSiO_3$ or $MgGeO_3$.

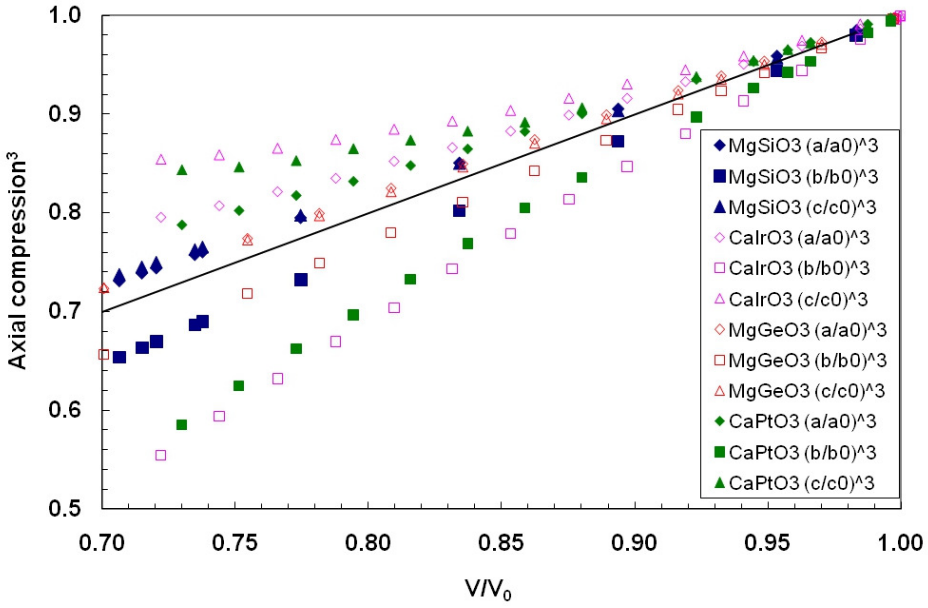

Figure 4-4: Normalised axial incompressibility $(i/i_0)^3$ for post-perovskite oxides. The solid line is the isotrope.

Figure 4-5 shows the axial incompressibilities of fluoride post-perovskites; there is little difference between their anisotropies. They are more anisotropic than $MgSiO_3$ and $MgGeO_3$ but less anisotropic than $CaIrO_3$ and $CaPtO_3$ at the same V/V_0.

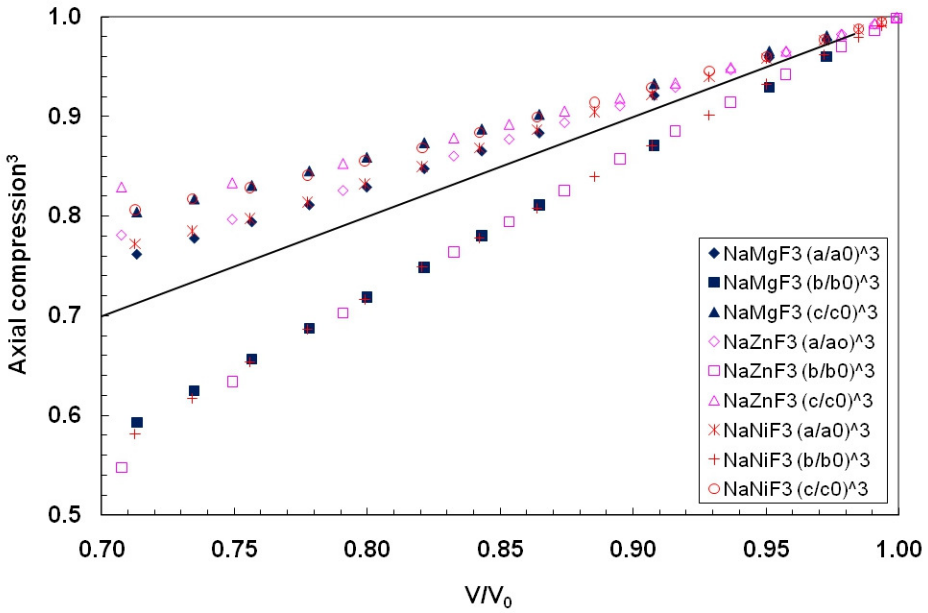

Figure 4-5: Normalised axial incompressibility $(i/i_0)^3$ for post-perovskite fluorides.

	$MgSiO_3$	$MgGeO_3$	$CaIrO_3$	$CaPtO_3$	$NaMgF_3$	$NaZnF_3$	$NaNiF_3$	$MgHAlO_3$
Volume								
V_0 (Å^3)	165.8(2)	188.6(2)	232.16(8)	236.73(8)	231.77(7)	240.2(4)	232.63(7)	195.2(2)
K_0 (GPa)	232.26(1)	178.954(9)	168.564(5)	156.079(4)	60.731(1)	65.88(1)	64.226(2)	146.819(7)
K'_0	3.910(7)	4.20(2)	4.16(2)	4.30(1)	4.53(1)	4.36(9)	4.86(2)	4.14(2)
***a*-axis**								
a_0 (Å)	2.7144(2)	2.8325(4)	3.1975(8)	3.1731(7)	3.050(5)	3.0973(6)	3.0650(5)	2.8071(4)
K_0 (GPa)	235.9(5)	204(1)	181(4)	174(4)	52(5)	69(1)	78(1)	198.5(9)
K'_0	4.421(8)	4.69(2)	9.17(2)	7.2(2)	8.9(7)	6.9(2)	6.4(1)	3.95(1)
***b*-axis**								
b_0 (Å)	9.1992(8)	9.392(3)	9.785(6)	9.917(8)	10.213(8)	10.280(5)	10.172(5)	9.379(2)
K_0 (GPa)	167.3(3)	161(1)	114(2)	120(3)	43.2(4)	46.3(8)	46.8(9)	145.2(9)
K'_0	3.543(4)	3.57(2)	2.61(3)	2.53(4)	3.03(1)	2.83(6)	3.09(7)	3.77(1)
***c*-axis**								
c_0 (Å)	6.717(2)	6.972(1)	7.311(2)	7.409(4)	7.455(4)	7.555(4)	7.432(3)	7.254(4)
K_0 (GPa)	227(2)	184(1)	236(11)	153(11)	55(4)	56(3)	74(4)	130(2)
K'_0	5.08(4)	5.40(3)	9(1)	15(1)	15(1)	16(1)	11.0(7)	4.91(5)
V/V_0 min.	0.36	0.54	0.68	0.63	0.65	0.67	0.69	0.56

Table 4-1: Volumetric and axial EOS parameters for simulated post-perovskites. V/V_0 min. specifies the minimum value of V/V_0 used in the EOS, where V_0 is the volume at 0 GPa and V is the volume at the highest pressure simulated.

The volumetric and axial BM3 EOS parameters were determined for the simulated post-perovskites (Table 4-1) as described in Section 3.9.1. These simulated values are compared with experimental values in Section 10.2.2. The higher compressibility of the fluoride post-perovskites compared with oxide post-perovskites may be due to the higher electronegativity of the F^- ion compared to that of the O^{2-} ion: bonds which are more ionic such as A-F and B-F bonds will be weaker than A-O and B-O bonds (e.g. Woodward, 1997b)(see Section 5.4.1), leading to higher fluoride compressibility. In the simulated post-perovskite $MgSiO_3$ $\kappa_a \approx \kappa_c > \kappa_b$, but in the simulated post-perovskite $MgHAlO_3$ $\kappa_a > \kappa_b > \kappa_c$ (Figure 4-6). The increased compressibility of the *c*-axis in $MgHAlO_3$ may be due to a decrease in repulsion between O2 anions separated by the O2e-O2f interatomic distance (Figure 1-1), caused by the location of the H cation between them. This is supported by the 53% higher compressibility of the void in $MgHAlO_3$ compared with $MgSiO_3$ PPV.

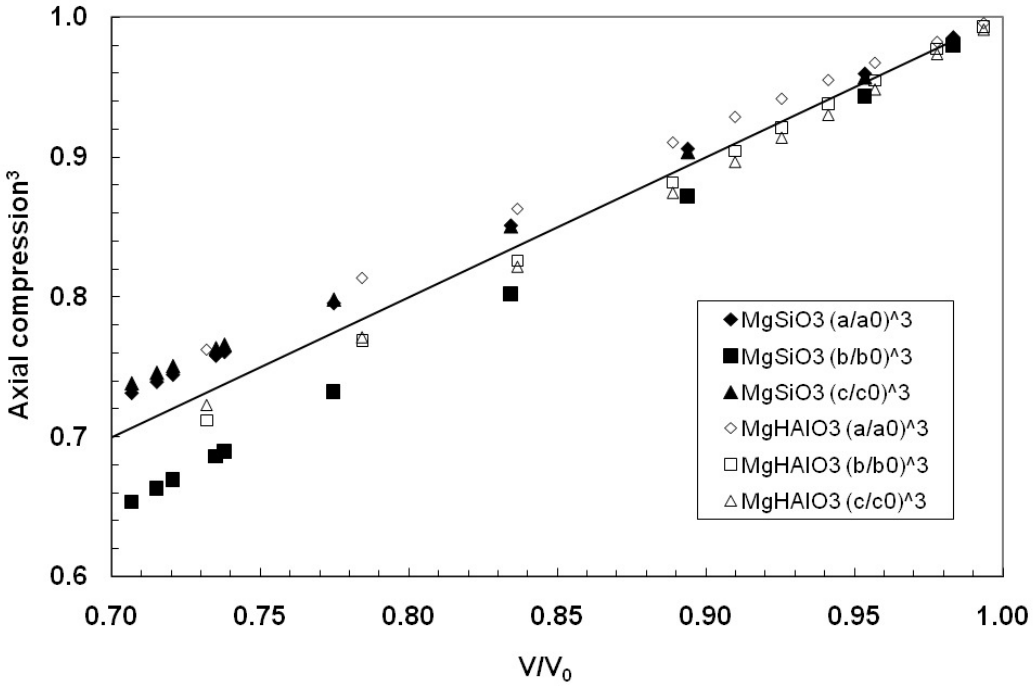

Figure 4-6: Simulated axial compressibilities of $MgSiO_3$ and $MgHAlO_3$ post-perovskites.

4.2.2 Compression of hendecahedra and octahedra

The AX_8 hendecahedron is more compressible than the BX_6 octahedron in all of the post-perovskites simulated in the present work. The EOS parameters for the hendecahedra and octahedra are shown in Table 4-2. Figure 4-7a to Figure 4-7d show the simulated volumes of the post-perovskite hendecahedra and octahedra, and the percentage of the unit-cell volume which each represents. MgO_8 hendecahedra are significantly smaller than the other post-perovskite hendecahedra due to the Mg cation being smaller (1.03 Å) than the Ca (1.26 Å) and Na (1.32 Å) cations (Shannon, 1976).

The percentage of the unit-cell volume occupied by hendecahedra falls as the pressure increases, because hendecahedra are more compressible than octahedra. The void volume is the volume of the unit-cell not occupied by hendecahedra or octahedra. The proportion of the unit-cell occupied by the void volume rises with increasing pressure (Figure 4-7f) for all of the post-perovskites simulated, because the hendecahedral volume is larger than the octahedral volume, and the hendecahedral compressibilities are greater than those of the unit-cells. In terms of the volumes of octahedra, hendecahedra and void relative to the unit-cell, $NaMgF_3$ is the analogue most similar to post-perovskite $MgSiO_3$.

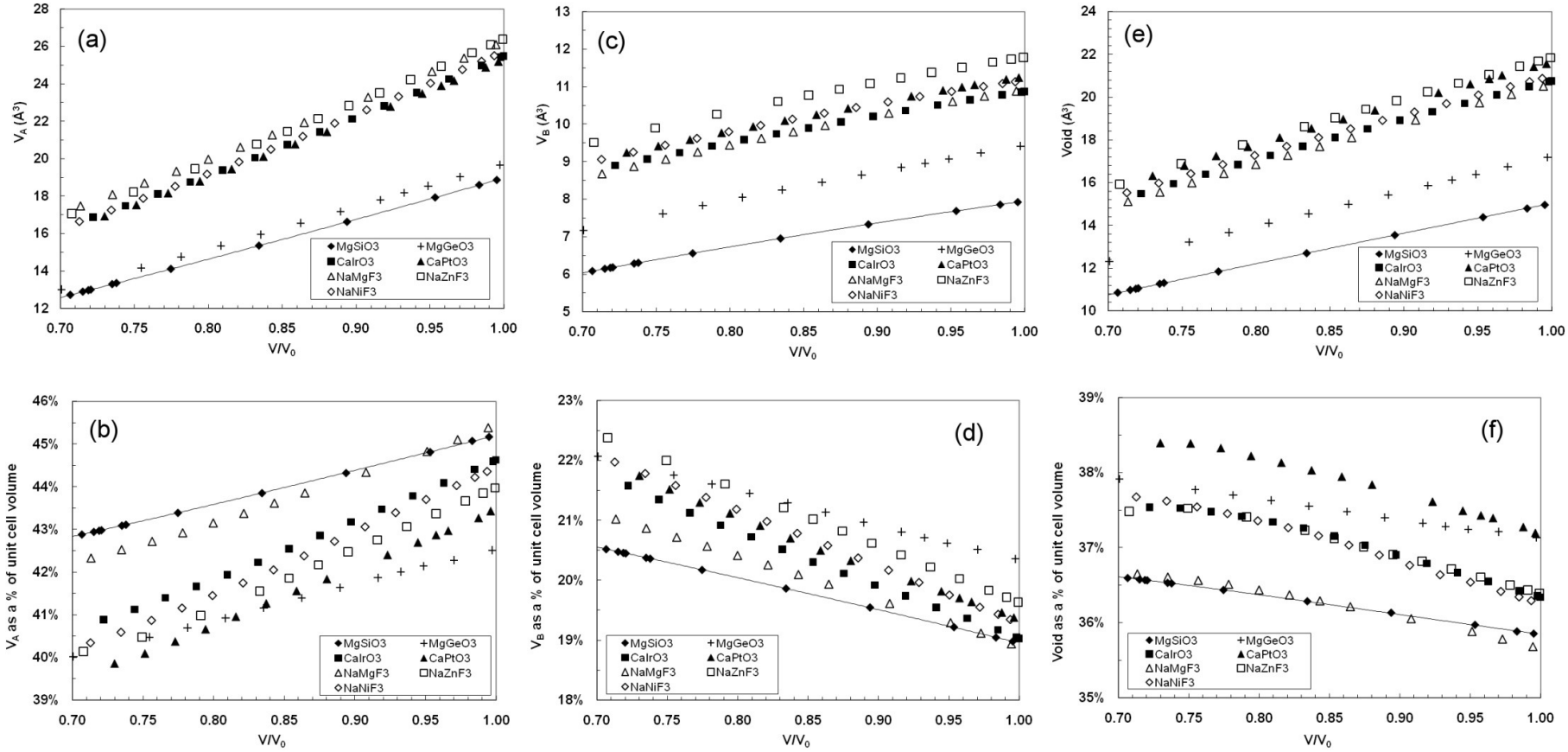

Figure 4-7: (a) Volume of one hendecahedron V_A (b) Hendecahedral volume as a % of unit-cell volume (c) Volume of one octahedron V_B (d) Octahedral volume as a % of unit-cell volume (e) Volume of void/4 (f) Void volume as % of unit-cell volume. The trend lines fitted to $MgSiO_3$ data points are for guidance only.

	$MgSiO_3$	$MgGeO_3$	$CaIrO_3$	$CaPtO_3$	$NaMgF_3$	$NaZnF_3$	$NaNiF_3$	$MgHAlO_3$
V_A (Å^3)	18.91(2)	19.740(8)	25.58(6)	25.5(1)	26.29(2)	26.6(1)	25.82(3)	19.97(1)
V_B (Å^3)	7.81(3)	9.39(1)	10.865(7)	11.24(1)	10.908(5)	11.75(2)	11.154(4)	9.838(9)
K_A (GPa)	173.0(7)	149.6(4)	120(3)	106(5)	45.3(4)	40(2)	45.5(5)	145.7(9)
K_B (GPa)	371(9)	281(4)	325(5)	293(7)	108.5(8)	138(6)	136(1)	195(2)
K'_A	3.889(1)	3.921(4)	3.97(5)	4.25(9)	4.25(2)	4.5(1)	4.21(3)	3.96(1)
K'_B	3.91(2)	4.58(4)	5.6(1)	5.7(1)	5.02(4)	4.65(3)	5.65(6)	4.27(3)
V_A/V_B	2.42(1)	2.102(3)	2.354(5)	2.27(1)	2.410(2)	2.26(1)	2.315(3)	2.030(2)
K_B/K_A	2.15(5)	1.88(3)	2.71(7)	2.8(1)	2.40(3)	3.4(2)	3.00(4)	1.34(2)

Table 4-2: EOS parameters and ratios for the octahedron (A) and hendecahedron (B) for simulated post-perovskites. For K and K' the values listed are those at $P = 0$.

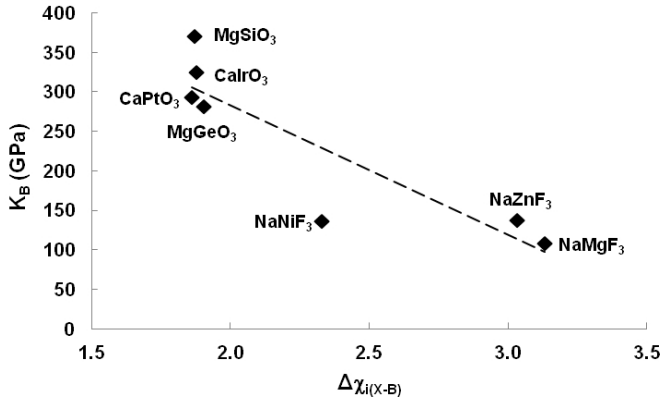

Figure 4-8: The difference in electronegativities between the B cation and the X anion $\Delta\chi_{i(X-B)}$ and the octahedral incompressibility K_B.

The difference in electronegativities between the B cation and the X anion, $\Delta\chi_{i(X-B)}$, is negatively correlated (R^2 = 78%) with the octahedral incompressibility K_B for the oxide and fluoride post-perovskites simulated in the present work (Figure 4-8). The electronegativity scale χ_i tabulated by Li and Xue (2006) is described in Section 5.4.1. A low electronegativity difference is usually associated with a higher bond covalence (Mizoguchi *et al*., 2004a). This supports the concept of stronger, more covalent

octahedral bonding where the X-B electronegativity difference is small (Woodward, 1997b)(see Section 5.4.1).

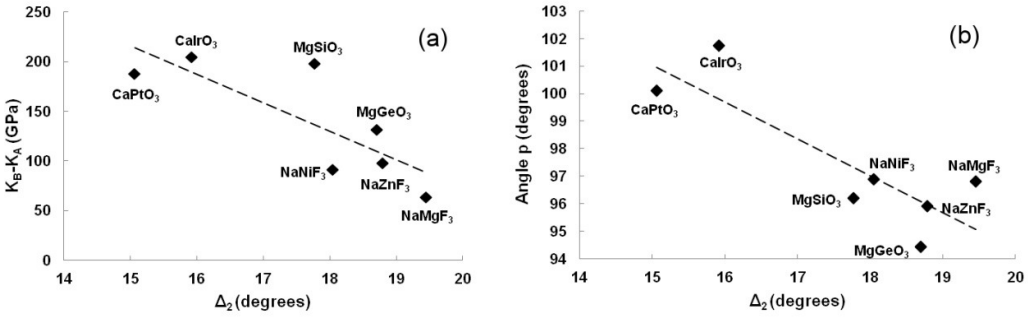

Figure 4-9: (a)The difference between hendecahedral and octahedral incompressibilities K_B-K_A and the Δ_2 tilt angle (b) the angle p and the Δ_2 tilt angle.

For the oxide and fluoride post-perovskites simulated in the present work ($MgHAlO_3$ excepted), the difference between hendecahedral and octahedral incompressibilities K_B-K_A is negatively correlated ($R^2 = 63\%$) with the Δ_2 tilt angle (Figure 4-9a). Since $K_B > K_A$ this means that a less compressible hendecahedron is associated with greater octahedral distortion. The Δ_2 tilt angle is also negatively correlated ($R^2 = 71\%$) with angle p (Figure 4-9b), another element of octahedral distortion.

4.2.3 Atomic coordinates and angles

The changes with increasing pressure in the 4 variable atomic coordinates in the post-perovskite structure are shown in Figure 4-10. $NaMgF_3$ is the analogue whose atomic coordinates most closely track those of $MgSiO_3$. The largest difference in atomic coordinates between $MgGeO_3$ and $MgSiO_3$ occurs for X1 *y*, because the GeO_6 octahedron is larger (see Figure 4-7c) and more tilted (Δ_1 is larger: see Figure 4-11a) than the SiO_6 octahedron. Increasing pressure leads in general to a decrease in angle Δ_1, an increase in angle Δ_2, and (within the range of V/V_0 between 1.0 to 0.8) a decrease in angle p; the net effect is a decrease in the angular distortion of the octahedra, discussed in the following section and shown in Figure 4-13b.

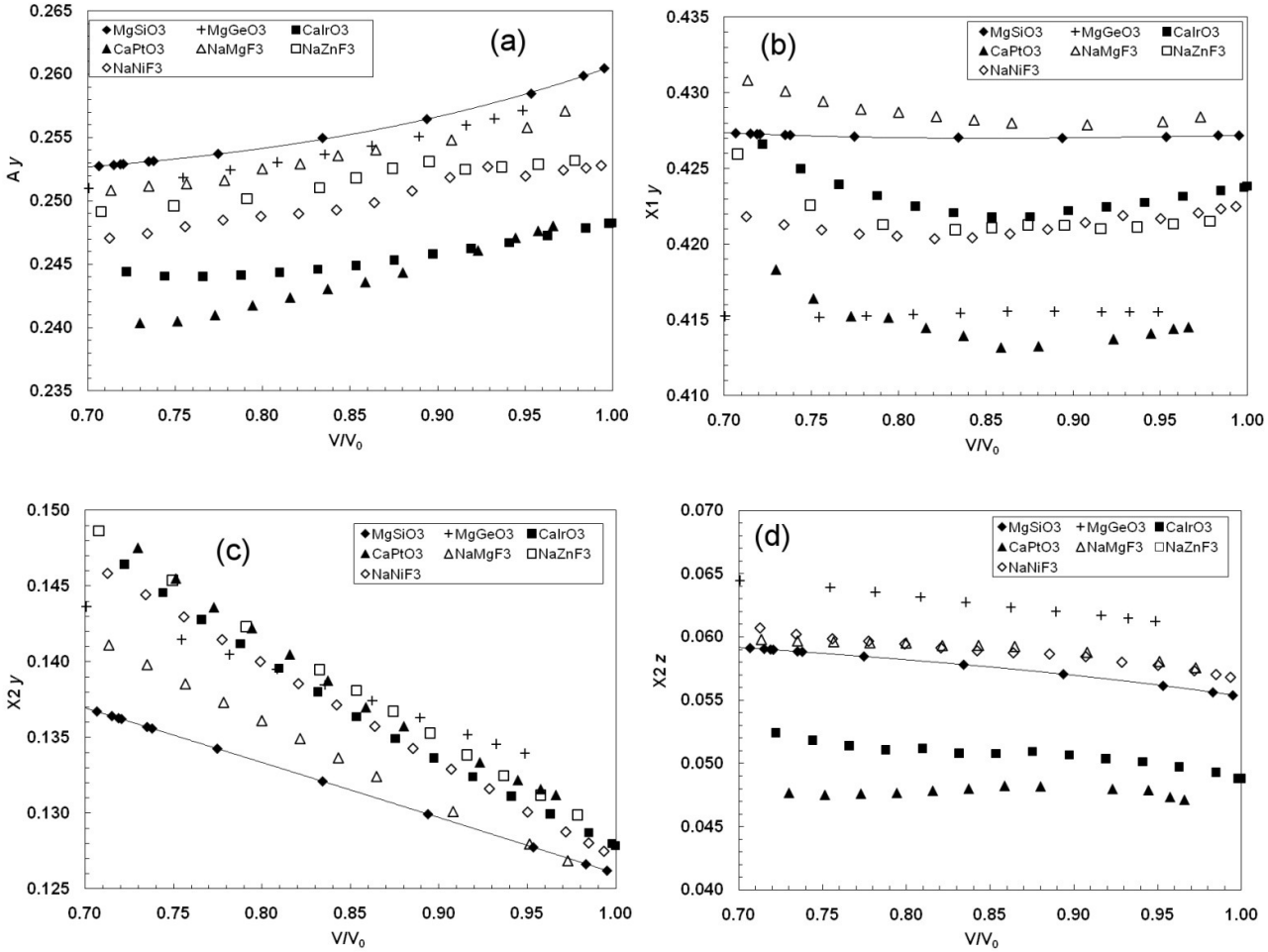

Figure 4-10: ABX_3 post-perovskite variable atomic coordinates (a) A y (b) X1*y* (c) X2*y* (d) X2*z*. The trend lines fitted to $MgSiO_3$ data points are for guidance only.

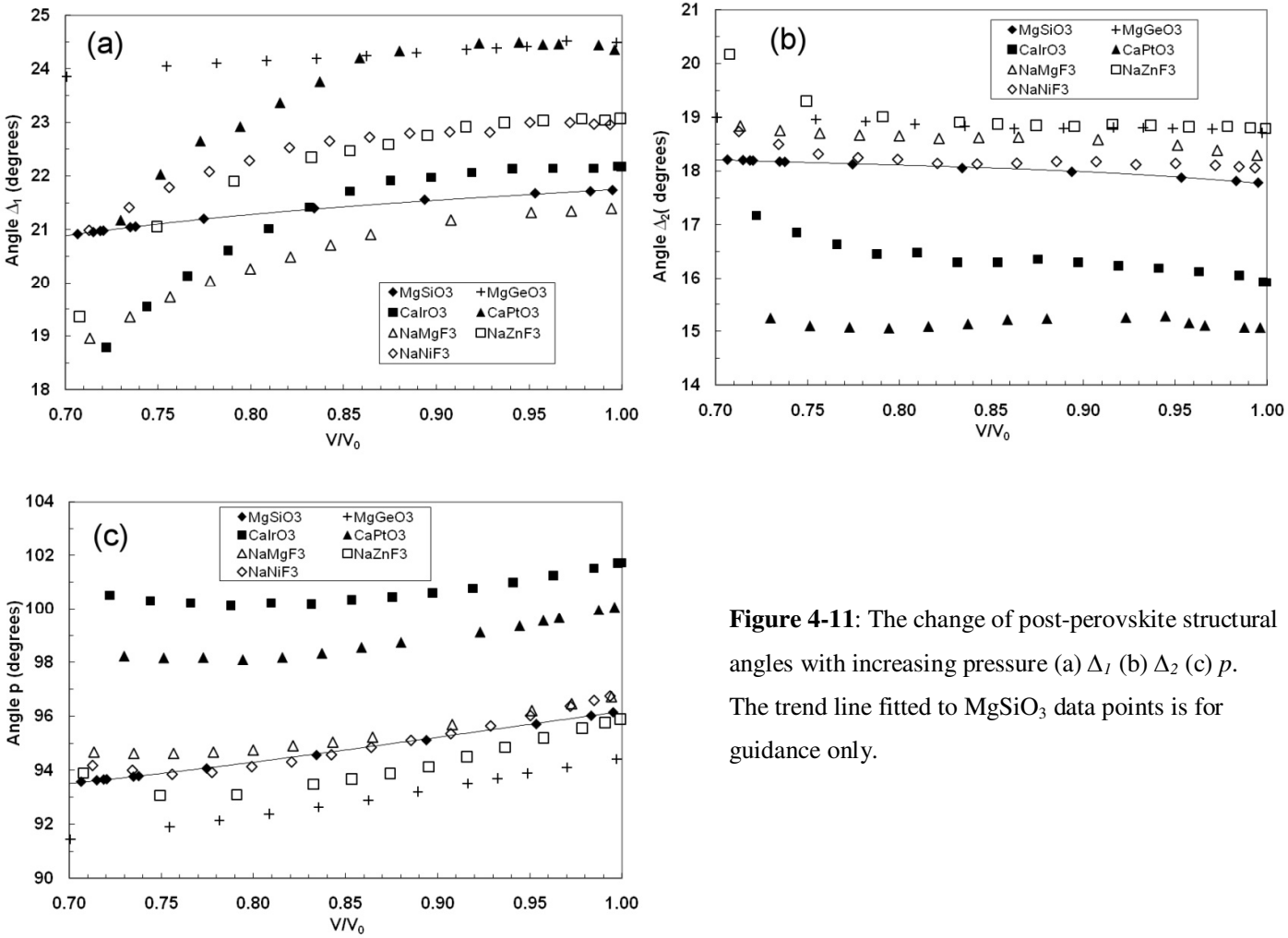

Figure 4-11: The change of post-perovskite structural angles with increasing pressure (a) Δ_1 (b) Δ_2 (c) p. The trend line fitted to $MgSiO_3$ data points is for guidance only.

4.2.4 Bond lengths and octahedral distortion

The changes in simulated post-perovskite bond lengths in compression are shown in Figure 4-12. In $MgGeO_3$ the Mg-O1 and Mg-O2 bond lengths are similar to those of $MgSiO_3$, but the larger Ge-O1 and Ge-O2 octahedral bond lengths reflect the larger size of the GeO_6 octahedra.

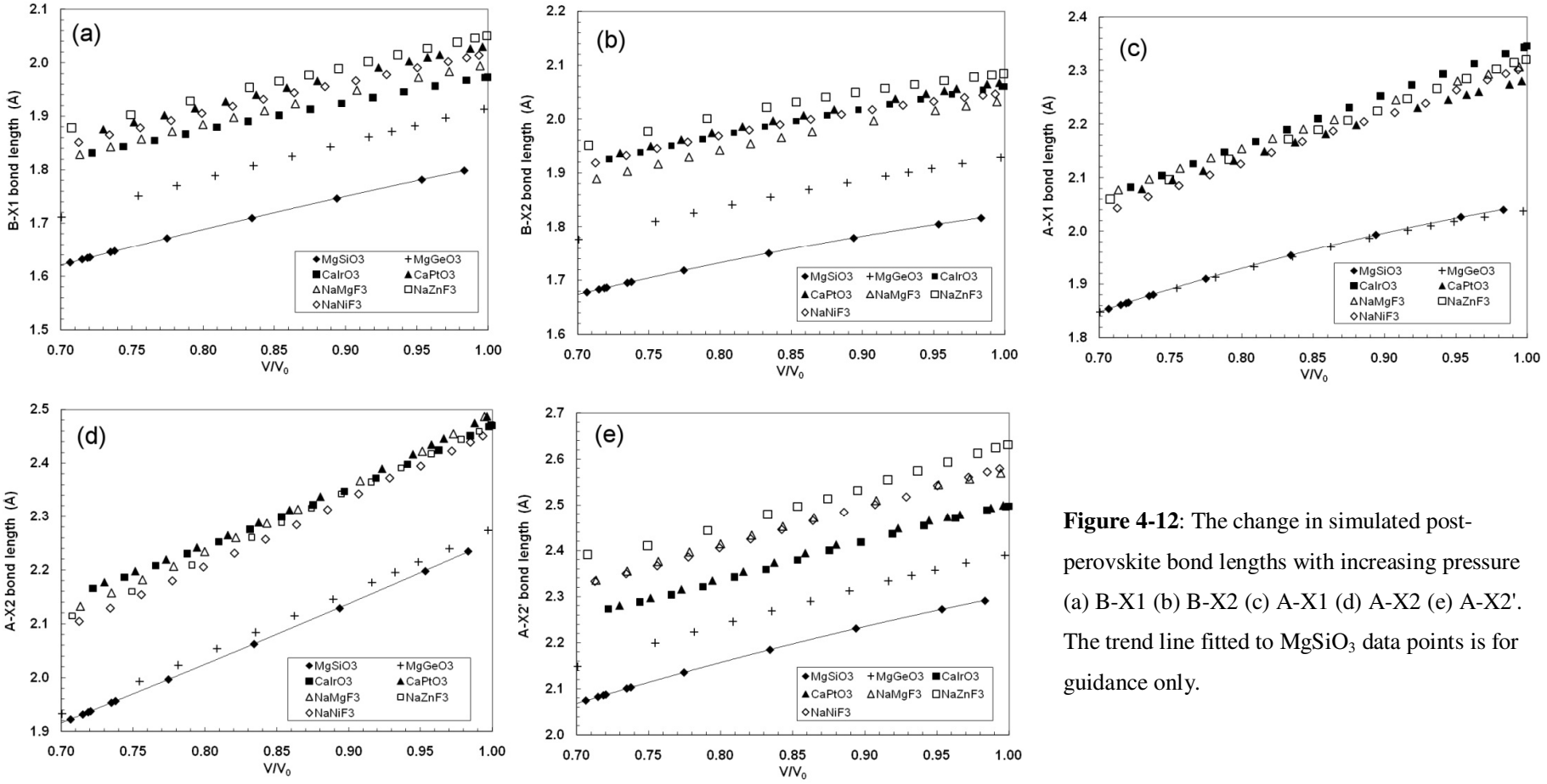

Figure 4-12: The change in simulated post-perovskite bond lengths with increasing pressure (a) B-X1 (b) B-X2 (c) A-X1 (d) A-X2 (e) A-X2'. The trend line fitted to $MgSiO_3$ data points is for guidance only.

The distortion of the post-perovskite octahedra from the regular form is illustrated in Figure 4-13. The bond length ratio B-X1/B-X2 should be equal to 1 if the apical X1 atoms are the same distance from the central B atom as are the X2 atoms around the octahedron's central plane. Figure 4-13a shows that $CaIrO_3$ has by far the highest distortion of B-X1/B-X2 away from a value of 1, with the most "squashed" octahedron. The B-X1/B-X2 distortion increases in all compounds as pressure increases. The octahedral angular variance (OAV) is the mean square deviation from 90° of the twelve X-B-X angles a_i in the octahedron:

$$OAV = \frac{1}{12}\sum_{i=1}^{12}(a_i - 90^{\circ})^2 \tag{4.1}$$

This measure of angular distortion decreases as angle p moves towards 90° and Δ_1-Δ_2 moves towards 0°. Figure 4-13b shows that the OAV and therefore the octahedral angular distortion decreases as pressure increases. The OAV of $MgGeO_3$ and of the fluoride post-perovskites is much more similar to that of $MgSiO_3$ than is the OAV of $CaIrO_3$ or $CaPtO_3$. $CaIrO_3$ and $CaPtO_3$ have the most distorted octahedra of the post-perovskites simulated.

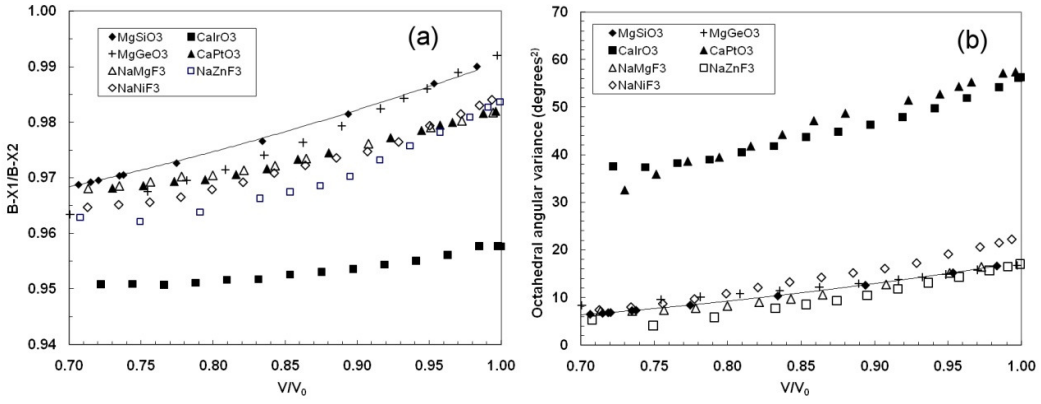

Figure 4-13: Octahedral distortion (a) bond length ratio B-X1/B-X2 (b) octahedral angular variance.

The low B-X1/B-X2 ratio in $CaIrO_3$ compared with $CaPtO_3$ (Figure 4-13a) has been identified as arising from the different bonding associated with the d^5 and d^6 electron configurations, as a result of the Jahn-Teller effect (Section 4.5), which distorts the octahedra so that the Ir-O1 bond is significantly shorter than Ir-O2 bond (Inaguma *et al.*, 2008).

4.3 Molecular dynamics simulation of post-perovskite structures

This Section describes the results of MD simulation of changes in octahedral bond lengths with increasing temperature. Other results of MD simulation of post-perovskite structures are described and compared with experimental results in Chapter 10.

4.3.1 Instantaneous and averaged-structure octahedral bond lengths

The mean, mode (most frequently occurring value) and median (mid-point of the population) bond lengths for MD simulated post-perovskite B-O1 and B-O2 octahedral bonds were calculated for $MgSiO_3$ (at 136 GPa), $CaPtO_3$ and $CaIrO_3$ (at 0 GPa) as described in Section 3.9.4. Previous simulation of $NaMgF_3$ perovskite has shown that the apparent contraction of the Mg-F octahedral bond in experiment arises from large spatial anisotropy in the distribution of F^- ions (Street *et al.*, 1997). Experimental measurements of $CaIrO_3$ (Martin *et al.*, 2007a; Martin 2008) revealed a similar tendency, and it appears that the same effect may be visible in $CaPtO_3$ (the present work: Figure 9-13a in Section 9.3), although it is less obvious in this compound.

The simulated Si-O1 bond length distributions for post-perovskite $MgSiO_3$ over the range of temperatures shown in Figure 4-14 are typical of the distributions obtained.

The mode, mean and median simulated octahedral bond lengths for $MgSiO_3$ (at 136 GPa), $CaPtO_3$ and $CaIrO_3$ (at 0 GPa) are shown in Figure 4-15 together with the values calculated for the average simulated crystal structure. The median (mid-point of the population) becomes larger than the mode (most frequently occurring value) as temperature increases and the distributions acquire asymmetric "tails" at longer bond lengths.

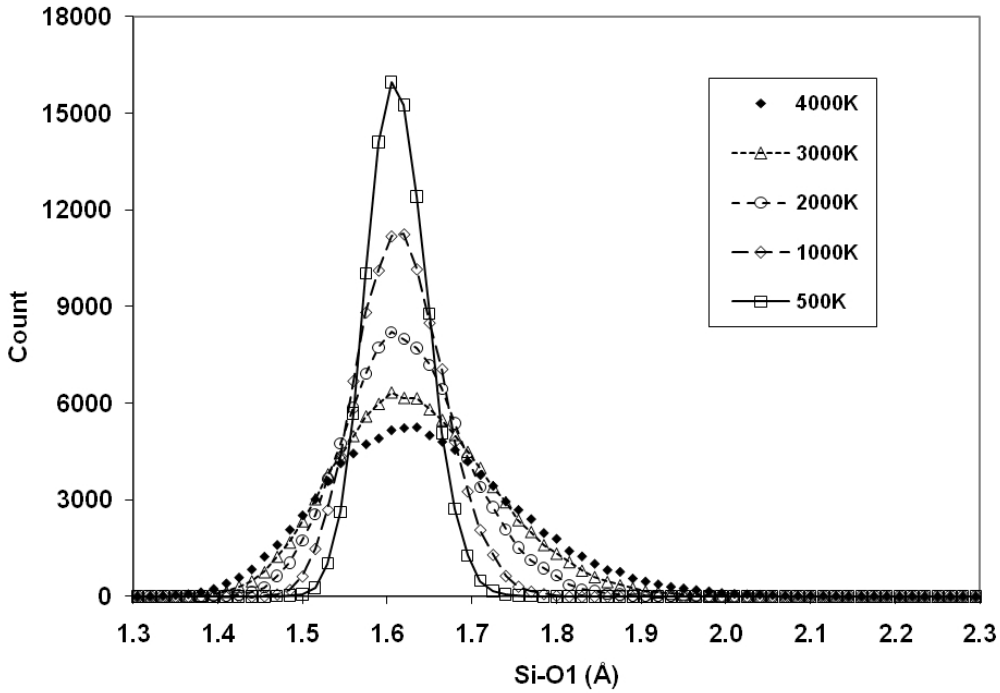

Figure 4-14: Simulated Si-O1 bond length distributions for post-perovskite $MgSiO_3$.

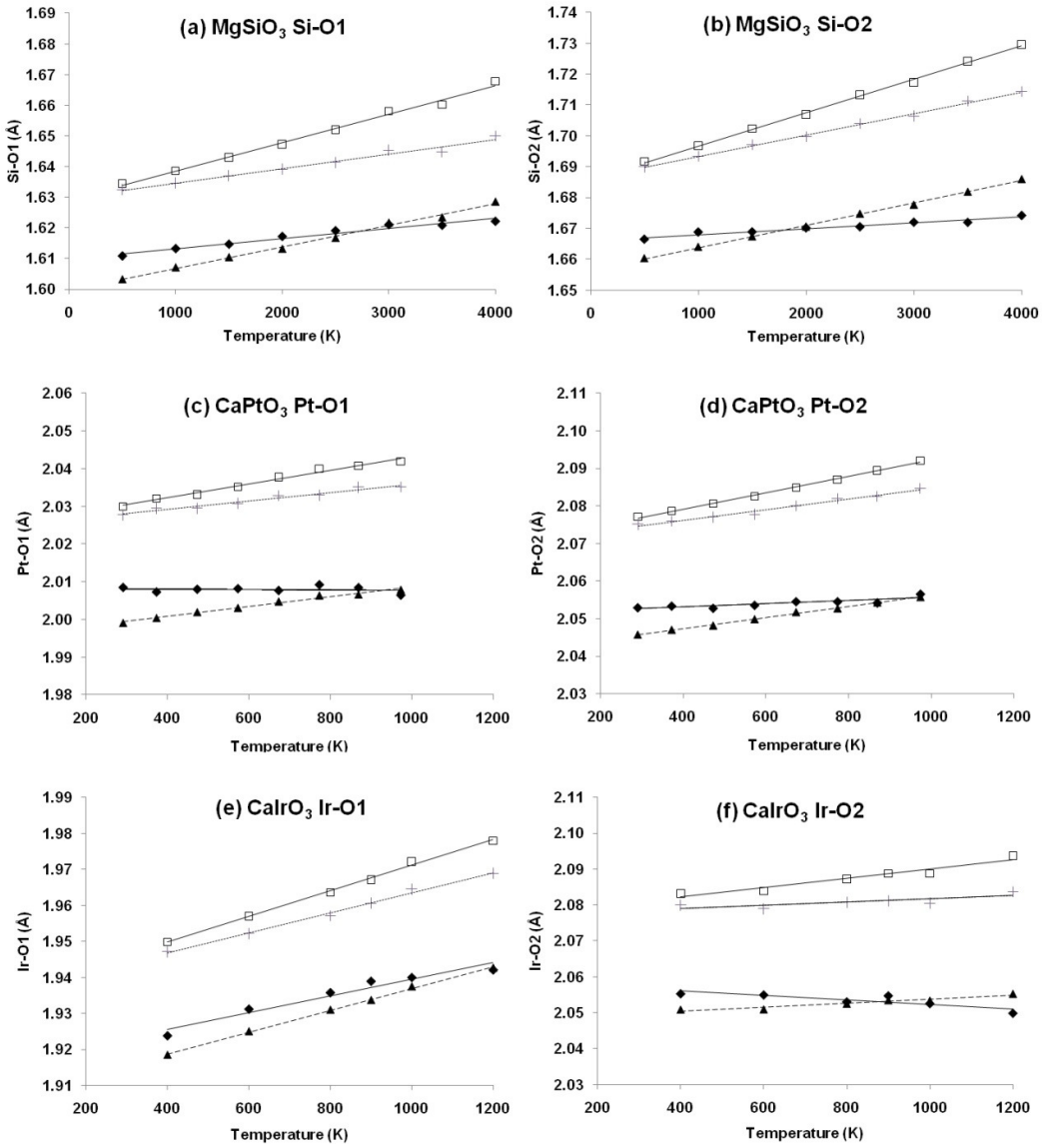

Figure 4-15: Mode (diamond), mean (square), median (triangle) and averaged-structure (cross) simulated octahedral bond lengths for $MgSiO_3$ Si-O1 (a) and Si-O2 (b), $CaPtO_3$ Pt-O1 (c) and Pt-O2 (d) and $CaIrO_3$ Ir-O1 (e) and Ir-O2 (f). Note that the temperature scale differs for $MgSiO_3$.

4.3.2 The effect of thermal motion on instantaneous octahedral bond lengths

Each mean value shown in Figure 4-15 is the average of the instantaneous bond lengths, calculated from the atomic coordinates, for each of the occurrences of the bond in the (Z=12) unit-cell for each of the time steps in the MD simulation. For the averaged-structure value, each atomic coordinate was first averaged across all time steps and then averaged over all of its occurrences in the 60-atom unit-supercell. These averaged atomic coordinates were used to calculate the simulated bond lengths, angles and polyhedron volumes in expansion which are compared with experimental results in Chapter 10. These calculated bond lengths are referred to here as averaged-structure bond lengths. Note that Figure 4-15(f) shows that the averaged-structure Ir-O2 bond length is effectively invariant with temperature.

Figure 4-15 also shows that the (instantaneous) mean bond lengths increase faster with rising temperature than those of the averaged-structure. This is because the components of thermal motion of the X (oxygen) atom perpendicular to the B-X bond result in an instantaneous bond length which is larger than the bond length calculated from the average positions of the atoms (Figure 4-16).

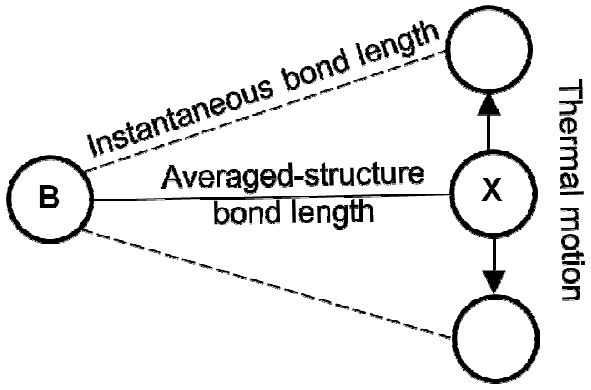

Figure 4-16: Effect of thermal motion on B-X bond length.

The ratios of the mean instantaneous bond length expansivity to the averaged-structure bond length expansivity are shown in Table 4-3. The faster expansion of the instantaneous compared with the average-structure bond length is greatest for the $CaIrO_3$ Ir-O2 bond, and least for its Ir-O1 bond. This means that the effect of thermal motion in increasing the instantaneous Ir-O1 bond length is less than might be

expected by comparison with $MgSiO_3$ and $CaPtO_3$. This may be due to the distortion of the IrO_6 octahedron by the Jahn-Teller effect (Section 4.5.3).

	$MgSiO_3$ 136 GPa	$CaPtO_3$ 0 GPa	$CaIrO_3$ 0 GPa
B-O1	1.91	1.61	1.29
B-O2	1.55	1.57	2.81
(B-O1)/(B-O2)	1.23	1.02	0.46

Table 4-3: Simulated instantaneous/averaged-structure octahedral bond length expansivity ratios.

The angle Δ_1 is expected to decrease with temperature in corner-linked structures where $K_A < K_B$ (Hazen and Finger, 1979: Angel *et al.*, 2005). The faster expansion of the instantaneous Ir-O2 bond length compared with that of Ir-O1 in $CaIrO_3$ when compared with the similar ratio in $CaPtO_3$ may contribute towards the difference in the direction of change of the angles Δ_1 as temperature is increased (see Sections 10.5.1 and 10.9).

4.4 Athermal simulation of transitions in post-perovskite-related materials

4.4.1 Introduction

Chapter 5 describes a largely empirical method for predicting post-perovskite stabilisation pressures using ionic electronegativity, ionic radii and octahedral tilt. However, it is useful to be able to provide alternative, more precise predictions of these pressures for comparison with experiment using *ab initio* simulation. Where the range of experimental stabilisation pressures is not well constrained, these simulations can also be used to investigate the feasibility of stabilising other related compounds.

At 0 K the enthalpy of a compound is equal to its Gibbs free energy. A phase change or chemical reaction can therefore be predicted from athermal simulation (at 0 K) when the enthalpy of the two polymorphs or of the reactants and the products is the same, as described in Section 3.9.3. I used this method to calculate the phase change pressures predicted by athermal simulation from perovskite to post-perovskite phases for $MgSiO_3$, $MgGeO_3$, $NaMgF_3$, $NaZnF_3$ and $NaNiF_3$:

$$ABX_3 \text{ perovskite} \Rightarrow ABX_3 \text{ post-perovskite} \qquad (4.2)$$

I hypothesised that a hexagonal polymorph of olivine (δMg_2SiO_4) could exist with a structure similar to the known compound Ca_2IrO_4, which had been produced as a by-product in the synthesis of post-perovskite $CaIrO_3$ (see Section 6.4.1). The hypothetical compound $Ca_2Mg_4Si_3O_{12}$ would then have the same structure as δMg_2SiO_4, but with Ca atoms substituted in some of the Mg positions (see Figure 15-1 Ca site 2). I therefore also used this method to calculate predicted transition pressures for the reactions

$$MgSiO_3 \text{ post-perovskite} + MgO \Rightarrow \text{hexagonal } Mg_2SiO_4 \qquad (4.3)$$

$$2CaSiO_3 + MgSiO_3 \text{ (perovskite or post-perovskite)} + 3MgO \Rightarrow Ca_2Mg_4Si_3O_{12} \qquad (4.4)$$

The transition pressure in each case was found by calculating the pressure at which the enthalpy of the products was the same as the enthalpy of the reactants.

4.4.2 Enthalpy calculation

The structure of each compound was specified in the VASP POSCAR file, and the convergence of its internal energy was checked as described in Section 3.4. The internal energy of all of the compounds converged satisfactorily using the standard settings for the present work of $\boldsymbol{k}$-points 555, ENMAX and ENAUG 800 eV. A number (at least 13) of athermal (0 K) simulations were then run at fixed volumes corresponding to a range of pressures from 0 GPa up to high-pressure.

The free energies and volumes from these simulations were fitted using a third order Birch-Murnaghan E-V EOS to calculate the internal energy E_0, the volume V_0, bulk incompressibility K_0 and its derivative with respect to pressure K'_0 at 0 GPa and 0 K. The difference between the total enthalpy of the product(s) and that of the reactant(s) was minimised to zero by varying the volumes of each of the reactants simultaneously, subject to the constraint of equal pressure for all products and reactants, using their E-V EOSs and Excel Solver. The resulting transition/reaction pressure was therefore the point at which the difference between the enthalpy of the product(s) and that of the reactant(s) became zero, without taking account of any activation energy barrier.

4.4.3 Transition pressures

The athermal (0 K) simulation transition pressures shown in column 2 of Table 4-4 are adjusted to show in column 3 the pressure expected at 300 K, by adding the additional pressure calculated using the Clapeyron slope (see Section 3.9.3) shown in column 4. The Clapeyron slopes for $NaBF_3$ post-perovskites are assumed to be 8, because this assumption gives a reasonable approximation to the experimental value for $NaMgF_3$, for which the phase change from perovskite to post-perovskite takes place between 13 and 20 GPa at room temperature (Hustoft *et al.*, 2008).

Transition	Simulated transition pressure GPa	Simulated transition pressure GPa adjusted to 300 K	Clapeyron slope MPa/K	Experimental transition pressure adjusted to 300 K GPa
$MgSiO_3$ perovskite to post-perovskite	90.7[f]	94.7	13.3[a]	93.2 [a]
$MgGeO_3$ perovskite to post-perovskite	48.9[f]	51.3	8[b]	51.0 [b]
$NaMgF_3$ perovskite to post-perovskite	12.6[f]	15.0	8	16.5 [c]
$NaNiF_3$ perovskite to post-perovskite	4.0[d]	6.4	8	9.6 [d]
$NaZnF_3$ perovskite to post-perovskite	9.1[f]	11.5	8	14.0 [e]
δMg_2SiO_4	-18.7[f]	-	-	-
$Ca_2Mg_4Si_3O_{12}$	-11.7 [f]	-	-	-

[a]Tateno *et al.* (2009)
[b]Hirose *et al.* (2005)
[c]Hustoft *et al.* (2008)
[d]present work (see Section 6.8.3)
[e]Yakovlev *et al.* (2009); Yakovlev *et al.* (2009a)
[f]present work

Table 4-4: Transition pressures calculated from athermal simulation.

The simulated phase change pressures for post-perovskites in column 3 of Table 4-4 show good agreement with the experimental pressures in column 5 after both are adjusted to 300 K. This gives some confidence that this method is appropriate for oxide post-perovskites, or at least those whose octahedral cation is not a transition series element. For fluoride post-perovskites, there is a significant range of experimental transition pressures for $NaMgF_3$ (13-20 GPa in Hustoft *et al.* (2008)) and for $NaZnF_3$ (14-22 GPa in Yakovlev *et al.* (2009)). The comparison with the transition pressures from athermal simulation, adjusted for an estimated Clapeyron slope, is therefore likely to have a larger uncertainty.

The transition pressures for δMg_2SiO_4 and $Ca_2Mg_4Si_3O_{12}$ are negative because the enthalpy balances do not favour these transitions at any pressure above these negative pressures: these hexagonal compounds are therefore unlikely to exist.

The relationship between the pressure of the transition from the perovskite to the post-perovskite phase and other post-perovskite characteristics (ionic size, electronegativity etc.) is examined further in Chapter 5.

4.5 Octahedral distortion and the Jahn-Teller effect

4.5.1 Transition element *d*-orbitals

The Jahn-Teller (JT) effect describes the geometrical distortion of non-linear degenerate molecules which cannot be stable (Jahn and Teller, 1937). Electron orbitals are said to be degenerate if one electron can occupy either of two orbitals of equal energy. A non-linear molecule with a degenerate electronic ground state undergoes a geometrical distortion which removes the degeneracy and lowers the overall energy of the complex. The JT effect often occurs in octahedral complexes of the transition elements, and it has been comprehensively studied in perovskites (e.g. Goodenough, 1998; Lufaso and Woodward, 2004; Carpenter and Howard, 2009). The JT effect may also occur in $CaPtO_3$ and $CaIrO_3$ post-perovskites, where the transition elements Pt and Ir have 5*d*-orbitals. It may also affect $NaZnF_3$, $NaNiF_3$, $NaCoF_3$ and $NaMnF_3$ post-perovskites where the transition elements Zn, Ni, Co and Mn have 3*d*-orbitals, and $CaRuO_3$ (Kojitani *et al.*, 2007) and $CaRhO_3$ (Shirako *et al.*, 2009) where the transition elements Ru and Rh have 4*d*-orbitals. It will not affect $MgSiO_3$, $MgGeO_3$ or $NaMgF_3$ where the B atoms are not transition elements.

There are 5 *d*-orbitals (shown in Figure 4-17), whose shapes represent the angular distribution probabilities for electrons in each orbital. Figure 4-17 and the following explanation of *d*-orbitals are adapted from Putnis (1992).

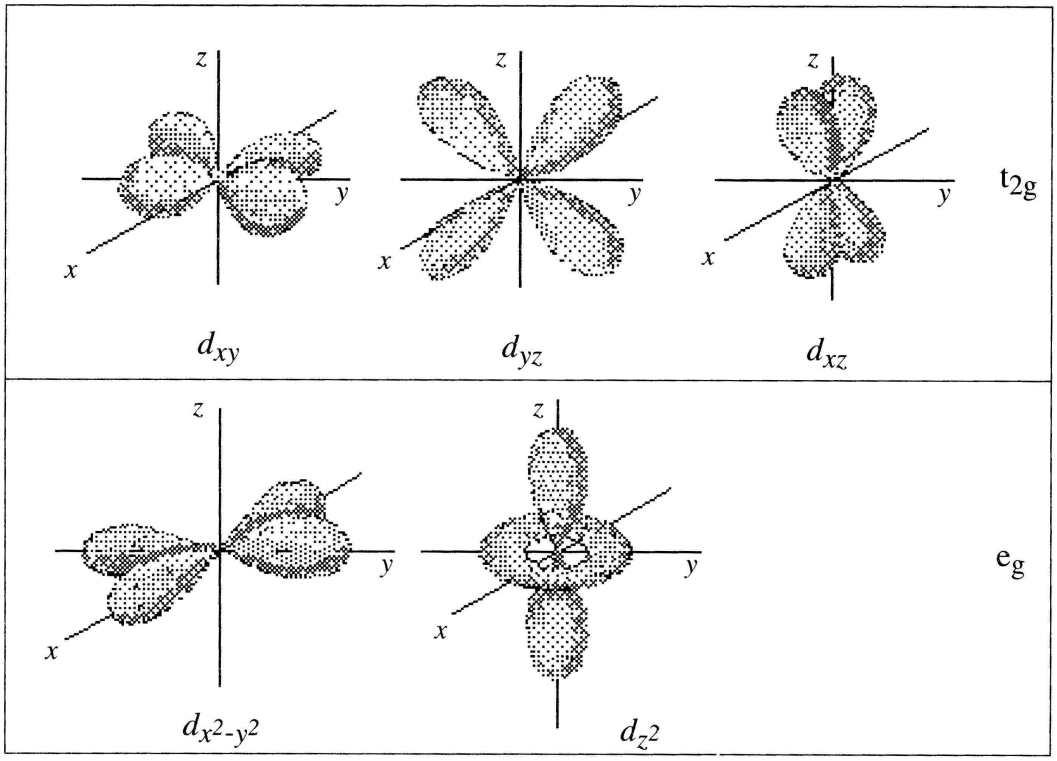

Figure 4-17: d atomic orbitals, representing regions which contain most of the electron density (Putnis, 1992). *x*, *y* and *z* are the local coordinate axes at the transition metal site.

4.5.2 Energy splitting of *d*-orbitals

The *d*-orbitals are divided into 3 t_{2g} and 2 e_g orbitals, named from the symmetry of the wave functions of the electrons. Each orbital can accommodate 2 electrons with opposite spins in the low-spin state which minimizes inter-electron repulsion. Partly filled orbitals are occupied by electrons spreading out over as many orbitals as possible (Hund's rule), with one electron in each before any pairing of spins takes place. In the low-spin state electrons are paired where possible. In a free ion or an ion in a spherical field all the d electrons have equal probability of being in any of the *d*-orbitals, which all have the same energy.

When the ion is in a crystal structure, the relative energies of the *d*-orbitals are controlled by the repulsive energies of the anions coordinated to the ion. This is where the symmetry of the orbitals is important; if the lobes of the electron distributions of

the different orbitals point directly towards the anions, electrons in these (non-bonding) orbitals are repelled to a greater extent and their energy is raised relative to the orbitals which project between the anions. In a transition metal oxide octahedron, the lobes of the e_g orbitals point towards the oxygen anions and the lobes of the t_{2g} orbitals lie between the oxygen anions. The resulting split in the energy of the *d*-orbitals produces an energy reduction for electrons in t_{2g} relative to those in e_g orbitals (Figure 4-18).

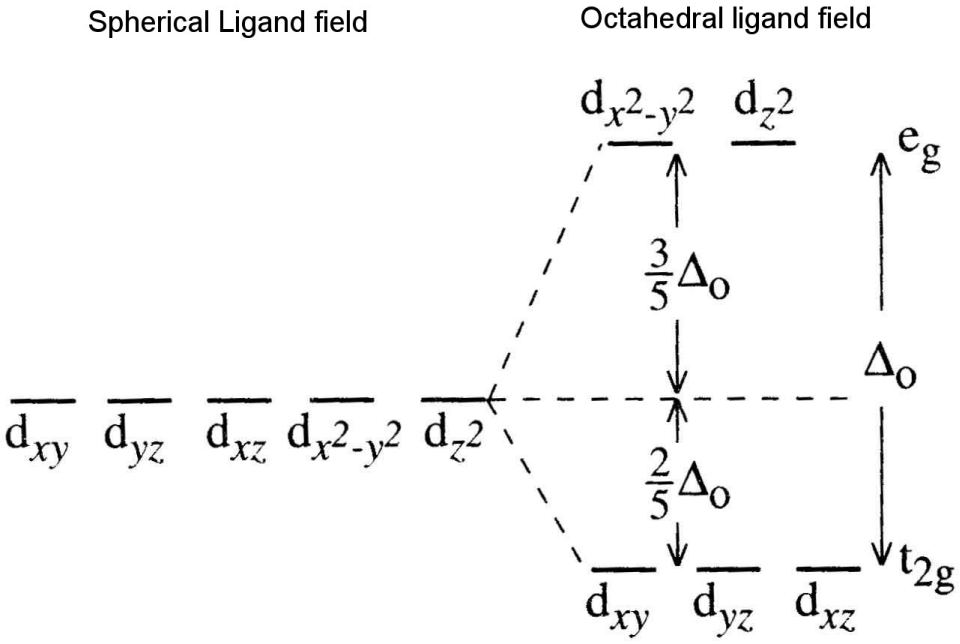

Figure 4-18: Energy level splitting of *d*-orbitals (Putnis, 1992).

The splitting of these energy levels (Δ_0) is such that the average energy stays the same. If all five orbitals were each occupied by one electron, the two electrons in e_g would raise the energy by 3/5 Δ_0, while the three t_{2g} electrons would each reduce the energy by 2/5 Δ_0, giving a net energy change of zero. However if the B cation contained only three d electrons and they were all in t_{2g} orbitals then there would be a net reduction of energy by 6/5 Δ_0. This energy reduction is the crystal field stabilisation energy (CFSE).

Hund's rule states that lower energy is achieved if electrons are placed in separate degenerate orbitals with the same spin: this keeps electrons further apart, decreases

electron-electron repulsion, and minimises exchange energy. However as the gap Δ_0 between the two energy levels becomes larger, lower energy is achieved by allowing more electrons to fill t_{2g} rather than e_g orbitals, with two electrons of opposite spin occupying the same t_{2g} orbital. Then if the cation has more than the maximum of six electrons which the t_{2g} orbitals can accommodate, the additional electrons occupy the e_g orbitals.

The two e_g orbitals ($d_{x^2-y^2}$ and d_{z^2}) are degenerate if they are occupied by three electrons: the third electron can occupy either e_g orbital. The two e_g orbitals are doubly degenerate (spin up or down) if they are occupied by only one electron. The system can move to a lower energy state if degeneracy is lifted by displacing oxygen anions surrounding the transition element cation. The additional elastic energy from displacing the oxygen anions is balanced by the reduced electronic energy.

4.5.3 Distortion of octahedra

The most commonly described form of JT distortion of an octahedron involves a change in position of the X1 apical anion. If the octahedron is shrunk along its *z*-axis by reducing the B-X1 bond length, the d_{z^2} orbital is more overlapped with the apical X1 anion *p*-orbital. Then the electron occupying the (non-bonding) d_{z^2} orbital is more strongly repelled by the X1 anion than the electrons in the $d_{x^2-y^2}$ orbitals are by the X2 anions, so d_{z^2} has a higher energy than $d_{x^2-y^2}$ and occupation of the $d_{x^2-y^2}$ orbital makes the system more stable. The e_g orbitals are now no longer degenerate because they have different energies. The degeneracy may also be lifted by elongating the octahedron along its *z*-axis (changing the symmetry from cubic to tetragonal) instead of shrinking it, and then occupation of the d_{z^2} orbital makes the system more stable. An alternative would be for the degeneracy to be lifted by changing angle p so that the energy of the $d_{x^2-y^2}$ orbital was reduced, although this would increase the energy of the t_{2g} d_{xy}orbital as the X2 atoms moved away from $d_{x^2-y^2}$ towards d_{xy}. A similar distortion in perovskites is described by Goodenough (2004: Figure 19b).

A low-spin d-electron configuration occurs when as many electrons as possible have matched spins in each of the t_{2g} and e_g orbitals. A high-spin configuration occurs when

the electrons follow Hund's rule in occupying as many orbitals as possible with the same spin.

In octahedral complexes the JT effect is strongest when an odd number of electrons occupy the e_g orbitals (three for d^9, one for low-spin d^7 and for high-spin d^4). The JT effect is only seen in insulating compounds with localized electrons. It is not found in metallic materials, such as in $LaNiO_3$ perovskite with its Ni^{3+} low-spin d^7 ions (Mazin *et al*., 2007).

Degeneracy in t_{2g} orbitals results in a weaker JT effect than degeneracy in e_g orbitals. Shrinkage or elongation of the octahedron results in a much smaller change of repulsion between an oxygen anion and an electron in a t_{2g} orbital, because the lobes of these orbitals lie between oxygen anions rather than pointing directly at them.

Other possible distortions of the post-perovskite octahedron include changes in the positions of the X1 anion along the unit-cell *b*-axis, and of the X2 anion along the unit-cell *b* and *c* axes, corresponding to changes in the Δ_1, Δ_2 and *p* angles. The distortion of the octahedron in the post-perovskite structure is defined by the difference in angles Δ_1-Δ_2 and *p* and in the bond length ratio (B-X1)/(B-X2). If Δ_1-Δ_2 and *p* remain constant, and if the *d*-orbitals of the B cation rotate about the *a*-axis following the X anions, then the relative energy levels of the t_{2g} and e_g orbitals will not change as Δ_1 and Δ_2 change. (This is true to a first-order approximation: the energy levels could change due to interaction with charges outside the octahedron).

Angles Δ_1 and Δ_2 are defined with respect to the axes of the unit-cell rather than with respect to the *d*-orbital axes of the B cation. If Δ_1-Δ_2 or *p* change as a result of movement of X anions, or if the *d*-orbitals of the B cation do not rotate about the *a*-axis following the X anions, then the energy levels of the *d*-orbitals relative to each other will change as a result of change in Δ_1, Δ_2 or *p* angles. DFT simulation includes these effects through its modelling of the electron densities. A distortion by rotation of the octahedron about the *c*-axis to create a difference in energy levels between d_{yz} and d_{xz} orbitals is forbidden by the *Cmcm* symmetry of the post-perovskite structure.

The experimental elongation of the central plane of the post-perovskite $CaPtO_3$ octahedron along the *a*-axis (angle $p > 90°$) is attributed to the repulsive electronic interaction between the filled t_{2g} orbitals (Inaguma *et al.,* 2008). Pt-O1 and Pt-O2 distances are more similar to each other than are Ir-O1 and Ir-O2 distances in post-perovskite $CaIrO_3$ (see also Section 9.4.2). This is presumed by Inaguma *et al.* (2008) to arise from differences in bonding associated with Ir^{4+} d^5 and Pt^{4+} d^6 electron configurations.

4.5.4 Distortion and electronic configuration

All transition element-localised electrons in transition element complexes are best considered as *d*-orbital electrons (Green, 2003). This means that tetravalent transition element ions in post-perovskites are formed by the loss of all the outermost *s*-orbital electrons, plus as many *d*-orbital electrons as are required to achieve the tetravalent state. Magnetic susceptibility measurements indicate that the Pt $5d^9$ $6s^1$ atom in $CaPtO_3$ becomes the tetravalent cation Pt^{4+} in the low-spin state with an electron configuration of t_{2g}^6 e_g^0 (Inaguma *et al.*, 2008; Ohgushi *et al.*, 2008). Rh $4d^8 5s^1$ becomes low-spin Rh^{4+} $4d^5$ with t_{2g}^5 (Shirako *et al.,* 2009), and Ru $4d^7$ $5s^1$ becomes low-spin Ru^{4+} $4d^4$ with t_{2g}^4 (Zhong *et al.*, 2010). Ir $5d^7$ $6s^2$ becomes Ir^{4+} $5d^5$ (Inaguma *et al.,* 2008; Ohgushi *et al.,* 2008), which is also likely to be low-spin.

Expected JT effects for octahedrally coordinated oxides are shown in Table 4-5.

Number of d electrons	1	2	3	4	5	6	7	8	9	10
High-spin	W	W	N	S	N	W	W	N	S	N
Low-spin	W	N	W	W	W	N	S	N	S	N
Covalent								Ru	Rh,Ir,Co	Pt,Zn,Ni
Ionic				Ru^{4+}	Ir^{4+},Rh^{4+}	Pt^{4+}	Co^{2+}	Ni^{2+}		Zn^{2+}

Table 4-5: JT effects for octahedral coordination. W: weak JT effect (degeneracy in t_{2g} orbitals). S: strong JT effect (degeneracy in e_g orbitals). N: no JT effect (no degeneracy). Covalent: completely covalent electronic configuration. Ionic: completely ionic tetravalent electronic configuration.

Published results indicate that the B ions shown in Table 4-5 are low-spin in ABX_3 post-perovskite compounds, with the exception of Co^{2+} (high-spin). Then Table 4-5 suggests that there will be no JT effect for Pt, a strong JT effect for covalent Ir and Co and a weak JT effect for ionic Ir^{4+} and for (high-spin) Co^{2+}.

The strength of the JT effect for octahedrally coordinated Ir, Rh, Ru and Co cations is likely to vary depending on the degree of ionicity/covalency of the B-O bonds. Where bonding is completely ionic, the level of occupation of the *d*-orbitals should be consistent with the tetravalence of the cation: Ir^{4+} will be $5d^5$ and Pt^{4+} will be $5d^6$. Completely covalent bonding should populate the *d*-orbitals with the atomic d and s valence electrons: Ir should be $5d^7 6s^2$, equivalent to $5d^9$, and Pt should be $5d^9\ 6s^1$, equivalent to $5d^{10}$.

In practice the degree of ionicity/covalency is likely to vary with temperature and pressure. Rising pressure increases covalency in transition metal oxides (Demazeau *et al.*, 1997) and suppresses the Jahn-Teller effect due to delocalisation of electrons into ligand (O) orbitals (Loa *et al*., 2001; Keppler *et al*., 2007). Rising temperature increases ionicity (Fei *et al*., 1994).

4.6 Summary of simulation results

1. Fluoride post-perovskites, and oxide post-perovskites with transition element B atoms, are more compressible than oxide post-perovskites with main group B atoms. The structural behaviour of post-perovskite $MgGeO_3$ is the most similar of the analogues to that of $MgSiO_3$, although the effect of the larger Ge atom is to increase the Δ_1 and Δ_2 tilt angles. Even so, the octahedral distortion of $MgGeO_3$ is similar to that of $MgSiO_3$. $NaMgF_3$ is the most analogous of the fluoride post-perovskites to $MgSiO_3$, in particular in terms of the volumes of octahedra, hendecahedra and void relative to the unit-cell.

2. Axial compression shows that $CaIrO_3$ is more anisotropic than $CaPtO_3$, and both are more anisotropic than $MgSiO_3$ and $MgGeO_3$. Fluoride post-perovskites are more anisotropic than $MgSiO_3$ and $MgGeO_3$ but less anisotropic than $CaIrO_3$ and $CaPtO_3$ at the same V/V_0.

3. The X1 y atomic coordinate determines the Δ_1 angle, and the X2 z coordinate has the most effect on the Δ_2 angle. All of the post-perovskite analogues show non-monotonic variability in these two coordinates and hence in these angles. This variability, which is very low in $MgGeO_3$, is in general more marked for $V/V_0 <$ ~ 0.9. Fluoride analogues show non-monotonic variability in A y for $V/V_0 <$ ~ 0.95.

4. A less compressible hendecahedron is associated with greater octahedral distortion in the oxide and fluoride post-perovskites simulated in the present work. A small X-B electronegativity difference is associated with stronger, more covalent octahedral bonding.

5. $CaIrO_3$ and $CaPtO_3$ have octahedral O-B-O angles which show higher variance from 90° than those of the other post-perovskites.

6. The effect of thermal motion in increasing the simulated instantaneous Ir-O1 bond length is much less than might be expected by comparison with $MgSiO_3$ and $CaPtO_3$. This may be due to the distortion of the IrO_6 octahedron by the Jahn-Teller effect.

7. Differences between the simulated compressive structural behaviours of post-perovskite $MgSiO_3$ and those of the hypothetical post-perovskite $MgHAlO_3$ are likely to be due to the presence of the H atom in a tetrahedral site linked to two O2 and two O1 atoms. This is supported by the 53% higher compressibility of the void in $MgHAlO_3$ compared with $MgSiO_3$ PPV.

5 Empirical prediction of post-perovskite phase stabilisation pressures

5.1 Introduction

I found that the simulated post-perovskites described in Chapter 4 can be ordered according to their bulk incompressibilities, their octahedral tilt angle Δ_1 and so on. However, I wanted to identify underlying characteristics of each compound which would explain these sequences. Ohgushi *et al.* (2008) speculated that Ir-O and Pt-O bonds are strongly covalent because of the high electronegativity of Ir and Pt. I therefore examined the electronegativity differences between B and X atoms and between A and X atoms in ABX_3 post-perovskites to see whether these could explain the order of each sequence. Other factors to be considered included the role of the ionic radii of the A, B and X atoms and their *t*-factor (see Section 5.6.1) in determining whether a post-perovskite phase would be formed, and at what pressure, as highlighted by Tateno *et al.* (2006).

With these ideas in mind, I developed the empirical approach described in this Chapter for predicting whether an oxide post-perovskite phase is likely to occur, and the stabilisation pressure P_S required for it to do so. This approach is based on a simple combination of ionic radii, electronegativities and octahedral tilt in the perovskite phase, using experimental data; it is therefore much less computationally expensive than the DFT calculations discussed in Chapter 4. The predicted stabilisation pressure is critical to synthesising a new post-perovskite experimentally. The extension of this approach to fluoride post-perovskites (see Section 5.11) led to the synthesis, during the present work, of two new post-perovskites, $NaNiF_3$ and $NaCoF_3$ (see Section 6.8.3).

Finally, the DFT simulations described in Section 5.12 indicate that the octahedral angular distortion of some of the perovskite phases which transform to the post-perovskite phase may exhibit a minimum (as pressure increases) near the pressure at which the transition takes place.

5.2 Factors determining stabilisation pressure

ABO_3 oxide post-perovskites (except $CaIrO_3$) must be synthesised at high-pressure and (except $CaIrO_3$, $CaPtO_3$ and $NaIrO_3$) are always formed by compressing the perovskite phase. However, the simple oxides Fe_2O_3, Al_2O_3 and Mn_2O_3 also form post-perovskites at high-pressure. For Fe_2O_3 (Ono and Ohishi, 2005) and Al_2O_3 (Oganov and Ono, 2005), the transformation from the corundum structure to the post-perovskite phase proceeds *via* the Rh_2O_3 (II)(*Pbcn,* space group number 60) structure, while Mn_2O_3 transforms directly from the bixbyite structure to the post-perovskite structure (Santillan *et al.,* 2006).

Knowledge of the expected pressure at which the post-perovskite phase forms is very important when developing new post-perovskite analogues. The primary motivation for the study of post-perovskite analogue phases is to provide materials that are stable at low (ideally at ambient) pressure and whose physical properties can be easily measured; this knowledge can then be used, in combination with computer simulations, to elucidate the physical properties that $MgSiO_3$ is likely to exhibit in the deep Earth. To date, many such experiments have been carried out on $CaIrO_3$ (e.g. Boffa Ballaran *et al.*, 2007; Lindsay-Scott *et al.*, 2007; Martin *et al.*, 2007a; Martin *et al.*, 2007b; Hunt *et al.*, 2009; Walte *et al.*, 2009; Liu *et al.*, 2011) as this compound forms a post-perovskite structure at ambient pressure. The pressure required to produce post-perovskite structured materials varies from 0 GPa to ~130 GPa, so it is necessary to have a method for predicting whether the post-perovskite phase is likely to form and for estimating the required pressure.

The propensity of an ABO_3 compound to form a post-perovskite structured phase must depend on the relative sizes of the three ions and the strengths of the bonds between them. The best correlation with the stabilisation pressure P_S is obtained for a parameter, based on differences in electronegativity and ionic sizes of the B and O ions, that reflects both the bonding and the dimensions of the BO_6 octahedra. The formation of a post-perovskite phase from a perovskite phase requires transformation of the 3-dimensional BO_3 framework of corner-linked octahedra found in the perovskite structure into the 2-dimensional, edge-shared and corner-linked sheets of octahedra that are present in the post-perovskite structure.

The correlation between the pressure above which the post-perovskite phase is stable (P_S) with parameters based simply on the sizes of the A and B cations is less good, which suggests that the approach of including electronegativities is worthwhile: the covalency of the B-O bond stabilizes the edge-sharing post-perovskite structure by comparison with the perovskite structure (Ohgushi *et al.*, 2008). However, for a given B-cation, the post-perovskite structure will exist only if the A-cation is also of a suitable size. As discussed previously by other authors (see Section 5.3 below), this linkage between the sizes of the A and B cations can be accounted for in terms of a tolerance factor calculated from the ionic radii, and by considerating the octahedral tilting in the perovskite phase.

5.3 Previous work

The phase diagrams of ABO_3 analogues of $MgSiO_3$ in the post-perovskite and perovskite regions have been extensively studied both experimentally (e.g. Boffa Ballaran *et al.,* 2007; Shim *et al.,* 2008; Komabayashi *et al.,* 2008; Yamazaki *et al*., 2011) and computationally (e.g. Tsuchiya and Tsuchiya, 2007a, 2007b; Stølen and Trønnes, 2007; Fang and Ahuja, 2006; Matar *et al.,* 2008). Goldschmidt diagrams (Goldschmidt, 1926) have been used to analyse the perovskite to post-perovskite transitions in different compounds in terms of the A and B cation radii (e.g. Tateno *et al.,* 2006, 2010; Fujino *et al.,* 2009; Bremholm *et al*., 2011). It has also been suggested that the covalency of the B-O bonds in post-perovskite ABO_3 may be a controlling parameter for the transition (Ohgushi *et al.,* 2008; Bremholm *et al*., 2011; Okada *et al*., 2011). The relative degree of covalency and ionicity in a bond depends on the difference between the electronegativities of the atoms involved; bonds between atoms having a larger difference in electronegativies will be more ionic in character. For metal-oxide bonds, the covalency of the bond increases as both the electronegativity and oxidation state of the metal ion increases (Mizoguchi *et al.,* 2004a).

The prediction of perovskite structures has also been extensively studied. Previous work in this area has included studies based on cation-anion ionic radii (Muller and Roy, 1974) or pseudopotential radii (Burdett *et al*., 1982: Price *et al*., 1982). Other studies were based on combinations of anion-cation electronegativity difference with average principal quantum number (Mooser and Pearson, 1959) or with ionic radii (Giaquinta and zur Loye, 1994). Ye *et al.* (2002) performed a multivariate analysis of perovskite-forming factors and concluded (like Liang *et al.*, 2004) that face sharing rather than corner linking of BO_6 octahedra (e.g. $BaNiO_3$ – see Section 5.4.2) is more likely if the electronegativity difference between B and O ions is small enough, due to reduced repulsion between B ions. Other studies have classified ABX_3 perovskites in terms of the *t* factor (see Section 5.6.1 for definition and further discussion of this factor) and an octahedral factor r_B/r_X, for oxides (Feng *et al.*, 2008) and for fluorides (Li *et al.*, 2008).

5.4 Construction of an empirical stabilisation factor for post-perovskite phases

5.4.1 Electronegativity difference

Electronegativity values may be defined in a number of ways. Those tabulated quite recently by Li and Xue (2006), χ_i, provide the best fit to the experimental data on post-perovskite stabilisation pressure. The much older, commonly-used, Pauling electronegativities, χ_P, (Pauling, 1960; see also Allred, 1961) lead to similar results for most compounds (see Section 5.5.1). The χ_i values presented by Li and Xue (2006) are based on effective ionic potentials defined by the ionization state and ionic radii of the elements and include entries for atoms in different oxidation states, with different coordination numbers, and with different spin states. The electronegativity difference between O and B atoms is defined as

$$\Delta\chi_{i(O-B)} = \chi_{iO} - \chi_{iB} \tag{5.1}$$

where χ_{iO} and χ_{iB} are the electronegativities (as defined by Li and Xue, 2006) of the O and B atoms respectively. A similar quantity calculated using the Pauling electronegativity scale is denoted by $\Delta\chi_{P(X-B)}$, where the subscript *X* denotes a general anion.

Ohgushi *et al.* (2008) found that, in post-perovskite compounds which can be synthesised at ambient pressure, the difference in the Pauling electronegativity values ($\Delta\chi_{P(X-B)}$) is small, suggesting that the post-perovskite structure is stabilised if the B-X bond is more covalent in character. Okada *et al.* (2011) suggested that the low covalency of Ti-O bonds contributed to the inability of $MnTiO_3$ perovskite to form the post-perovskite phase under pressure. If the stabilisation of post-perovskite phases is assumed to be associated with a particular degree of covalency of the B-X bonds, it is likely that, since the covalency of bonds is a positive function of pressure, the observations of Ohgushi *et al.* (2008) might be extended to explain the pressure stabilisation of the post-perovskite structure. So the difference in electronegativity between the X and B species might provide a useful predictor of post-perovskite stabilisation pressure for those compounds which form post-perovskite phases.

5.4.2 Ionic radii

Although a reasonable correlation exists between P_S and $\Delta\chi_{P(O-B)}$ for most post-perovskite oxides, further investigation shows that the trend in P_S can be better predicted by using a parameter incorporating $\Delta\chi_{i(O-B)}$ but which also takes account of the relative sizes of the B and O ions.

A combination of ionic radii that has been commonly used to explain perovskite stability is that giving the tolerance factor, t (see Section 5.6.1). However, other combinations of ionic radii have also been employed; for example, Liang *et al.* (2004) discussed the stability of the perovskite structure in complex halides and its propensity to transform into the $BaNiO_3$ structure (which contains face-shared BX_6 octahedra) in terms of three empirically-chosen parameters, one derived from the electronegativity difference between the B and X ions and two involving the ionic radii. The inverse of one of the two parameters used by Liang *et al.* (2004), namely $\frac{(r_B + r_X)}{r_B}$, can be combined with $\Delta\chi_{i(O-B)}$ to form a *stabilisation factor*, Ψ_S, such that

$$\Psi_S = \frac{(r_B + r_O)}{r_B}\Delta\chi_{i(O-B)}.$$

5.4.3 The stabilisation factor Ψ_S

Ψ_S provides an easily-calculated value (see, for example, Table 5-2) that shows a good correlation with P_S (see Figure 5-1) via the equation:

$$P_S = a\,\Psi_S + b \qquad (5.2)$$

Clearly, in considering the stability of the post-perovskite phase, the synthesis temperature is also important. However, the measured Clapeyron slopes of the perovskite/post-perovskite phase boundaries (see Table 5-1) indicate that the effect of temperature on the transition pressure is generally of the order of 10 GPa per 1000 K and is, therefore, small compared to the range of stabilisation pressure, which is greater than 100 GPa. The experimental pressure-temperature conditions of stabilisation in Table 5-1 are therefore corrected, using known or estimated Clapeyron slopes, to their hypothetical values at 300 K.

5.4.4 Comparison with experiment

The experimental values of P_S, corrected to 300 K, for the ABO_3 compounds are shown in Figure 5-1; the data used to derive these points are given in Table 5-1. The line in Figure 5-1 shows the linear fit of P_S to Equation 5.2, with P_S = 89.7(71) Ψ_S – 454(39) GPa. It can be seen that the correlation is very good, with R^2 = 0.95; all of the data points (with the exception of that for $CaRhO_3$, for which the value of the Clapeyron slope is in some doubt) fall within ~14 GPa of their predicted values from the linear fit. However, the plot clearly shows that the value of Ψ_S is not the only factor controlling post-perovskite structure stabilisation as, for example, although $CaRuO_3$ and $CaRhO_3$ have almost identical values of Ψ_S they have a significant difference in stabilisation pressure.

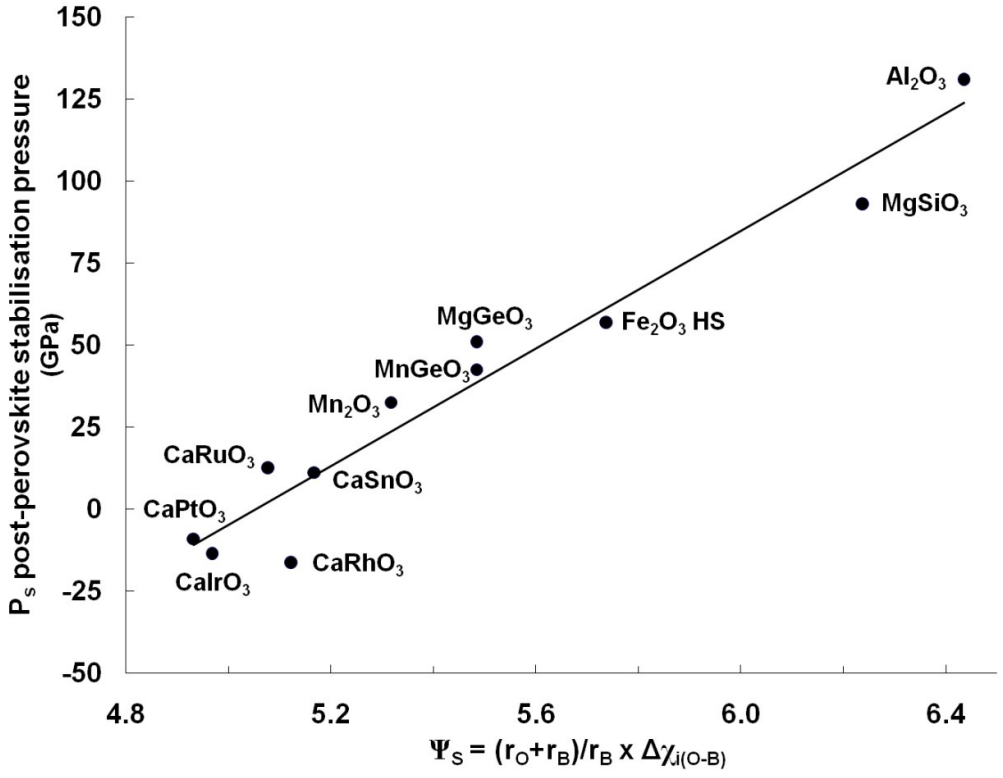

Figure 5-1: The relationship between the post-perovskite stabilisation pressure, *Ps*, and the stabilisation factor, Ψ_S, (see text for definitions) for post-perovskite oxides. Experimental data for ABO_3 compounds (corrected to 300K – see Table 5-1) are indicated by symbols. The line shows the fit of Equation 5.2 to the data: P_S = 89.7(71) Ψ_S – 454(39) GPa (R^2 = 0.95).

Compound	$\Delta\chi_{i(O-B)}$	$\frac{(r_B + r_O)}{r_B}$	Ψ_S	Transition conditions (experiment)	Clapeyron slope (MPa K^{-1})	Stabilisation pressure, P_S, extrapolated to 300K	Source
$MgSiO_3$	1.871	3.333	6.237	136 GPa at 3520K	13.3	93.2 GPa	Tateno *et al.* (2009).
Al_2O_3	2.245	2.867	6.436	126.9 GPa at 1750K	-2.9	131.1 GPa	Ono *et al.* (2006a)
Fe_2O_3	2.202	2.605	5.736	59 GPa at 1200K	2.2	57.0 GPa	Ono and Ohishi (2005)
Mn_2O_3	1.846	2.881	5.318	27-38 GPa at 300K		32.5 GPa (mean)	Santillan *et al.* (2006)
$MnGeO_3$	1.904	2.881	5.485	62.5 GPa at 1800K	13	42.5 GPa	Yamazaki *et al.* (2011)
$MgGeO_3$	1.904	2.881	5.485	63 GPa at 1800 K	8	51.0 GPa	Hirose *et al.* (2005)
$CaRuO_3$	1.910	2.658	5.077	24.4 GPa at 1473K	10	12.7 GPa	Kojitani *et al.* (2007)
$CaRhO_3$	1.895	2.703	5.122	4 GPa at 1493K	Assume 17 as for $CaIrO_3$	-16.3 GPa	Shirako *et al.* (2009)
$CaPtO_3$	1.863	2.647	4.931	4 GPa at 1073K	Assume 17 as for $CaIrO_3$	-9.1 GPa	Ohgushi *et al.* (2008)
$CaIrO_3$	1.877	2.647	4.969	0 GPa at 1100K	17	-13.6 GPa	Sugahara *et al.* (2008) Hirose and Fujita (2005) (for Clapeyron slope)
$CaSnO_3$	2.052	2.518	5.167	40 GPa at 2000 K	17	11.1	Tateno *et al.* (2010)

Table 5-1: Experimental formation conditions and calculated stabilisation factors of oxide post-perovskites.

Column 2: Electronegativity differences, $\Delta\chi_{i(O-B)}$, calculated using values taken from Li and Xue (2006). For Mn_2O_3 the value for Mn(IV) was adopted, as no value is given for Mn(III); this would correspond to the charge disproportionation into $Mn^{2+}Mn^{4+}O_3$ discussed by Santillan *et al.* (2006). For Fe_2O_3 the high-spin value was taken (Shim *et al.*, 2009).

Column 3: Size factor, $\frac{(r_B + r_O)}{r_B}$; values calculated using ionic radii ("CR" values for a coordination number of VI) taken from Shannon (1976). For Mn and Fe the values were chosen to correspond to the choice of electronegativities.

Column 4: Stabilisation factor $\Psi_S = \frac{(r_B + r_O)}{r_B}\Delta\chi_{i(O-B)}$

Column 7: post-perovskite stabilisation pressures, P_S, calculated as indicated in columns 5 – 6. The stabilisation pressures were taken from the sources listed (Column 8) and corrected to a common temperature value of 300 K using the Clapeyron slopes given in Column 6: this may result in a negative value for P_S. For all compounds except $CaIrO_3$ and $CaPtO_3$ the experimental transition conditions (Column 5) were taken to be the minimum pressures at which the post-perovskite phase has been reported to form from the perovskite phase. For $CaIrO_3$ and $CaPtO_3$, the post-perovskite phase has been synthesised directly from the metal oxides; the transition condition was then taken to be the minimum pressure at which this reaction has been reported to occur.

The correction of P_S values to a common temperature of 300 K has only a small effect on the goodness of fit to Equation 5.2. Using the uncorrected pressure values given in column 5 of Table 5-1 gives a very slightly worse correlation, with $R^2 = 0.93$.

However, correction to 300 K allows the method to be extended to predict the position of perovskite-post-perovskite phase boundary, given a chosen temperature and an estimated value of the Clapeyron slope.

5.5 The factors affecting Ψ_S and its physical basis

5.5.1 Electronegativity scales

A fundamental issue in this approach is the question of which electronegativity scale should be used when calculating Ψ_S. It was found that the Ψ_S values obtained using the electronegativities tabulated by Li and Xue (2006) gave the best correlation with P_S. Although a similar linear relationship was found when Ψ_S was calculated using the Pauling electronegativity scale (as tabulated by Allred, 1961 and by Pauling 1960) the correlation, with $R^2 = 0.73$, was not as good, principally because the data point for Mn_2O_3 lay far from the line. Removal of the Mn_2O_3 data point from the fit gave a much better correlation, with $R^2 = 0.95$, but there is no *a priori* reason to exclude this compound and the method is clearly much less useful if one has to allow for exceptions.

The Pauling electronegativities are based on thermochemical data. Plots of P_S against the Ψ_S values calculated using electronegativities as defined from electrostatics by Allred and Rochow (1958; "χ" values) and from spectroscopy Allen (1989; "χ_{Spec}" values) gave much worse correlation coefficients, with $R^2 = 0.56$ (for a limited data set, as not all of the required electronegativity values were tabulated) and $R^2 = 0.12$, respectively. The advantage of the values tabulated by Li and Xue (2006), which are based on ionization energies and ionic radii, is that they take account of elements in different valence states, in different spin states (where applicable) and with different coordination numbers. In contrast, the Pauling values for elements in the transition block are for an oxidation state of II (see Allred, 1961) and so are probably less representative of the properties of the B cations as they occur in the ABO_3 post-perovskites.

5.5.2 Ψ_S and t as functions of pressure and temperature

Increasing pressure increases covalency in transition metal oxides (Demazeau *et al.*, 1997; Keppler *et al.*, 2007). Rising temperature increases ionicity (Fei *et al.*, 1994). This means that the $\Delta\chi_{i(O-B)}$ factor in $\Psi_S = \frac{(r_B + r_O)}{r_B}\Delta\chi_{i(O-B)}$ is likely to be a function of pressure and of temperature. The different rates of compression or expansion of

cations and anions will also affect r_A, r_B and r_O, making both the $\frac{(r_B + r_O)}{r_B}$ factor in Ψ_S and $t = \frac{1}{\sqrt{2}}\left(\frac{r_A + r_O}{r_B + r_O}\right)$ (see Section 5.6.1) functions of pressure and temperature. The empirical approach described here to calculate the value of Ψ_S and P_S uses ambient values for electronegativity and ionic radii, but nevertheless provides a rapid method for predicting the stabilisation pressure.

5.5.3 Transformation, inter- and intra-octahedral distortions

A survey of the ABX_3 compounds where X = S, Te or Se which form stable post-perovskite structures at ambient pressure (as reported in the Inorganic Crystal Structures Database; Fletcher *et al.* 1996)($ThMnTe_3$, $ThMgTe_3$, $UMnSe_3$, $UFeSe_3$, $ThMnSe_3$, $UFeS_3$, (La,Ce,Pr,Nd,Sm)$YbSe_3$ and $LaYbS_3$) shows that they have values of $\Delta\chi_{i(X-B)}$ that are less than 1.2, and consequently values of Ψ_S that are less than 4.0, much lower than those of the oxides discussed here (see Table 5-2 and Table 5-3). A similar survey of ABX_3 halides where X = Br or I which form stable post-perovskite structures at ambient pressure ($KTmI_3$, $KYbI_3$ and $InCaBr_3$) shows that they have values of $\Delta\chi_{i(X-B)}$ that are less than 1.6, and consequently values of Ψ_S that are less than 4.2. However, the observation that the transition pressure in the oxides is also dependent on $\frac{(r_B + r_O)}{r_B}$ suggests that the pressure at which the transformation to post-perovskite occurs is governed by intra-octahedral as well as inter-octahedral distortion. The reason for this is that it is expected that distortion of the BO_6 octahedron (a distortion which may be a necessary requirement if a transition from the corner-linked to the edge-shared octahedral network is to occur) will require less pressure as the B cation increases in size, as a larger B cation will produce a corresponding increase in the anion-anion distances and so reduce the rigidity of the octahedron.

5.5.4 The physical significance of lower O-B electronegativity differences

The phase transition from perovskite to post-perovskite structures may be influenced by the O-B electronegativity difference in the following way. As the electronegativity difference decreases, there is a higher probability that B atom valence electrons will be found closer to the B cation. The O anions will then be less negatively charged, reducing repulsion between anions in adjacent tilted octahedra. So it is possible that a lower value of $\Delta\chi_{i(O-B)}$ (or $\Delta\chi_{P(O-B)}$), which reduces anion repulsion, will have the same destabilising effect on the perovskite structure as an increase in pressure in compounds where increasing pressure increases octahedral tilts. Then compounds with a smaller $\Delta\chi_{i(O-B)}$ will tend to transform to a post-perovskite phase at lower pressures.

In this discussion applied pressure is assumed to be hydrostatic. Non-hydrostatic pressure enables the perovskite to post-perovskite transition in $NaMgF_3$ (Liu *et al.*, 2005). Deviatoric stresses in $NaMgF_3$ may help overcome kinetic barriers to this transition at room temperature (Hustoft *et al.*, 2008). Shear stress of around 9 GPa enables a partial perovskite to post-perovskite transition in $CaIrO_3$ at room temperature (Cheng *et al.*, 2010; Niwa *et al.*, 2010).

5.6 Other factors affecting the formation of post-perovskite phases

Even if further data show that the trend line in Figure 5-1 is robust, the relationship shown in the Figure is not, of itself, sufficient to determine whether a post-perovskite phase will form; other factors must also be taken into account. Previous work suggests that the most important of these factors are the relative sizes of the A and B cations and the extent of octahedral tilting in the perovskite phase.

5.6.1 The A cation and the t factor

Martin and Parise (2008) related the post-perovskite transition pressure to the ratio of the volumes of the A-cation and B-cation coordination polyhedra in the perovskite phase (V_A and V_B respectively), concluding that the transition will occur when V_A/V_B falls below 4.036, assuming regular (undistorted) octahedra. Avdeev *et al.* (2007) estimated this ratio as ~3.8, taking account of distortions in perovskite octahedra.

Fujino *et al.* (2009) suggested that, in ABO_3 orthorhombic perovskite compounds, there are two necessary requirements if the phase transition to a post-perovskite structure is to occur:

(i) the material must have a tolerance factor, t, given by

$$t = \frac{1}{\sqrt{2}}\left(\frac{r_A + r_O}{r_B + r_O}\right) \tag{5.3}$$

(Goldschmidt, 1926) of between 0.8 and 0.9 and

(ii) there is an increasing orthorhombic distortion with pressure.

So, for example, $CaSiO_3$ has a tolerance factor of 0.99, outside the requisite range, and therefore does not transform to a post-perovskite phase (at least below 149 GPa, Fujino *et al.* 2009).

5.6.2 Calculation of perovskite octahedral tilts

Tilt systems in perovskites have been widely discussed by, for example, Glazer (1972), Woodward (1997a, 1997b) and Howard and Stokes (1998). The importance of these tilts for the transition to the post-perovskite structure has been discussed by Kojitani *et al.* (2007), Martin and Parise (2008), Tateno *et al.* (2010) and most recently by Okada *et al*. (2011).

Recent work (Knight, 2009) has demonstrated how the effects of octahedral tilting and distortion in perovskites can be rigorously separated, but in order to ensure comparability with previous work on post-perovskites, the following Sections follow the simpler approach adopted by Kojitani *et al.* (2007), who used the method of O'Keeffe and Hyde (1977) to calculate an octahedral tilt angle in the perovskite phase, assuming regular undistorted octahedra, by means of the equation

$$\Phi = cos^{-1}\left(\frac{\sqrt{2}a^2}{bc}\right) \tag{5.4}$$

where Φ is the angle of tilt of the octahedral network about the [111] axis of the ideal cubic perovskite unit-cell (*i.e.* its aristotype) and a, b, and c are the lattice parameters of the orthorhombic structure in the *Pbnm* setting of the space group.

This approach is far from exact as it assumes that the octahedra are only tilted, but not distorted, in the orthorhombic phase, but it has the advantage that Φ can readily be calculated from the orthorhombic cell parameters. On the basis of similar calculations, Tateno *et al.* (2010) concluded that Φ would increase on compression and the compound would transform to the post-perovskite structure provided that Φ was greater about 13-15° at room pressure and temperature; conversely, if Φ was initially less than 13°, its value would reduce on compression and the post-perovskite phase would not form (see Figure 5-2).

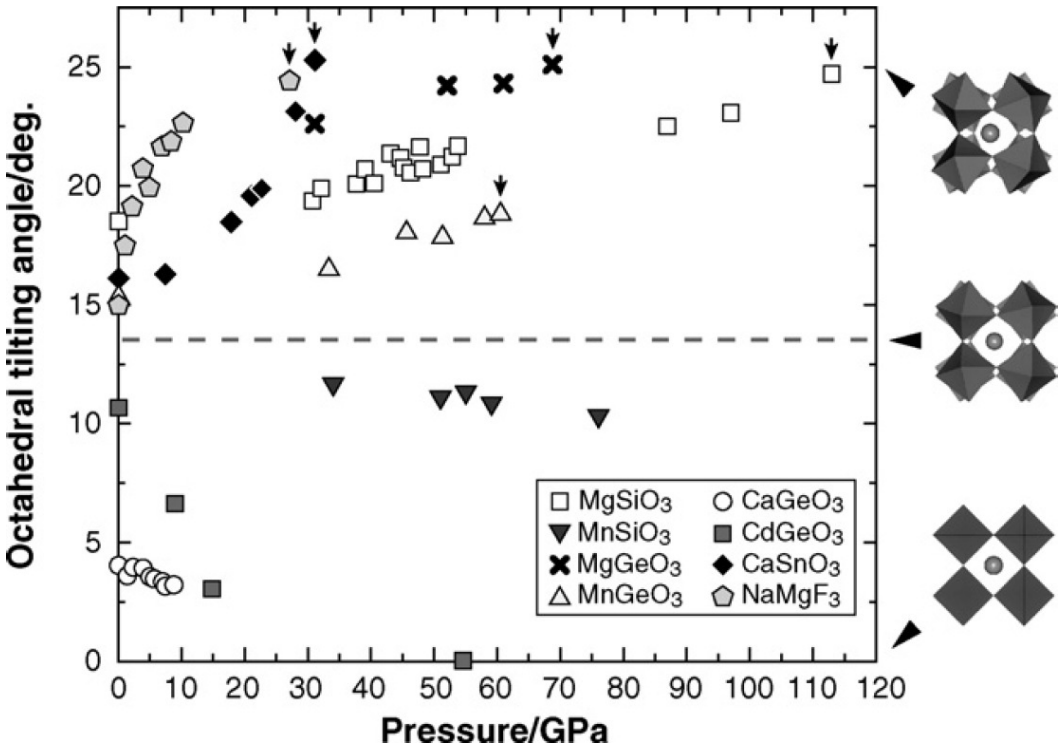

Figure 5-2: The BX_6 octahedral tilting angle of perovskites at 300 K as a function of pressure (from Tateno *et al*., 2010).

So perovskites such as $CdGeO_3$ (Tateno *et al.* 2006) and $MnSiO_3$ (Fujino *et al.* 2009), which show decreasing octahedral tilt with increasing pressure, do not transform to post-perovskites at experimentally accessible pressures. $MnTiO_3$ perovskite shows increasing octahedral tilt with increasing pressure, but decomposes into MnO and $MnTi_2O_5$ above 38 GPa and 2000 K because of the weak covalency of the Ti-O bonds (Okada *et al*., 2011). The tilts of $MgSiO_3$ perovskite octahedra (Ross and Hazen, 1989), $NaMgF_3$ perovskite octahedra (Zhao *et al*., 1993a) and of $(Ca,Sr)TiO_3$ perovskite octahedra (Carpenter *et al*., 2006) decrease with increasing temperature. In $MgSiO_3$, this is consistent with increasing temperature favouring the stability of the perovskite rather than the post-perovskite phase.

5.7 Calculation of *t*-factors

Calculation of the tolerance factor, *t*, provides a rapid, *a priori*, method of addressing the question of whether a post-perovskite phase of an ABO_3 compound is likely to exist. Since the trendline shown in Figure 5-1 appears also to be a good indicator for P_S in Al_2O_3 and Fe_2O_3, *t*-factor values for both $A^{2+}B^{4+}O_3$ and $A^{3+}B^{3+}O_3$ compounds have been calculated.

The calculation of *t* follows the method of Fujino *et al.* (2009) and Tateno *et al.* (2006, 2010), using the radii of the A and B cations in [8]-fold and [6]-fold coordination respectively (Shannon 1976). This means that the *t* factors derived in this way are calculated on a different basis to those usually presented for perovskites, in which the radius of the A-cation in [12]-fold coordination is used (e.g. Woodward, 1997b), and so cannot be compared directly. It should also be noted when comparing the values shown in Table 5-2 and Table 5-3 with those presented in the diagrams given by Fujino *et al.* (2009; Figure 4 of their paper) and by Tateno *et al.* (2006; Figure 5 and 2010; Figure 6) that there is an inconsistency in the *y*-axis scale used by these previous authors; although in both cases the radius of the A-cation in [8]-fold coordination was used to calculate the *t*-factor values, the *y*-axis scale giving the size of the A-cation is presented in terms of the radius of this cation in [6]-fold, rather than [8]-fold, coordination.

In Table 5-2 and Table 5-3, known post-perovskites are indicated by shading and compounds for which post-perovskite phases were not found in laser-heated diamond-anvil-cell (DAC) experiments are indicated by boxes; however, the pressure used in some of these experiments may have been insufficient to produce the post-perovskite phase – see Table captions and discussion below.

5.7.1 *t*-factors for $A^{2+}B^{4+}O_3$ post-perovskites

Table 5-2 shows the values of the *t*-factor (Equation 5.3) calculated for 276 pairs of A^{2+} and B^{4+} ions. The table is arranged such that the rows are in order of the stabilisation pressure predicted by Equation 5.2.

$A^{2+}B^{4+}O_3$	r_B	$\Delta X_{i(O-B)}$	$(r_O+r_B)/r_B$	$\Psi_s = \Delta\chi_{i(O-B)} \times (r_O+r_B)/r_B$	Predicted Ps at 300 K (GPa)	t factor calculated using A^{2+} VIII coordinated r_A											
B^{4+}			VI coordinated r_B			Ba	Pb	Sr	Eu	Hg	Ca	Cd	Mn HS	Fe HS	Co HS	Zn	Mg
Si	0.540	1.871	3.333	6.237	106	1.108	1.057	1.045	1.041	0.998	0.990	0.982	0.927	0.911	0.904	0.904	***0.900***
Ge	0.670	1.904	2.881	5.485	39	1.033	0.986	0.975	0.971	0.931	*0.923*	*0.916*	***0.865***	**0.850**	**0.843**	***0.843***	***0.839***
Ti	0.745	2.028	2.691	5.458	36	0.995	0.949	*0.938*	0.935	0.896	***0.889***	***0.882***	*0.832*	*0.818*	0.811	0.811	0.808
V	0.720	1.963	2.750	5.398	31	1.007	0.961	0.950	0.946	0.907	***0.900***	***0.893***	**0.843**	0.829	0.821	0.821	0.818
Mn(IV)	0.670	1.846	2.881	5.318	24	1.033	0.986	0.975	0.971	0.931	*0.923*	0.916	**0.865**	**0.850**	**0.843**	**0.843**	**0.839**
Zr	0.860	2.148	2.465	5.295	22	0.941	**0.897**	***0.887***	***0.884***	**0.847**	***0.841***	0.834	0.787	0.774	0.767	0.767	0.764
Nb	0.820	2.068	2.537	5.246	17	0.959	0.914	*0.904*	0.901	**0.863**	***0.857***	**0.850**	0.802	0.789	0.782	0.782	0.778
Sn	0.830	2.052	2.518	5.167	10	0.954	0.910	***0.900***	**0.897**	**0.859**	***0.853***	***0.846***	*0.798*	0.785	0.778	0.778	0.775
Ta	0.820	2.023	2.537	5.132	7	0.959	0.914	0.904	0.901	**0.863**	**0.857**	**0.850**	0.802	0.789	0.782	0.782	0.778
Rh	0.740	1.895	2.703	5.122	6	0.997	0.951	0.940	*0.937*	**0.898**	***0.891***	**0.884**	0.834	0.820	0.813	0.813	0.810
Hf	0.850	2.052	2.482	5.094	4	0.945	0.901	***0.891***	**0.888**	**0.851**	**0.845**	**0.838**	0.791	0.777	0.771	0.771	0.767
W	0.800	1.974	2.575	5.083	3	0.968	0.923	0.913	0.910	**0.872**	**0.865**	**0.858**	0.810	0.796	0.789	0.789	0.786
Ru	0.760	1.91	2.658	5.077	2	0.987	0.942	*0.931*	0.928	**0.889**	***0.882***	**0.875**	0.826	0.812	0.805	0.805	0.802
Mo	0.790	1.95	2.595	5.060	1	0.973	0.928	0.918	0.914	**0.876**	***0.869***	**0.862**	0.814	0.800	0.793	0.793	0.790
Pd	0.755	1.882	2.669	5.023	-3	0.990	0.944	0.933	0.930	**0.891**	**0.884**	**0.877**	0.828	0.814	0.807	0.807	0.804
Re	0.770	1.905	2.636	5.022	-3	0.982	0.937	0.927	0.923	**0.885**	**0.878**	**0.871**	0.822	0.808	0.801	0.801	0.798
Ir	0.765	1.877	2.647	4.969	-8	0.985	0.939	0.929	0.925	**0.887**	***0.880***	**0.873**	0.824	0.810	0.803	0.803	0.800
Pt	0.765	1.863	2.647	4.931	-11	0.985	0.939	0.929	0.925	**0.887**	**0.880**	**0.873**	0.824	0.810	0.803	0.803	0.800
Te	1.110	2.291	2.135	4.892	-15	**0.841**	0.803	0.794	0.791	0.758	0.752	0.746	0.704	0.692	0.686	0.686	0.683
Tb	0.900	2.025	2.400	4.860	-17	*0.923*	**0.881**	***0.871***	**0.868**	0.832	0.825	0.818	0.773	0.759	0.753	0.753	0.750
Ce	1.010	2.15	2.248	4.832	-20	***0.878***	**0.838**	*0.829*	0.825	0.791	0.785	0.779	0.735	0.723	0.716	0.716	0.713
Pr	0.990	2.112	2.273	4.800	-23	***0.886***	**0.845**	***0.836***	0.833	0.798	0.792	0.786	0.742	0.729	0.723	0.723	0.720
Pb	0.915	2.012	2.377	4.783	-24	0.917	**0.875**	***0.865***	**0.862**	0.826	*0.819*	0.813	0.767	0.754	0.748	0.748	0.744
O	1.26				r_A (Å)	1.56	1.43	1.40	1.39	1.28	1.26	1.24	1.10	1.06	1.04	1.04	1.03

Table 5-2: The tolerance factor, *t*, for some actual and hypothetical $A^{2+}B^{4+}O_3$ post-perovskite phases (after Fujino *et al.*, 2009).

The ionic radii were taken from Shannon (1976), using the values in [8]-fold coordination for A and [6]-fold coordination for B (note that since the *t*-factor uses the sum of cation and oxygen anion radii, its value is independent of whether Shannon's "CR" or "IR" radii are used) . HS indicates the high-spin ion.

Values shown in bold lie in the range $0.835 \leq t \leq 0.900$. This is a slightly greater range than is found in materials known to form post-perovskite phases (see text).

Values in italics correspond to compounds known to crystallise (under some conditions of temperature and pressure) in a perovskite structure with space group *Pbnm* or its equivalent in an alternative setting (*i.e.* Space Group No. 62 in the International Tables for X-ray Crystallography).

Shaded entries (e.g. $MgSiO_3$) indicate compounds for which post-perovskite phases have been observed.

Entries in boxes (e.g. $CaSiO_3$) indicate compounds for which post-perovskite phases have not been observed, despite attempts to synthesise them; note, however, that although $CdGeO_3$ (110 GPa; Tateno *et al.*, 2006), $CaSiO_3$ and $FeSiO_3$ (149 GPa; Fujino *et al.*, 2009) have been compressed to above the predicted stabilisation pressure, $MnSiO_3$ (85 GPa) and $CoSiO_3$ (79 GPa) have not (Fujino *et al.*, 2009). $CaReO_3$ has been compressed to 25 GPa at 1400 K (Hirai *et al*., 2011). $Ca_{1-x}Sr_xIrO_3$ tends to form a perovskite rather than a post-perovskite phase at 4 GPa and 1150 C for $x > 0.3$, and forms no post-perovskite for $x > 0.7$ (Cheng *et al*., 2011), reflecting a change in *t*-factor from 0.880 ($CaIrO_3$) to 0.929 ($SrIrO_3$).

$FeTiO_3$ was observed to break down into complex oxides at 42-53 GPa and 2000 K (Wu *et al.*, 2009; Nishio-Hamane *et al*., 2010). $MnTiO_3$ also breaks down into MnO and amorphous $MnTi_2O_5$ above 38 GPa at 2000 K (Okada *et al*., 2011).

The tolerance factors, *t*, for some hypothetical $A^{2+}B^{4+}O_3$ post-perovskite phases which are likely either to be highly toxic (Os), highly toxic and radioactive (Po) or to have a short half-life (Tc 4.3 days) are omitted from this Table. Bold (but not italic) entries within the *t*-factor range occur for $BaPoO_3$ (0.852), $CaOsO_3$ (0.878), $CdOsO_3$ (0.871), $CaTcO_3$ (0.871) and $CdTcO_3$ (0.864). Predicted Ps values in GPa at 300 K are -29 (Po), -11 (Os) and 11 (Tc).

Examination of the entries in Table 5-2 shows that $0.839 \leq t \leq 0.900$ for all known $A^{2+}B^{4+}O_3$ post-perovskite oxides; since the lower limit on t appears to be less well constrained than the upper limit (see below), all compositions that have a t-factor in the range $0.835 \leq t \leq 0.900$ are indicated in bold type. Italic script indicates materials known to form an orthorhombic perovskite with space group *Pbnm* (or its equivalent, e.g. *Pnma*, in another setting, *i.e.* having space group number 62 in the International Tables for X-ray Crystallography). Entries in bold, italic script therefore indicate the most likely candidates to form post-perovskites.

Orthorhombic perovskite phases of $CaPtO_3$ and Mn_2O_3 have not yet been reported, but these compounds form post-perovskites and so it is clearly not an absolute requirement for post-perovskite formation that the entry in the Table be in italics. Similarly, the range of t-factors indicated by bold type should be regarded as indicative rather than absolute. Fujino *et al.* (2009) suggest that values of t in the range $0.8 \leq t \leq 0.9$ are appropriate for post-perovskite formation, but the lower limit of t may be set by $MnTiO_3$ perovskite, which has a t-factor of 0.832 and decomposes into other oxides above 38 GPa at 2000 K (Okada *et al.*, 2011). The range of $0.835 \leq t \leq 0.900$ in Table 5-2 and Table 5-3 highlights the most likely candidates. The hypothetical compound $CaReO_3$ has a t-factor within this restricted range but no perovskite phase has been reported, and this may account for the failure of attempts to synthesise it in post-perovskite form up to 25 GPa and 1400 K (Hirai *et al.*, 2011).

At first sight, the upper limit of t would appear to be very well defined, lying between 0.900 and 0.904, since $MgSiO_3$ has a post-perovskite phase but attempts to prepare this polymorph of $CoSiO_3$ by laser heating in a DAC have proved unsuccessful (Fujino *et al.*, 2009). However, the experiments on $CoSiO_3$ were carried out to only 79 GPa and 2000 K, which is predicted to be insufficient to form the post-perovskite structure. So the experiments on $FeSiO_3$, in which no transition was observed to 149 GPa and 1800 K (Fujino *et al.* 2009), should probably be regarded as more definitive in determining the upper limit of the t-factor, which must therefore lie between 0.900 and 0.911.

5.7.2 Calculation of *t*-factors for $A^{3+}B^{3+}O_3$ post-perovskites

The values of the t-factor for 570 $A^{3+}B^{3+}$ compounds are given in Table 5-3.

$A^{3+}B^{3+}O_3$	r_B	$\Delta\chi_{i(O-B)}$	$(r_O+r_B)/r_B$	$\Psi_s = \Delta\chi_{i(O-B)} \times (r_O+r_B)/r_B$	Predicted Ps at 300 K (GPa)	t factor calculated using A^{3+} VIII coordinated r_A																		
B^{3+}			VI coordinated r_B			Bi	La	Ce	Pr	Nd	Sm	Eu	Gd	Tb	Dy	Y	Ho	Er	Tm	Yb	Lu	In	Sc	Fe HS
Al	0.675	2.245	2.867	6.436	124	0.939	0.936	0.929	0.923	0.917	*0.906*	*0.901*	***0.896***	***0.892***	***0.887***	***0.884***	***0.883***	**0.878**	**0.875**	**0.872**	**0.869**	**0.848**	*0.830*	0.797
Co LS	0.685	2.065	2.839	5.863	73	0.934	0.931	0.925	*0.918*	*0.912*	*0.901*	**0.897**	**0.892**	***0.887***	***0.882***	***0.879***	***0.878***	**0.874**	**0.870**	**0.867**	**0.864**	**0.843**	0.825	0.793
Cr	0.755	2.171	2.669	5.794	66	*0.902*	***0.898***	**0.892**	***0.886***	***0.880***	**0.870**	**0.865**	***0.861***	***0.856***	***0.852***	***0.849***	***0.847***	***0.844***	***0.840***	***0.837***	*0.834*	0.814	*0.797*	0.765
Ga	0.760	2.179	2.658	5.792	66	**0.900**	***0.896***	**0.890**	***0.884***	***0.878***	**0.868**	**0.863**	***0.859***	**0.854**	**0.850**	**0.847**	**0.845**	**0.842**	**0.838**	**0.835**	0.832	0.812	0.795	0.763
V	0.780	2.213	2.615	5.788	66	**0.891**	***0.887***	***0.881***	**0.876**	***0.870***	**0.859**	**0.855**	***0.850***	***0.846***	***0.841***	***0.838***	***0.837***	*0.833*	0.830	0.827	0.824	0.804	0.787	0.756
Ni LS	0.700	2.063	2.800	5.776	65	0.927	0.924	0.917	*0.911*	*0.905*	***0.894***	***0.890***	***0.885***	**0.880**	***0.876***	**0.873**	***0.871***	**0.867**	**0.864**	***0.860***	**0.858**	**0.837**	0.819	0.786
Ti	0.810	2.259	2.556	5.773	65	**0.878**	***0.874***	**0.869**	**0.863**	***0.857***	***0.847***	**0.842**	***0.838***	0.833	0.829	*0.826*	0.825	0.821	0.818	0.815	0.812	0.793	0.775	*0.745*
Fe HS	0.785	2.202	2.605	5.736	61	***0.889***	***0.885***	**0.879**	***0.873***	***0.868***	***0.857***	***0.853***	***0.848***	***0.844***	***0.839***	***0.836***	***0.835***	*0.831*	*0.828*	*0.825*	*0.822*	0.802	0.785	0.754
Co HS	0.750	2.137	2.680	5.727	60	0.904	0.901	**0.895**	***0.889***	***0.883***	***0.872***	**0.868**	**0.863**	***0.858***	***0.854***	***0.851***	**0.850**	**0.846**	**0.842**	**0.839**	**0.836**	0.816	0.799	0.767
Ni HS	0.740	2.108	2.703	5.697	58	0.909	0.905	**0.899**	***0.893***	***0.887***	***0.876***	***0.872***	***0.867***	**0.863**	***0.858***	**0.855**	***0.854***	**0.850**	**0.846**	***0.843***	**0.840**	0.820	0.803	0.771
Sc	0.885	2.343	2.424	5.679	56	**0.847**	***0.844***	**0.838**	*0.833*	*0.827*	*0.817*	*0.813*	*0.809*	*0.804*	*0.800*	0.797	*0.796*	0.792	0.789	0.786	0.784	0.765	0.748	0.719
Ru	0.820	2.182	2.537	5.535	43	**0.874**	***0.870***	**0.865**	***0.859***	**0.853**	**0.843**	**0.838**	0.834	0.829	0.825	0.822	0.821	0.817	0.814	0.811	0.808	0.789	0.772	0.741
Rh	0.805	2.136	2.565	5.479	38	***0.880***	***0.877***	**0.871**	***0.865***	***0.859***	***0.849***	***0.844***	**0.840**	***0.836***	0.831	0.828	0.827	0.823	0.820	0.817	0.814	0.794	0.777	0.746
Y	1.04	2.418	2.212	5.348	26	0.790	*0.787*	0.782	0.777	0.771	0.762	0.758	0.754	0.750	0.746	0.744	0.742	0.739	0.736	0.733	0.731	0.713	0.698	0.670
In	0.940	2.278	2.340	5.331	25	*0.826*	*0.823*	0.817	0.812	0.806	0.797	0.793	0.788	0.784	0.780	0.777	0.776	0.773	0.769	0.767	0.764	*0.746*	0.730	0.701
Pd	0.900	2.196	2.400	5.270	19	**0.841**	***0.838***	0.832	0.827	0.821	0.812	0.807	0.803	0.799	0.795	0.792	0.791	0.787	0.784	0.781	0.778	0.759	0.743	0.714
Lu	1.001	2.327	2.259	5.256	18	0.804	*0.801*	*0.795*	*0.790*	*0.785*	0.775	0.771	0.767	0.763	0.759	0.757	0.755	0.752	0.749	0.746	0.743	0.726	0.710	0.682
Er	1.03	2.32	2.223	5.158	9	0.794	*0.790*	0.785	0.780	0.775	0.765	0.761	0.757	0.753	0.749	0.747	0.746	0.742	0.739	0.736	0.734	0.716	0.701	0.673
Tm	1.02	2.303	2.235	5.148	8	0.797	*0.794*	*0.789*	0.783	0.778	0.769	0.765	0.761	0.757	0.753	0.750	0.749	0.746	0.742	0.740	0.737	0.720	0.704	0.676
Gd	1.078	2.372	2.169	5.144	8	0.777	0.774	0.769	0.764	0.759	0.750	0.746	0.742	0.738	0.734	0.732	0.730	0.727	0.724	0.721	0.719	0.702	0.687	0.659
Ho	1.041	2.325	2.210	5.139	8	0.790	*0.787*	0.781	0.776	0.771	0.762	0.758	0.754	0.750	0.746	0.743	0.742	0.739	0.736	0.733	0.730	0.713	0.698	0.670
Tb	1.063	2.348	2.185	5.131	7	0.782	0.779	0.774	0.769	0.764	0.755	0.751	0.747	0.743	0.739	0.736	0.735	0.732	0.729	0.726	0.724	0.706	0.691	0.664
Yb	1.008	2.279	2.250	5.128	7	0.801	*0.798*	*0.793*	*0.788*	0.782	0.773	0.769	0.765	0.761	0.757	0.754	0.753	0.750	0.746	0.744	0.741	0.723	0.708	0.680
Dy	1.052	2.332	2.198	5.125	6	0.786	0.783	0.778	0.773	0.767	0.758	0.754	0.750	0.746	0.742	0.740	0.739	0.735	0.732	0.729	0.727	0.710	0.694	0.667
Ce	1.15	2.41	2.096	5.051	0	0.754	0.751	0.746	0.741	0.736	0.727	0.724	0.720	0.716	0.712	0.710	0.709	0.705	0.702	0.700	0.697	0.681	0.666	0.640
La	1.172	2.431	2.075	5.045	-1	0.747	0.744	0.739	0.734	0.729	0.721	0.717	0.713	0.709	0.706	0.703	0.702	0.699	0.696	0.693	0.691	0.675	0.660	0.634
Sm	1.098	2.348	2.148	5.042	-1	0.771	0.768	0.763	0.757	0.752	0.743	0.739	0.736	0.732	0.728	0.725	0.724	0.721	0.718	0.715	0.713	0.696	0.681	0.654
Pr	1.13	2.384	2.115	5.042	-1	0.760	0.757	0.752	0.747	0.742	0.733	0.730	0.726	0.722	0.718	0.716	0.715	0.711	0.708	0.706	0.703	0.686	0.672	0.645
Nd	1.123	2.376	2.122	5.042	-1	0.763	0.760	0.755	0.750	0.744	0.736	0.732	0.728	0.724	0.720	0.718	0.717	0.713	0.710	0.708	0.705	0.688	0.674	0.647
Eu	1.087	2.325	2.159	5.020	-3	0.774	0.771	0.766	0.761	0.756	0.747	0.743	0.739	0.735	0.731	0.729	0.728	0.724	0.721	0.719	0.716	0.699	0.684	0.657
O	1.26				r_A (Å)	1.310	1.300	1.283	1.266	1.249	1.219	1.206	1.193	1.180	1.167	1.159	1.155	1.144	1.134	1.125	1.117	1.060	1.010	0.920

Table 5-3: The tolerance factor, *t*, for some actual and hypothetical $A^{3+}B^{3+}O_3$ post-perovskite phases (after Fujino *et al.*, 2009).

The ionic radii were taken from Shannon (1976), using the values in [8]-fold coordination for A and [6]-fold coordination for B. Note that since the *t*-factor uses the sum of cation and oxygen anion radii, its value is independent of whether Shannon's "CR" or "IR" radii are used.

Values shown in bold lie in the range, $0.835 \leq t \leq 0.900$ (see text).

Values in italics correspond to compounds known to crystallise (under some conditions of temperature and pressure) in a perovskite structure with space group *Pbnm* or its equivalent in an alternative setting (*i.e.* Space Group No. 62 in the International Tables for X-ray Crystallography).

The shaded entry for Fe_2O_3 indicates that the post-perovskite phase of this compound has been observed (Ono and Ohishi, 2005; transition at 1200 K from *Pbcn* Rh_2O_3(II) structure).

Ardit *et al*. (2010) found that $YCrO_3$ perovskite did not change from its perovskite *Pbnm* structure when compressed to 60 GPa at room temperature. Similarly, Loa *et al*. (2007) found that $YTiO_3$ perovskite did not change from its perovskite *Pbnm* structure when compressed to 30 GPa at room temperature.

The question of the appropriate range of factors leading to post-perovskite formation for the $A^{3+}B^{3+}O_3$ oxides shown in this table is more debatable. The compounds that are known to form post-perovskite phases are Mn_2O_3, Fe_2O_3 and Al_2O_3. However, since Li and Xue (2006) give no entry for Mn^{3+} in their electronegativity tables, following the suggestion by Santillan *et al.* (2006), Mn_2O_3 has been considered here as an $A^{2+}B^{4+}O_3$ compound. For Fe_2O_3 $t = 0.754$. The corresponding value for Al_2O_3 cannot be calculated as there is no entry for Al^{3+} in [8]-fold coordination in the list of ionic radii given by Shannon (1976) but, since the ratio of the radii in [8]-fold and [6]-fold coordination is similar for all of the ions listed in Table 5-3, the value of t is likely also to be ~0.75 for Al_2O_3.

In constructing Table 5-3 it is assumed that, since neither Al_2O_3 (Ono *et al.* 2006a) nor Fe_2O_3 (Ono and Ohishi 2005; Ito *et al.* 2009; Wilson and Russo 2009) form a perovskite phase, the low t-factor for Fe_2O_3 can be regarded as anomalous. Bold type is therefore used in Table 5-3 to indicate the same t-factor range as was used for the $A^{2+}B^{4+}$ oxides in Table 5-2. As before, compounds known to crystallise as orthorhombic perovskites with space group *Pbnm* (or equivalent) are indicated by italic script.

5.8 Prediction of stabilisation pressures

5.8.1 Use of the method

The trendline shown in Figure 5-1 is only a guide to the pressure required to form a post-perovskite phase. As demonstrated by the examples of $CaRuO_3$ and $CaRhO_3$, the method is not exact; these compounds have identical A-cations and very similar Ψ_S values but experiments have indicated that a difference in pressure of ~20 GPa is required for their formation (see Table 5-1). However, the relationship between Ps and Ψ_S is sufficiently strong to provide a useful and very rapid indicator of the pressure necessary to form the post-perovskite phase in both $A^{2+}B^{4+}O_3$ and $A^{3+}B^{3+}O_3$ compounds.

The entries in the tolerance factor tables (Table 5-2 and Table 5-3) must also be treated as indicative rather than exact. The upper limit on the tolerance factor for post-perovskite formation (especially for the $A^{2+}B^{4+}$ oxides) seems likely to lie in the range 0.900 to 0.911. The entries in bold in these Tables are, therefore, best viewed as

indicative of the compounds most likely to form post-perovskites, rather than as providing a definitive list.

With the possible exception of Mn_2O_3 (reported to transform to the post-perovskite structure from the bixbyite structure at a sample temperature that "did not exceed a few hundred K"; Santillan *et al.*, 2006), all of the ABO_3 compounds have required high temperatures to synthesise the post-perovskite phases. This means that thermal energy is required to overcome the activation barrier to disrupting the 3-dimensional BO_3 octahedral framework of the perovskite. The Clapeyron slopes for the boundaries of the post-perovskite phase of the ABO_3 oxides listed in Table 5-1 are in the range 10 – 20 MPa K^{-1} and so, for transformation temperatures of 1500 K and 2000 K respectively, it is necessary to add 12 – 24 GPa or 17 – 34 GPa to the predicted values of *Ps*.

5.8.2 $A^{2+}B^{4+}O_3$ candidates for post-perovskite structure

Examination of Table 5-2 suggests that new $A^{2+}B^{4+}O_3$ post-perovskites are likely to be relatively rare. It is also possible that constraints on the octahedral tilt angles in the perovskite phase will further reduce the number of likely candidate compounds (see below). Of the silicates listed in Table 5-2, only $CoSiO_3$ and $ZnSiO_3$ would appear to offer the prospect of forming a post-perovskite, though even these compounds may lie just outside the allowable range of *t*. If these two compounds do transform then, assuming a transformation temperature of 2000 K, they should do so at a pressure of between 124 GPa and 141 GPa.

Of the A-cations listed in Table 5-2, Sr, Ca, Cd and Hg provide the greatest number of compounds with suitable *t*-factors. For $CaSnO_3$, the predicted value for *Ps* of 11 GPa at 300 K is in very good agreement with an earlier prediction, based on athermal *ab initio* simulations, that the post-perovskite transition should occur at ~12 GPa at 0 K (Tsuchiya and Tsuchiya, 2006), but lower than the stabilisation pressure of 58 GPa predicted by Martin and Parise (2008). Experimental work showed that the post-perovskite phase was not formed below 18 GPa at room temperature (Schneider *et al.,* 2008) and apparently not below 70 GPa in laser heated DAC experiments (Tateno *et al.,* 2006). However, in more recent experiments (Tateno *et al.* 2010) it was found that $CaSnO_3$ does indeed transform to a post-perovskite phase at 40 GPa and 2000 K, and

that the Clapeyron slope of the phase boundary is 17 MPa K^{-1}. Using the range of Clapeyron slopes suggested above, the predicted value of *Ps* lies in the range 28 – 45 GPa at 2000 K. If the experimental value of the Clapeyron slope is used, *Ps* is then predicted to be 40 GPa at this temperature, in exact agreement with the experiment.

The entries in Table 5-2 suggest that $CaTiO_3$ (t = 0.889) and $CdTiO_3$ (t = 0.882) are also candidates for transformation to the post-perovskite phase. From athermal density functional theory calculations, Wu *et al.* (2005) predicted that a transformation in $CaTiO_3$ to the post-perovskite phase should occur at 30 GPa, in fair agreement with the value calculated here of *Ps* of 37 GPa at 300 K. Experimentally, Gillet *et al.* (1993) reported that there was no major structural change in $CaTiO_3$ below 22 GPa at room temperature, but this pressure is below the predicted value of *Ps*. Guennou *et al.* (2010) similarly reported no structural change in $CaTiO_3$ up to 60 GPa, but this was also at room temperature.

Tateno *et al.* (2006) reported that (like $CaSnO_3$) $CaTiO_3$ did not transform below 70 GPa on laser heating but in view of the fact that more recent experiments have revealed that a transition in $CaSnO_3$ does occur, $CaTiO_3$ might repay further investigation; at 2000 K, the predicted value of *Ps* lies in the range from 54 – 71 GPa. However, calculation of the octahedral tilt angle, Φ, as described in Section 5.6.2 above, suggests that $CaTiO_3$ may be a less suitable candidate for post-perovskite formation than $CdTiO_3$. For $CaTiO_3$, using the lattice parameters at 296 K reported by Yashima and Ali (2009), the tilt is Φ = 9.8º at ambient pressure, which is below the critical range of 13 -15º proposed by Tateno *et al.* (2010), while for $CdTiO_3$ Φ = 15.5º (lattice parameters taken from Sasaki *et al.*, 1987). There does not appear to be any experimental work at high-pressure published on $CdTiO_3$, but athermal first-principles calculations (Fang and Ahuja, 2006) have indicated that a transition to the post-perovskite structure should occur at 64 GPa, somewhat higher than the value for P_S of 37 GPa at 300 K predicted by Equation 5.2.

Other *Pbnm* perovskite compounds with suitable *t*-factors that can possibly be excluded on the grounds that their octahedral tilts are too low are $SrHfO_3$ (Kennedy *et al.,* 1999), $SrSnO_3$ (Green *et al.,* 2000) and $CaVO_3$ (Garcia-Jaca *et al.,* 1995). For $SrHfO_3$, the predicted value for P_S is 4 GPa at 300 K, or 21 – 38 GPa at 2000 K, but Φ

= 3.9º at room temperature, which is well below the limit proposed by Tateno *et al.* (2010). No work on this compound appears to have been carried out at high-pressure, but it is known to have a number of high-temperature phase transitions (Kennedy *et al.,* 1999). Similarly, $SrSnO_3$ has a number of high-temperature phase transitions (Glerup *et al.,* 2005) but no reports of studies at simultaneous high-pressure and temperature have been reported; assuming that the Clapeyron slope is the same as for $CaSnO_3$, at 2000 K the post-perovskite phase might be expected to form at ~ 40 GPa. No experimental work on $CaVO_3$ appears to have been carried out at high-pressures and temperatures, other than an investigation of its electrical properties to ~1.6 GPa (Zhou and Goodenough, 1996); the predicted value for *Ps* is ~5 GPa lower than that for $ATiO_3$ compounds, *i.e.* 49 – 66 GPa at 2000 K.

In both $SrSnO_3$ and $CaVO_3$, distortion of the octahedra results in $a > b$ (for the *Pbnm* setting) and Equation 5.4 cannot then be used to determine Φ, as it results in $cos(\Phi)$ being greater than 1. However, since the crystal structures of $CaVO_3$ and $SrSnO_3$ are known, it is possible to estimate Φ "microscopically" from the atomic coordinates by means of the equations given in Zhao *et al.* (1993b; Appendix A). For $SrSnO_3$ (Green *et al.*, 2000), $\Phi = 12.3º$; for $CaVO_3$ (Garcia-Jaca *et al.*, 1995), the distortion of the octahedra is such that significantly different tilts are obtained from the coordinates of the two oxygen atoms, giving $10.7º < \Phi < 13.8º$. Although it might be considered that these values of Φ are only a little below the limit suggested by Tateno *et al.* (2010), they are, in fact, less favourable than might at first appear since for compounds where both methods of calculating Φ may be used it is found that the values of Φ calculated "microscopically" are almost invariably greater than those obtained from Equation 5.4.

An *ab initio* study by Cai *et al.* (2011) predicted that $SrRuO_3$ *Pnma* perovskite will transform to post-perovskite at about 40 GPa (effectively at 0 K). However, this perovskite has a *t* factor of 0.931 and $\Phi = 8.0º$ at room temperature (calculated using Equation 5.4, from the lattice parameters at 290 K of Bushmeleva *et al.*, 2006), both of which are outside the suggested limits; experimental evidence is required.

If material is to be synthesised in moderately large amounts, it is clearly desirable to limit the pressure required to about 20 GPa as samples may then be prepared using large-volume, multi-anvil presses. In this connection, the compounds $SrPbO_3$ and

$BaCeO_3$ might seem attractive as they have suitable *t*-factors and predicted values of P_S that are negative at 300 K, being even lower than that of $CaIrO_3$. However, although $SrPbO_3$ and $BaCeO_3$ form orthorhombic (*Pbnm*) perovskites at room temperature, their tilt angles are fairly small and so they are unlikely to form post-perovskites. For $SrPbO_3$, $\Phi = 11.5°$ (calculated using Equation 5.4, from the lattice parameters of Fu and Ijdo, 1995). For $BaCeO_3$ (Knight and Bonanas, 1995) the lattice parameters are such that Φ cannot be calculated from Equation 5.4; using the microscopic method gives $13.3° < \Phi < 13.7°$.

It is known that $BaCeO_3$ undergoes a series of phase transitions at high-temperature (Knight, 1994) but $SrPbO_3$ remains orthorhombic to at least 1033 K (Hester *et al.*, 2002). Unfortunately, no experimental studies of $SrPbO_3$ at high-pressure have been reported and high-pressure investigations of $BaCeO_3$ have been confined to measurements at room temperature. It is known from Raman spectroscopy (Loridant and Lucazeau, 1999) that $BaCeO_3$ undergoes two high-pressure phase transitions (at 22 GPa and 28 GPa) but it has not been suggested that either of these is to the post-perovskite structure. No simultaneous high-pressure, high-temperature studies of either $BaCeO_3$ or $SrPbO_3$ have been reported. Once again, such studies would be very desirable since, if a post-perovskite phase can be formed at high-pressure and temperature, it seems likely that this material might be recoverable to ambient pressure.

It would also be of interest to investigate $BaCeO_3$ or $SrPbO_3$ by high-pressure neutron diffraction at ambient temperature to determine the mechanism by which the perovskite deforms (see Section 11.8.2). This is because an alternative explanation for the failure of these compounds to form post-perovskite phases at ambient pressure is provided by the work of Knight *et al.* (2005), who studied the structure of $SrCeO_3$ at high-pressure. They found that $SrCeO_3$ behaved atypically, in that the dominant compression mechanism was bond shortening rather than increased tilting of the CeO_6 octahedra. They further suggested that the behaviour of $SrPbO_3$ was also atypical when compared to that of other perovskites having Sr as the A cation.

Since $BaPrO_3$ ($\Phi = 4.3°$; cell parameters from Knee *et al.*, 2009) and $SrTbO_3$ ($\Phi = 11.5°$; cell parameters from Tezuka *et al.*, 1998) can also be excluded on the grounds of unsuitable tilt angles, it appears that $SrPrO_3$ is the most promising candidate compound

for a new post-perovskite that might form at very low pressure (P_S = -22 GPa at 300 K) . Although the *t*-factor for $SrPrO_3$ is outside the range found in known post-perovskites, it is only marginally so, with $t = 0.836$. The octahedral tilts in $SrPrO_3$ are also just within the requisite range suggested by Tateno *et al.* (2010), as $\Phi = 14.3°$ (cell parameters at 300 K from Thundathil *et al.*, 2005). Very little work appears to have been done on $SrPrO_3$ and clearly both experimental and computational studies to assess the possibility of a perovskite to post-perovskite transition would be highly desirable.

Further inspection of Table 5-2 suggests that $CaMoO_3$ is the next suitable compound with a low stabilisation pressure, having a predicted value of P_S of 1 GPa at 300 K. This compound appears also to have suitable values of the *t*-factor (0.869) and of the octahedral tilts, $\Phi = 14.6°$ (cell parameters from de la Calle *et al.*, 2006). No studies, either experimental or computational, of $CaMoO_3$ have been reported at high-pressure.

5.8.3 $A^{3+}B^{3+}O_3$ candidates for post-perovskite structure

To date, there appears to have been little effort made to prepare $A^{3+}B^{3+}O_3$ post-perovskites, despite the fact that many rare-earth compounds crystallise as *Pbnm* orthorhombic perovskites. Examination of Table 5-3 suggests, however, that there are relatively few obvious candidates likely to form post-perovskites at very low pressures. Compounds such as $LaYbO_3$, $CeYbO_3$, $PrYbO_3$ and $LaHoO_3$ all have a predicted value of P_S of 7 – 8 GPa at 300 K and all have large octahedral tilts, with $18.3° < \Phi < 20.0°$ (calculated from the lattice parameters given by Ito *et al.*, 2001); however, their *t*-factors all lie well outside the range found in the $A^{2+}B^{4+}O_3$ post-perovskites, with $0.787 < t < 0.798$.

A more interesting possibility is provided by $LaPdO_3$, although the predicted value of P_S (20 GPa at 300 K) in this compound is much higher. $LaPdO_3$ has a value of *t* (0.838) that is only very marginally lower than that observed in the $A^{2+}B^{4+}O_3$ post-perovskite compounds and its value of $\Phi = 16.2°$ (calculated from the lattice parameters of Kim *et al.*, 2001) is well inside the range required by Tateno *et al.* (2010). Very little work on $LaPdO_3$ has been reported and none at high pressures.

Ardit *et al*. (2010) observed no change in the perovskite *Pbnm* structure of $YCrO_3$ up to 60 GPa at room temperature, although its P_S is predicted to be 66 GPa at 300 K with *t* factor of 0.849. The lattice parameters of $YCrO_3$ are such that Φ cannot be calculated from Equation 5.4, but the microscopic method gives $\Phi = 20.9°$. This compound therefore remains a candidate for the transition to post-perovskite structure, although at a pressure beyond that attainable using a multi-anvil press. Ardit *et al.* (2010) also noted that the distortion in compression of the perovskite unit cell in $YCrO_3$, $YTiO_3$ and $YAlO_3$ is related to both the initial octahedral tilt angles and to r_A.

5.9 Summary of oxide candidates for post-perovskite stabilisation

A summary of the properties of the $A^{2+}B^{4+}O_3$ compounds considered most likely to transform to post-perovskites is shown in Table 5-4 (i). Definitions of the parameters listed in this Table are given in Section 5.4 and Section 5.6: *t* = tolerance factor; Φ = octahedral tilt angle; Ψ_S = stabilisation factor; P_S (300 K) = stabilisation pressure at 300 K predicted from the regression line shown in Figure 5-1; P_S (1500 K) = estimated stabilisation pressure at 1500 K, assuming that the Clapeyron slope of the phase boundary lies in the range 10 – 20 MPa K^{-1}. For $CdSnO_3$, $CaNbO_3$, $CaZrO_3$ and $CdTiO_3$ the values of Φ were calculated from the cell parameters published by Mizoguchi *et al.* (2004b), Istomin *et al.* (1998), Levin *et al.* (2003; at 298 K) and Sasaki *et al.* (1987) respectively. For $ZnGeO_3$ the value of Φ is that at 15.6 GPa, calculated from the cell parameters of Yusa *et al.* (2006).

It can be seen that, of all of the compounds listed in Table 5-2, only seven candidate phases fall into the required ranges of tolerance factor (*t*) and octahedral tilt angle (Φ). The $A^{2+}B^{4+}O_3$ compounds shown in bold italic script in Table 5-2 that are not listed here have been excluded by reason of having a value of Φ that is too low. The values for some of these materials are only just inside the acceptable ranges. It therefore seems likely that very few new $A^{2+}B^{4+}O_3$ post-perovskites remain to be discovered.

Compound	t	Φ (degrees)	Ψ_S	P_S (300 K) (GPa)	P_S (1500 K) (GPa)
(i) $A^{2+}B^{4+}O_3$ Compounds					
$SrPrO_3$	0.836	14.3	4.80	-23	-11 – 1
$CaMoO_3$	0.869	14.6	5.06	1	13 – 25
$CdSnO_3$	0.846	16.2	5.17	10	22 – 34
$CaNbO_3$	0.857	14.6	5.25	17	29 – 41
$CaZrO_3$	0.841	16.8	5.30	22	34 – 46
$CdTiO_3$	0.882	15.5	5.46	36	48 – 60
$ZnGeO_3$	0.843	19.2	5.49	39	51 – 63
(ii) $A^{3+}B^{3+}O_3$ Compounds					
$LaPdO_3$	0.838	16.2	5.27	19	31 – 43
$LaRhO_3$	0.877	16.5	5.48	38	50 – 62

Table 5-4: Properties of some oxide perovskites likely to form post-perovskites.

Examination of Table 5-3 suggests that new $A^{3+}B^{3+}O_3$ post-perovskites may be more numerous, but there is less certainty as to the range of tolerance factor that is suitable for the $A^{3+}B^{3+}$ oxides. The two entries shown for the $A^{3+}B^{3+}O_3$ compounds in Table 5-4 (ii) are illustrative rather than exhaustive. Of those $A^{3+}B^{3+}O_3$ compounds with suitable values of t and Φ, $LaPdO_3$ has the lowest predicted stabilisation pressure.

None of these $A^{3+}B^{3+}O_3$ compounds, however, are predicted to transform within the pressure range accessible with a large-volume multi-anvil press (MAP) so Table 5-4 (ii) contains only the values for $LaPdO_3$ and for $LaRhO_3$. The former is the $A^{3+}B^{3+}O_3$ phase that is predicted to have the lowest stabilisation pressure. The latter is one example chosen from the list of compounds containing rare-earths (such as the RERhO$_3$ series, with RE = La, Pr, Nd, Sm, Eu, Tb, studied by Macquart *et al.* (2006) which all have $\Phi > 16.5$º) that might be expected to transform at higher pressures.

5.10 Addendum: $NaIrO_3$ – a post-perovskite with a pentavalent B ion

At a very late stage in the preparation of this thesis, the post-perovskite $NaIrO_3$ with cations Na^+ and Ir^{5+} was reported (Bremholm *et al*., 2011). This section has therefore been added to discuss the implications of this discovery for the work described in this Chapter. The synthesis of $NaIrO_3$ took place at high-pressure (4.5 GPa) and high-temperature (800 °C). This implies a stabilisation pressure at 300 K of P_S = -9 GPa, assuming a reduction by ~13 GPa due to a Clapeyron slope value of dP/dT of 17 MPa K^{-1} as for $CaIrO_3$, although this may not be appropriate for a $A^+B^{5+}O_3$ compound. The Ψ_S value for $NaIrO_3$ is 4.37 and its t-factor is 0.926. This t-factor is larger than that of (for example) $CaIrO_3$, because the Na^+ cation is larger that the Ca^{2+} cation, and the Ir^{5+} cation is smaller than the Ir^{4+} cation. The smaller Ir^{5+} cation has a higher electronegativity (2.183) than the larger Ir^{4+} cation (1.881), so the B^{5+}-O bond is more covalent than the B^{4+}-O bond, reducing the value of Ψ_S. It is possible that the higher bond covalence relaxes the constraint of the t-factor, so that a $A^+B^{5+}O_3$ post-perovskite structure is stabilised at a larger t-factor value than that occurring for $A^{2+}B^{4+}O_3$ in the range of $0.835 \leq t \leq 0.900$.

Figure 5-3a shows the $NaIrO_3$ stabilisation pressure of -9 GPa at 300 K plotted against Ψ_S, with the linear fit to the other post-perovskite stabilisation data values shown as a solid line. This linear fit gives an estimated stabilisation pressure for $NaIrO_3$ at 300 K of -61 GPa, and the offset from the experimental value (adjusted to 300 K) is 53 GPa. Figure 5-3b shows a linear fit including the $NaIrO_3$ value, resulting in $P_S = 75(9)\Psi_S - 371(49)$ GPa ($R^2 = 0.87$).

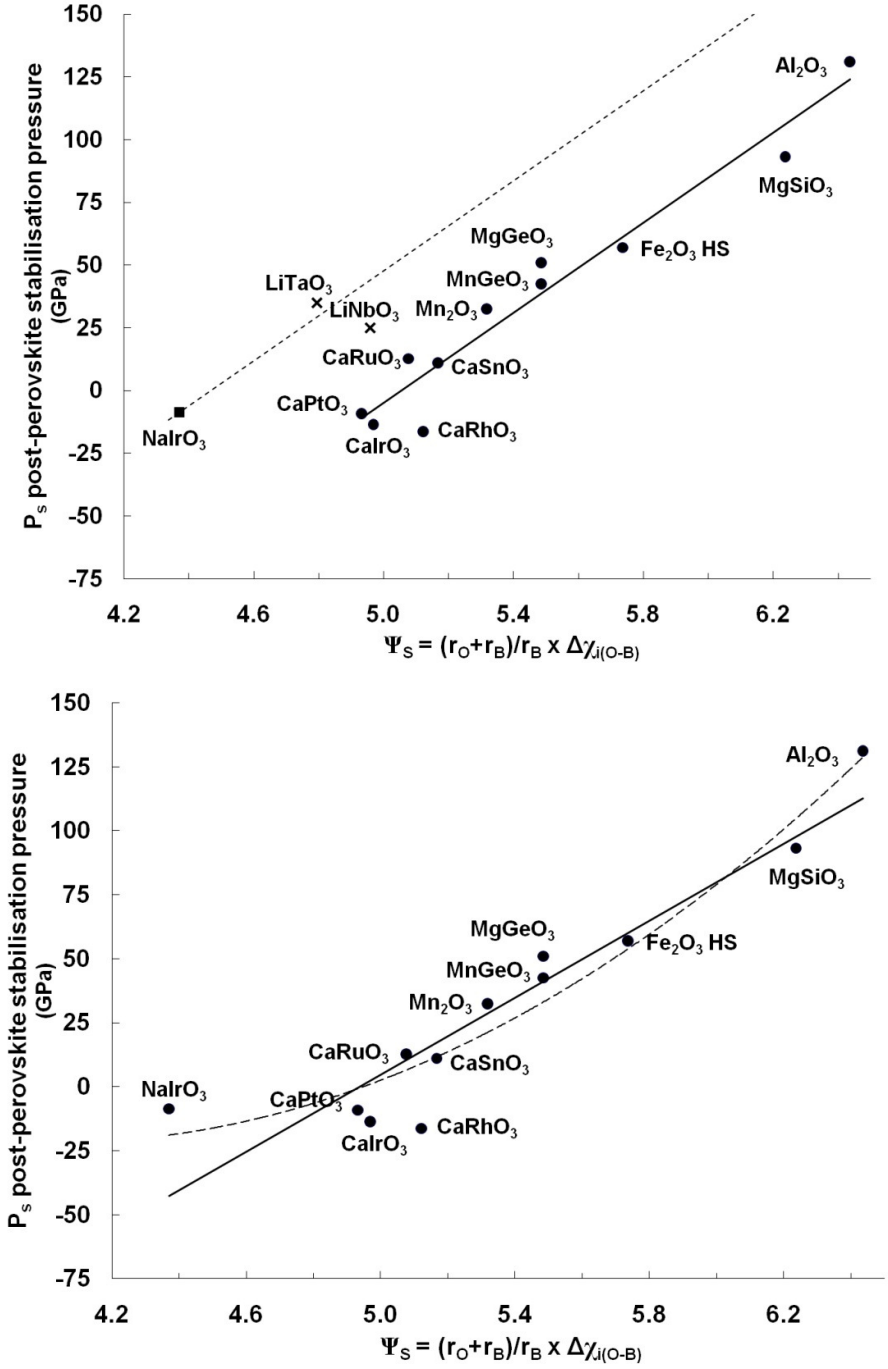

Figure 5-3: The relationship between the post-perovskite stabilisation pressure, *Ps*, and the stabilisation factor, Ψ_S (a) with the $NaIrO_3$ data value (solid square) excluded from the linear fit (solid line) of Equation 5.2. The dotted line represents the prediction from the offset linear fit (see text) for other $A^{+}B^{5+}O_3$ post-perovskites listed in Table 5-5. (b) With the $NaIrO_3$ data value included in the linear fit (solid line) of Equation 5.2. A second order polynomial fit ($Ps = 26.083\ \Psi_S^2 - 210.370\ \Psi_S + 402.320$) is shown as a dashed line. The stabilisation of post-perovskite Li compounds (crosses in (a)) has not been confirmed, and these are not included in the fits.

Table 5-5 shows $\Delta\chi_{i(O-B)}$ for the VI-coordinated B^{5+} cations of period II, III, IV, V and VI elements which have pentavalent cations. The stabilisation pressures P_S in the sixth column of Table 5-5 are predicted from the linear fit (excluding $NaIrO_3$), offset by 53 GPa, as shown by the dotted line in Figure 5-3a. $NaPtO_3$ post-perovskite is predicted to have a stabilisation pressure of -3 GPa at 300 K or 10 GPa at 800 °C, assuming a Clapeyron slope of 17 MPa K^{-1} and taking no account of any *t*-factor or octahedral tilt constraints. If the $A^{+}B^{5+}O_3$ post-perovskites were subject to the second-order relationship shown by the dashed line in Figure 5-3b, the predicted stabilisation pressures would be lower still, as shown in the seventh column of Table 5-5.

B^{5+} cation	r_B	$\Delta\chi_{i(O-B)}$	$(r_O+r_B)/r_B$	$\Psi_s = \Delta\chi_{i(O-B)} \times (r_O+r_B)/r_B$	Predicted Ps at 300 K (GPa) from a linear fit	Predicted Ps at 300 K (GPa) from a 2nd order fit	*t*-factor (Li^+)	*t*-factor (Na^+)	*t*-factor (K^+)
Au	0.710	1.563	2.775	4.337	-12	-19	0.833	0.926	1.045
Ir	0.710	1.575	2.775	4.370	-9	-19	0.833	0.926	1.045
Pt	0.710	1.599	2.775	4.437	-3	-18	0.833	0.926	1.045
Bi	0.900	1.863	2.400	4.471	0	-17	0.759	0.845	0.953
Rh	0.690	1.591	2.826	4.496	3	-16	0.841	0.936	1.055
Ru	0.705	1.659	2.787	4.624	14	-13	0.835	0.928	1.047
N	0.270	0.819	5.667	4.641	16	-12	1.072	1.192	1.345
I	1.090	2.171	2.156	4.681	19	-11	0.698	0.776	0.876
Mo	0.750	1.752	2.680	4.695	21	-10	0.816	0.908	1.024
W	0.760	1.767	2.658	4.697	21	-10	0.812	0.903	1.019
Ta	0.780	1.833	2.615	4.794	29	-7	*0.804*	*0.894*	1.009
Sb	0.740	1.787	2.703	4.830	33	-5	0.820	*0.912*	1.029
V	0.680	1.728	2.853	4.930	42	-1	0.846	0.940	1.061
As	0.600	1.599	3.100	4.957	44	0	0.882	0.981	1.106
Nb	0.780	1.896	2.615	4.959	44	1	0.804	*0.894*	*1.009*
P	0.520	1.619	3.423	5.542	97	38	0.922	1.025	1.156

Table 5-5: Period II, III, IV, V and VI elements with the electronegativity (Li and Xue, 2006) differences $\Delta\chi_{i(O-B)}$ between O and their VI-coordinated pentavalent cations, and the predicted stabilisation pressures based on: (column 6) a linear fit of the stabilisation pressure, *Ps* and the stabilisation factor, Ψ_S (excluding $NaIrO_3$ and Li compounds) increased by 53 GPa (dotted line in Figure 5-3a): (column 7) a second-order fit including $NaIrO_3$ (dashed line in Figure 5-3b). A Clapeyron slope of 17 MPa K^{-1} (as for $CaIrO_3$) would increase the values of *Ps* by ~13 GPa at 800 °C. The *t*-factors for compounds where a space group 62 perovskite-type polymorph has been reported are italicised, as is the *t*-factor for $NaNbO_3$ (space group 57 perovskite Pbcm). $KTaO_3$, $KSbO_3$ and $KBiO_3$ form cubic perovskites.

The very approximate estimates of stabilisation pressures in Table 5-5 are of course based on only one $A^+B^{5+}O_3$ post-perovskite data point. However, they may help to prioritise further syntheses and computer simulation of candidate $A^+B^{5+}O_3$ post-perovskites at high-pressure. Any formation of $A^+B^{5+}O_3$ post-perovskites may be subject to additional constraints related to their *t*-factor (examples are shown for Li^+, Na^+ and K^+ in the final three columns of Table 5-5) and to their perovskite octahedral tilt angle Φ (where they form a perovskite); it is not known whether any $A^+B^{5+}O_3$ perovskites transform to the post-perovskite phase. Ilmenite-structured $NaSbO_3$ is reported by Mizoguchi *et al.* (2004a) to have transformed to a perovskite phase at 10.5 GPa and 1150 °C, and this paper lists a number of other $A^+B^{5+}O_3$ perovskites and ilmenites (A = Na, K ; B = Nb, Ta, Sb, Bi).

$NaPtO_3$ and $NaRhO_3$ have similar *t*-factors to $NaIrO_3$ (see the penultimate column of Table 5-5), and may be primary candidates for post-perovskite syntheses, together with $NaAuO_3$ if a suitable reaction can be identified. Their stabilisation pressures at 800 °C using the offset linear fit are predicted to be 10 GPa ($NaPtO_3$) and 16 GPa ($NaRhO_3$), within the pressure range available in a MAP.

The *t*-factors of most of the $Li^+B^{5+}O_3$ compounds listed in the 8th column of Table 5-5 are significantly less than that of $NaIrO_3$, because the Li^+ cation is smaller than the Na^+ cation. If the higher B^{5+}-O covalence implies a higher *t*-factor range than the $A^{2+}B^{4+}O_3$ range of $0.835 \leq t \leq 0.900$, then most of these Li^+ compounds may have *t*-factors that are too small to allow stabilisation of $Li^+B^{5+}O_3$ post-perovskites. However, phase changes in $LiNbO_3$ and $LiTaO_3$, at ~25 GPa and ~35 GPa respectively, produced diffraction patterns similar to those seen in Fe_2O_3 at ~60 GPa (at room temperature) (Yagi, 1994; Li, 2007). If this phase of Fe_2O_3 was the post-perovskite phase reported later by Ono and Ohishi (2005) as being formed at a pressure equivalent to 57 GPa at 300 K, then this may indicate that $LiNbO_3$ and $LiTaO_3$ were in fact undergoing transitions to post-perovskite phases. If these two Li compounds do form post-perovskite phases, this implies that the higher B^{5+}-O bond covalence relaxes the lower *t*-factor constraint (from 0.835 to 0.804 or less) as well as the upper one, which from the case of $NaIrO_3$ is seen to be increased from 0.900 to 0.926 or more.

It would be interesting to examine the potential perovskite to post-perovskite transitions of $NaPtO_3$, $NaRhO_3$ and other candidate $A^+B^{5+}O_3$ compounds at high-

pressure using *ab initio* computer simulation, including modelling the perovskite octahedral tilt angle Φ. These could include mixed-valence solid solutions such as (Na, Ca)IrO_3. Further simulation could be used to assess the suitability of any such post-perovskite phases as analogues of $MgSiO_3$ post-perovskite.

5.11 Stabilisation of fluoride post-perovskites

Post-perovskite fluorides may also provide very suitable analogues of post-perovskite $MgSiO_3$. It may be possible to find a similar relationship to that described in Section 5.4.4 that allows prediction of the stabilisation pressure in ABF_3 post-perovskite fluorides. However, at present the available data from which such relationships might be inferred are limited. Experimental results are available for $NaMgF_3$ (Hustoft *et al.,* 2008), $NaZnF_3$ (Yakovlev *et al.,* 2009, 2009a), $NaNiF_3$ (the present work) and $NaCoF_3$ (Dobson *et al*., 2011) for which the Ψ_S values are 7.47, 7.13, 7.30 and 7.14 respectively (see Table 5-6). For $NaMgF_3$, the transition from the perovskite to post-perovskite phase occurs at 30 GPa and 2000 K, with a Clapeyron slope of 6 – 10 MPa K^{-1} (Hustoft *et al.,* 2008); these data give an experimental P_S value, corrected to 300 K, of between 13 and 20 GPa. For $NaZnF_3$, Yakolev *et al.* (2009) found that the onset of the transition to the post-perovskite phase occurred at around 14 GPa at ~300 K. The $NaNiF_3$ transition from perovskite to post-perovskite took place at or below 15 GPa and at 700 ºC, and the $NaCoF_3$ transition took place at or below 14 GPa at 480 ºC (see Section 6.8.3).

These post-perovskite fluorides appear to have similar tolerance factors to those of the oxides, with t = 0.866, 0.857 and 0.879 for $NaMgF_3$, $NaZnF_3$ and $NaNiF_3$ respectively (see Table 5-6). The transition pressures from DFT simulations for these fluoride post-perovskites are shown in Table 4-4, and the relationship between P_S and Ψ_S is shown in Figure 5-4.

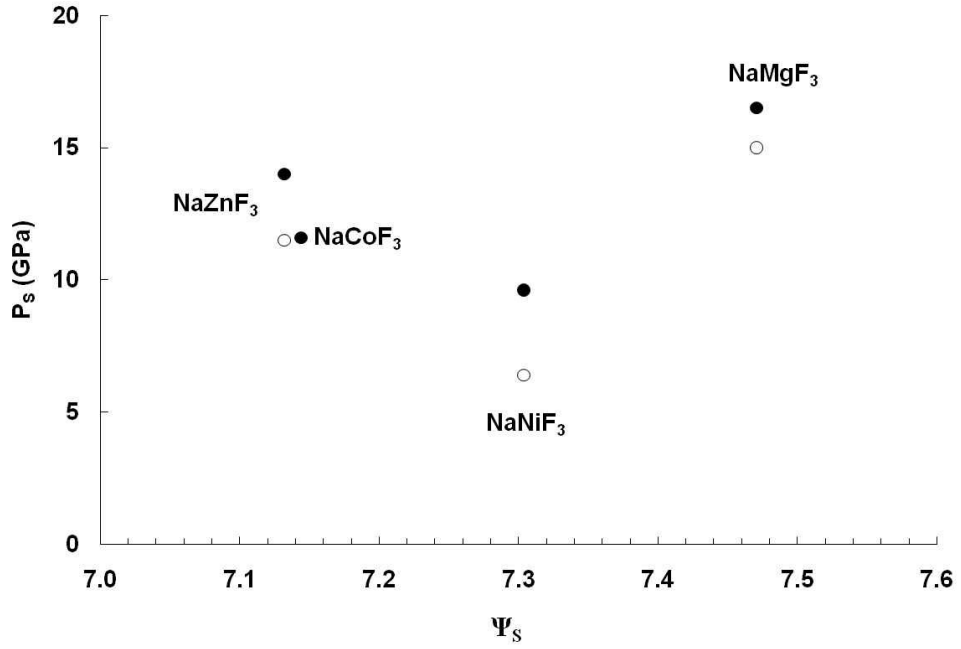

Figure 5-4: The relationship between the post-perovskite stabilisation pressure *Ps*, and the stabilisation factor Ψ_S for post-perovskite fluorides. Solid points denote experimental data. Open points are from DFT simulations corrected to 300 K using a Clapeyron slope of 8 (Section 4.4.3): no simulation has been carried out yet for $NaCoF_3$. The transition pressures from simulations for the three compounds are on average 2.4 GPa lower than the experimental stabilisation pressures.

It is apparent that more data are required to define any relationship between P_S and Ψ_S for fluoride post-perovskites. However, the values of Ψ_S for these fluorides are sufficient to show that, if a linear relationship between Ψ_S and P_S does exist for the fluorides, the equation of the line must be different from that for the oxides.

The Ψ_S values for the fluorides listed as crystallising as orthorhombic perovksites by Woodward (1997b) and by Liang *et al.* (2004) (no further examples were found in the Inorganic Crystal Structure Database; Fletcher *et al.,* 1996) range from ~5.9 (for $KHgF_3$) to ~ 8.0 for $NaFeF_3$ (high-spin Fe), with the value for $NaMgF_3$ ($\Psi_S = 7.5$) falling next highest in the range. So if a linear relationship similar to that shown in Figure 5-1 does exist for these materials, then the stabilisation pressure should be less than that of $NaMgF_3$ in all cases, with the possible exception of $NaFeF_3$. $KHgF_3$ is predicted to require the lowest pressure. Table 5-6 lists the fluoride perovskites which

are most likely to form post-perovskites, in addition to $NaMgF_3$, $NaZnF_3$, $NaNiF_3$ and $NaCoF_3$ which do form post-perovskites. P_S cannot yet be predicted for compounds which have not been reported to form post-perovskites because any relationship between Ψ_S and P_S is currently unknown.

Compound	t	Φ (degrees)	Ψ_S
$KHgF_3$	0.813	10.7	5.9
$KAgF_3$	0.885	15.6	6.4
$KCdF_3$	0.881	4.7	6.5
$KCaF_3$	0.862	9.3	6.6
$KPdF_3$	0.917	8.1	6.6
$NaMnF_3$ HS	0.822	19.1	6.9
$NaZnF_3$	0.857	17.2	7.1
$NaCoF_3$ HS	0.855	17.7	7.1
$NaNiF_3$	0.879	14.0	7.3
$NaMgF_3$	0.866	15.0	7.5
$NaFeF_3$ HS	0.915	21.7	8.0

Table 5-6: Properties of some fluoride perovskites likely to form post-perovskites. HS indicates the high-spin state.

The compounds shown in Table 5-6 are all perovskites with space group 62 (*i.e.* Pnma, Pbnm, Pmcn) and tolerance factors (t) between 0.81 and 0.92. Post-perovskite fluorides could conceivably differ from post-perovskite oxides in having t factors outside the approximate range of 0.839 – 0.900. Similarly, their octahedral tilt angle (Φ) could lie below the post-perovskite oxide approximate threshold of 13 – 15°. Several other perovskite fluorides whose space group is not 62 have t factors within the oxide t factor range, such as $RbCaF_3$, $RbHgF_3$, $NaCuF_3$, $NaVF_3$ and a range of $AgMF_3$ compounds where M = Pd, Mn (HS), Cr (HS), V, Cu, Zn, Co (HS) and Mg. However, in view of the fact that most known post-perovskites have space group 62 perovskite phases, the possible transition of perovskites in Table 5-6 to post-perovskites should be investigated before that of those do not have space group 62 perovskite phases.

5.12 The perovskite to post-perovskite phase transition and the distortion of perovskite octahedra

The phase transition from perovskite to post-perovskite structures involves a change from a 3-dimensional network of corner-linked octahedra in the perovskite structure to sheets of edge-shared and corner-linked octahedra in the post-perovskite structure. This transition could take place directly from octahedral tilting and distortion as a result of compression of the perovskite structure (Tsuchiya *et al.*, 2004), or via polytypic "kinked" stacking-fault structures intermediate between the perovskite and post-perovskite phases (Oganov *et al.*, 2005; Tschauner *et al.*, 2008).

Shirako *et al.* (2009) found that $CaRhO_3$ has a phase intermediate between perovskite and post-perovskite; this intermediate phase probably has edge-sharing RhO_6 octahedra like the post-perovskite structure, but its powder X-ray diffraction pattern was not consistent with those of any of the proposed stacking-fault phases.

Compression may cause instability in the perovskite structure by increasing the displacement of the oxygen anions through tilting and distortion of the octahedra. Martin and Parise (2008) have suggested that the transition to the post-perovskite phase in ABO_3 compounds occurs when the increasing tilts of quasi-rigid octahedra reduce the distance between O anions in separate octahedra, so that this distance approaches the distance between O anions in the same octahedron. Then the transition pressure will be determined by inter-octahedral repulsion of the anions. However, DFT modelling in the present work (below) suggests that changes in O-O distances due to the distortion of non-rigid octahedra may also be a factor in the transition; an empirical relationship is observed between the pressure at which the minimum octahedral angular variance occurs, and the transition pressure to the post-perovskite phase.

The pressure dependence of the distortion of the BX_6 octahedra in the perovskite phases of $MgSiO_3$, $MgGeO_3$, $CaSiO_3$, $NaMgF_3$, $NaZnF_3$ and $NaNiF_3$ was simulated at 0 K using VASP. The lowest mean octahedral angular variance (see Section 4.2.4) for oxides occurred in $CaSiO_3$, and the highest in $MgGeO_3$ (Figure 5-5a). The lowest variance for fluorides occurred in $NaMgF_3$ (Figure 5-5b).

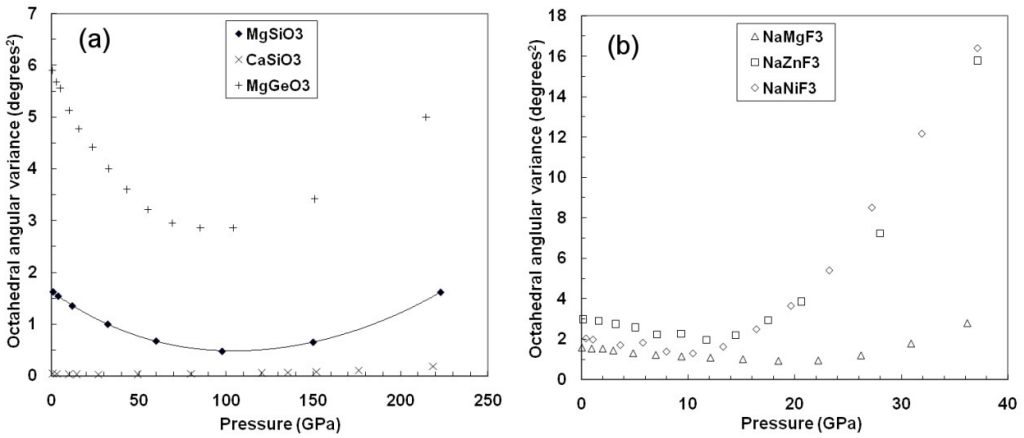

Figure 5-5: Perovskite mean octahedral angular variance from DFT simulations for (a) oxides (b) fluorides. The pressures at which the minimum variance occurs are estimated as (in GPa) 113.89 ($MgSiO_3$), 101.31 ($MgGeO_3$), 18.31 ($NaMgF_3$), 7.67 ($NaNiF_3$) and 9.74 ($NaZnF_3$).

As pressure increased, the simulated mean octahedral angular variance of each perovskite (except $CaSiO_3$) decreased to a minimum and then increased. $CaSiO_3$ perovskite did not show a minimum in the variation of its mean octahedral angular variance with pressure. No transition to post-perovskite has been found experimentally for this perovskite below 149 GPa (Fujino *et al.,* 2009) and this transition is also not predicted by *ab initio* simulation, even at high-temperature (Li *et al.*, 2005; Stixrude *et al.*, 2007).

The pressures at which the minimum octahedral angular variance of the simulated perovskites (excluding $CaSiO_3$ perovskite) occurs are correlated to their simulated and experimental pressures of transition to post-perovskite (at 0 K) with $R^2 = 89\%$ (see Figure 5-6). However, more data points are required to confirm any relationship.

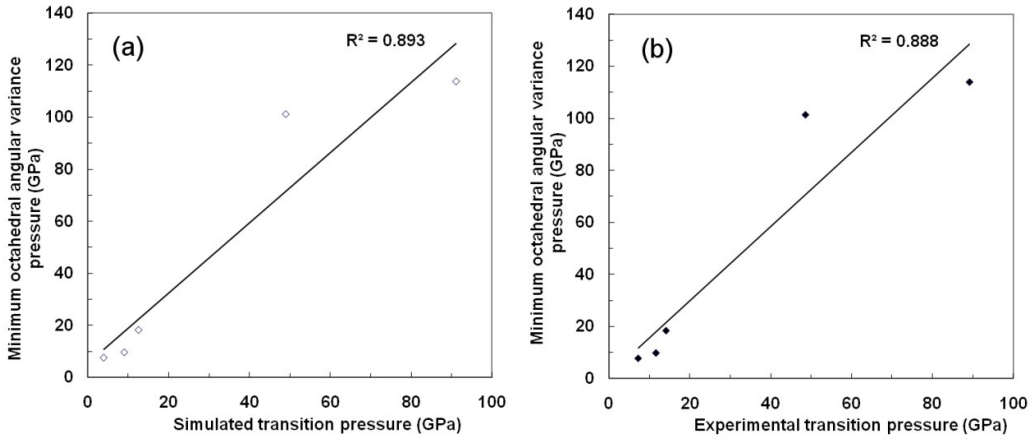

Figure 5-6: Correlations between the pressure at which the minimum octahedral angular variance occurs in DFT simulation of the perovskites shown in Figure 5-5 plotted against (a) simulated perovskite to post-perovskite transition pressure (b) experimental perovskite to post-perovskite transition pressure.

It is possible that once the minimum octahedral angular distortion is reached in these perovskites (with the exception of $CaSiO_3$), a further increase in pressure will result in transformation to the post-perovskite structure (provided that the *t*-factor and octahedral tilt angle are favourable) because the post-perovskite structure has a lower energy than an increasingly distorted perovskite structure.

5.13 Summary of prediction of post-perovskite phase stabilisation pressures

1. The pressure required to produce post-perovskite structured materials varies from 0 GPa to ~130 GPa, so it is very desirable to have a method for predicting whether the post-perovskite phase is likely to form and for estimating its stabilisation pressure.

2. The best correlation with the stabilisation pressure of post-perovskite oxides is obtained for a parameter, Ψ_S, based on differences in electronegativity and ionic sizes of the B and O ions, that reflects both the bonding and the dimensions of the BO_6 octahedra. Current data indicate that an $A^{2+}B^{4+}O_3$ post-perovskite oxide will only be stabilised if its tolerance factor – which takes account of the A, B and O ionic radii – is within the (approximate) range 0.835 - 0.900, and if the octahedral tilt of its perovskite phase is greater than 13-15°.

3. It is possible that a lower electronegativity difference between the B^{4+} cation and the O^{2-} anion, which reduces anion-anion repulsion, will have the same destabilising effect on the perovskite structure as an increase in pressure in compounds where increasing pressure increases octahedral tilts. Then compounds with a smaller electronegativity difference will tend to transform to a post-perovskite phase at lower pressures.

4. New $A^{2+}B^{4+}O_3$ post-perovskites are likely to be relatively rare. There may be more $A^{3+}B^{3+}O_3$ post-perovskites, but these may require higher stabilisation pressures than are available in a multi-anvil press. Candidates for both types are shown in Table 5-4.

5. $NaPtO_3$ and $NaRhO_3$ have similar tolerance factors to the newly-discovered $Na^{+}Ir^{5+}O_3$, and may be primary candidates for post-perovskite syntheses at pressures accessible in a multi-anvil press.

6. It may be possible to correlate the stabilisation pressure for post-perovskite fluorides with ionic electronegativities and radii, and with octahedral tilts, in the same way as suggested here for post-perovskite oxides. However, at present not enough data is available to establish a relationship between these factors. If there

is such a relationship, it is already apparent that its equation will be different from that of the post-perovskite oxides.

7. *Ab initio* modelling of some perovskite oxides and fluorides shows that there is (with the exception of $CaSiO_3$) an empirical relationship between the pressure at which the minimum octahedral angular variance occurs, and the transition pressure to the post-perovskite phase. It is possible that once the minimum octahedral angular distortion is reached in these perovskites, a further increase in pressure will result in transformation to the post-perovskite structure (provided that the *t*-factor and octahedral tilt angle are favourable) because the post-perovskite structure has a lower energy than an increasingly distorted perovskite structure.

6 Synthesis and analysis of samples

In this Chapter I describe my experiments to synthesise post-perovskite-structured phases, both powders and single crystals, in order to measure their equations of state, their structural changes with pressure and temperature, and their morphology.

I attempted three types of synthesis during the present work: single crystal post-perovskite $CaIrO_3$, polycrystalline post-perovskite $CaPtO_3$, and post-perovskite fluorides. Professor D.P. Dobson prepared and carried out the piston-cylinder experiments, and prepared, assembled and disassembled components for nearly all of the multi-anvil press (MAP) experiments. I assisted with preparation of ceramic octohedra, reactants, monitoring pressure and temperature, recording and analysis of experimental data for most of the experiments.

This synthesis work predated the analysis and identification of further perovskites likely to form post-perovskites (Sections 5.9 and 5.11). Recommendations for further syntheses are shown in Section 11.8.1.

6.1 Synthesis of oxide post-perovskites

Chapter 5 describes my approach to predicting the pressure at which an ABO_3 oxide post-perovskite phase may be expected to stabilise, given the elements A and B. So far, relatively few ABO_3 post-perovskite phases have been reported. Post-perovskite $CaIrO_3$ has been synthesised at ambient pressure. Post-perovskite $CaPtO_3$ (Ohgushi *et al.*, 2008) and $CaRhO_3$ (Shirako *et al.*, 2009) have been synthesised at 4 GPa, and post-perovskite $CaRuO_3$ at 24 GPa (Kojitani *et al.*, 2007). Post-perovskite $CaIr_{1-x}Pt_xO_3$ requires a pressure of 15 GPa and 1573 K rather than 3 or 10 GPa in order to form homogenous solid solutions (Hirai *et al.*, 2011). The synthesis of $NaIrO_3$ took place at 4.5 GPa and 800 °C (Bremholm *et al.*, 2011).

I synthesised polycrystalline post-perovskite $CaIrO_3$ previously at UCL (Lindsay-Scott *et al.*, 2007), but it shows significant structural distortion due to the Jahn-Teller effect. In the present work, I synthesised single-crystal $CaIrO_3$ in order to study its thermoelastic properties with greater accuracy than would be possible using polycrystalline samples (see Section 6.4.2)

I also synthesised polycrystalline post-perovskite $CaPtO_3$, because:

- $CaPtO_3$ does not exhibit structural distortion due to the Jahn-Teller effect, and is therefore likely to be a better analogue than $CaIrO_3$ or $CaRhO_3$ for post-perovskite $MgSiO_3$ (see Table 4-5)
- $CaPtO_3$ may be synthesised at relatively low pressure (4 GPa), unlike other analogues such as $CaRuO_3$, $MnGeO_3$ and $MgGeO_3$ (see Table 5-1). It is therefore more feasible to synthesise the relatively large volume required for the neutron diffraction experiments necessary to study structural change at high-pressure and at high-temperature
- $CaPtO_3$ is stable when quenched to ambient temperature.

6.2 Synthesis of fluoride post-perovskites

$NaMgF_3$ (Liu *et al.,* 2005) and $NaZnF_3$ (Yakovlev *et al.*, 2009; Yakovlev *et al.*, 2009a) also form post-perovskite phases, although both post-perovskite phases are metastable at ambient pressure. I examined the post-perovskite phase stabilisation factors, octahedral tilts and *t*-factors of the perovskites $NaNiF_3$, $NaCoF_3$ and $NaMnF_3$ (see Section 5.11 and Table 5-6). These factors and tilts favour the formation of post-perovskite phases. I also simulated the phase change between perovskite and post-perovskite in $NaNiF_3$, predicting that it would occur at a pressure of 6.4 GPa at 300K (see Section 4.4.3). The present work therefore investigated experimentally the synthesis of $NaNiF_3$, $NaCoF_3$ and $NaMnF_3$ post-perovskites.

6.3 Synthesis methods

I used four synthesis methods: heating at ambient pressure with a flux, heating at high-pressure in a MAP, heating at high-pressure in a piston-cylinder apparatus, and wet chemistry.

MAP experiments

Samples were heated at high-pressure in a Walker cell – a modified Kawai-type 6-8 MAP (Figure 6-1). In this type of apparatus the pressure is generated by using 8 WC anvils separated by gaskets. Pressures of between 1.5 and 15 GPa at temperatures up to 800 °C, measured by a W/Re thermocouple, were used. The use of an Inconel furnace instead of a graphite one helped to minimise the reduction of $CaPtO_3$ at high-temperature and pressure (Figure 6-2).

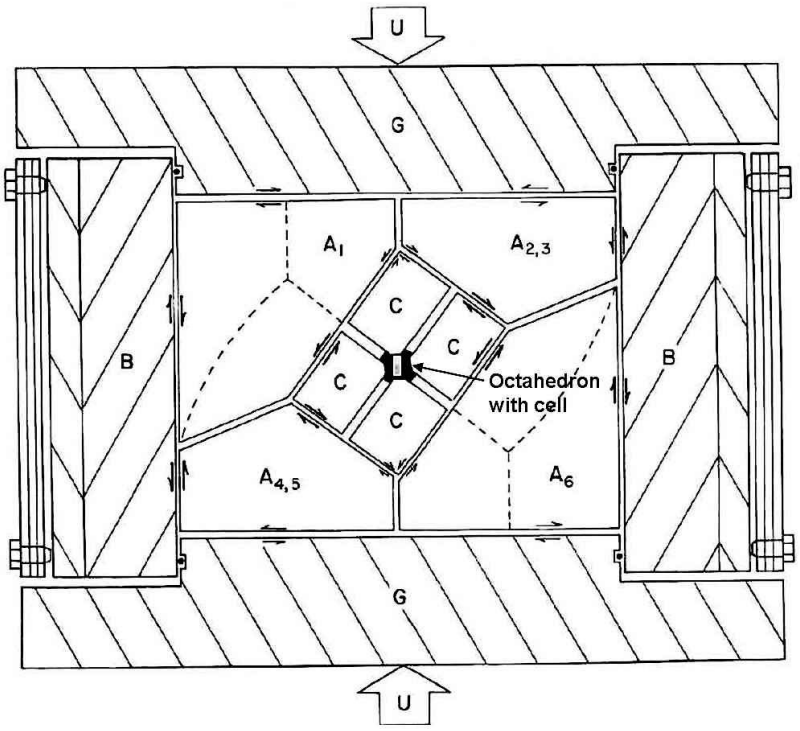

Figure 6-1: Walker cell (modified Kawai multi-anvil press). A_n – anvil-driving (first stage) wedges guided by bore of containment ring B. C – 8 (second stage) WC cubic anvils. U – uniaxial thrust delivered through pressure distribution plates G (Walker, 1991).

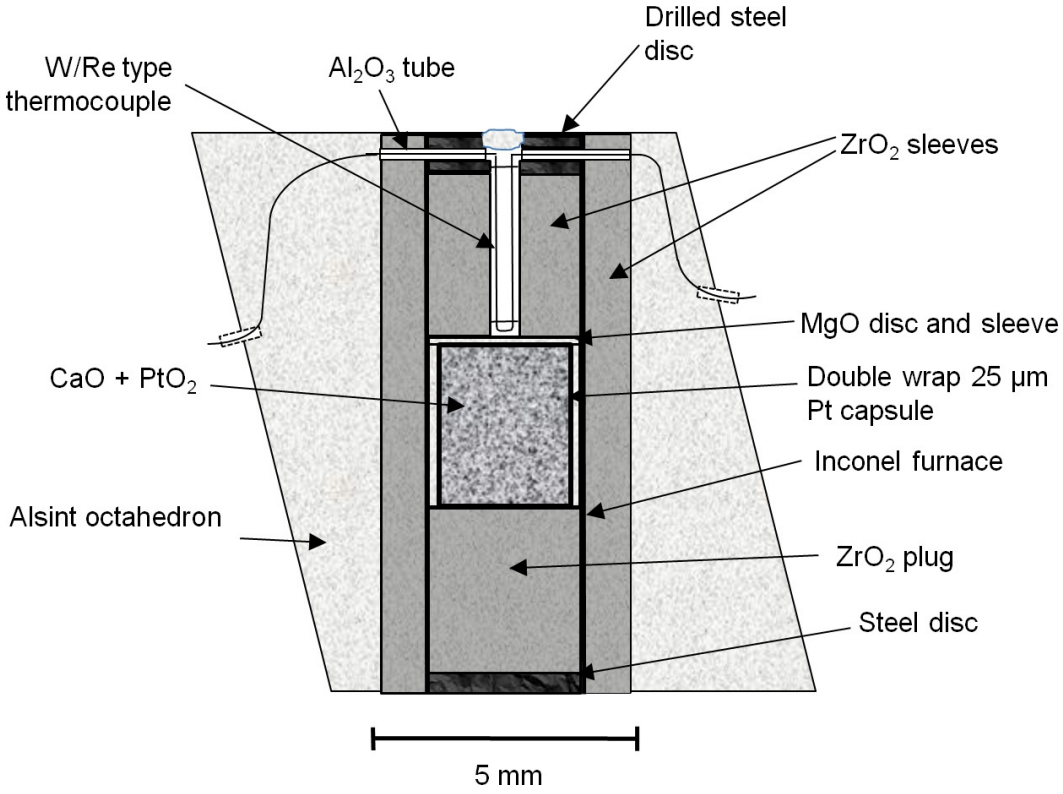

Figure 6-2: Typical multi-anvil press cell assembly for experiments up to 2 GPa. The octahedron length is 18 mm and is compressed by 11 mm-truncated WC anvils.

Piston cylinder experiment

Heating at high-pressure in a Boyd-England end-loaded piston-cylinder apparatus allowed larger sample volumes at pressures up to 2 GPa (Figure 6-3 and Figure 6-4). An Inconel furnace was used to prevent reduction of PtO_2. The MgO is softer than the ZrO_2, producing a more hydrostatic pressure environment.

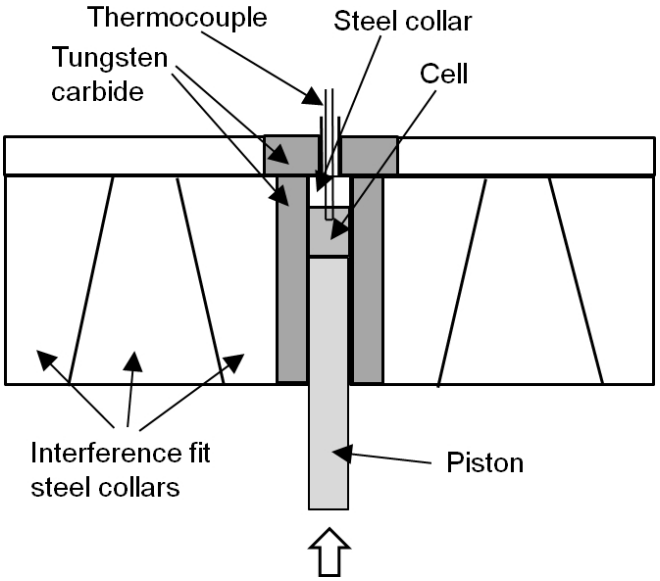

Figure 6-3: Piston-cylinder press

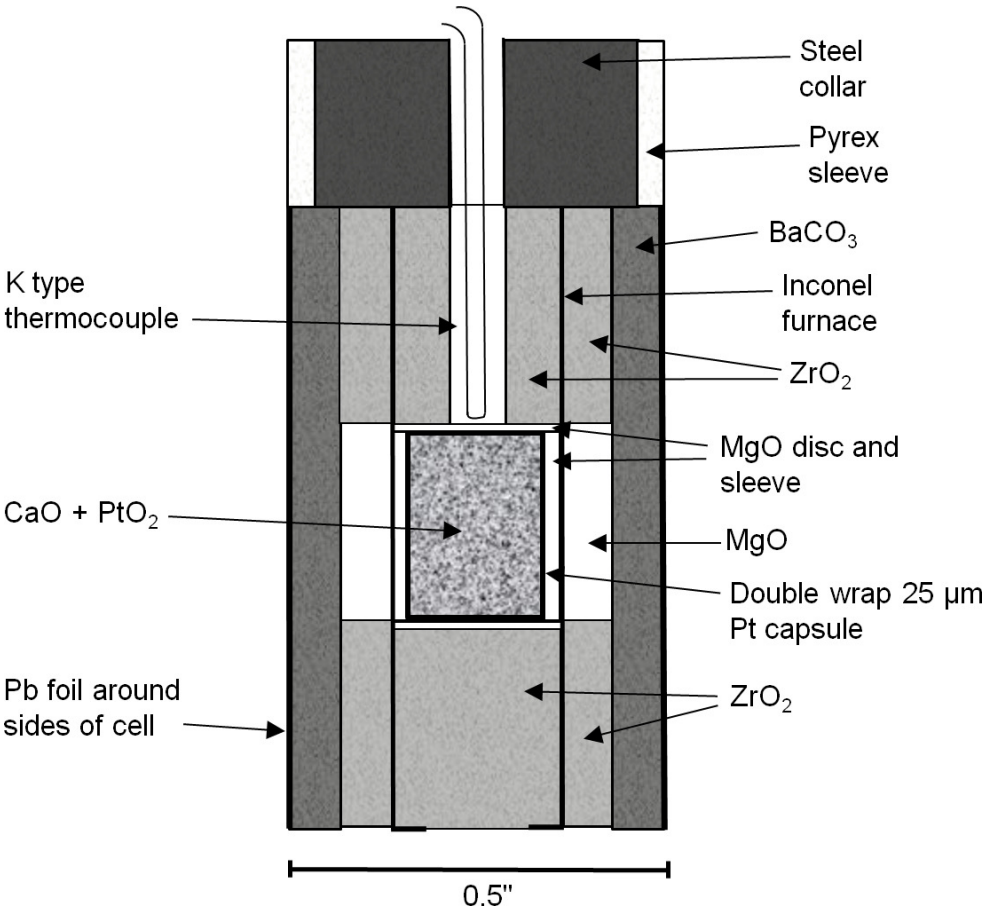

Figure 6-4: Typical piston-cylinder cell assembly

Sample analysis

Each experimental sample was quenched to room temperature, and the pressure was gradually reduced to ambient pressure. Samples were prepared for X-ray analysis as a thin smear on an "off-axis" silicon plate (*i.e.* one cut so as to produce no Bragg reflections) and the powder pattern was recorded using the UCL Earth Sciences PANalytical X'Pert Pro diffractometer with Co $K\alpha_1$ radiation (40 KV, 30 mA), scanning over the range $10^o < 2\theta < 90^o$. The initial analyses of X-ray powder diffraction patterns used the PANalytical X'Pert HighScore Plus software. I used the General Structure Analysis System (GSAS) suite of programs (Larson and Von Dreele, 1994) with the Graphical User Interface for GSAS .EXP files (EXPGUI; Toby, 2001) to obtain unit-cell parameters and structural data by Rietveld refinement. All GSAS refinements of X'Pert Pro analyses included dispersion corrections for X-ray scattering ($\Delta f'$ and $\Delta f''$; Cooper, 1963).

6.4 Syntheses of $CaIrO_3$

6.4.1 Single crystal synthesis of $CaIrO_3$ – heating at ambient pressure

Three syntheses of post-perovskite $CaIrO_3$ single crystals were attempted. These used as starting material previously synthesised polycrystalline post-perovskite $CaIrO_3$ (Lindsay-Scott *et al.*, 2007) mixed with Na_2CO_3 or NaCl fluxes, and heated at ambient pressure in a furnace (experiment 4). Each of the two samples of $CaIrO_3$ was ground with its flux under acetone and packed into a Pt boat covered with a Pt foil lid. The boats were placed in MgO powder in an Al_3O_3 crucible, heated at 930 ^oC for 17 hours, and cooled over 3 days. After cleaning with distilled water and ultrasound, stubby black acicular crystals were recovered which were ~12μm wide and up to 150μm long.

The experiment was repeated using temperature cycling to obtain larger crystals. Crystals produced from both fluxes in the previous experiment were ground with Na_2CO_3 flux and heated in an Al_2O_3 crucible with a "sawtooth" temperature-time path to ensure that the system remained in the growth-dominated rather than nucleation-dominated regime (Dobson and Jacobsen, 2004). After heating at 950 ^oC for 64 hours, the sample was cooled using 8 cooling/heating cycles down to 650 ^oC over 9 days before being quenched to room temperature. This produced black acicular matted crystals typically 50-150μm wide and up to 2.5mm long (experiment 5)(Figure 6-5).

X-ray diffraction analysis of sample crystals from both of these experiments using a Stoe-Weissenberg camera showed that the crystals were not composed of post-perovskite $CaIrO_3$, but were instead hexagonal Ca_2IrO_4 ($P\bar{6}2m$; Babel *et al.*, 1966, see Appendix C - Chapter 15). Ca_2IrO_4 has been reported as a by-product of the synthesis of $CaIrO_3$ (post-perovskite and perovskite) synthesis in previous work (e.g. Cheng *et al.*, 2010).

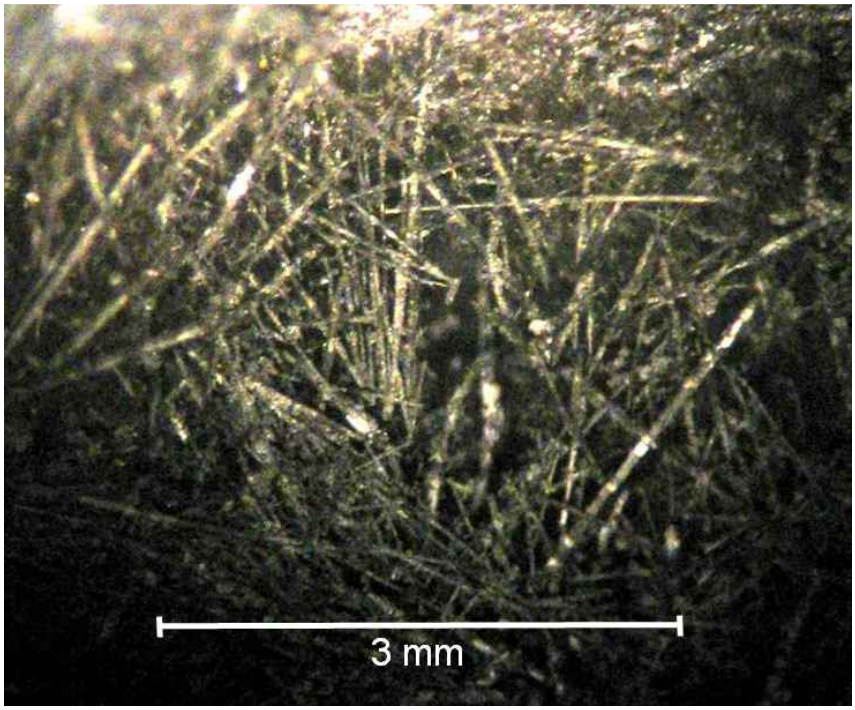

Figure 6-5: Optical micrograph of post-perovskite Ca_2IrO_4 crystals.

In the third ambient-pressure synthesis, polycrystalline post-perovskite-structured $CaIrO_3$ was mixed with a eutectic flux mixture of 1:1.27 $NaCl:Na_2CO_3$, heated at 700°C for 64 hours and cooled over 3 days (experiment 6). The black polycrystalline product contained Ca_2IrO_4 with some post-perovskite $CaIrO_3$. In view of the failure of these synthesis experiments to produce significant amounts of post-perovskite $CaIrO_3$, it was decided to try the single crystal synthesis under pressure to contain oxygen and prevent the reaction of $CaIrO_3$ to form Ca_2IrO_4.

6.4.2 Single crystal synthesis of $CaIrO_3$ – heating at high-pressure in a MAP

This experiment used a multi-anvil press (MAP) for high-pressure synthesis of single crystal post-perovskite $CaIrO_3$ at 1.5-2.0 GPa and 1200 ^oC (experiment 7).

Previously synthesised polycrystalline post-perovskite $CaIrO_3$ (Lindsay-Scott *et al.*, 2007) was ground under acetone with NaCl flux and $KClO_4$. The $KClO_4$ oxidant was added to prevent conversion of the $CaIrO_3$ to Ca_2IrO_4 plus Ir metal. The reactant proportions by weight were 3:2:1 $CaIrO_3$:NaCl: $KClO_4$. The reactants were sealed in a Pt capsule, separated from the graphite furnace by a MgO sleeve, all within a zirconia cylinder (see Figure 6-2). Well-formed euhedral sub-rectangular black crystals were produced, up to 150μm long with aspect ratios between 1.5:1 and 3.5:1 (Figure 6-6). Smaller octahedral crystals of IrO_2 were also present, up to 10μm across.

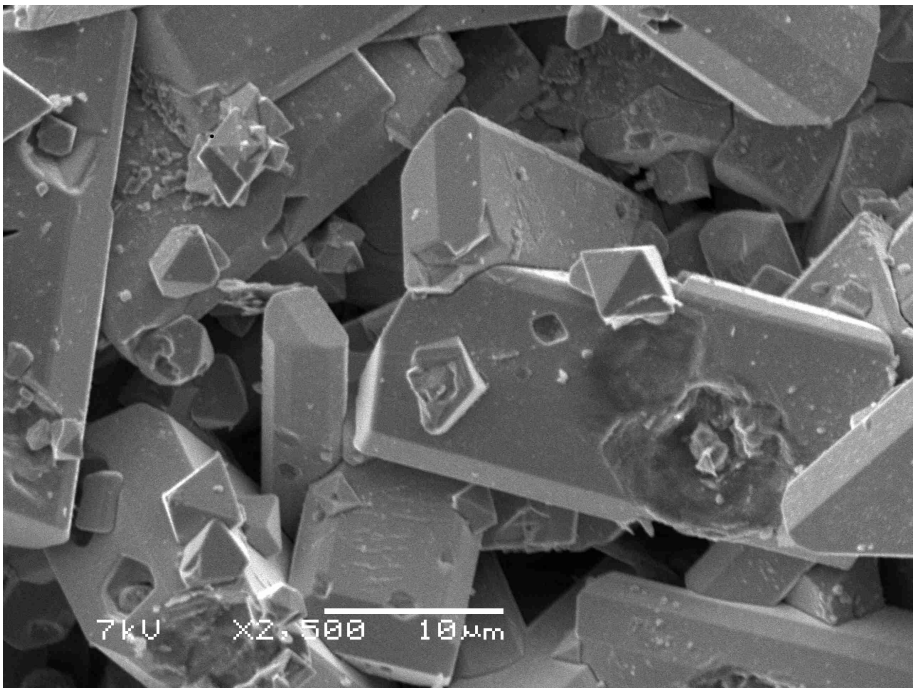

Figure 6-6: Post-perovskite $CaIrO_3$ crystals (SEM image).

Analysis of the X-ray powder diffraction pattern using the PANalytical X'Pert HighScore Plus software (XU516) identified the synthesis products as post-perovskite $CaIrO_3$ and IrO_2 with $NaClO_2$ and $KClO_4$. Electron probe investigation of these post-perovskite $CaIrO_3$ single crystals showed a slight deficiency in Ir compared with Ca,

giving a Ca:Ir ratio of 1.09(3):1 sampled across 10 crystals. These crystals were also studied using a scanning electron microscope (SEM) (see Section 6.7).

A single post-perovskite $CaIrO_3$ crystal 130 μm x 50 μm x 25 μm was examined by X-ray diffraction to confirm that the *a*-axis was parallel to the long axis of the crystal (Sugahara *et al.*, 2008). This examination used a Stoe Weissenberg cylindrical camera, with Cu K_α X-radiation and Ni filtering. The crystal was mounted with its long axis perpendicular to the X-ray beam. When the crystal was rotated about its long axis, 26 pairs of diffraction spots were observed (Figure 6-7). From the layer-line spacing the rotation axis was found to have a periodicity of 3.158(4) Å, confirming that the *a*-axis was parallel to the long axis of the crystal. Iterative calculation was used to find the other unit-cell parameters (given *a*) by minimising the χ^2 difference between the calculated and observed values of the 2θ diffraction angles for the 26 observations. The value for *a* and the values calculated for *b* of 9.868(13) Å and for *c* of 7.304(10) Å compared well with the values found previously by X-ray powder diffraction: a = 3.14554(5) Å, b = 9.86370(8) Å, and c = 7.29697(10) Å (Lindsay-Scott *et al.*, 2007).

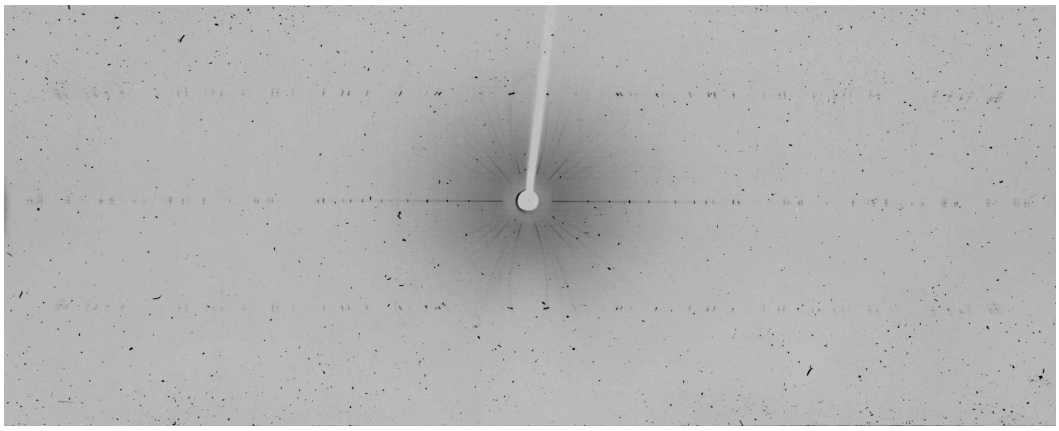

Figure 6-7: X-ray diffraction pattern from a single crystal of post-perovskite $CaIrO_3$.

X-ray data sets were collected from a single crystal of $CaIrO_3$ using the Oxford Diffraction Gemini single crystal diffractometer at STFC Rutherford Appleton Laboratory, UK between 100 K and 260 K at ambient pressure, with the intention of studying structural changes. However, it proved impossible to devise an absorption correction using the software supplied which would be adequate for accurate structural refinements. As the cell parameters had already been measured at a range of

temperatures by X-ray powder diffraction, this work did not provide any new information and is not reported here. However, some of the $CaIrO_3$ post-perovskite single crystals prepared in the present work have been used in subsequent experiments by other members of the UCL mineral physics group (e.g. McCormack *et al.*, 2010).

6.5 Syntheses of $CaPtO_3$

6.5.1 Post-perovskite $CaPtO_3$ synthesis – MAP at UCL

The first $CaPtO_3$ synthesis used a stoichiometric mixture of CaO (0.1907 g) and PtO_2 (0.7730 g) ground under acetone with a 2:1 mixture by weight of NaCl flux (0.6672 g) and $KClO_4$ (0.3334 g), sealed in a Pt capsule with a graphite furnace (experiment 8, XU528). It was heated in a MAP at 3.5-4 GPa for 1 hour at 800 ^oC, and then heated for 1.5 hours at 1200 ^oC. The assembly was then cooled over 3 hours to 660 ^oC. X-ray powder diffraction analysis indicated the presence of post-perovskite $CaPtO_3$, which showed a similar peak pattern to that of $CaIrO_3$ when adjusted for the published unit-cell parameters of post-perovskite $CaPtO_3$ (Ohgushi *et al.*, 2008). However, there were also significant amounts of other CaPt and NaPt oxides.

The next synthesis used a stoichiometric powder mixture of PtO_2 and CaO, ground under acetone in a mortar and sealed in a Pt capsule with a Pt furnace, rather than a graphite furnace, to help prevent reduction of $CaPtO_3$ to other oxides (experiment 16). The CaO was baked at 1000 °C beforehand to remove any moisture. After 22 hours at 4 GPa and 800 ^oC in a MAP, a well-sintered black (with yellow/green overtones) sample was found by X-ray powder diffraction analysis to contain post-perovskite $CaPtO_3$, with alumina from the furnace assembly (Figure 6-8).

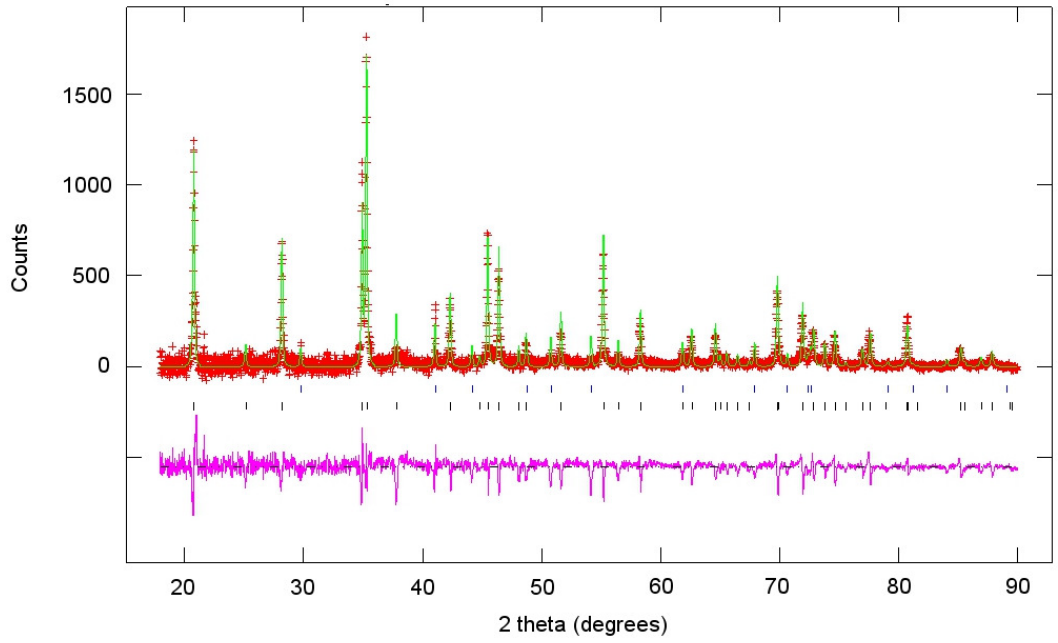

Figure 6-8: Observed (points), calculated (line) and difference (lower trace) X-ray powder diffraction patterns for Le Bail refinement of post-perovskite $CaPtO_3$ with alumina (background subtracted). The tick marks show the positions of the (from the bottom upwards) $CaPtO_3$ post-perovskite and alumina (Al_2O_3)(XU588).

This synthesis was repeated for 20 hours at 780 ^{o}C and 4 GPa, producing a sample of similar appearance consisting of $CaPtO_3$ but with no alumina (experiment 17)(Figure 6-9).

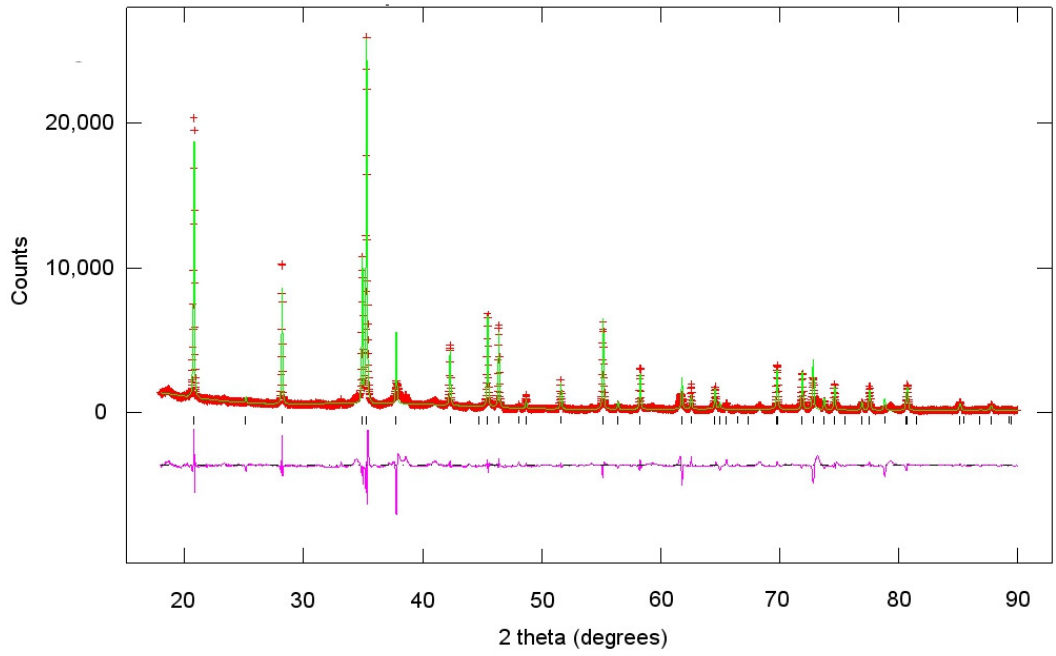

Figure 6-9: Observed (points), calculated (line) and difference (lower trace) X-ray powder diffraction patterns for Le Bail refinement of post-perovskite $CaPtO_3$ without alumina. The tick marks show the positions of the Bragg reflections of $CaPtO_3$ post-perovskite (XU624).

6.5.2 Post-perovskite $CaPtO_3$ synthesis – piston-cylinder press

A synthesis of post-perovskite $CaPtO_3$ using a Boyd-England end-loaded piston-cylinder apparatus was then tested to take advantage of this apparatus' greater sample volume. This synthesis used a stoichiometric powder mixture of PtO_2 and baked CaO, ground together in a dry mortar and sealed in a 175 mm^3capacity Pt capsule with an inconel furnace and K-type thermocouple (experiment 18). This was compressed to 2 GPa for 23 hours at 800 ^oC. This produced a grey-black polycrystalline sample with small pale green-yellow crystals, which X-ray powder diffraction analysis (XU628) showed to consist of post-perovskite $CaPtO_3$ and a tetragonal form of $CaPt_2O_4$ (Cahen *et al.*, 1974).

6.5.3 Post-perovskite $CaPtO_3$ synthesis – large volume high-pressure at NIMS

The volume of sample required for PEARL and HRPD experiments at ISIS was up to 12 times as large as the 50 mm^3 produced in the previous MAP synthesis. Dr. T. Taniguchi was requested to prepare a larger volume of post-perovskite $CaPtO_3$, using

experimental parameters from the present work, on the high capacity belt-type high-pressure apparatus at the National Institute for Materials Science (NIMS), Tsukuba, Ibaraki, Japan.

The starting material was a stoichiometric powder mixture of PtO_2 and CaO, ground together in a mortar and sealed in a Pt capsule. This was compressed to 4 GPa, heated to 800 ^{o}C for 24 hours and then quenched to room temperature prior to slow decompression. The recovered dark-yellow powder was characterized by X-ray powder diffraction using the UCL Earth Sciences PANalytical X'Pert Pro diffractometer. The sample (Figure 6-10) was found to contain orthorhombic post-perovskite $CaPtO_3$ (*Cmcm:* see Table 6-1), with minor amounts of cubic $Ca_xPt_3O_4$ ($Pm\bar{3}n$; a = 5.7064(1) Å, V = 185.82(1) Å^3; Bergner and Kohlhaas, 1973) and traces of cubic Pt ($Fm\bar{3}m$; a = 3.9262(2) Å, V = 60.52(1) Å^3; Holmes *et al.*, 1989).

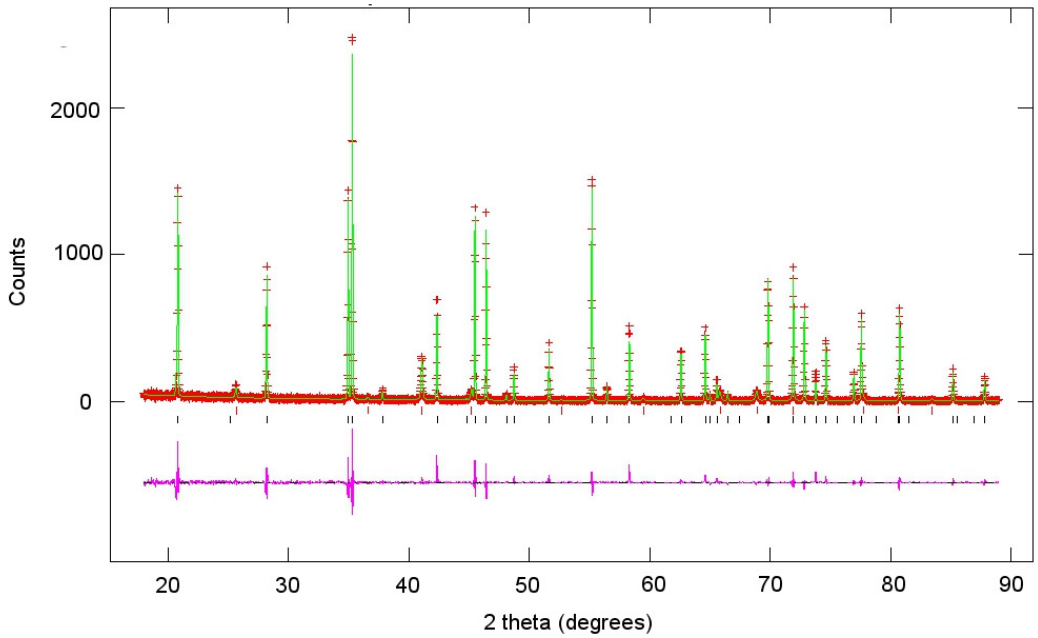

Figure 6-10: Observed (points), calculated (line) and difference (lower trace) X-ray powder diffraction patterns for Le Bail refinement of post-perovskite CaPtO from NIMS. The tick marks show the positions of the Bragg reflections of (from the bottom upwards) $CaPtO_3$ post-perovskite and cubic $Ca_xPt_3O_4$ (XU630, 2 phases).

The lattice parameters for the $CaPtO_3$ (estimated from a LeBail refinement of the data, see below) were found to be in reasonable agreement with those previously reported at ambient pressure and temperature (see Table 6-1).

	a(Å)	b(Å)	c(Å)	Volume (Å^3)
The present work	3.12612(2)	9.91709(6)	7.34952(5)	227.850(2)
Ohgushi *et al.*, 2008	3.12607(1)	9.91983(4)	7.35059(3)	227.942(2)
Inaguma *et al.*, 2008	3.1232(4)	9.912(1)	7.3459(9)	227.41(5)

Table 6-1: Unit-cell parameters and unit-cell volume for $CaPtO_3$ at ambient pressure and temperature; the numbers in parentheses are estimated standard uncertainties and refer to the least-significant digits.

The products of this synthesis totalled ~300 mm^3. A subsequent sample also produced by Dr. Taniguchi at NIMS brought the total volume of post-perovskite $CaPtO_3$ to ~600 mm^3.

6.6 Thermal dissociation of $CaIrO_3$ and $CaPtO_3$ post-perovskites

The phase equilibria in the CaO-IrO_2-Ir system heated in air have been studied by McDaniel and Schneider (1972). They found that changes in the ratio of CaO:IrO_2 from 1:1 to 4:1 coupled with rising temperature gave rise to oxides of the composition $CaIrO_3$ (perovskite and post-perovskite), Ca_2IrO_4 and Ca_4IrO_6 (see Figure 6-11).

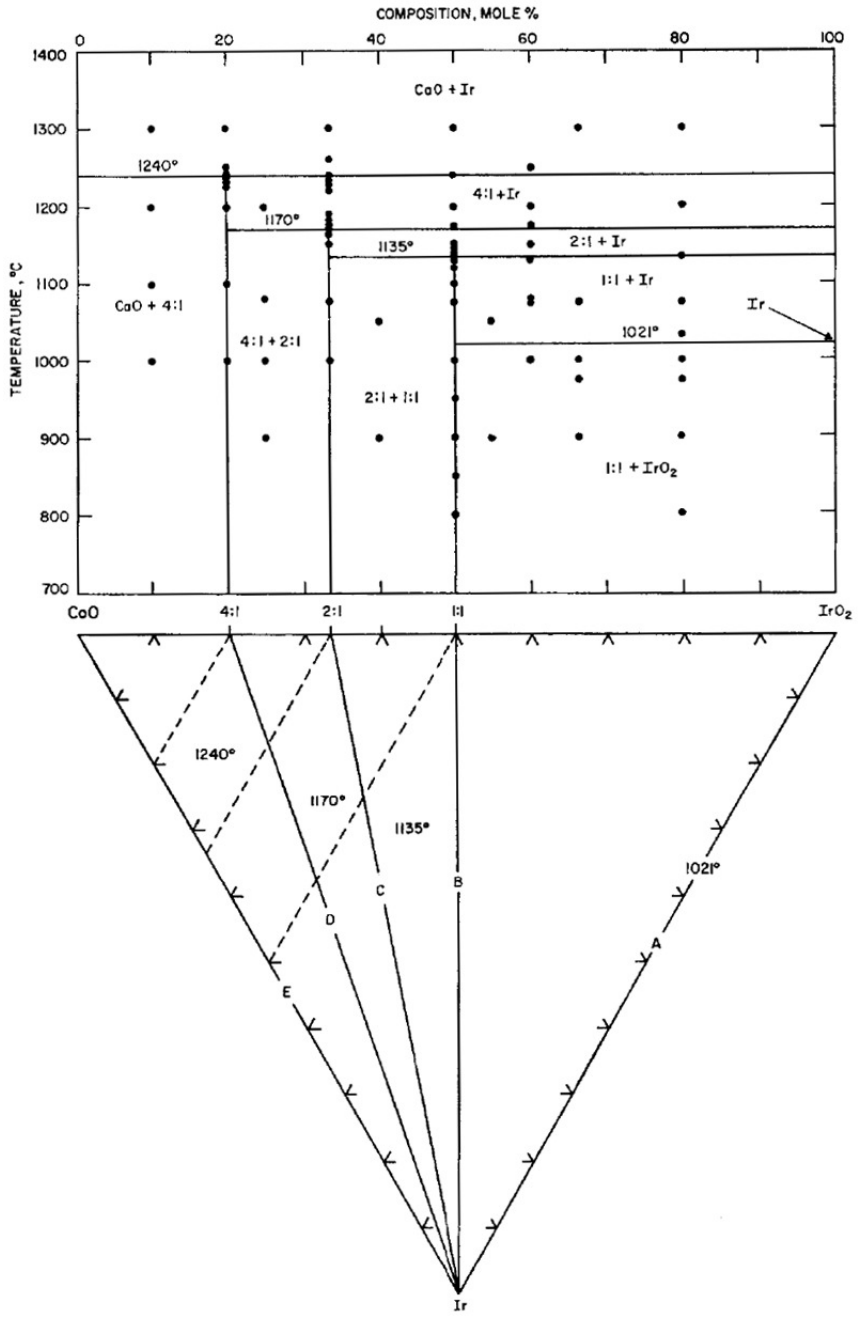

Figure 6-11: Phase equilibria in the CaO-IrO_2-Ir system heated in air (McDaniel and Schneider, 1972). 1:1 indicates 1 CaO : 1 IrO_2

The reactions and transition temperatures between these Ca-Ir-O compounds (from McDaniel and Schneider, 1972), and between similar Pt compounds shown in Figure 6-12 and Figure 6-13 (the present work), are listed below.

$$IrO_2 \rightarrow Ir + O_2 \quad \text{at 1021 °C} \quad (6.1)$$

$$2CaIrO_3 \rightarrow Ca_2IrO_4 + Ir + O_2 \quad \text{at 1135 °C} \quad (6.2)$$

$$2Ca_2IrO_4 \rightarrow Ca_4IrO_6 + Ir + O_2 \quad \text{at 1170 °C} \quad (6.3)$$

$$Ca_4IrO_6 \rightarrow 4CaO + Ir + O_2 \quad \text{at 1240 °C} \quad (6.4)$$

$$PtO_2 \rightarrow Pt + O_2 \quad \text{at 600 °C} \quad (6.5)$$

$$2Ca_2PtO_4 + 2Pt + O_2 \rightarrow 2CaPt_2O_4 + 2CaO \quad \text{at 650 °C} \quad (6.6)$$

$$4CaPtO_3 \rightarrow Ca_4PtO_6 + 3Pt + 3O_2 \quad \text{at 850 °C} \quad (6.7)$$

$$2Ca_2PtO_4 \rightarrow Ca_4PtO_6 + Pt + O_2 \quad \text{at 850 °C} \quad (6.8)$$

It was necessary to establish the transition temperature at which post-perovskite $CaPtO_3$ breaks down in preparation for the high-temperature neutron diffraction experiment at ISIS (Section 9.2), so a high-temperature X-ray powder diffraction study was carried out on polycrystalline post-perovskite $CaPtO_3$ at ambient pressure in air. The sample of post-perovskite $CaPtO_3$ synthesised in a MAP at UCL also contained Ca_2PtO_4 and PtO_2 impurity phases from the synthesis and, to reduce the amount of material required for the experiment, the specimen in the diffractometer was composed of a packed cake of MgO powder with the $CaPtO_3$ sample sprinkled on to the top surface.

In the first experiment the sample was heated from 25 °C to 750 °C, measuring the diffraction pattern at 50 °C intervals between 500 °C and 750 °C. Since the post-perovskite $CaPtO_3$ persisted to 750 °C, in a second experiment the same sample was heated from 25 °C to 1000 °C to observe the breakdown of post-perovskite $CaPtO_3$. The X-ray patterns from the first heating run are shown in Figure 6-12, and from the second run in Figure 6-13.

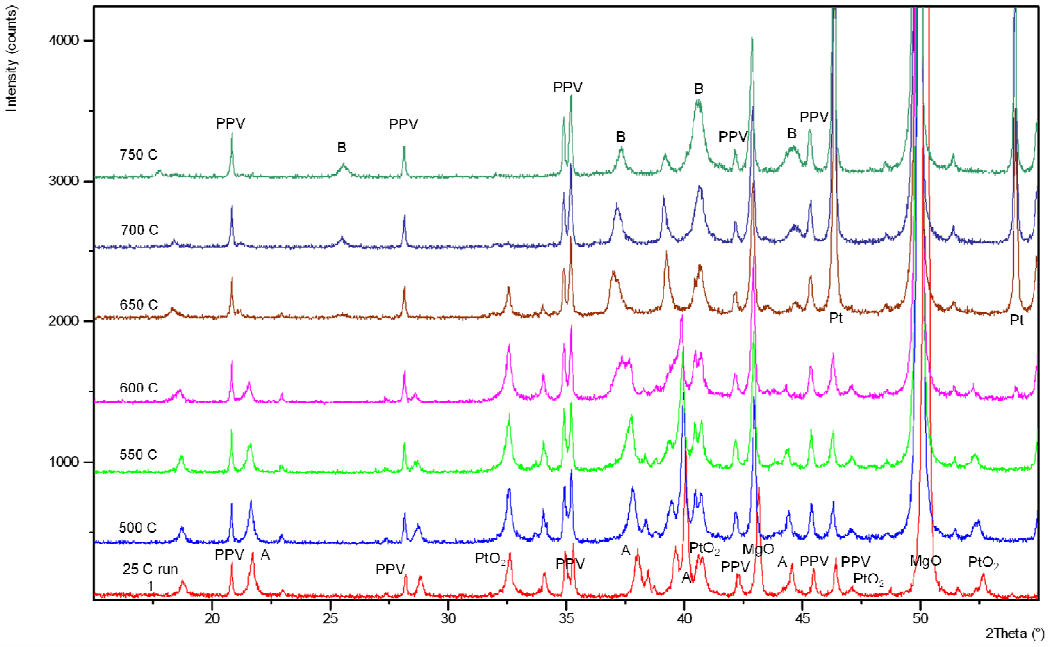

Figure 6-12: Heating to 750 °C. PPV – post-perovskite $CaPtO_3$. A – Ca_2PtO_4 ($\boldsymbol{P\bar{6}\,2m}$). B – platinum bronze $CaPt_2O_4$ ($\boldsymbol{P4_2/mmc}$)(Cahen *et al.*, 1974)(XU533, XU534).

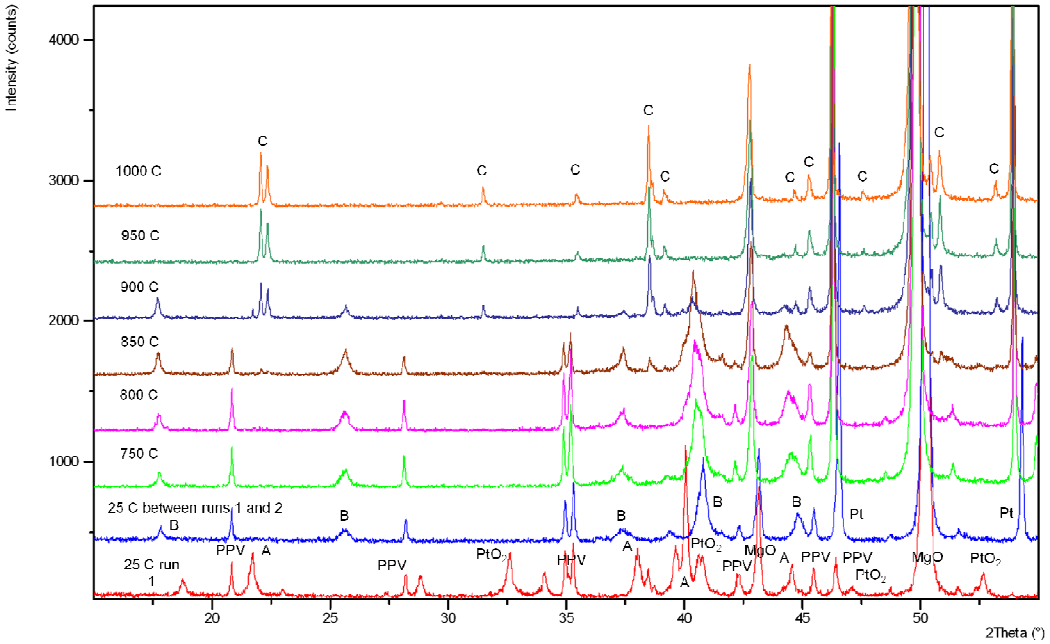

Figure 6-13: Heating to 1000 °C. PPV – post-perovskite $CaPtO_3$. A – Ca_2PtO_4 ($\boldsymbol{P\bar{6}\,2m}$). B – platinum bronze $CaPt_2O_4$ ($\boldsymbol{P4_2/mmc}$) (Cahen *et al.*, 1974). C – Ca_4PtO_6 ($\boldsymbol{R\bar{3}\,c}$)(Claridge *et al.*, 1997)(XU535).

In the first experiment, peaks marked A and PtO_2 disappear above 650 °C. The A peaks were identified as Ca_2PtO_4 ($P\bar{6}\,2m$), which although not previously reported has the same structure as Ca_2IrO_4 (Babel *et al.*, 1966). Peaks marked B appeared from 650 °C to 900 °C, and were identified as tetragonal platinum bronze $CaPt_2O_4$ ($P4_2$/mmc; Cahen *et al.*, 1974). Peaks marked C appeared from 900 °C and were identified as trigonal Ca_4PtO_6 ($R\bar{3}c$; Claridge *et al.*, 1997).

Equations (6.5) to (6.8) show the transition temperatures between these Pt compounds. Peaks unmarked in Figure 6-12 and Figure 6-13 may be due to compounds of Na and K introduced by the NaCl and $KClO_4$ reactants.

The post-perovskite peaks shown in Figure 6-13 persisted to 850 °C, but were absent at 900 °C. The neutron diffraction experiments described in Section 9.2 (each of ~ 5 hours duration) show that post-perovskite dissociation products were absent from the sample (sealed in a vacuum) at 596 °C but began to appear in the first 700 °C run. So post-perovskite $CaPtO_3$ is metastable in air for periods of less than 2 hours at 850 °C, but dissociation occurs at lower temperatures when heated for a longer time in a sealed evacuated container.

The comparison of the transition temperatures between Pt oxides shown in Equations (6.5) to (6.8) with those between Ir compounds shown in Equations (6.1) to (6.4) shows that the Pt oxides dissociate in air at temperatures 300 – 500 °C lower than their Ir counterparts, consistent with the Pt-PtO buffer system being more oxidising than the Ir-IrO system.

6.7 Scanning Electron Microscope study of $CaIrO_3$ single crystal morphology

A sample of $CaIrO_3$ single crystals was prepared (as described in 6.4.2), coated with a carbon film and viewed in a Jeol JSM-6480LV SEM. There were two types of euhedral crystals visible. A small proportion of these were octahedra about 4 microns from apex to apex. Most of the euhedral and subhedral crystals visible were elongated with length/breadth ratios between 2 and 6, with a sub-elliptical cross-section with major/minor axis ratios of 1.5 to 2. These compared with the needle-shaped post-perovskite $CaIrO_3$ crystals reported by Sugahara *et al.* (2008), and this identification was confirmed by X-ray powder diffraction. Single-crystal diffraction (Section 6.4.2) confirmed that the long axis of the crystal was the *a*-axis. On closer examination, the sub-elliptical cross-section proved to be a polyhedron with 12 sides, typically measuring 10 x 15 microns (Figure 6-14). Opposite pairs of these sides were parallel, although some pairs could be very short. The two members of a pair might be of unequal length, but they were parallel.

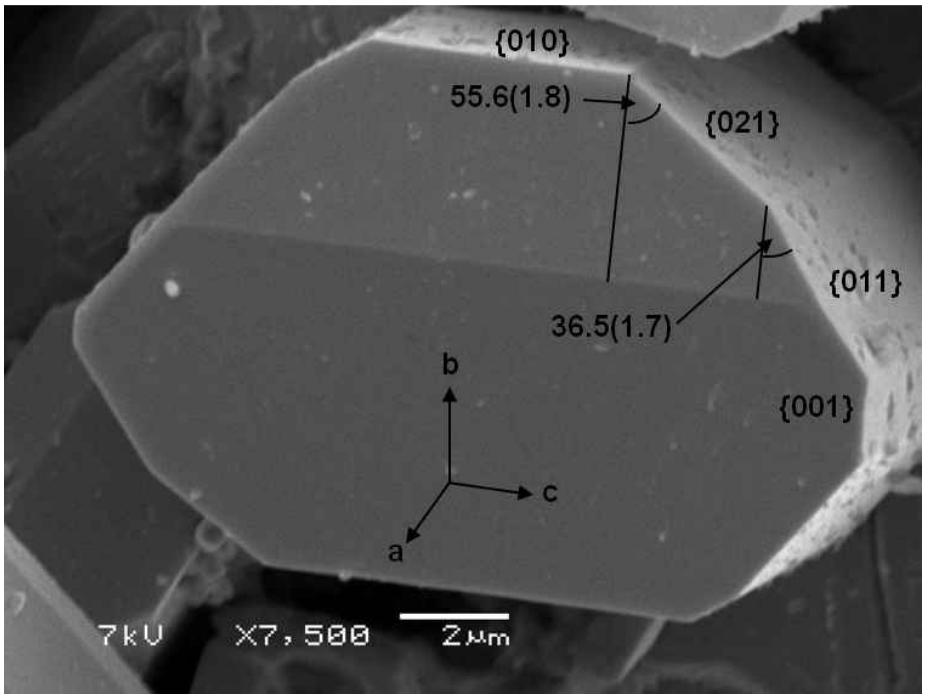

Figure 6-14: $CaIrO_3$ single crystal 12 sided view. Angles and their ESDs are shown in degrees.

To index the faces of the crystals, the sample was rotated so as to bring one of the orthogonal axes of a euhedral crystal sub-parallel to the viewing direction. 25 images of crystals were recorded. Most of the crystals imaged were oriented so that their longest axis was parallel to the viewing direction, showing the 12-sided view. Some of the images were oriented so that their shortest axis was parallel to the viewing direction, showing a 6 sided view (Figure 6-15).

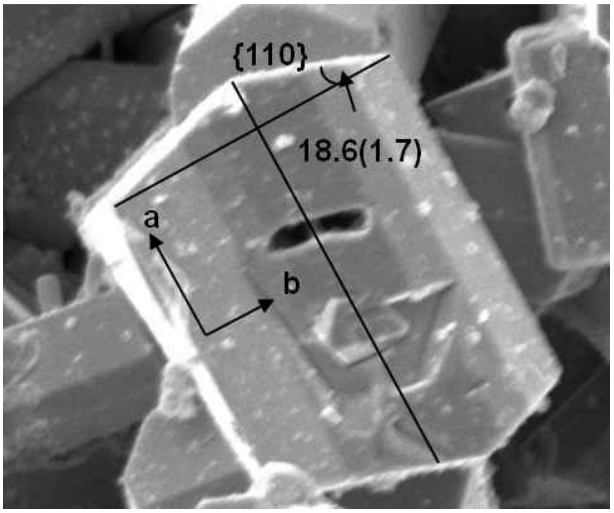

Figure 6-15: $CaIrO_3$ single crystal 6 sided view. An angle and its ESD is shown in degrees.

The objective of the SEM study was to identify possible crystal forms (families of planes) by measuring the angles between the crystal faces in the SEM images and comparing these with angles calculated from known cell parameters *a, b* and *c*. When the crystal faces in a view had been identified, then axes were linked to the longest, intermediate and shortest crystal dimensions. Previous work using transmission electron microsopes identified the longest, needle-like dimension as the *a*-axis of post-perovskite $CaIrO_3$ crystals (Miyajima *et al.*, 2006) and of post-perovskite $CaPtO_3$ crystals (Ohgushi *et al.*, 2008).

The method used was to measure the angle between each pair of adjacent sides in the 12 sided and 6 sided views. Because opposite pairs of sides were parallel, this meant that there were (for orthorhombic or higher symmetry) 4 instances of each of 2 unique angles in the 12 sided view, and 4 instances of the single unique angle in the 6 sided view.

Each angle was measured using one of two methods. Where the meeting points of the sides were clearly visible in an image, the (x,y) coordinates of each of the 12 or 6 meeting points were measured by recording its cursor position when viewed in Adobe Photoshop. The angle between each pair of sides was then deduced using trigonometry and reduced to an acute angle. Where the meeting points of the sides were not clearly visible in an image, the sides were extended by ruling on a paper print of the image and the angles were measured manually.

The two main sources of error were the accuracy of the measurement of the (x,y) coordinates, and the direction of view being off-axis where it was not possible to perfectly align the axis of the crystal with the viewing direction. In practice the variation in measured angles due to an off-axis viewing direction proved to be larger than measurement inaccuracies. The off-axis viewing direction error was reduced by using all the instances of the angles for the 12 or 6 sided views.

Angles in 9 12-sided views were measured (7 in Photoshop, 2 from paper) and in a single 6-sided view (in Photoshop). The angles corresponding to a range of forms {011} {021}…. and {110} {120}…. and {101} {102} were calculated. The best fit between observed and calculated angles was found to be with the longest (needle) axis of the crystal corresponding to the *a*-axis (consistent with previous work), the semi-minor pseudo-elliptical axis to the *b*-axis and the semi-major axis to the *c*-axis. This is shown in Table 6-2 with Figure 6-14 for the 12 sided view and Figure 6-15 for the 6 sided view.

Angle #	1	2	3
Observed angle in degrees (ESD)	55.6(1.8)	36.5(1.7)	18.6(1.7)
Number of observations	33	35	4
Best fit form for axes shown	{021}	{011}	{110}
Angle in degrees calculated from published cell parameters (Sugahara *et al.*, 2008)	55.94(3)	36.49(3)	17.68(4)
Angle in degrees calculated from published cell parameters for next best fit (*b* and *c* axes exchanged)	53.51(3)	34.06(3)	23.31(3)

Table 6-2: $CaIrO_3$ single crystal indexing results

The identification of the axes has been confirmed using electron backscatter diffraction at Bayerisches Geoinstitut, Universität Bayreuth, Bayreuth, Germany for post-perovskite $CaIrO_3$ crystals from the same synthesis: the *a*-axis is perpendicular to the 12-sided section, the *b*-axis corresponds to the semi-minor axis and the *c*-axis to the semi-major axis (McCormack, 2011).

The acicular form of the $CaIrO_3$ crystals with elongation along the *a*-axis may be related by lattice preferred orientation to the [100]{010} glide system deformation texture observed in $CaIrO_3$ post-perovskite by Walte *et al*. (2009) and recently in $CaPtO_3$ post-perovskite by McCormack *et al*. (2011). The results of Walte *et al*. predict a widespread shear wave splitting with fast horizontal S-waves (assuming material spreading parallel to the core-mantle boundary), which is compatible with seismic studies. Downwelling material that undergoes a phase transformation may develop a transformation texture that would locally result in vertically polarized fast S-waves. The results of McCormack *et al*. suggest that texture resulting from shape-preferred orientation in post-perovskite may also generate seismic anisotropy in D".

6.8 Syntheses of fluoride perovskites and post-perovskite $NaNiF_3$

6.8.1 Fluoride perovskite synthesis – wet chemistry

The first method examined for the preparation of post-perovskite fluoride compounds was to prepare a fluoride perovskite and then transform it to its post-perovskite phase at high-temperature and pressure. Fluoride perovskites have been synthesized by precipitation from solutions of metal fluorides and chlorides. This method was used to synthesize $NaZnF_3$, $NaMnF_3$ and $NaCoF_3$ perovskites.

$NaZnF_3$

For $NaZnF_3$, 0.39g of NaF powder was dissolved in deionised water. A 250% excess of $ZnCl_2$ was dissolved in deionised water and added gradually to the warmed NaF solution. A cloudy white precipitate formed which after filtering and drying was found using X-ray powder diffraction to be perovskite $NaZnF_3$(experiment 13, XU571).

$NaCoF_3$

A similar procedure using a solution of $CoCl_2$ produced a pink precipitate containing perovskite $NaCoF_3$ mixed with $CoF_2.4H_2O$ (experiment 25, XU707).

$NaNiF_3$

When this method was used with $NiCl_2$, the mainly amorphous products included NiO and NaF, but no perovskite $NaNiF_3$ was detected (experiments 14 and 15, XU581-585).

$NaMnF_3$

Reacting NaF with a solution of $MnCl_2$ produced a pale pink precipitate containing perovskite $NaMnF_3$(experiment 24, XU703). When this perovskite was heated and compressed to 15 GPa in a MAP, the products included MnF_2 but not post-perovskite $NaMnF_3$.(experiment 26a, XU708, XU709, XU718).

The perovskite $NaZnF_3$ and perovskite $NaCoF_3$ were not compressed and heated to produce post-perovskite because it was concluded that high-pressure synthesis starting with stoichiometric mixtures of the simple fluorides was likely to produce post-perovskites which were less contaminated by other synthesis products.

6.8.2 $NaNiF_3$ and $KCaF_3$ perovskite synthesis – piston-cylinder press

In this experiment, and in the following set of experiments, post-perovskite fluoride synthesis was attempted directly from the fluorides of their constituent cations. A stoichiometric 1:1 mixture of polycrystalline NaF and NiF_2 was ground in a dry mortar, sealed in a Pt capsule, heated to 700 °C and compressed to 2 GPa in a piston-cylinder press: products included $NaNiF_3$ perovskite but not post-perovskite (experiment 28, XU735). The same procedure using a stoichiometric 1:1 mixture of KF and CaF_2 produced a mixture of $KCaF_3$ perovskite and hexagonal K_2CaF_4, an isomorph of hexagonal Ca_2IrO_4 (experiment 30, XU748)(see Section 6.4.1).

6.8.3 Synthesis of post-perovskite $NaNiF_3$ – MAP

A stoichiometric mixture of polycrystalline NaF and NiF_2 was ground in a dry mortar, sealed in a Pt capsule, compressed to 15 GPa and heated to 700 °C for 2 hours in a MAP (experiment 26b). The major products found, identified by X-ray powder diffraction (XU714/5), were NaF, NiF_2 and post-perovskite $NaNiF_3$ (Figure 6-16). Post-perovskite $NaNiF_3$ has not been previously reported, and is described in Dobson *et al*. (2011).

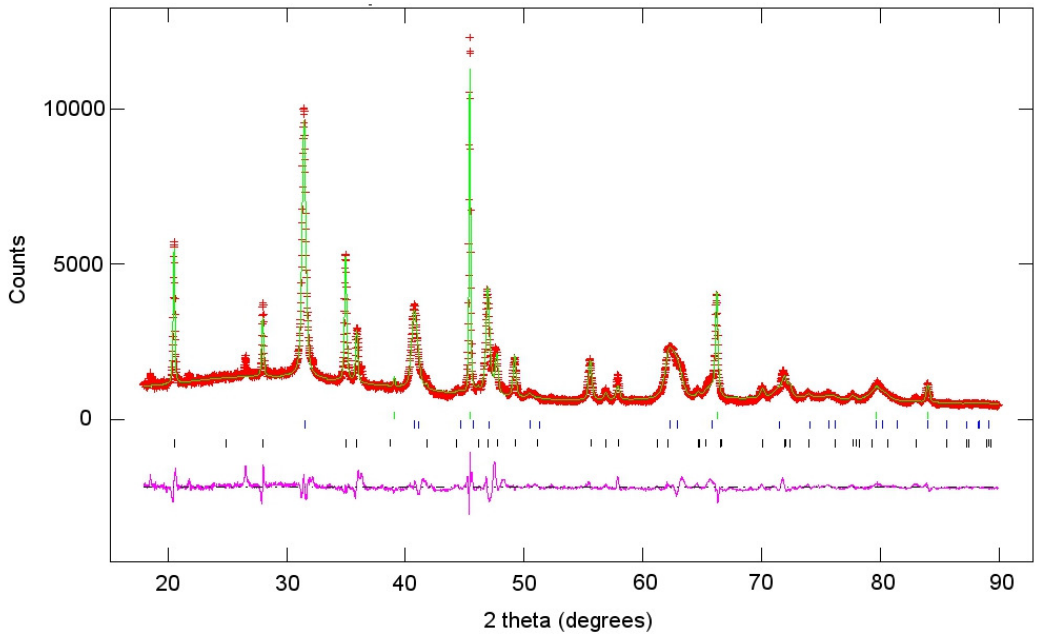

Figure 6-16: Observed (points), calculated (line) and difference (lower trace) X-ray powder diffraction patterns for Rietveld refinement of post-perovskite $NaNiF_3$. The tick marks show the positions of the Bragg reflections of (from the bottom upwards): $NaNiF_3$ post-perovskite, orthorhombic NiF_2 and NaF (villiaumite)(XU715).

Unit-cell data for this sample of post-perovskite $NaNiF_3$ obtained at ambient conditions from a Rietveld refinement using GSAS are shown in Table 6-3, together with experimental data for $NaMgF_3$ at 54 GPa (Martin *et al.*, 2006a). The experimental data for $NaZnF_3$ were measured on decompression to 2.18 GPa (Yakovlev *et al.*, 2009). It can be seen that unit-cell ratios *b*/*a* and *c*/*a* are very similar for post-perovskite $NaNiF_3$ and $NaZnF_3$. Differences in these ratios for $NaMgF_3$ at 54 GPa may be due to differences between axial compressibilities; the simulated compressibility of the $NaMgF_3$ *b*-axis is ~20% greater than that of the *a* or *c* axes (see Section 10.2).

	$NaNiF_3$[a]	$NaMgF_3$[b]	$NaZnF_3$[c]
Volume (Å^3)	224.273(17)	155.9(1)	226.71(14)
a-axis (Å)	3.0291(2)	2.7164(16)	3.0335(7)
b-axis (Å)	10.0208(6)	8.3810(5)	10.0316(34)
c-axis (Å)	7.3885(4)	6.8487(25)	7.4502(18)
b/a	3.31	3.09	3.31
c/a	2.44	2.52	2.46

Table 6-3: Post-perovskite fluoride structural data from experiment.

a – the present work (ambient pressure)(and Dobson *et al.*, 2011)

b – Martin *et al*. (2006a)(54 GPa)

c – Yakovlev *et al.* (2009)(2.18 GPa)

Since the experiments described above were carried out, post-perovskite $NaCoF_3$ has also been synthesised at or below 14 GPa at 480 ºC in the MAP at UCL by Professor D.P. Dobson (Dobson *et al.*, 2011), with a Clapeyron slope of 15.5 MPa K^{-1}.

6.9 Summary of syntheses and analyses

1. Single crystals of post-perovskite $CaIrO_3$ were synthesised by heating at 1200 °C at 1.5-2.0 GPa in a MAP and analysed by X-ray diffraction.
2. An examination of single crystals of post-perovskite $CaIrO_3$ in a scanning electron microscope showed that the longest (needle) axis of the crystals corresponded to the *a*-axis (consistent with previous work), the semi-minor pseudo-elliptical axis to the *b*-axis and the semi-major axis to the *c*-axis.
3. Polycrystalline post-perovskite $CaPtO_3$ was synthesised at 780 °C and 4 GPa in a MAP and analysed by X-ray powder diffraction. Larger volumes of polycrystalline post-perovskite $CaPtO_3$ were subsequently synthesised in a piston-cylinder press at 800 °C and 2 GPa, and in a high-capacity belt-type apparatus at 800 °C and 4 GPa. The products were analysed by X-ray diffraction, and the lattice parameters were found to be in reasonable agreement with those previously reported at ambient pressure and temperature.
4. Polycrystalline post-perovskite $CaPtO_3$ was tested for thermal dissociation by heating from 500 °C to 1000 °C in steps of 50 °C. Post-perovskite $CaPtO_3$ was found to be metastable in air for periods of less than 2 hours at 850 °C, but a later experiment (described in Section 9.2) found that dissociation occurs at lower temperatures when heated for a longer time in a sealed evacuated container.
5. Pt oxides dissociate in air at temperatures 300 – 500 °C lower than their Ir counterparts, consistent with the Pt-PtO buffer system being more oxidising than the Ir-IrO system.
6. The previously unreported post-perovskite fluoride $NaNiF_3$ was synthesised at 700 °C and 15 GPa in a MAP and analysed by X-ray powder diffraction. Its unit-cell ratios *b*/*a* and *c*/*a* are very similar to those reported for post-perovskite $NaZnF_3$.

7 Studying post-perovskite by X-ray and neutron diffraction

This Chapter describes the X-ray and neutron diffraction facilities which I used in the present work, and the relative advantages and disadvantages of X-ray diffraction compared with neutron diffraction for the post-perovskite oxides $CaPtO_3$ and $CaIrO_3$ whose synthesis has been described in Chapter 6. This Chapter also describes the effect of diffuse scattering on crystal structure measurements in high-temperature diffraction studies, and my use of Rietveld and LeBail refinement of diffraction results.

7.1 X-ray and neutron diffraction facilities

Two types of X-ray powder diffraction were used in the present work. The PANalytical X'Pert Pro diffractometer at UCL is equipped with a Ge(111) incident-beam monochromator and uses Co $K\alpha_1$ radiation with a wavelength of 1.78965 Å (40 kV, 30 mA). Samples analysed at ambient temperature were prepared as a thin deposit on an "off-axis" silicon plate (*i.e.* one cut so as to produce no Bragg reflections) or on a glass microscope cover slip. High-temperature studies were made using an Anton Paar HTK1200N sample stage. Samples of post-perovskite $CaPtO_3$ were sprinkled on top of a cake of MgO powder for high-temperature analysis so as to reduce the amount of material required and prevent contamination of the alumina sample holder for the high-temperature stage. Data analysis was carried out with X'Pert Pro HighScore Plus software for search/matching against the ICDD database, and with the GSAS (Larson and Von Dreele, 1994) and EXPGUI (Toby, 2001) suite of programs.

The high-pressure X-ray diffraction study of post-perovskite $CaPtO_3$ described in Chapter 8 used beamline ID09 at the European Synchrotron Research Facility (ESRF), Grenoble. I am indebted to Dr. W. Crichton at ESRF for his assistance with this experiment.

The neutron powder diffraction studies of $CaPtO_3$ (see Chapter 9) were carried out at two instruments at the ISIS neutron source, STFC Rutherford Appleton Laboratory, U.K. The PEARL Beamline high-pressure facility, HiPr (ISIS Annual Report, 1996) is a medium-resolution, high-flux diffractometer which is optimized for data collection from a Paris–Edinburgh press with opposed anvils. The main transverse detector bank

is made up of 9 detector modules, covering the scattering angle interval $83^o < 2\theta < 97^o$, which typically yield diffraction patterns over the *d*-spacing range ~0.5 < *d* < 4.1 Å at a resolution of $\Delta d/d \approx 0.8\%$. The low-*T* and high-*T* (ambient *P*) studies were both made using the high-resolution powder diffractometer (HRPD) (Ibberson *et al.*, 1992), using the $2\theta = 168^o$ (backscattering) detector bank, with $\Delta d/d \approx 4 \times 10^{-4}$ and a *d*-spacing range of 0.6 – 2.6 Å (see Chapter 9.2). My thanks are due to Dr. M. Tucker (PEARL) and Dr. K. Knight (HRPD) at ISIS for their assistance with several experiments.

7.2 X-ray and neutron scattering and absorption

7.2.1 X-ray scattering and absorption

X-rays are diffracted by the electrons surrounding an atom's nucleus, and so an atom scatters X-rays in proportion to the number of electrons in that atom. The degree of scattering by the (fewer) electrons of an atom with a smaller atomic number decreases faster with increasing $\sin(\theta)/\lambda$ (where 2θ is the angle of diffraction) than that of a (heavier) atom with a larger atomic number; the scattering factor for the heavier atom with a denser, more concentrated electron cloud decreases more slowly as $\sin(\theta)/\lambda$ increases, since a smaller atom will have a smaller path difference within it for any given value of $\sin(\theta)/\lambda$. So the scattering from the heavier atoms in a material containing a mixture of lighter and heavier atoms will tend to dominate the signal from lighter atoms in the diffraction pattern, especially at short d-spacings. This is very disadvantageous for structural studies of post-perovskite analogues such as $CaIrO_3$ and $CaPtO_3$ which contain the heavy transition elements Ir and Pt, because establishing the positions of the O atoms accurately becomes very difficult.

The linear X-ray absorption coefficient μ of a material can be determined from the sum over all elements of the products of the mass attenuation coefficient (μ/ρ) and the mass fraction g_i of each element in the material, multiplied by the density of the material (ρ) such that:

$$\mu = \rho \sum_i \left(\frac{\mu}{\rho}\right)_i g_i \qquad (7.1)$$

The attenuation of the X-ray beam is then given by:

$$\frac{I}{I_0} = exp[-\mu x] \tag{7.2}$$

where I_o is the incident intensity, x is the thickness of the material, and the intensity after attenuation is I. Mass attenuation coefficients vary with X-radiation energy (and hence wavelength) and by element. So the absorption coefficient μ is 1925 cm^{-1} for post-perovskite $CaIrO_3$ with Co $K\alpha_1$ radiation and 610 cm^{-1} with Mo $K\alpha$ radiation. Post-perovskite $CaPtO_3$ has a μ of 2003 cm^{-1} for Co $K\alpha_1$ radiation.

These very high absorption coefficients mean that X-rays are strongly attenuated by these materials. This greatly hinders single-crystal X-ray diffraction studies of $CaIrO_3$ and $CaPtO_3$, especially since the crystals are typically needle-shaped (Sugahara *et al.*, 2008); the *a*-axis of a single crystal is significantly longer, which leads to much greater attenuation of X-rays travelling parallel to that direction. This will adversely affect the refinement of structural parameters, especially atomic displacement factors. X-ray diffraction analysis of single-crystal $CaIrO_3$ by Hirai *et al.* (2009) included refinement of structure and atomic displacement factors from crystals (assumed to be cylindrical) which were 20-25 times as long as they were broad (205 or 250 x 10 x 10 microns). The relative transmission factor is proportional to $e^{(-(length-breadth)\,x\,\mu)}$, where length and breadth refer to the relevant proportions of the single crystal. The attenuation of the transmitted beam of Mo $K\alpha$ X-rays in the analysis of Hirai *et al.* varied between the *a*-axis and other axes by factors of 6.8 x 10^{-6} and 4.4 x 10^{-7} for the two crystals measured. X-ray diffraction analysis of single-crystal $CaIrO_3$ by Sugahara *et al.* (2008) included refinement of structure and atomic displacement factors from a crystal which was 10 times as long as it was broad (100 x 10 x 10 microns), with attenuation varying between the *a*-axis and other axes by 4.1 x 10^{-3}. The attenuation along the 10 micron *b* and *c*-axes of the crystals was about 0.5, so transmission could take place in these directions through the whole crystal. Transmission sub-parallel to the *a*-axis would take place in near-surface layers only, since the transmitted intensity along the long axis of the crystal would be attenuated by 2.2 x 10^{-3} (100 microns) or 2.4 x 10^{-7} (250 microns). Hirai *et al.* (2009) concluded that differences between the results of their refinements and those of Sugahara *et al.* (2008) were due to the

inadequacy of the absorption correction made in the earlier work. This example illustrates the difficulty of using X-ray diffraction for structural analysis of the post-perovskite analogues $CaIrO_3$ and $CaPtO_3$, which contain heavy transition elements with high X-ray absorption coefficients.

7.2.2 Neutron scattering and absorption

In contrast to X-rays, neutrons are scattered by atomic nuclei; the range of values for their scattering length is much smaller than the range of values for X-ray atomic scattering factors. The neutron scattering lengths do not increase with atomic number. They may however vary widely for atoms with similar atomic numbers, or even between different isotopes of the same element (see Figure 7-1).

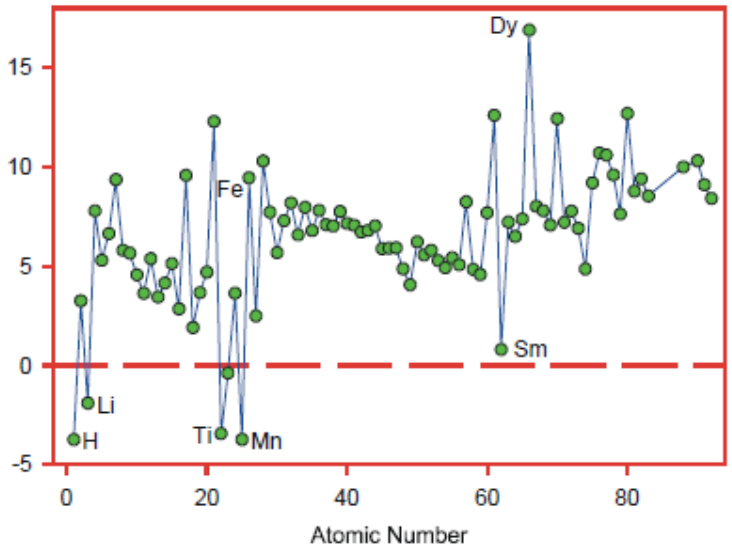

Figure 7-1: The variation in neutron scattering length with atomic number up to U (Z=92)(ISIS Neutron training course, 2010).

This means that although Ir and Pt are still strong scatterers (Table 7-1), the contribution to the neutron diffraction pattern due to lighter atoms such as O and Ca will be proportionally much greater. The scattering length will also not reduce with increasing angle of diffraction, because there is very little phase difference due to neutron scattering from different parts of the nucleus. So the neutron diffraction peaks for small *d*-spacing will be relatively stronger than those at high 2θ in an X-ray diffraction pattern, giving better information on crystal structure (Giacovazzo, 1992).

Absorption of neutrons by different elements will affect the strength of the diffraction pattern. Unfortunately the absorption of neutrons by Ir is extremely high, making $CaIrO_3$ an unsuitable compound for study by neutron diffraction (Table 7-1). It is therefore preferable to use post-perovskite $CaPtO_3$ for neutron diffraction rather than $CaIrO_3$ because Pt is far less absorbing of neutrons than Ir, although the effect is still not negligible (see Section 9.2.1).

Element	Atomic number	Bound coherent scattering length (fm) (1 fm = 10^{-15}m)	Absorption cross Section (barn) (1 barn = 100fm^2)
O	8	5.803	0.00019
Ca	20	4.70	0.43
Ir	77	10.6	425
Pt	78	9.60	10.3
F	9	5.84	0.0096
Co	27	2.49	37.18
Ni	28	10.3	4.49
Zn	30	5.68	1.11

Table 7-1: Neutron scattering lengths and absorption cross-sections (Sears, 1992)

Neutrons interact more weakly with matter than X-rays, so they penetrate further into the bulk of the material, reducing surface effects. However this means that larger volumes of sample are required, which is a disadvantage where the sample must be prepared at high-pressure in a piston cylinder or MAP. The larger volume required also limits the pressure attainable in in-situ high-pressure studies.

In time-of-flight neutron diffraction (as used in the present work), the pulsed polychromatic beam contains neutrons of a range of different wavelengths. The *d*-spacing in Ångstroms is

$$d = \frac{0.001977t}{L\,sin\,(\theta)} \tag{7.3}$$

where L is the distance in metres from the source to the sample, t is the time-of-flight in microsesonds, and 2θ is the angle between the detector and the beam (ISIS Neutron training course, 2010). In practice several banks of detectors are used, each with its

own *d*-spacing range.

Neutron diffraction using the time-of-flight method has the additional advantage that the resolution of the diffractometer is effectively constant across the whole diffraction pattern. This allows precise determination of unit-cell parameters from strong Bragg reflections at large *d*-spacings. This is therefore a better technique for this purpose than using angle-dispersive X-ray diffraction, where the high 2θ diffraction peaks needed for precise cell parameter determination are significantly reduced in intensity by thermal vibration of the atoms and the reduction in the atom's form factor.

7.3 Bragg reflections and diffuse scattering

The analysis of Bragg reflections using elastic scattering of X-rays or neutrons assumes an infinite, perfectly ordered repeating arrangement of atoms in a crystal. The effect of thermal motion of the atoms is assumed to be averaged over the whole structure. However, when imperfections in the crystal structure are correlated between the unit cells of the crystal, structured diffuse scattering takes place; the correlated imperfections alter the periodicity of the crystal lattice, and, for example, satellite diffraction spots may be produced either side of the Bragg reflections (Wood, 1977; Guinier, 1963).

Thermal motion of atoms reduces the intensity of the Bragg reflections because of the reduction in electron density (for X-rays) or the reduction in atomic density (for neutrons) at the average locations of the atoms in the crystal. This effective increase in the atomic sizes with rising temperature makes X-ray scattering from atoms fall off more rapidly with increasing $\sin(\theta)/\lambda$. The directional dependency of these effects in an anisotropic crystal lattice allows the measurement of anisotropic atomic displacements (see, for example, Table 9-8).

The thermal vibration (phonons) of the atoms in the crystal lattice is a form of crystal imperfection, but one that is periodic: the motion of atoms in adjacent unit cells is correlated. Phonons produce relatively weak sets of satellite diffraction spots either side of the sharper Bragg reflections, so that the Bragg reflections are surrounded by more diffuse intensity; the energy and wavelength of phonons in a crystal can be measured using the inelastic scattering of neutrons. The perturbation in the structure

factor of a crystal lattice caused by perturbations from the average unit cell, of which this periodic motion is an example, can be described as (Wood, 1977; Guinier, 1963):

$$F_n = \overline{F} + \varphi_n \tag{7.4}$$

where φ_n is the perturbation in the structure factor F_n of the nth cell, and the mean structure factor $\overline{F} = I/N \sum F_n$ where I is the intensity of the diffraction and N is the number of cells. Then the scattering power of the crystal is:

$$I_n(\boldsymbol{s}) = \sum_n \sum_{n'} F_n F_{n'}^* exp[-2\pi i \boldsymbol{s_0}.(\boldsymbol{x_n} - \boldsymbol{x_{n'}})] \tag{7.5}$$

where $\boldsymbol{x_n}$ is the position vector of the nth cell. Equation 7.5 can be reduced to:

$$I(\boldsymbol{s}) = \sum_m \left|\overline{F}\right|^2 \exp(2\pi i \boldsymbol{s}.\boldsymbol{x_m}) + \sum_m \overline{\varphi_n \varphi_{n+m}^*} \exp(2\pi i \boldsymbol{s}.\boldsymbol{x_m}) \tag{7.6}$$

Bragg scattering *Diffuse scattering*

The first term in Equation 7.6 is the same as that obtained from a perfect crystal in which all unit cells have the average structure; this describes Bragg reflections from the average ideal lattice. Rietveld refinement of structural models based on diffraction data use intensity only from the first term, establishing average atomic positions and interatomic distances.

The second term in Equation 7.6 is the diffuse scattering, not located at the Bragg maxima. The second term contains information on instantaneous atomic positions and interatomic distances. The coefficients $\overline{\varphi_n \varphi_{n+m}^*}$ depend on the correlations between the fluctuations of the structure factor between pairs of cells separated by a given vector. The pair-distribution function approach was used by Martin (2008) to study this effect by examining changes in the structure of post-perovskite $CaIrO_3$ as a result of heating from 325 K to 1114 K; this study found that the average long-range structure visible in Rietveld refinement was distinct from the short-range structure (≤ 18 Å). This is discussed in relation to experimental measurement of $CaPtO_3$ post-

perovskite in Section 9.4.4. An advantage of MD simulation is that it estimates instantaneous atomic positions and interatomic distances, from which averages can be derived, as described for the post-perovskites $MgSiO_3$, $CaPtO_3$ and $CaIrO_3$ in Section 4.3 and for $NaMgF_3$ perovskite in Street *et al.* (1997).

7.4 X-ray and neutron diffraction analysis

I analysed X-ray and neutron diffraction patterns using the GSAS suite of programs with the EXPGUI graphical interface. These analyses are presented in Chapters 8 (ESRF experiment), 9.1 (PEARL experiment) and 9.2 (HRPD experiment).

7.5 Rietveld and LeBail refinement

Rietveld refinement uses a least-squares based minimization algorithm to obtain the best fit between a structural model and a powder pattern (Young, 1995). The model is refined by fitting unit-cell parameters, atomic positions, occupancies, displacement parameters, background, peak shapes, phase fractions, absorption and preferred orientation. Estimates for intensities can be made from the model even when reflections are completely overlapped. I used Rietveld refinement for structural analysis of neutron diffraction experiments so that changes in the post-perovskite $CaPtO_3$ structure at high-temperature and high-pressure could be determined (see Chapter 9).

The Le Bail refinement method (Le Bail *et al.*, 1988) estimates reflection intensities without a structural model. Using the equally-weighted method, all calculated reflection intensities are initially set equal to each other and are then freely refined so as to give the best fit to the diffraction pattern (effectively ignoring the crystal structure). The Fcalc (weighted) Le Bail method uses intensities calculated from the crystal structure as the initial model. The Le Bail method can be used to refine unit-cell parameters, background and peak shapes to produce optimal peak intensities. LeBail refinement converges more slowly than Rietveld refinement, but its unit-cell values are not influenced by preferred orientation or by other defects in the intensity calculation. I used LeBail refinement for analysis of the X-ray synchrotron high-pressure experiment, which was expected to provide accurate measurements of the unit-cell parameters of post-perovskite $CaPtO_3$ (see Chapter 8). However this method did not provide accurate atomic structure, as described in Section 7.2.1.

8 An X-ray powder diffraction study of $CaPtO_3$ at high-pressure

8.1 Introduction

In this Chapter I describe measurements of the unit-cell volume and unit-cell parameters (but not the atomic coordinates) of $CaPtO_3$ to 40 GPa using X-ray synchrotron radiation at the European Synchrotron Radiation Facility (ESRF), in order to determine its equation of state and to assess the similarity of its behaviour under compression to that of $CaIrO_3$ and $MgSiO_3$. I chose $CaPtO_3$ for this experiment because I expected it to be a better analogue of $MgSiO_3$ than $CaIrO_3$, as described in Section 6.1. Most of the work described in this Chapter was published as Lindsay-Scott *et al.* (2010). $CaPtO_3$ had previously been studied only at ambient pressure and temperature (Ohgushi *et al.*, 2008; Inaguma *et al.*, 2008). Boffa Ballaran *et al.* (2007) and Martin *et al.* (2007a) measured the bulk and axial incompressibilities of $CaIrO_3$, and very recently Liu *et al.* (2011) measured its bulk incompressibility and the temperature derivative of this incompressibility.

8.2 Experimental method

The synthesis and characterisation of the post-perovskite $CaPtO_3$ used in this experiment is described in Section 6.5.3.

A selected portion of the sample was loaded, with a helium pressure medium, into a 150 μm diameter hole in a 40 μm thick steel gasket mounted between two opposed 300 μm diamond culets of a Boehler-Almax-type membrane-driven diamond-anvil cell (DAC) (Figure 8-1a and Figure 8-1d).

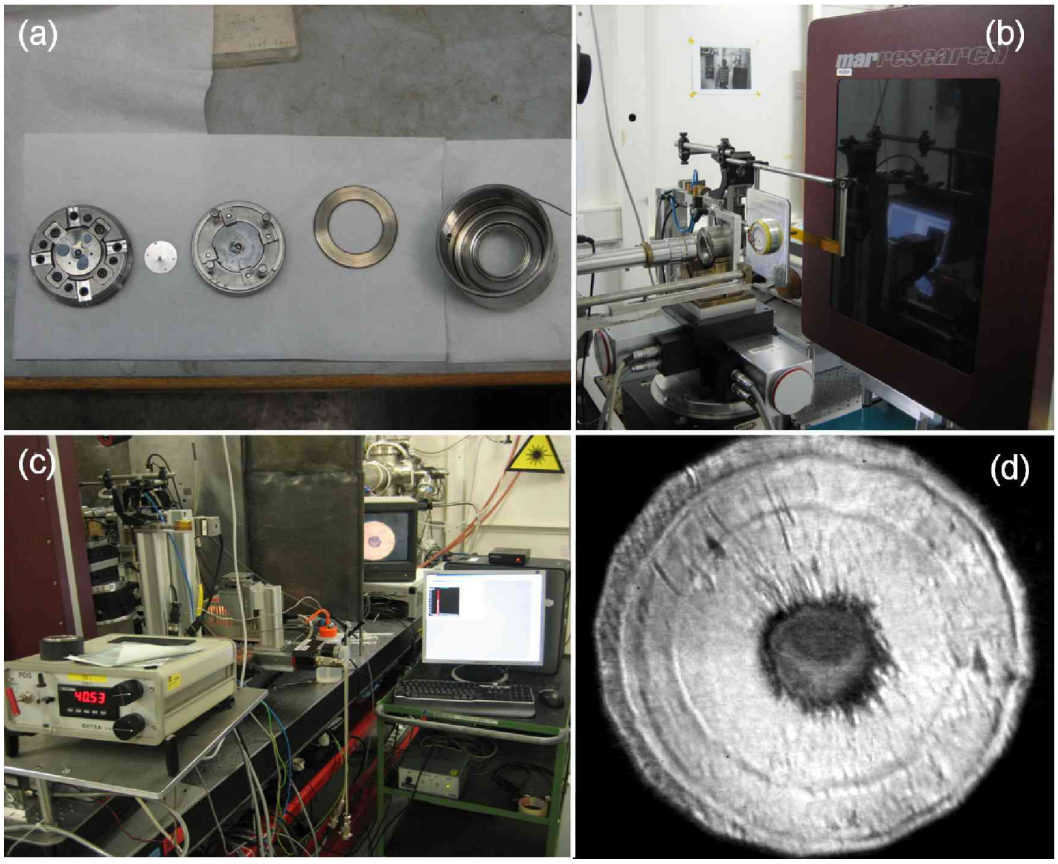

Figure 8-1: Experimental configuration (a) DAC assembly components (b) DAC mounted with imaging plate (c) Helium pressure controller and ruby fluorescence monitor (d) image of gasket and sample at high-pressure.

The general principles of the DAC are shown in Figure 8-2. Diffraction patterns were collected in a DAC on the ID09 beamline at the ESRF, using a monochromatic wavelength of 0.41456 Å on a mar555 image plate detector (Figure 8-1b and Figure 8-1c).

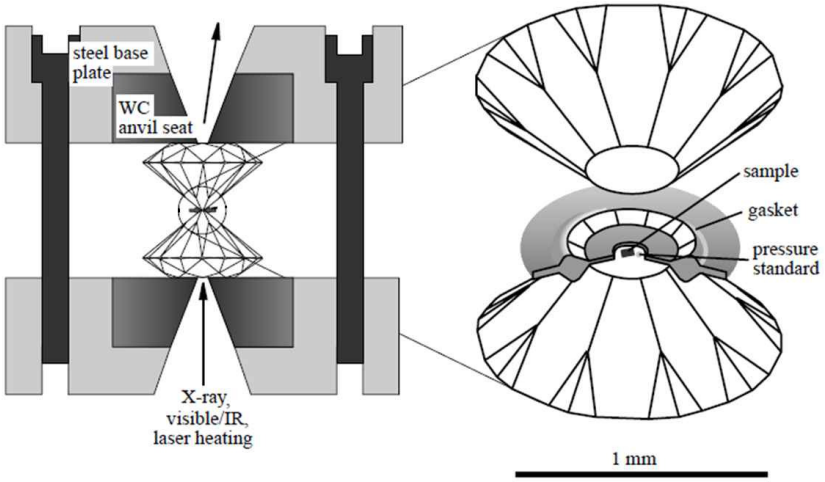

Figure 8-2: DAC with X-ray powder diffraction. Force is applied to the back of the diamonds by tightening the screws connecting the base plates. The diamonds compress the small sample volume between their tips and the metal gasket, shown in the enlargement. The sample and a pressure standard are surrounded by a soft pressure medium and experience nearly perfect hydrostatic pressure (diagram from Vočadlo and Dobson, 1999).

The detector was positioned at 358.71 mm from the sample, so as to cover a range $0^{o} < 2\theta < 37.9^{o}$; the exposure time was ~ 1 second. Data were collected with increasing pressure from 2.90(2) GPa to 42.50(4) GPa, with a final pattern recorded at 1.21(1) GPa after decompression. The 2θ *vs* Intensity patterns used in the powder refinement were obtained by integrating around the Debye-Scherrer rings, after correction for detector distortion and tilt, using the Fit2D package (Hammersley *et al.*, 1995).

The pressure values in Table 8-1 for each data collection point were obtained from the relative shift of the wavelength of the ruby-R_1 fluorescence line ($\Delta\lambda/\lambda_0$), using the equation P (GPa) = $(A/B)\{[1 + (\Delta\lambda/\lambda_0)]^B - 1\}$, where A = 1904 GPa and B = 10.32(7), from the pressure-scale calibration of Jacobsen *et al.* (2008) for helium pressure media. The choice of pressure scale is discussed in Section 8.2.1. Ruby measurements were made before (λ_a) and after (λ_b) each diffraction pattern was recorded and the value of $\Delta\lambda$ was then calculated using their mean. The uncertainties in the pressure values, due to relaxation of the cell during the collection of each diffraction pattern, were derived assuming that the uncertainty in the fluorescence wavelength was $(\lambda_a - \lambda_b)/4$ (*i.e.* that the observations corresponded to a mean value +/- two standard uncertainties). The

uncertainty in the parameter *B* given by Jacobsen *et al.* (2008) was also included in the calculation. It should, in principle, have been possible also to use the platinum present in the sample as an internal standard, but in practice there was insufficient platinum present to allow this to be done reliably in any of the experiments.

8.2.1 Choice of pressure scale

The ESRF ruby fluorescence monitor used during the experiment reported pressure using the pressure scale of Mao *et al.* (1978). Recording the ruby fluorescence wavelength before and after each pressure reading enabled the pressure for each data point to be calculated from the wavelength shift using not only the Jacobsen *et al.* (2008) pressure scale that was finally adopted, but also other pressure scales. Figure 8-3 shows the pressure for each data point calculated using 5 published pressure scales. The relative values of the pressures as calculated from the different pressure scales were consistent with those compared in Jacobsen *et al.* (2008). Piermarini *et al.* (1975) and Mao *et al.* (1978) used a methanol-ethanol pressure medium, which becomes non-hydrostatic above ~9.8 GPa (Angel *et al.*, 2007). Mao *et al.* (1986) used quasi-hydrostatic conditions with an argon pressure medium. Dewaele *et al.* (2004) and Jacobsen *et al.* (2008) used helium as a pressure medium. The Jacobsen *et al.* (2008) pressure scale re-calibrated the ruby-pressure gauge for helium-loaded DACs against MgO, taking account of the softer helium pressure medium, and this scale was selected as being the most suitable for use in the present work.

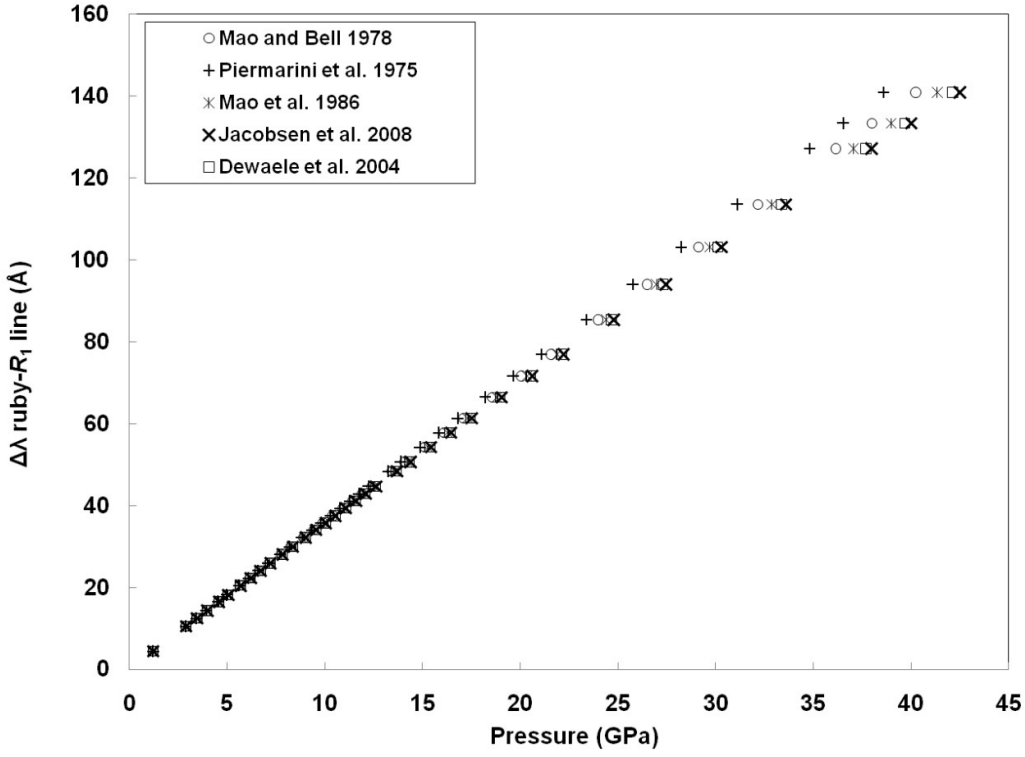

Figure 8-3: Experimental pressures calculated using different ruby-R_1 pressure calibration scales.

8.2.2 Details of the refinement process

The diffraction patterns were fitted, over the range $3.16^{o} < 2\theta < 33.2^{o}$, to obtain unit-cell parameters using the Le Bail method (Le Bail *et al.*, 1988) implemented in the GSAS suite of programs (Larson and Von Dreele, 1994) with the EXPGUI graphical interface (Toby, 2001). However, it should be noted that in both Table 6-1 and Table 8-1 the resulting unit-cell parameter values listed are probably less accurate than might be expected from the stated uncertainties, which are as reported by the Le Bail fits using GSAS; for further discussion of the importance of systematic errors in profile refinement of X-ray powder data see e.g. Thompson and Wood (1983).

The Fit2D .chi output files specified a 2θ measurement interval of 0.0188 degrees. However, GSAS .RAW files only allow intervals in degrees specified to 3 decimal places. The Fit2D .chi files were therefore converted to a fixed-format ASCII file acceptable to the PANalytical X'Pert Pro HighScore analysis program using a FORTRAN program CHIASC which I wrote. I then used the PANalytical X'Pert HighScore Plus software to convert this data to GSAS .raw format; this software interpolated the data points to adjust them from 2θ measurement intervals of 0.0188 to intervals of 0.019 degrees, using the maximum three decimal places acceptable to GSAS.

I used LeBail refinement to analyse these high-pressure data from the ESRF because the objective was to determine the unit-cell parameters, not the crystal structure (atomic coordinates). It was anticipated that atomic positions of O atoms could not be reliably determined because of the dominant X-ray scattering from the Pt atoms. In fact Rietveld analysis of a few pressure points found that the atomic coordinates had significantly different values from those from the high-pressure neutron diffraction experiment at ISIS (Section 9.1). The percentage changes in atomic coordinates with increasing pressure were much larger than in the ISIS experiment.

The lineshape used in the GSAS refinements was "profile function number 2", which is based on a pseudo-Voigt function (Larson and von Dreele, 1994). The phases included in the refinement were post-perovskite $CaPtO_3$, $CaPt_3O_4$ and Pt. At pressures above 12.6 GPa diffraction peaks characteristic of hexagonal ($P6_3/mmc$) He crystals were observed (Mao *et al.*, 1988) and so this phase was also included. Examples of the

fitted diffraction patterns at 2.90(2) GPa and 42.50(4) GPa are shown in Figure 8-4. Typical values of χ^2, R_p and R_{wp} were 15.56, 0.0052 and .0092 respectively at 2.90(2) GPa and 54.55, 0.0103 and 0.0170 at 42.50(4) GPa.

As mentioned earlier, Pt in the small quantity present in the sample proved to be unsuitable as a pressure calibrant. It overestimated pressure compared with the ruby calibrant.

Some Pt peaks had their intensities smeared out by LeBail refinement so that the calculated peak had a much lower intensity compared with the observed peak. It transpired that this was not due to over-large values for the profile parameters GU GV GW LX LY, although these may have been a consequence of the problem. It seemed rather to be due to a mismatch of the (automatically refined) background, as shown by non-matching of the background at the highest 2θ angles. When LeBail refinement calculates a zero intensity for a peak, subsequent refinements are not able to recover from this position, which is a drawback of the method (Toby, 2006). The solution was to use model (or F-calc) weighted (rather than equally weighted) LeBail refinement and to use a graphically-fitted background, different for each pressure point, which was then not refined. Following the procedure proposed by Toby (2006), the LeBail refinements were carried out with 0 cycles several times while the χ^2 value converged and the intensities were fitted, before the number of refinement cycles was increased and the cell parameters were allowed to vary.

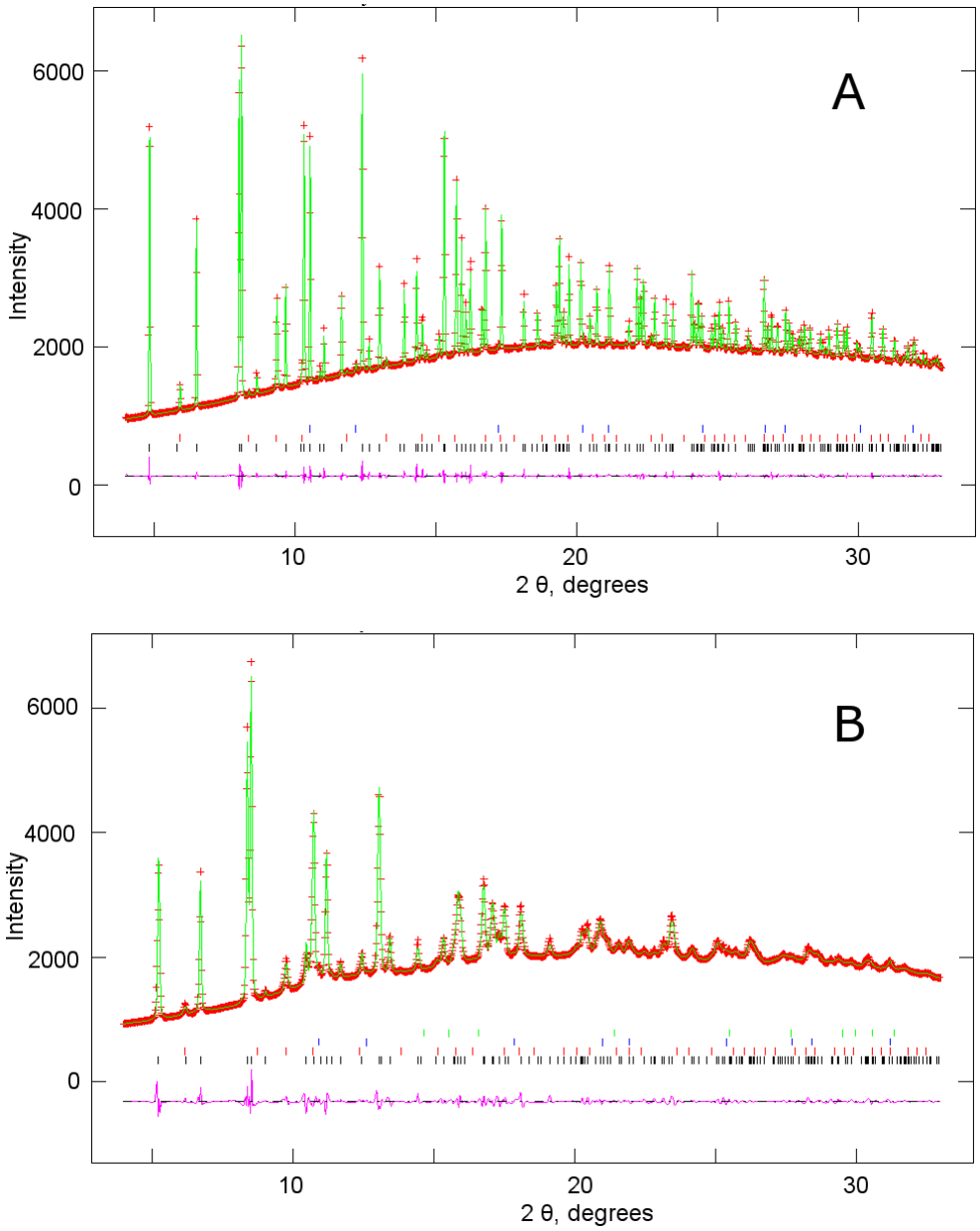

Figure 8-4: Observed (points), calculated (line) and difference (lower trace) X-ray powder diffraction patterns (λ = 0.41456 Å) for $CaPtO_3$ at: (A) 2.90(2) GPa and (B) 42.50(4) GPa. The tick marks show the positions of the Bragg reflections of (from the bottom upwards): $CaPtO_3$, $CaPt_3O_4$, Pt and (Figure 8-4 (B) only) He.

It can be seen that the Bragg reflections in Figure 8-4 (B) are broader, due to the development of non-hydrostatic stresses; after decompressing the sample, the widths of the reflections returned to their original low-pressure values. Figure 8-5 shows the X-

ray powder diffraction line broadening in more detail at successively higher pressures for part of the 2θ range.

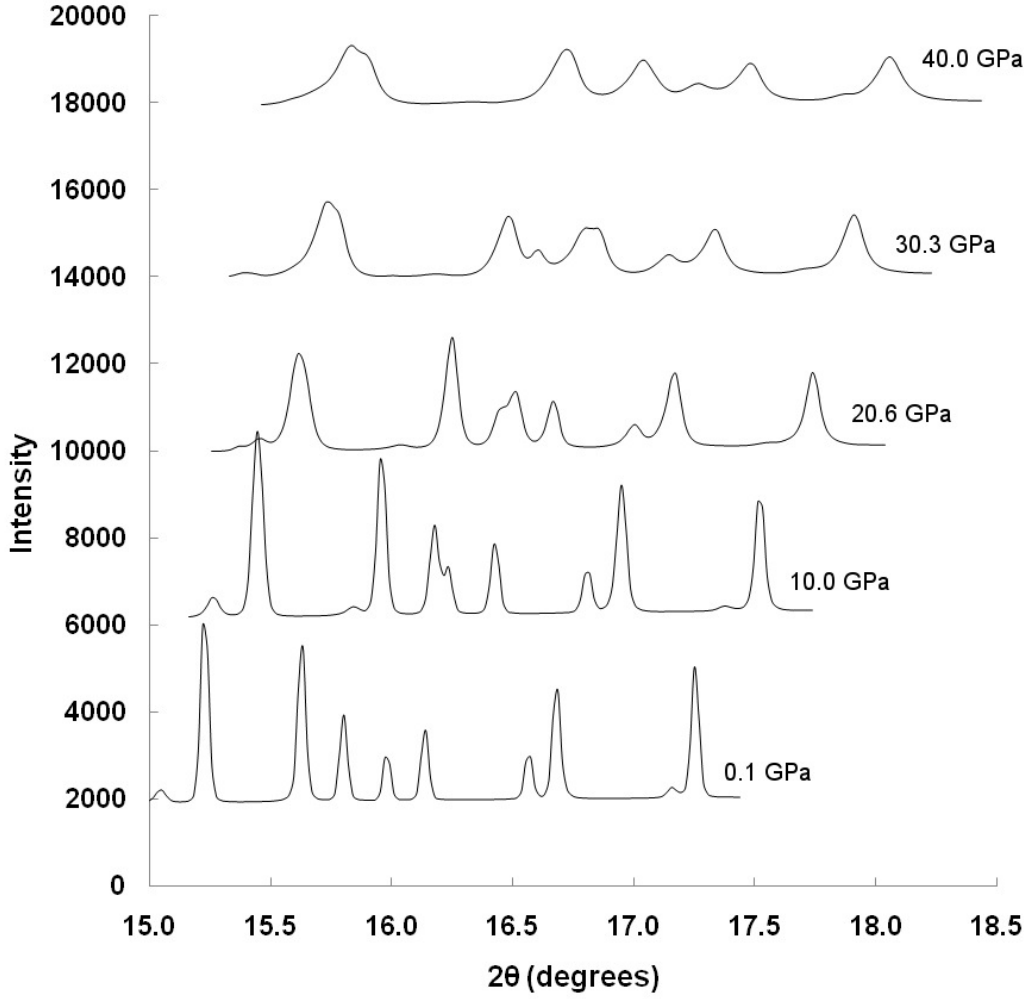

Figure 8-5: Sample X-ray powder diffraction observed line broadening for $CaPtO_3$ compression. The intensity of each set of data after the first one is offset by an additional intensity of 4000.

The onset of this line broadening is clearly indicated in the refined values of the GSAS profile parameters; these are effectively invariant until ~16 GPa, but at higher pressures the values of some of the profile coefficients alter systematically. In particular, the coefficient *U* (which affects the Gaussian variance of the Bragg peaks via a term in $Utan^2(\theta)$; Caglioti *et al.*, 1958) increases (see Figure 8-6) with the

increase becoming marked above ~22 GPa, an effect that can be attributed to non-uniform strain in the crystallites (Larson and von Dreele, 1994).

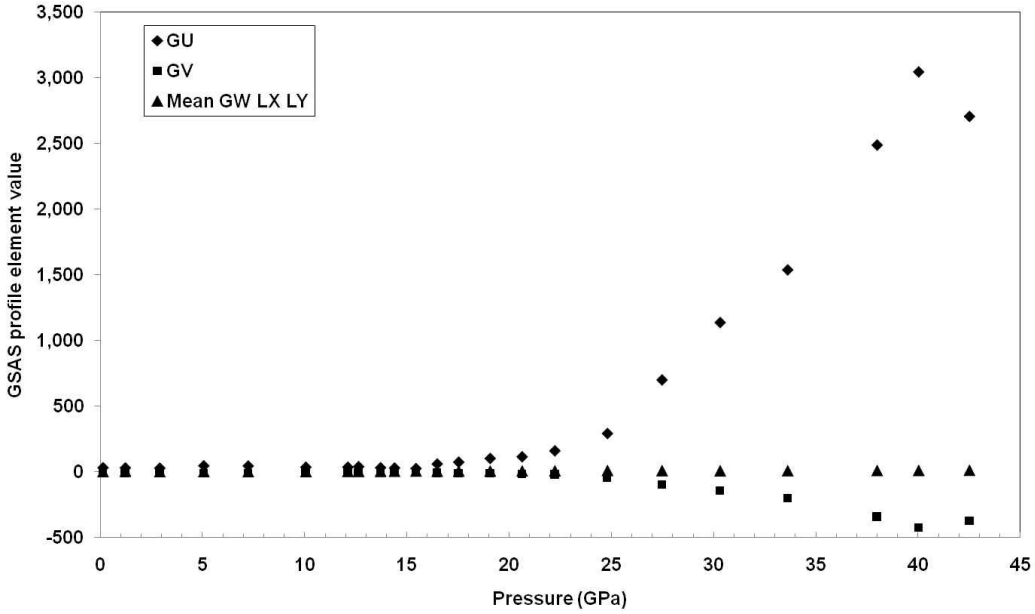

Figure 8-6: GSAS profile parameters. GU – U coefficient. GV – V coefficient. Mean GW LX LY – mean value of W, X and Y coefficients. These data points overlap so their mean is plotted instead.

Possible sources of non-hydrostatic stresses in the experiment are solidification of the helium pressure medium and grain-grain interactions in the $CaPtO_3$ sample. This line broadening does not appear to lead to any systematic errors in the refined values of the cell parameters (see Figure 8-7 and Figure 8-8), but it does increase their estimated uncertainties, which are greater by about a factor of seven at ~40 GPa than at pressures below ~7 GPa (Table 8-1).

8.3 Results

The observed unit-cell volume and unit-cell parameters of $CaPtO_3$ between 1.21 GPa and 42.50 GPa are listed in Table 8-1 and plotted in Figure 8-7 and Figure 8-8.

P (GPa)	a(Å)	b(Å)	c(Å)	Volume (Å^3)
2.90(2)	3.11291(2)	9.84590(9)	7.32129(6)	224.393(4)
3.45(1)	3.11050(2)	9.83073(9)	7.31545(6)	223.695(4)
3.98(1)	3.10794(2)	9.81702(9)	7.31008(6)	223.036(4)
4.59(1)	3.10502(2)	9.80079(7)	7.30368(5)	222.263(2)
5.05(3)	3.10275(2)	9.78895(9)	7.29884(6)	221.685(4)
5.69(2)	3.09984(2)	9.77312(9)	7.29270(6)	220.933(4)
6.20(2)	3.09763(2)	9.76146(9)	7.28801(6)	220.370(4)
6.71(2)	3.09572(2)	9.75077(9)	7.28391(6)	219.869(4)
7.22(2)	3.09357(3)	9.73904(10)	7.27951(7)	219.320(4)
7.84(1)	3.09084(3)	9.72520(10)	7.27384(6)	218.645(4)
8.37(2)	3.08839(3)	9.71204(11)	7.26870(7)	218.021(5)
9.02(2)	3.08566(3)	9.69559(11)	7.26296(7)	217.288(5)
9.55(3)	3.08358(3)	9.68384(10)	7.25855(7)	216.747(5)
10.04(2)	3.08195(3)	9.67358(10)	7.25490(7)	216.290(4)
10.55(3)	3.08001(3)	9.66289(10)	7.25109(7)	215.805(4)
11.08(3)	3.07811(3)	9.65200(11)	7.24707(7)	215.310(5)
11.59(3)	3.07627(3)	9.64136(11)	7.24333(7)	214.833(5)
12.10(2)	3.07409(3)	9.62936(12)	7.23903(8)	214.287(5)
12.62(3)	3.07204(3)	9.61759(12)	7.23493(8)	213.761(5)
13.70(5)	3.06793(4)	9.59463(13)	7.22645(9)	212.715(6)
14.38(2)	3.06576(4)	9.58160(13)	7.22187(9)	212.142(6)
15.43(3)	3.06221(4)	9.56182(16)	7.21496(11)	211.256(7)
16.46(2)	3.05840(4)	9.54021(15)	7.20764(11)	210.303(7)
17.52(3)	3.05471(5)	9.51746(18)	7.20009(12)	209.329(8)
19.06(4)	3.04976(6)	9.48918(22)	7.19095(15)	208.104(10)
20.62(3)	3.04465(6)	9.45945(23)	7.18141(15)	206.830(10)
22.22(4)	3.03963(7)	9.42972(28)	7.17183(18)	205.565(12)
24.79(2)	3.03231(9)	9.38640(37)	7.15781(25)	203.729(17)
27.46(2)	3.02459(11)	9.33593(40)	7.14297(30)	201.699(19)
30.30(2)	3.01617(13)	9.28288(52)	7.12716(33)	199.551(23)
33.61(4)	3.00811(14)	9.22671(55)	7.11284(37)	197.416(26)
37.98(5)	2.99721(16)	9.15550(64)	7.09562(42)	194.710(29)
40.02(3)	2.99209(16)	9.11863(64)	7.08734(43)	193.369(29)
42.50(4)	2.98668(15)	9.08541(61)	7.07981(42)	192.112(28)
1.21(1)	3.12155(4)	9.88679(14)	7.33933(9)	226.507(6)

Table 8-1: Unit-cell parameters and unit-cell volume for $CaPtO_3$ as a function of pressure. The data were recorded in the order shown. The numbers in parentheses are estimated standard uncertainties and refer to the least-significant digits.

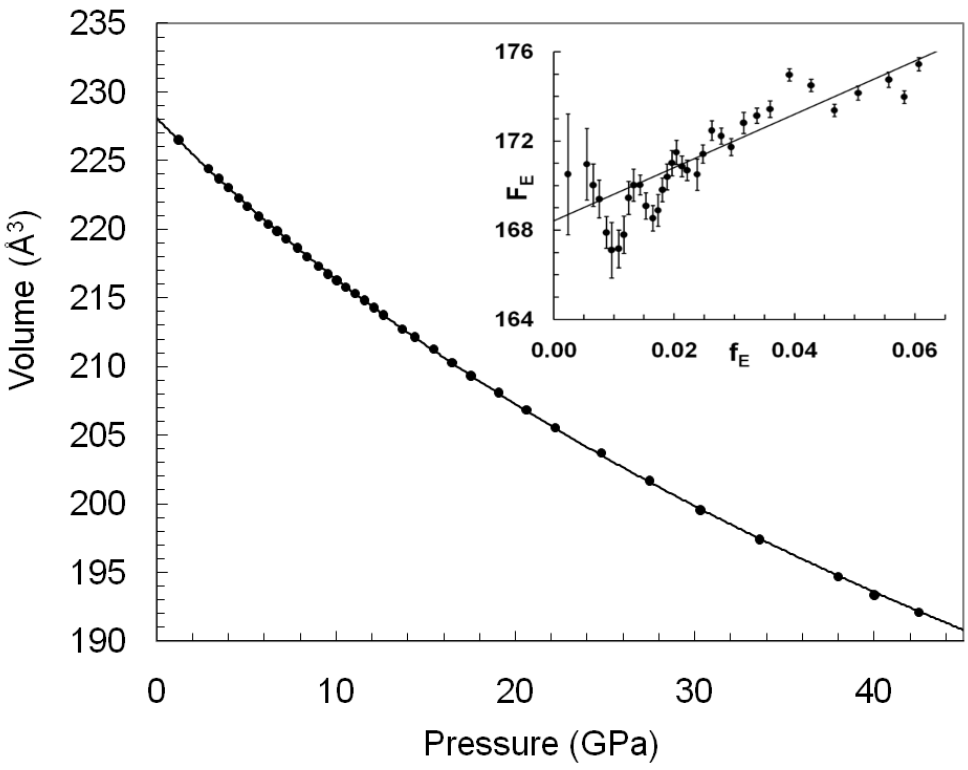

Figure 8-7: Unit-cell volume of $CaPtO_3$ between 1.21(1) GPa and 42.50(4) GPa. Experimental values are shown as points (error bars are smaller than the symbols used). The full line in this Figure and in Figure 8-8 and Figure 8-9 shows the fit of the data to a third-order Birch-Murnaghan EOS calculated using a program BM3BIS, which I wrote, based on a bisection root-finding algorithm. The inset shows the *f-F* plot for these data (see below in this Section), calculated using the value of V_0, 228.10(2) Å^3, from this fit (Table 8-2). The solid line shown in the inset is a weighted linear fit with $F_E = 120(11)f_E + 168.4(4)$ GPa. The value of the incompressibility, K_0, is equal to the intercept on the *y*-axis of the *f-F* plot; the value of its first derivative with respect to pressure, K'_0, is obtained *via* the relationship that the slope of the *f-F* plot is equal to $3K_0(K'_0 - 4)/2$ (Angel, 2000).

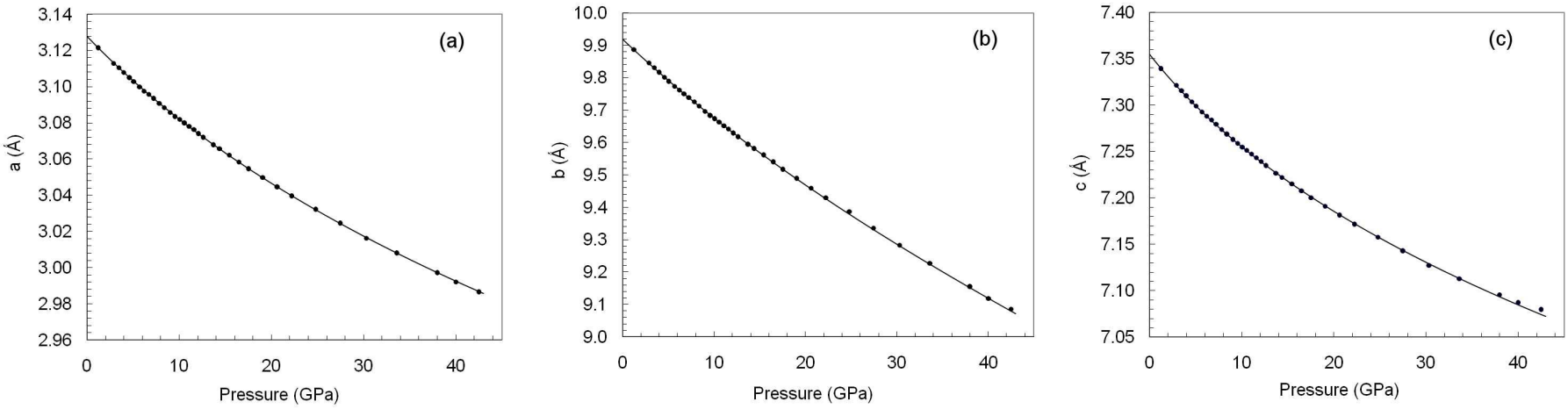

Figure 8-8: Variation of unit-cell parameters of $CaPtO_3$ with pressure. Experimental values are shown as points (error bars are smaller than the symbols used). Each full line shows the fit of the data to an axial EOS.

The data, including the decompression data point, both for the unit-cell volume and for the cubes of the unit-cell axes, were fitted to third-order Birch-Murnaghan equations of state (Birch, 1978) by non-linear least-squares using the EOS-fit program (Angel, 2000, 2001); the weighting scheme in the refinement used weights calculated from the errors in both the pressure and in the unit-cell volume and lattice parameters.

The resulting values of the three EOS parameters for each of the four fits using third-order Birch-Murnaghan equations of state are listed in Table 8-2. For the unit-cell axes, the values of K_0 and K'_0 are those obtained by fitting to the cubes of the lengths of the unit-cell axes. For comparison with the results of Martin *et al.* (2007a) the unit-cell volumes were also fitted to a second-order Birch-Murnaghan EOS. The resulting values of V_0 and K_0 were 227.95(2) Å^3 and 174.0(5) GPa respectively (with K'_0 fixed at 4).

	V_0	K_0 (GPa)	K'_0
Volume	228.10(2) Å^3	168.2(8)	4.51(6)
	a_0		
a-axis	3.12777(8) Å	195.7(8)	6.63(8)
	b_0		
b-axis	9.9191(5) Å	123.3(5)	2.37(3)
	c_0		
c-axis	7.3551(4) Å	192(2)	12.2(3)

Table 8-2: EOS parameters obtained by fitting the data shown in Table 8-1 to third-order Birch-Murnaghan equations of state.

If the ruby fluorescence pressure scale of Mao *et al.* (1986) is used instead of that of Jacobsen *et al.* (2008), the volumetric EOS parameters then become V_0 = 228.09(2) Å^3, K_0 = 168.8(8) GPa and K'_0 = 4.16(6) respectively. The more recent ruby scale of Dewaele *et al.* (2004), gives values that are not significantly different from those shown in Table 8-2, with V_0 = 228.10(2) Å^3, K_0 = 168.5(8) GPa and K'_0 = 4.39(6). The scale of Piermarini *et al.* (1975) gave the lowest pressures (see Figure 8-3).

The values of V_0, a_0, b_0, and c_0 in Table 8-2 are consistent both with the lattice parameters of $CaPtO_3$ from previous powder diffraction studies at ambient pressure (Ohgushi *et al.*, 2008; Inaguma *et al.*, 2008) and with those obtained in the present work during the sample characterisation (Table 6-1). There is, however, clearly a slight systematic offset between the two diffraction experiments as all of the values from this high-pressure study are slightly higher, by 0.1% for the unit-cell volume and 0.02 – 0.07 % for the unit-cell edges.

The good internal consistency of the high-pressure data sets can be demonstrated in two ways. Firstly, the values from the non-linear least-squares fit of the volumetric incompressibility (K_0) and of its first derivative with respect to pressure (K'_0) of 168.2(8) GPa and 4.51(6), respectively, are in good agreement with the corresponding values of 168.4(4) GPa and 4.47(4) obtained by weighted linear regression from the *f-F* plot (see e.g. Angel, 2000) shown as an inset in Figure 8-7. In this method of analysis, the incompressibility at zero pressure is obtained from a weighted linear fit of the normalised stress $F_E = \frac{P}{3f_E(1+2f_E)^{5/2}}$ against finite strain, $f_E = 0.5\left[\left(V_0/V\right)^{2/3} - 1\right]$. The correspondence of K_0 with experiment was not improved by fitting to a weighted second-order regression. Secondly, the value of V_0 obtained from the product of a_0, b_0, and c_0 is 228.19(2) Å^3, which differs by 0.09(3) Å^3 from that obtained when the volume is fitted directly.

The cyclicity of the *f-F* plot (inset in Figure 8-7) may have been an artefact of the (manual) pressure increase process, or it may have been due to successive gasket relaxations. Similar cyclicity was also present in *f-F* plots from DAC experiments in Boffa Ballaran *et al.* (2007) and Dobson *et al.* (2003).

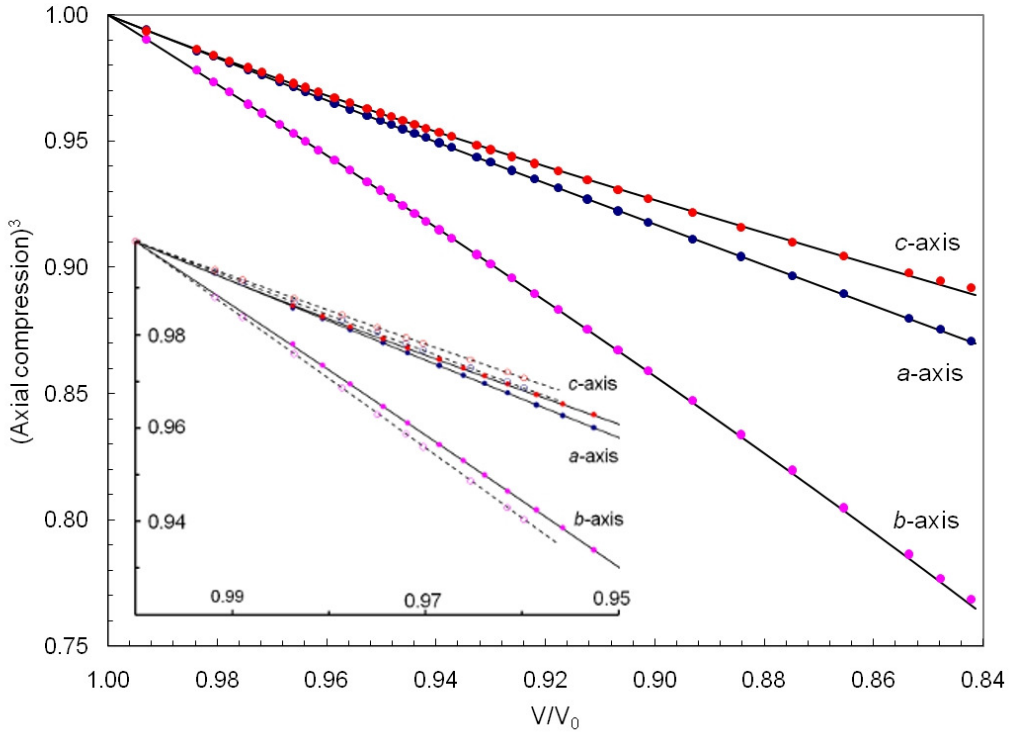

Figure 8-9: Axial compressions, i/i_0 (where $i = a$, b or c unit-cell parameter), of $CaPtO_3$, plotted as the ratios $(i/i_0)^3$. The symbols denote the experimentally-observed axial and volumetric values. The lines are derived from the axial equations of state, plotted against values of V/V_0 calculated from the volumetric EOS (Table 8-2). The inset to the figure shows a comparison of the values for $CaPtO_3$ (solid symbols and lines) with those for $CaIrO_3$ (open symbols and broken lines), as determined by Boffa Ballaran *et al.* (2007).

In addition to the $CaPtO_3$, there was a sufficient amount of the cubic $Ca_xPt_3O_4$ phase present in the sample to allow reliable determination of its cell parameter. By fitting the unit-cell volume to a third-order Birch-Murnaghan EOS, as described above, the following values were obtained: $V_0 = 186.00(3)$ Å^3; $K_0 = 213(1)$ GPa; $K'_0 = 4.9(1)$. When considering these results it should be remembered that this material has been reported to be of variable stoichiometry, with $0 \leq x \leq 1$ (Bergner and Kohlhaas, 1973).

8.4 Discussion and comparison with previous results

Figure 8-9 shows the relative compression of the three unit-cell axes, plotted as the cube of the axial compression ratios. It can be seen from Figure 8-9 that the compression is strongly anisotropic, being greatest for the *b*-axis (the direction perpendicular to the sheets of PtO_6 octahedra and Ca-ion interlayers) and smallest for the *c*-axis (along the chains of apex-linked PtO_6 octahedra).

8.4.1 Comparison with published *ab initio* simulations of $CaPtO_3$

The only previously published EOS parameters for $CaPtO_3$ with which to compare these results are those of Matar *et al.* (2008) who carried out an investigation of both post-perovskite and perovskite structured $CaPtO_3$ by athermal *ab initio* computer simulations using DFT with LDA pseudopotentials. The agreement of the experimental values (V_0 = 228.10(2) Å^3; K_0 = 168.2(8) GPa; K'_0 = 4.51(6)) with those from this simulation is surprisingly poor, as Matar *et al.* (2008) obtained V_0 = 212.14(5) Å^3 and K_0 = 222(1) GPa, with K'_0 = 4.59(8). Although LDA calculations commonly overestimate the binding of the atoms and so lead to calculated unit-cell parameters that are smaller than the experimental values, the discrepancy of 7% in V_0 is very large; similarly the value of K_0 from the computer simulations is over 30% greater than the experimental value. However, if the EOS parameters of Matar *et al.* are used to calculate K at the experimental value of V_0 a value of 157 GPa is obtained, in much closer agreement with the present work's experimental result (see also Section 10.2).

The reasons for this poor agreement are not clear, especially as Matar *et al.* (2008) also state that test calculations carried out using GGA, which commonly leads to an overestimate of the unit-cell volume, did not produce any significant improvement in the agreement between their calculated volume and the available experimental results. It is, perhaps, possible that the discrepancy is simply due to the lack of state points in the calculations, which appear to have been carried out at only six volumes, of which only three were for the material under compression. Unfortunately, no unit-cell parameters are given by Matar *et al.* (2008), only unit-cell volumes, and so it is impossible to determine whether their calculations produced a general underestimate of all three cell parameters or whether they failed to reproduce correctly the axial ratios of the crystal.

The simulated EOS values for $CaPtO_3$ from the present work using GGA (V_0 = 236.7 Å^3 and K_0 = 156.1 GPa, with K'_0 = 4.3) are in better agreement with experiment (see the discussion in Section 10.2.2); the simulated V_0 is 3.8% larger than experiment, the simulated K_0 is 7.2% smaller and the simulated K'_0 is 4.7% smaller.

8.4.2 Comparison with $CaIrO_3$

It is also of interest to compare these results with the experimental values of the EOS parameters for the other low-pressure post-perovskite analogue phase, $CaIrO_3$. From the present experiment, post-perovskite $CaPtO_3$ has a slightly larger unit-cell volume and lower value of K_0 than post-perovskite $CaIrO_3$. Boffa Ballaran *et al.* (2007) fitted a third-order Birch-Murnaghan equation to single-crystal X-ray data from post-perovskite $CaIrO_3$, obtaining V_0 = 226.38(1) Å^3 and K_0 = 181(3) GPa, with K'_0 = 2.3(8). Although the uncertainty is large, the value of K'_0 for $CaIrO_3$ is significantly lower than the corresponding value for $CaPtO_3$. Boffa Ballaran *et al.* (2007) used methanol-ethanol as their pressure medium, and the ruby scale of Mao *et al.* (1986); however, the difference in K'_0 cannot be attributed simply to differences in the pressure scale, since if the ruby scale of Mao *et al.* (1986) is applied to data from the present work it gives a value of K'_0 of 4.16(6) (see Section 8.3) that is still significantly higher than that of $CaIrO_3$.

Two other previous measurements of the compression of post-perovskite $CaIrO_3$ have been obtained using X-ray powder diffraction. Martin *et al.* (2007a) fitted a second-order Birch-Murnaghan equation, giving V_0 = 226.632(45) Å^3 and K_0 = 180.2(3) GPa, and Liu *et al.* (2011) fitted a third-order Birch-Murnaghan equation, giving V_0 = 226.543(158) Å^3 and K_0 = 169(5) GPa. The corresponding values for post-perovskite $CaPtO_3$ (V_0 = 227.95(2) Å^3, K_0 = 174.0(5) GPa, with K'_0 fixed at 4; see Section 8.3) show an increase in V_0 similar to that discussed above, although as K'_0 is fixed at 4 in both cases, the differences in the two fitted parameters are now not as large.

A further contrast in the behaviour of $CaPtO_3$ and $CaIrO_3$ lies in the relative unit-cell volumes and incompressibilities of the post-perovskite and perovskite structured forms of the two materials. For $CaIrO_3$, Boffa Ballaran *et al.* (2007) found experimentally that, at zero pressure, the ratio of the volumes of the post-perovskite and perovskite structured phases was 0.98656(6) and that the perovskite structured phase, with K_0 =

198(3) GPa and K'_0 = 1.2(8), was stiffer (at ambient pressure) than the post-perovskite structured phase. For $CaPtO_3$, the computer simulations of Matar *et al.* (2008), showed that, at zero pressure, the post-perovskite and perovskite structured phases have a similar volume ratio to that of $CaIrO_3$, 0.9878(13), but in this case the perovskite structured material is softer, with K_0 = 205(1) GPa and K'_0 = 4.42(5). However, this apparent difference in behaviour should probably be treated with caution. No experimental data for a perovskite structured phase of $CaPtO_3$ have, as yet, been published and in view of the discrepancy of the *ab initio* results of Matar *et al.* (2008) with the experimental values for post-perovskite $CaPtO_3$ it is probably unwise to rely upon them too closely.

The axial incompressibilities of $CaPtO_3$ are similar in form to those of $CaIrO_3$. The *a*-axis and *c*-axis of $CaPtO_3$ have the same incompressibility (within experimental uncertainty) at ambient pressure, but the *c*-axis stiffens faster than the *a*-axis, having a value of K'_0 that is greater by almost a factor of two; in contrast, the *b*-axis is much softer. If the crystal structure of post-perovskite $CaPtO_3$ is viewed in a naive way in terms of layers of PtO_6 octahedra separated by planar Ca-cation interlayers, this provides a ready explanation for the relative softness of the *b*-axis by reduction of the interlayer spacing. However, on this basis it is difficult to explain why the *c*-axis is the least compressible direction in the crystal, since this axis should be readily shortened by buckling of the planes of corner-linked octahedra. In contrast, a reduction of the length of the *a*-axis must involve distortion of the PtO_6 octahedra through shortening of the O-O distances aligned parallel to the *a*-axis. It has been suggested (Kubo *et al.*, 2008) that the relatively short O2e-O2f distance (see Figure 1-1) in post-perovskite $MgGeO_3$ between O atoms aligned with the *c*-axis compared with the relatively longer O2a-O2d distance (see Figure 1-4) along the *a*-axis results in a higher *c*-axis incompressibility, because of O-O repulsion. It can be seen from Figure 9-16 that the higher incompressibility and shorter length of the O2e-O2f distance in compression in post-perovskite $CaPtO_3$ - in comparison with the O2a-O2d distance - supports this hypothesis. This is discussed further in Section 9.4.1.

In Table 8-3, the ratios of the axial incompressibilities with respect to that of the *c*-axis, for both $CaPtO_3$ and $CaIrO_3$, are compared to those for $MgSiO_3$ and $Mg_{0.6}Fe_{0.4}SiO_3$.

	κ_a/κ_c	κ_b/κ_c
$CaPtO_3$ (ambient *P, T*)[a]	1.02(1)	0.64(1)
$CaIrO_3$ (ambient *P, T*)[b]	0.94(3)	0.51(1)
$MgSiO_3$ (135 GPa, 4000 K)[c]	0.84(6)	0.58(4)
$Mg_{0.6}Fe_{0.4}SiO_3$ (140 GPa, ambient *T*)[d]	1.05*	0.91*
$Mg_{0.9}Fe_{0.1}SiO_3$ (0 GPa, ambient *T*)[e]	0.93(8)	0.56(5)

Table 8-3: Experimental axial incompressibility ratios of some post-perovskite phases.

[a]the present work

[b]Boffa Ballaran *et al.* (2007)

[c]Guignot *et al.* (2007)

[d]Mao *et al.* (2010); *uncertainties not given

[e]Nishio-Hamane and Yagi (2009)

The low incompressibility of the *b*-axis relative to that of the *c*-axis in both $CaPtO_3$ and $CaIrO_3$ is similar in magnitude to that reported for $MgSiO_3$, at pressures and temperatures comparable to those expected in the D″ region of the Earth's mantle (Guignot *et al.*, 2007). However, much worse agreement is found with the axial incompressibility ratios for $Mg_{0.6}Fe_{0.4}SiO_3$ at 140 GPa and ambient temperature (Mao *et al.*, 2010). In this case, although the value for κ_a/κ_c agrees well with that from $CaPtO_3$, neither $CaPtO_3$ nor $CaIrO_3$ give a similar value for κ_b/κ_c (though the agreement for $CaPtO_3$ is somewhat better than for $CaIrO_3$). A more detailed comparison of the axial compressions of $CaPtO_3$ with previously published results for $CaIrO_3$ (Boffa Ballaran *et al.*, 2007) is shown as an inset to Figure 8-9. Clearly, at all pressures, $CaPtO_3$ is slightly less elastically anisotropic than $CaIrO_3$. This difference in anisotropy may be due to distortion of the IrO_6 octahedra in $CaIrO_3$, caused by the Jahn-Teller effect (Ohgushi *et al.*, 2008); the absence of this effect in $CaPtO_3$ may indicate that it is therefore a somewhat better low pressure analogue for post-perovskite $MgSiO_3$ at ambient pressure and temperature.

Further work on the structure of $CaPtO_3$ at high-pressure (at room temperature) and on its structure and thermal expansion (at atmospheric pressure) is described in Chapter 9.

8.5 Summary of X-ray powder diffraction study of $CaPtO_3$ at high-pressure

1. The isothermal incompressibility, at ambient temperature, of post-perovskite $CaPtO_3$ to 40 GPa was measured by X-ray powder diffraction using synchrotron radiation. A third-order Birch-Murnaghan EOS fitted to the experimental data gave V_0 = 228.10(2) Å^3, K_0 = 168.2(8) GPa and K'_0 = 4.51(6). Similar fits to the cube of each axis of the unit cell showed that the *b*-axis is the most compressible (b_0 = 9.9191(5) Å, K_0 = 123.3(5) GPa, K'_0 = 2.37(3)); the *a*-axis (a_0 = 3.12777(8) Å, K_0 = 195.7(8) GPa, K'_0 = 6.63(8)) and *c*-axis (c_0 = 7.3551(4) Å, K_0 = 192(2) GPa, K'_0 = 12.2(3)) are both much stiffer and have almost identical incompressibilities when the material is close to ambient pressure, but the *c*-axis shows greater stiffening on compression.
2. Comparison of these axial incompressibilities with those of $CaIrO_3$ shows that $CaPtO_3$ is slightly less anisotropic under compression (possibly because of the absence of Jahn-Teller distortion), suggesting that $CaPtO_3$ may be a somewhat better analogue of $MgSiO_3$.
3. The sample also contained minor amounts of a cubic $Ca_xPt_3O_4$ phase, for which the third-order Birch-Murnaghan equation of state parameters were found to be V_0 = 186.00(3) Å^3, K_0 = 213(1) GPa and K'_0 = 4.9(1).
4. Bragg reflections became broader with increasing pressure, particularly above ~22 GPa, due to non-uniform strain in the crystallites. This may have been due to solidification of the helium pressure medium and grain-grain interactions in the sample.

9 Neutron powder diffraction studies of $CaPtO_3$

In this Chapter I describe measurements of the unit-cell parameters and crystal structure of $CaPtO_3$ to 9.27 GPa at ambient temperature and from 2 K to 973 K (at ambient pressure) by time-of-flight neutron powder diffraction at the ISIS neutron source, STFC Rutherford Appleton Laboratory, UK. The objective was to compare the behaviour of the $CaPtO_3$ structure under compression and expansion to those of $CaIrO_3$ and $MgSiO_3$. The measurements of the volume and unit-cell of $CaPtO_3$ using X-ray diffraction in Chapter 8 were more precise, but accurate measurement of structural changes in compression and in expansion is only possible using neutron powder diffraction, as described in Chapter 7. Most of the work described in this Chapter was published as Lindsay-Scott *et al.* (2011).

9.1 Neutron diffraction powder study of $CaPtO_3$ at high-pressure

9.1.1 Experimental method

The post-perovskite $CaPtO_3$ sample used in this study was synthesised at high-pressure and high-temperature using a belt-type high-pressure apparatus at the National Institute for Materials Science, Tsukuba, Ibaraki, Japan, as described in Section 6.5.3. Each synthesis run produced ~0.9 g of product. The products from three such runs were mixed together before the neutron diffraction experiments to ensure sample uniformity.

The high-pressure neutron powder diffraction patterns were collected by the time-of-flight method with the PEARL Beamline high-pressure facility, HiPr (ISIS Annual Report, 1996), at ISIS. This medium-resolution, high-flux diffractometer is optimized for data collection from a Paris–Edinburgh press with opposed anvils (Figure 9-1).

Approximately 90 mm^3 of the powdered sample was loaded into an encapsulated gasket machined from null-scattering TiZr alloy, with deuterated methanol-ethanol as the pressure-transmitting fluid, so as to provide near-hydrostatic compression (Marshall and Francis, 2002). A 2 mm polycrystalline lead pellet, placed in the centre of the sample, provided a pressure calibrant (see e.g. Fortes *et al.*, 2007) that could be readily separated from the sample after the experiment. Scattering into the detectors from the tungsten carbide (WC) anvils of the pressure cell was reduced by covering

them with cadmium foil (Figure 9-2a) and by radial collimators. However, small peaks due to scattering from WC and also from the nickel binder in the anvils were still present in the diffraction patterns.

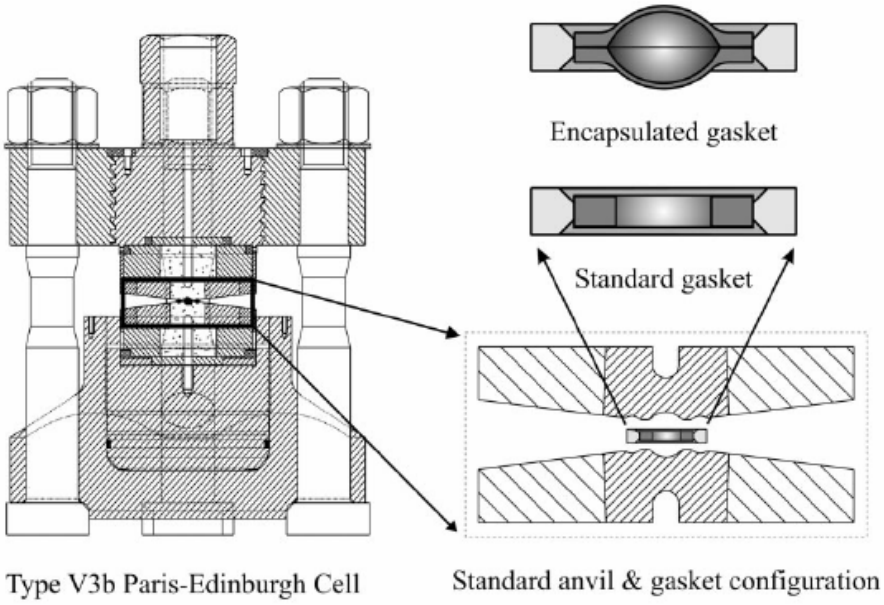

Figure 9-1: A Paris-Edinburgh pressure cell (left) with the encapsulated gasket design (right, upper) (Marshall and Francis 2002).

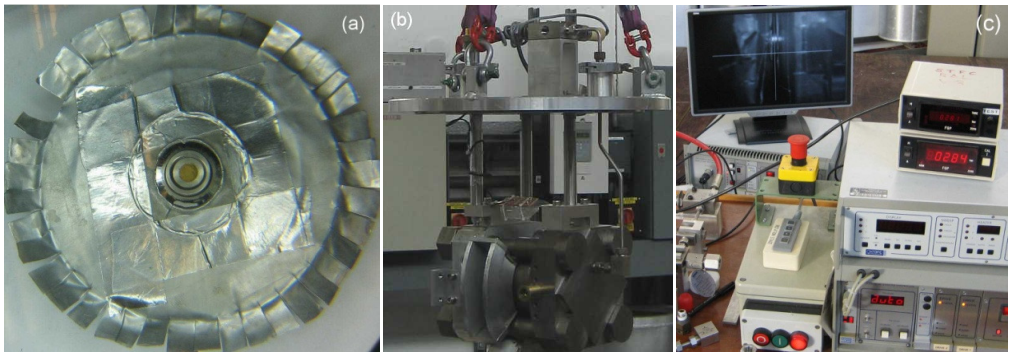

Figure 9-2: High-pressure configuration. (a) DAC loaded with dark-yellow $CaPtO_3$ powder and Pb pellet (b) Paris-Edinburgh cell being loaded into PEARL beamline (c) DAC position adjustment monitor and controller.

Data were collected (at ambient temperature) at pressures of approximately 0, 2.4, 5.1, 7.7 and 9.3 GPa, for counting time of between 8 and 18 hours. The cumulative ISIS proton beam current in μAh for each dataset is shown in the final column of Table 9-1.

Pressure (GPa)	V/V_0	Volume (Å^3)	a(Å)	b(Å)	c(Å)	Ca y	Ca Uiso	Pt Uiso	O1 y	O1 Uiso	O2 y	O2 z	O2 Uiso	µAh
0.02(5)	0.9999	227.97(1)	3.1264(1)	9.9200(5)	7.3504(3)	0.2510(4)	0.62(8)	0.13(4)	0.9185(4)	0.57(7)	0.6281(2)	0.0490(3)	0.54(5)	1980
2.38(7)	0.9862	224.83(2)	3.1144(2)	9.8565(7)	7.3243(5)	0.2512(5)	0.43(10)	0.03(5)	0.9181(5)	0.51(9)	0.6284(3)	0.0500(4)	0.44(7)	1320
5.07(7)	0.9721	221.62(2)	3.1018(2)	9.7900(6)	7.2979(4)	0.2494(5)	0.47(9)	0.06(5)	0.9177(5)	0.45(8)	0.6291(3)	0.0494(3)	0.45(7)	1815
7.69(9)	0.9593	218.71(2)	3.0903(2)	9.7296(8)	7.2738(6)	0.2502(6)	0.01(10)	-0.03(7)	0.9174(6)	0.45(11)	0.6303(4)	0.0486(5)	0.49(9)	1650
9.27(7)	0.9514	216.90(2)	3.0825(2)	9.6954(8)	7.2576(8)	0.2485(6)	0.54(12)	0.10(6)	0.9165(5)	0.12(9)	0.6300(3)	0.0482(4)	0.35(8)	2970

Table 9-1: Unit-cell volume, unit-cell parameters, atomic fractional coordinates, isotropic displacement parameters (Uiso) and cumulative ISIS proton beam current for $CaPtO_3$ as a function of pressure at 291K. The data were recorded in the order shown. The numbers in parentheses are estimated standard uncertainties and refer to the least-significant digits. Uiso values are x 10^2 Å^2. The value of V_0 used to calculate column 2 is 227.98(7) Å^3 (see Table 9-2).

After normalisation to the incident beam flux, focussing to a mean flight path and Bragg angle, and correction for detector efficiency, the logarithmically-binned diffraction patterns were fitted over the range $0.53 < d < 3.7$ Å to obtain unit-cell parameters and structural data by Rietveld refinement, implemented in the GSAS suite of programs (Larson and Von Dreele, 1994) with the EXPGUI graphical interface (Toby, 2001). Five phases were included in the refinement: post-perovskite $CaPtO_3$, cubic $CaPt_3O_4$ (~10 % by weight of the sample), Pb, WC, and Ni. Isotropic displacement parameters were used throughout, as anisotropic displacement parameters did not improve the fit. The χ^2 values for the fits were typically 1.47, with weighted profile R-factors (R_{wp}) typically 0.026. Examples of the fitted diffraction patterns at 0.02 GPa and 9.27 GPa are shown in Figure 9-3.

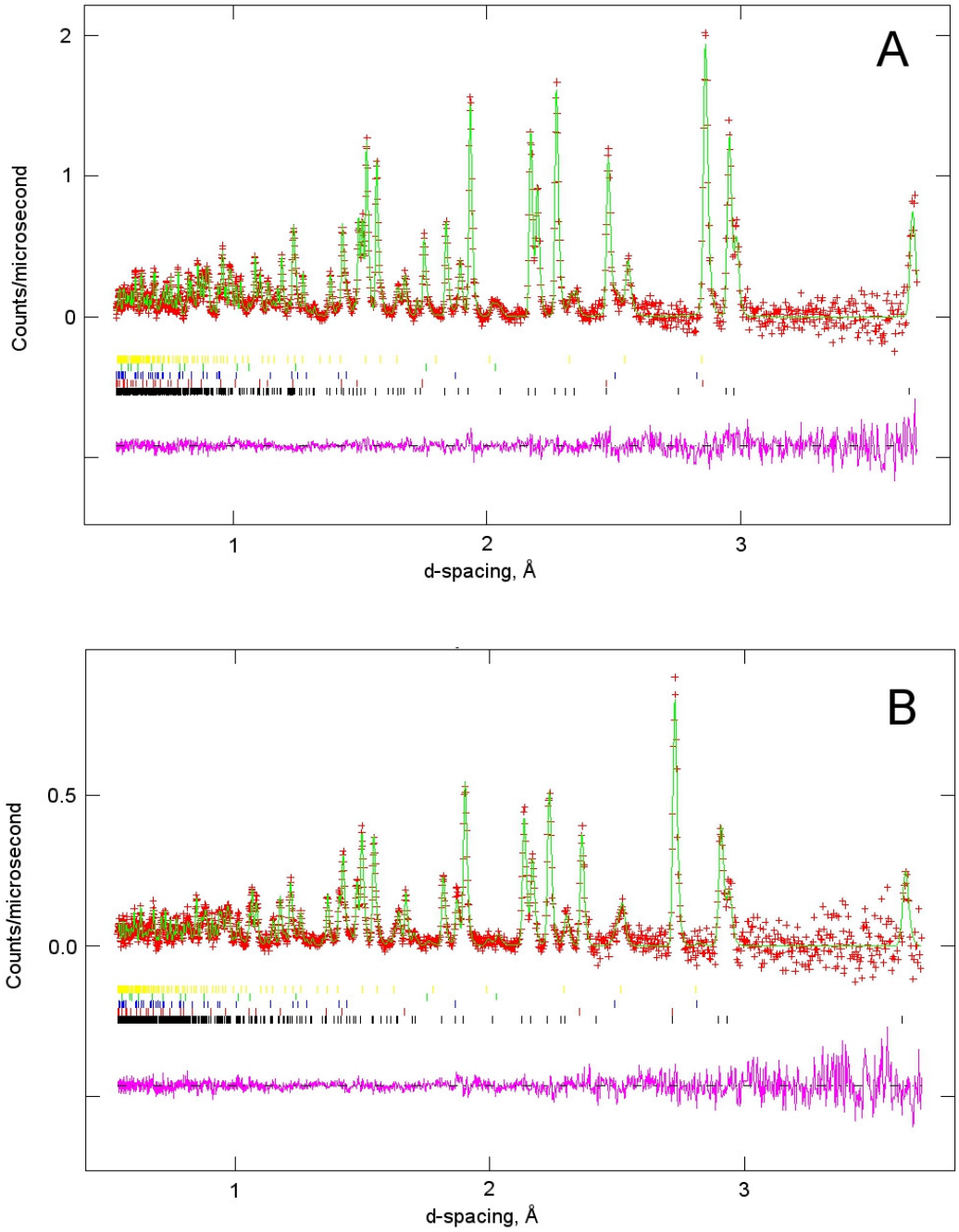

Figure 9-3: Observed (points), calculated (line) and difference (lower trace) neutron powder diffraction patterns (background subtracted) for Rietveld refinements of $CaPtO_3$ at ambient temperature and pressures of: (A) 0.02 GPa and (B) 9.27 GPa. The tick marks show the positions of the Bragg reflections of (from the bottom upwards): $CaPtO_3$, Pb, WC, Ni, and $CaPt_3O_4$.

9.1.2 Pressure dependence of the unit-cell parameters of $CaPtO_3$

The unit-cell volume and unit-cell parameters of post-perovskite $CaPtO_3$ at ambient temperature between 0.02 GPa and 9.27 GPa are listed in Table 9-1 and shown in Figure 9-4.

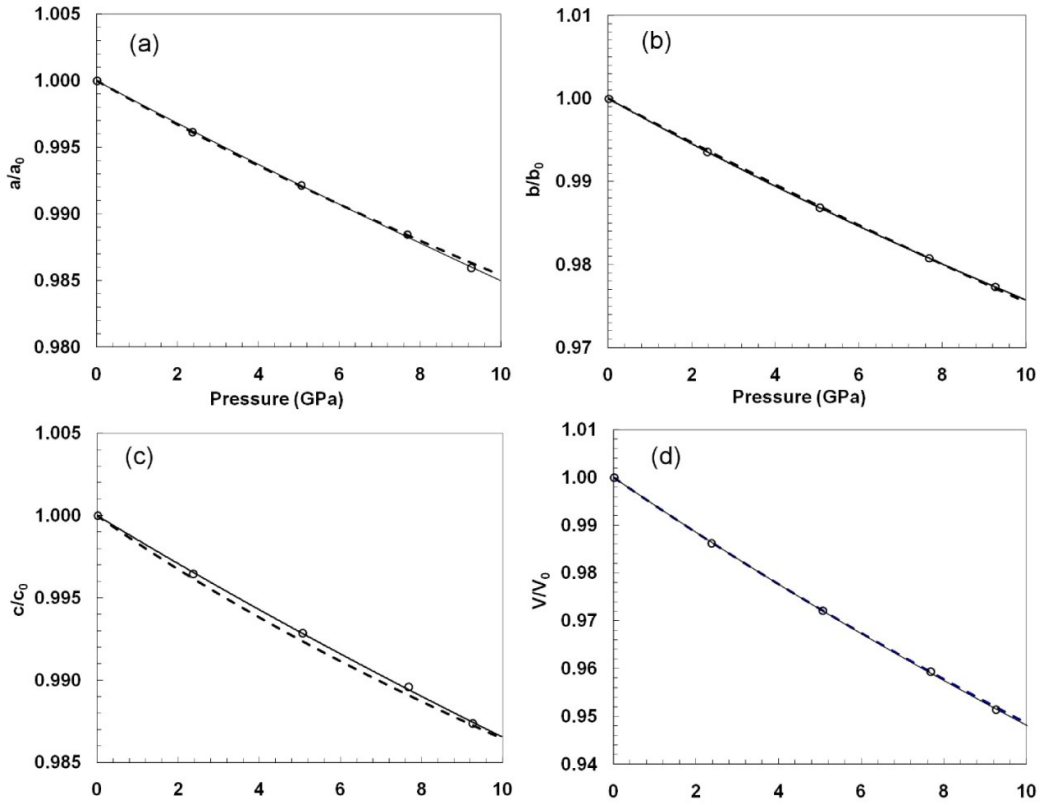

Figure 9-4: Unit-cell parameters (a) – (c) and unit-cell volume (d) of $CaPtO_3$, between 0.02 GPa and 9.27 GPa, as fractions of their EOS values at 0 GPa (see Table 9-2). Experimental values are shown as points (error bars are smaller than the symbols used). The full lines show the fits of these five data points to third-order Birch-Murnaghan EOSs (see Table 9-2). The axial EOS data points were calculated using the program BM3BIS referred to in Section 8.3. The dashed lines show third-order Birch-Murnaghan EOSs calculated using the parameters from the X-ray synchrotron experiment (see Table 9-2).

The volumetric and axial data were fitted to third-order Birch-Murnaghan equations of state (Birch, 1978) by non-linear least-squares using the EOS-fit program (Angel, 2000, 2001); in the case of the unit-cell axes, the cubes of their values were fitted. The weighting scheme in the refinement used weights calculated from the uncertainties in

both the pressure and in the unit-cell volume and unit-cell parameters. The resulting values of the 3 equation-of-state parameters for each of the 4 fits are listed in Table 9-2.

	V_0 (Å^3)	K_0 (GPa)	K'_0
Volume	227.98(7)	169(6)	4(1)
	228.10(2)	*168.2(8)*	*4.51(6)*
a-axis	3.1265(3)	206(8)	3(2)
	3.12777(8)	*195.7(8)*	*6.63(8)*
b-axis	9.9205(15)	118(4)	4(1)
	9.9191(5)	*123.3(5)*	*2.37(3)*
c-axis	7.3504(7)	223(10)	5(2)
	7.3551(4)	*192(2)*	*12.2(3)*

Table 9-2: EOS parameters obtained by fitting the data shown in Table 9-1 to third-order Birch-Murnaghan equations of state (upper values, shown in normal type). For the unit-cell edges, the values of K_0 and K'_0 are those obtained by fitting the cubes of the lengths of the unit-cell edges. The lower values, shown in italics, are those from synchrotron X-ray powder diffraction (to 40 GPa) at 298 K (Table 8-2). For comparison with the results of Martin *et al.* (2007a), the unit-cell volumes from the present work were also fitted to a second-order Birch-Murnaghan EOS. The resulting values of V_0 and K_0 were 227.98(6) Å^3 and 169(2) GPa respectively (with fixed K'_0 at 4).

The values are consistent with (but less precise than) those obtained from the synchrotron X-ray powder diffraction to 40 GPa shown in Table 8-2 , which are also shown for convenience in italics in Table 9-2. The variation between the two experiments in the axial values of K_0 and K'_0 may be due to the greater pressure range covered in the X-ray experiment. It can be seen from Figure 9-4 and Table 9-2 that the compression is strongly anisotropic, being greatest for the *b*-axis (i.e. for the direction perpendicular to the sheets of PtO_6 octahedra and Ca-ion interlayers) and smallest for the *c*-axis (i.e. along the chains of apex-linked PtO_6 octahedra).

9.2 Neutron diffraction powder study of $CaPtO_3$ as a function of temperature

9.2.1 Experimental method

The low-*T* and high-*T* (ambient *P*) studies were both made using the high-resolution powder diffractometer (HRPD) (Ibberson *et al.*, 1992) at the ISIS neutron source. This instrument, the highest-resolution diffractometer of its type ($\Delta d/d \approx 4 \times 10^{-4}$ in backscattering), has a total flight path of ~100 m and three banks of detectors, with $2\theta = 168^o$ ("backscattering bank"), $2\theta = 90^o$ ("90^o bank"), and $2\theta = 30^o$ ("low-angle bank"). All data were collected in the time-of-flight window from 30 – 130 ms, corresponding to a *d*-spacing range of 0.6 – 2.6 Å in the backscattering detectors. The sample environment for the low-*T* experiment (2 – 300 K) was an ISIS-facility He cryostat, with the powder sample, loosely packed into a rectangular aluminium sample "slab-can" (20 x 20 x 5 mm) with thin vanadium windows, held under a partial pressure of 30 mbar of He exchange gas; the temperature stability was ~±0.1 K throughout. After cooling to base temperature (2 K), data were collected for 80 μAh of cumulative ISIS proton beam current (equivalent to ~2.5 h on this instrument); the sample temperature was then increased to 10 K, and thereafter in steps of 10 K to 300 K, and data were collected for 10 μAh of proton beam current (~20 min) at each temperature to allow determination of the unit-cell parameters. Data suitable for structure refinements were then collected as follows; after counting for 80 μAh at 300 K, the temperature was decreased to 150 K (80 μAh) and then to 33 K (60 μAh), after which data sets were collected in increments of 33 K at six temperatures to 233 K (all 60 μAh) and finally at 266 K for 100 μAh.

After this low-*T* experiment, the sample was recovered for use in the high-*T* study. To reduce the rate of decomposition of the $CaPtO_3$ in the furnace vacuum, the powder sample was loosely packed in a silica glass tube of 6 mm internal diameter and 1 mm wall thickness which was then evacuated and sealed. This tube was placed in an 8 mm diameter cylindrical vanadium sample can, which was, in turn, attached to a centre stick and placed in an ISIS furnace, constructed with vanadium windings and vanadium windows; the temperature was controlled to better than ±0.2 K throughout.

Data were collected between 291 K and 973 K in a series of measurements designed to minimise the possibility of decomposition, which was expected to occur somewhere

above 873 K. Following a measurement at ambient temperature (291 K; 160 μAh), data for structure refinements were collected in 100 K temperature steps to 869 K (each counted for 160 μAh). The sample was then cooled to 423 K (a lower temperature was not practicable as the furnace responds very slowly below this temperature) and measurements were made at intervals of 25 K from 423 K to 973 K (10 μAh) for determination of the unit-cell parameters. Finally, four more measurements were made, all counted for 160 μAh; two at 973 K, one at 823 K and one at 623 K.

For the HRPD experiments, the data analysis was carried out with the backscattering data only ($2\theta = 168^{o}$), using a *d*-spacing range from 0.66 – 2.48 Å. Inclusion of the data from the 90^{o} detector bank offered little advantage as only 2 additional Bragg reflections were recorded; it was also desirable to avoid the possibility of having to introduce bank-dependent preferred orientation corrections into the refinement (see e.g. Fortes *et al.*, 2006). No further reflections could be seen in the low-angle bank.

Preliminary refinements of the structure revealed that the absorption of the sample, when combined with the differing sample geometries in the cryostat and in the furnace, was sufficient to cause a noticeable mismatch in the refined parameters from the datasets collected at room temperature during the heating and cooling experiments. The packing density of a similar $CaPtO_3$ sample was, therefore, measured and the MANTID suite of programs (MANTID, 2008, 2010) used to calculate and apply the appropriate absorption correction for each sample environment. After normalisation to the incident beam flux, focussing to a mean flight path and Bragg angle, and correction for detector efficiency, the logarithmically-binned backscattering data were analysed using the GSAS suite of programs (Larson and Von Dreele, 1994) with the EXPGUI graphical interface (Toby, 2001).

For the data collected with short counting times (10 μAh) Le Bail refinement (Le Bail *et al.*, 1988) was used to determine the unit-cell parameters. The F-calc weighted LeBail refinement refined the DIFA and Zero diffractometer parameters for the first furnace data point (291 K) so that its unit-cell parameters were aligned with those interpolated from the cryostat measurements of 290 K and 300 K. LeBail refinement showed a tendency to over-refine (increase the values of) profile parameters, spreading

out peaks. The refinement could not recover once a peak had become too spread out, as found in the synchrotron X-ray diffraction LeBail refinement (see Section 8.2).

The data collected for longer times were analysed by the Rietveld method to determine the crystal structure. Four phases were included in the refinements of the data collected with the sample in the cryostat: $CaPtO_3$ and $CaPt_3O_4$, $Ca(OH)_2$ (another minor impurity from the synthesis), and aluminium from the sample environment (peaks from the latter were very weak and not distinguishable above 100 K). The same set of phases (excluding aluminium) was used for the data collected in the furnace (the peaks from the residue from $Ca(OH)_2$ were not distinguishable by 673K after its dissociation).

Isotropic displacement parameters were used in all refinements, since, at temperatures below 673 K, the introduction of anisotropic displacements led to values that were not always positive definite for all atoms (O1 being the atom most commonly affected). However, at the three highest temperatures at which the structure was determined (673, 773 and 869 K), where the atom motions would be greatest, the Rietveld refinement was repeated using anisotropic displacement factors. Preferred orientation in the sample was modelled by an 8^{th} order spherical harmonic approximation; the mean texture index was 1.028 for the sample in the cryostat and 1.099 for the sample in the furnace. It was found that the last four data sets collected in the furnace (two at 973 K, at 823 K and at 623 K) showed significant amounts of dissociation products from the $CaPtO_3$ and so these data were discarded. Examples of the fitted diffraction patterns for the Rietveld refinements at 2K and at 869 K are shown in Figure 9-5.

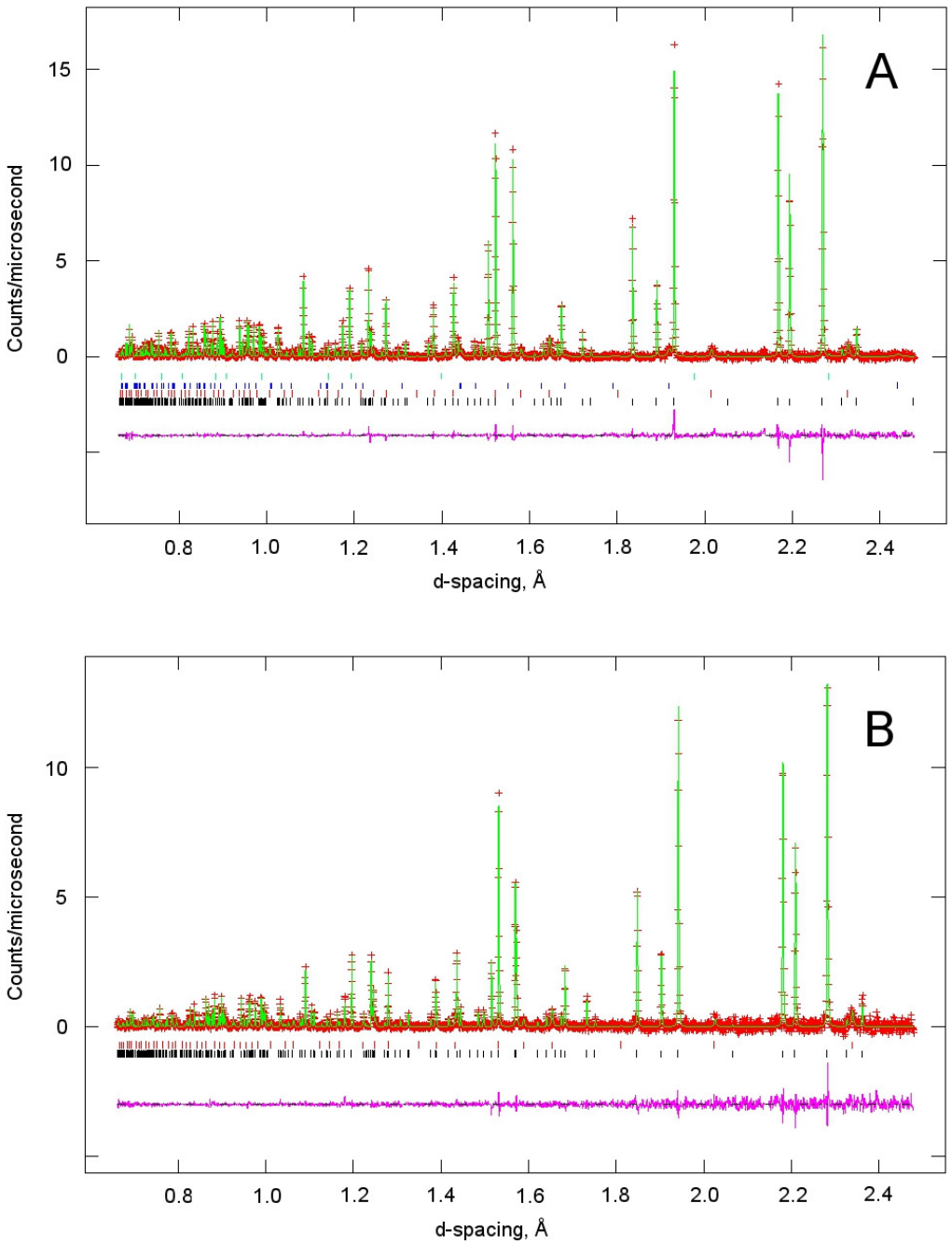

Figure 9-5: Observed (points), calculated (line) and difference (lower trace) neutron powder diffraction patterns (background subtracted) for Rietveld refinements of $CaPtO_3$ at ambient pressure and at: (A) 2 K and (B) 869 K. The tick marks show the positions of the Bragg reflections of (from the bottom upwards): $CaPtO_3$ and $CaPt_3O_4$, and (for 2 K refinement only) $Ca(OH)_2$ and aluminium.

For the data collected with the sample in the cryostat, the χ^2 values for the Rietveld fits were typically 1.90, with weighted profile R-factors typically 0.045; the corresponding values for the data collected using the furnace being 1.52 and 0.028 respectively. The LeBail fits gave values of χ^2 and R_{wp} of typically 0.96 and 0.076 in the cryostat and 1.11 and 0.055 in the furnace.

9.2.2 Temperature dependence of the unit-cell parameters of $CaPtO_3$

To ensure comparability of counting statistics, the unit-cell parameter measurements of $CaPtO_3$ between 2 K and 973 K (at ambient pressure) shown in Figure 9-6 and listed in Table 9-3 were all taken from Le Bail refinements of the datasets collected for 10 μAh.

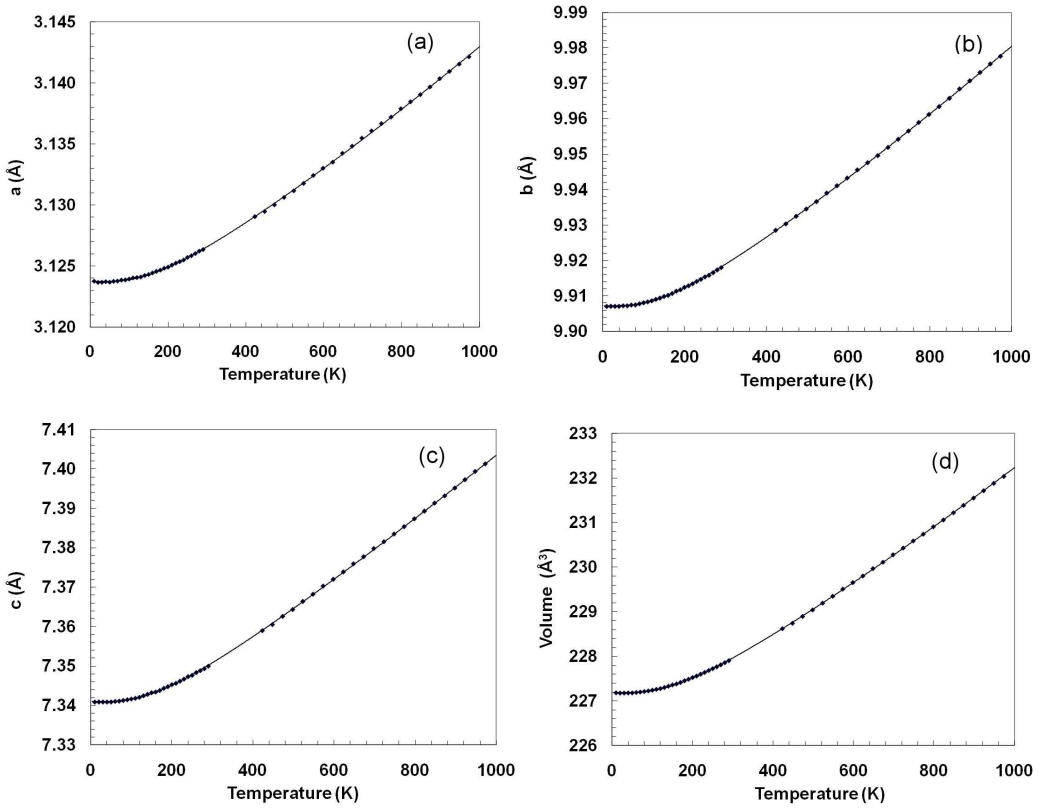

Figure 9-6: Unit-cell parameters (a) – (c) and unit-cell volume (d) of $CaPtO_3$ between 10 K and 973 K, at ambient pressure. Experimental values are shown as points (error bars are smaller than the symbols used). The full lines show the fit of the data to second-order Grüneisen approximations to the zero-pressure EOSs (see text for details).

Temperature (K)	Volume (Å^3)	*a*(Å)	*b*(Å)	*c*(Å)
Cryostat				
10	227.179(2)	3.12374(2)	9.90707(7)	7.34086(5)
20	227.173(2)	3.12365(2)	9.90712(7)	7.34088(5)
30	227.174(2)	3.12366(2)	9.90711(7)	7.34087(5)
40	227.177(2)	3.12370(2)	9.90712(7)	7.34086(5)
50	227.178(2)	3.12367(2)	9.90726(7)	7.34087(5)
60	227.187(2)	3.12373(2)	9.90726(7)	7.34102(5)
70	227.196(2)	3.12376(2)	9.90748(7)	7.34110(5)
80	227.208(2)	3.12383(2)	9.90752(7)	7.34127(5)
90	227.222(2)	3.12385(2)	9.90784(7)	7.34144(5)
100	227.239(2)	3.12392(2)	9.90811(7)	7.34163(5)
110	227.257(2)	3.12401(2)	9.90836(7)	7.34182(5)
120	227.274(2)	3.12405(2)	9.90867(7)	7.34206(5)
130	227.299(2)	3.12409(2)	9.90907(7)	7.34246(5)
140	227.328(2)	3.12421(2)	9.90944(7)	7.34282(5)
150	227.357(2)	3.12429(2)	9.90989(7)	7.34323(5)
160	227.379(2)	3.12443(2)	9.91021(7)	7.34341(5)
170	227.412(2)	3.12455(2)	9.91073(7)	7.34378(5)
180	227.451(2)	3.12465(2)	9.91139(7)	7.34433(5)
190	227.484(2)	3.12480(2)	9.91177(7)	7.34476(5)
200	227.523(2)	3.12490(2)	9.91245(7)	7.34527(5)
210	227.556(2)	3.12507(2)	9.91291(7)	7.34560(5)
220	227.597(2)	3.12523(2)	9.91347(7)	7.34616(5)
230	227.637(2)	3.12535(2)	9.91411(7)	7.34668(5)
240	227.681(2)	3.12549(2)	9.91472(7)	7.34730(5)
250	227.722(2)	3.12570(2)	9.91539(7)	7.34765(5)
260	227.764(2)	3.12584(2)	9.91586(7)	7.34833(5)
270	227.808(2)	3.12601(2)	9.91659(7)	7.34882(5)
280	227.856(2)	3.12621(2)	9.91737(7)	7.34931(5)
290	227.901(2)	3.12634(2)	9.91802(7)	7.34996(5)
Furnace				
423	228.620(3)	3.12904(3)	9.92856(10)	7.35897(8)
448	228.740(3)	3.12946(3)	9.93036(10)	7.36051(8)
473	228.894(3)	3.13001(3)	9.93250(10)	7.36258(8)
498	229.040(3)	3.13062(3)	9.93456(10)	7.36434(7)
523	229.192(3)	3.13116(3)	9.93663(10)	7.36639(8)
548	229.348(3)	3.13176(3)	9.93905(11)	7.36821(8)
573	229.508(3)	3.13241(3)	9.94112(10)	7.37028(8)
598	229.655(3)	3.13301(3)	9.94329(10)	7.37200(8)
623	229.803(3)	3.13350(3)	9.94558(11)	7.37387(8)
648	229.968(3)	3.13423(3)	9.94761(11)	7.37593(8)
673	230.112(3)	3.13482(3)	9.94960(11)	7.37772(8)
698	230.279(3)	3.13547(4)	9.95192(12)	7.37980(8)
723	230.430(3)	3.13607(3)	9.95422(12)	7.38153(8)
748	230.589(3)	3.13667(3)	9.95656(12)	7.38349(8)
773	230.742(3)	3.13720(3)	9.95894(12)	7.38536(8)
798	230.907(4)	3.13789(5)	9.96122(17)	7.38734(11)
823	231.061(3)	3.13846(4)	9.96342(13)	7.38929(8)
848	231.222(3)	3.13904(4)	9.96577(13)	7.39132(8)
873	231.388(3)	3.13967(3)	9.96842(12)	7.39317(8)
898	231.553(3)	3.14035(4)	9.97070(13)	7.39515(8)
923	231.717(3)	3.14094(3)	9.97305(12)	7.39725(8)
948	231.883(3)	3.14154(3)	9.97546(11)	7.39935(8)
973	232.038(3)	3.14214(3)	9.97762(11)	7.40127(8)

Table 9-3: Unit-cell parameters and unit-cell volume for $CaPtO_3$ as a function of temperature (ambient *P*); all values are from Le Bail refinement of data collected for 10 μAh cumulative beam current. The numbers in parentheses are estimated standard uncertainties and refer to the least-significant digits.

The analysis of these results, presented below, uses a similar approach to that described for $CaIrO_3$ by Lindsay-Scott *et al.* (2007). Linear and volumetric thermal expansion values above room temperature in the form tabulated by Fei (1995) were obtained by fitting the data from 423 K to 973 K to

$$V(T) = V_{Tr} \exp\left[\int_{Tr}^{T} \alpha(T) dT \right] \quad (9.1)$$

where V_{Tr} is the volume at a chosen reference temperature, T_r, (here taken to be 300 K) and $\alpha(T)$ is the volumetric thermal expansion coefficient, having the form

$$\alpha(T) = a_0 + a_1 T \quad (9.2)$$

The resulting values of V_{Tr}, a_0 and a_1 are shown in Table 9-4, together with those obtained from similar fits to determine the linear thermal expansion coefficients of the three axes of the unit-cell. The values of a_0 listed in Table 9-4 indicate that expansion is anisotropic and also that this anisotropy differs from that shown by $CaPtO_3$ on compression (see Section 9.4.1). On heating, the *b*-axis expands at approximately the same rate as the volumetric (bulk) value divided by three, while the *c*-axis expands faster than *b*, and the *a*-axis expands more slowly.

	Value at *Tr* (300 K)	a_0	a_1
Volume	227.887(8) $Å^3$	2.365(34) x 10^{-5} K^{-1}	5.05(48) x 10^{-9} K^{-2}
a-axis	3.12607(7) Å	0.694(22) x 10^{-5} K^{-1}	1.10(31) x 10^{-9} K^{-2}
b-axis	9.91849(15) Å	0.713(15) x 10^{-5} K^{-1}	2.71(22) x 10^{-9} K^{-2}
c-axis	7.34978(13) Å	0.957(17) x 10^{-5} K^{-1}	1.25(24) x 10^{-9} K^{-2}

Table 9-4: Volumetric and linear thermal expansion parameters for $CaPtO_3$. For details see text; to reduce the effect of rounding errors in any subsequent calculations using these coefficients the values in the table are sometimes reported to one more significant figure than is justified by their estimated standard uncertainty (estimated standard deviation).

A more physically meaningful interpretation of the thermal expansion curve, encompassing its full temperature range, can be obtained using Grüneisen approximations for the zero-pressure EOS; this approach also allows investigation of the dynamics of the material by enabling estimates of the Debye temperature to be made. For data covering a wide temperature range, the second-order Grüneisen approximation (see Section 16.1 Appendix D) is more appropriate than the first-order approximation (Vočadlo *et al.*, 2002) and this takes the form

$$V(T) = V_0U/(Q - bU) + V_0 \tag{9.3}$$

where $Q = V_0K_0/\gamma'$ and $b = (K_0'-1)/2$; γ' is a Grüneisen parameter (assumed constant, Wallace, 1998); K_0 and K_0' are, respectively, the isothermal incompressibility and its first derivative with respect to pressure at $T = 0$, and V_0 is the volume at $T = 0$. The internal energy U may be calculated using the Debye approximation (see *e.g.* Poirier, 2000) from

$$U(T) = 9Nk_BT(\frac{T}{\theta_D})^3 \int_0^{\theta_D/T} \left(\frac{x^3}{e^x - 1}\right) dx \tag{9.4}$$

where N is the number of atoms in the unit-cell, k_B is Boltzmann's constant and θ_D is the Debye temperature.

The solid line in Figure 9-6d shows the result obtained from fitting the data for $V(T)$ to Equation 9.3 by weighted non-linear least-squares. Equation 9.3 has also been used to fit the data for $a(T)$, $b(T)$ and $c(T)$ and these results are similarly shown as solid lines in Figure 9-6a – Figure 9-6c. Figure 9-6 indicates that this model provides an excellent description of the behaviour both of the cell volume and of the individual cell parameters over the full temperature range of the experiment. This point is further illustrated in Figure 9-7, which shows the behaviour of the resulting volumetric thermal expansion coefficient of $CaPtO_3$, $\alpha(T)$, obtained from

$$\alpha(T) = (1/V)(\mathrm{d}V/\mathrm{d}T) \tag{9.5}$$

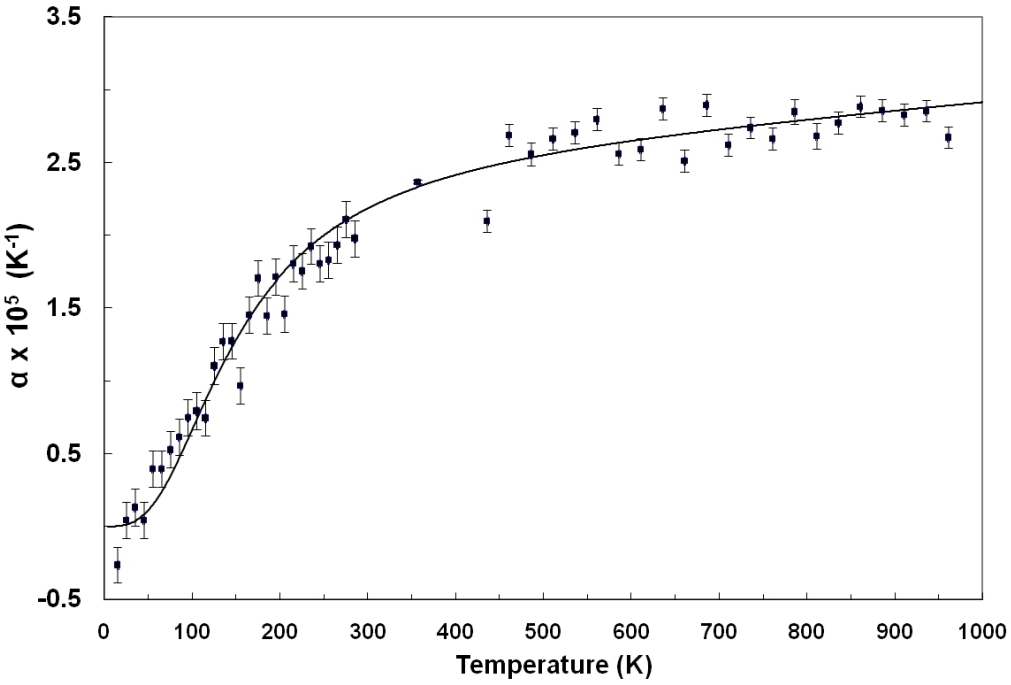

Figure 9-7: Volumetric thermal expansion coefficient of $CaPtO_3$ as a function of temperature. The points were obtained by numerical differentiation of the data shown in Figure 9-6d; the solid line was obtained *via* Equation 9.3.

The full line in Figure 9-7 gives the result obtained by differentiation of Equation 9.3, while the points show the results from simple numerical differentiation by differences of the *V(T)* data. Again, the agreement is very good, with little indication in this case that neglect of anharmonicity has led to an underestimate of the thermal expansion coefficient at high temperatures (see e.g. Wood *et al.* 2002).

The values of the four fitted parameters in the Grüneisen approximations for *a(T), b(T), c(T)* and *V(T)* are shown in Table 9-5.

	θ_D	Q	V_0	b
V	615(8) K	3.16(3) x 10^{-17} J	227.186(3) Å^3	3.4(4)
			a_0	
a-axis	648(13) K	11.37(17) x 10^{-17} J	3.12373(2) Å	14(2)
			b_0	
b-axis	574(7) K	9.79(9) x 10^{-17} J	9.90724(4) Å	12(1)
			c_0	
c-axis	624(10) K	7.96(9) x 10^{-17} J	7.34100(4) Å	5(1)

Table 9-5: Fitted parameters for the second-order Grüneisen approximations to the isobaric equations of state of $CaPtO_3$.

The Debye temperatures obtained by fitting all three of the axes and the volume are quite similar, with the sequence for the three axes, $\theta_{Db} < \theta_{Dc} \approx \theta_{Da}$. The volumetric fit gives θ_D of 615(8) K, which is in reasonable agreement with the value of 530 K reported by Ohgushi *et al.* (2008) from measurements of the specific heat between 1.8 K and 300 K; the difference between the two Debye temperatures, at least in part, may arise simply from the much wider temperature range of this experiment. These Debye temperatures are similar to, though a little lower than, that for $CaIrO_3$ (θ_D = 703(11) K) obtained by fitting Equation 9.3 to X-ray powder diffraction data (Lindsay-Scott *et al.*, 2007). The Debye temperature calculated for a (similarly polycrystalline) sample of post-perovskite $CaIrO_3$ using measurements of acoustic velocity data at ambient conditions was lower at 508 K (Liu *et al*., 2011).

It is interesting to compare the value of θ_D for post-perovskite $CaPtO_3$ obtained from thermal expansion with that obtained by Ohgushi *et al*. (2008) from specific heat measurements. By fitting a Debye model to the isobaric heat capacity data for $CaPtO_3$ tabulated by Ohgushi *et al.* (2008), a slightly higher value for θ_D, 545(4) K, than that published was obtained, with a very similar form of misfit between the observed and calculated heat capacity curves (Figure 9-8). On converting the isobaric C_P values to their isochoric equivalents (C_V) by means of the relationship $C_V = C_P - \alpha^2 KVT$, where the values of α and V were taken from this experiment and K was taken from Table 8-2, the value of θ_D = 546(7) K was obtained (Figure 9-9).

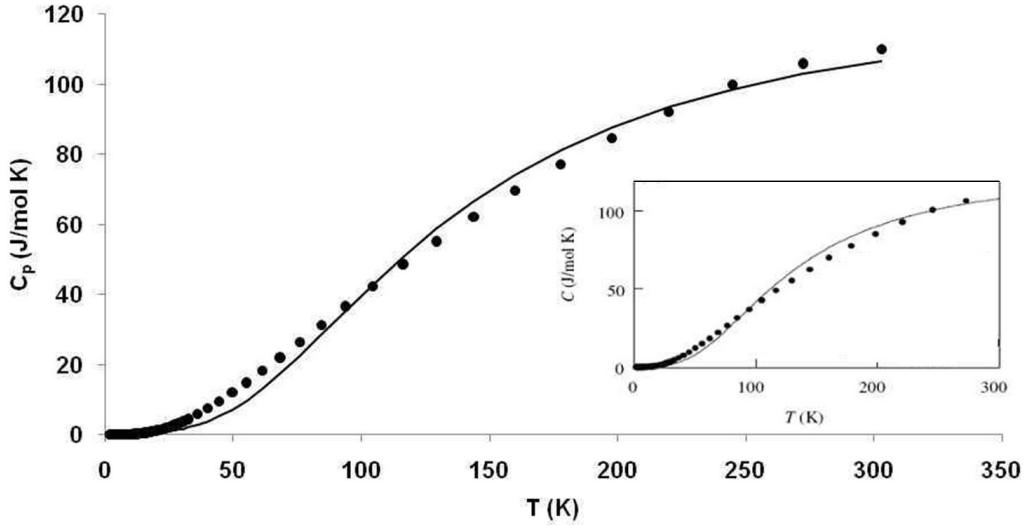

Figure 9-8: The temperature dependence of isobaric specific heat C_p (Ohgushi *et al.*, 2008) for $CaPtO_3$ PPV fitted to a single Debye model. The inset shows the analysis as presented by Ohgushi *et al.* (2008).

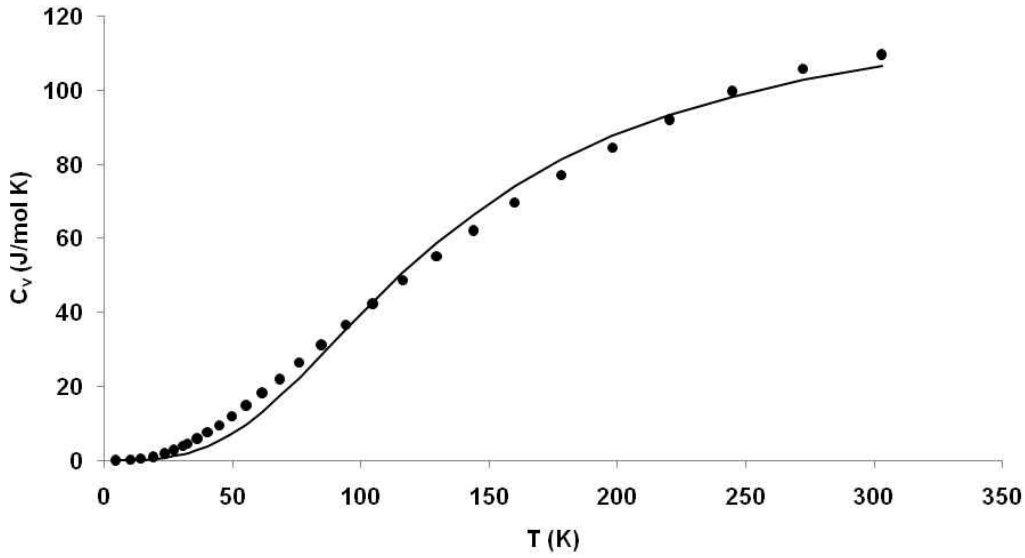

Figure 9-9: The temperature dependence of isochoric specific heat C_v (Ohgushi *et al.*, 2008) for $CaPtO_3$ PPV fitted to a single Debye model.

In fact the specific heat curve can be better represented by a model with two Debye moments with different characteristic temperatures θ_D^A and θ_D^B (Fortes *et al.*, 2008), where the two Debye temperatures correspond to different vibrational wave numbers, such that

$$U(T) = 9\mathrm{N}k_B\left[\, Xf\left(\frac{\theta_D^A}{T}\right) + Yf\left(\frac{\theta_D^B}{T}\right)\right] \tag{9.6}$$

where $f(\theta_D/T)$ is the Debye function, and X and Y are mixing parameters. Fitting C_v using this approach gives $\theta_D^A = 295(4)$ K and $\theta_D^B = 811(3)$ K with X = 0.309(8), Y = 0.829(6) and a much improved fit (Figure 9-10).

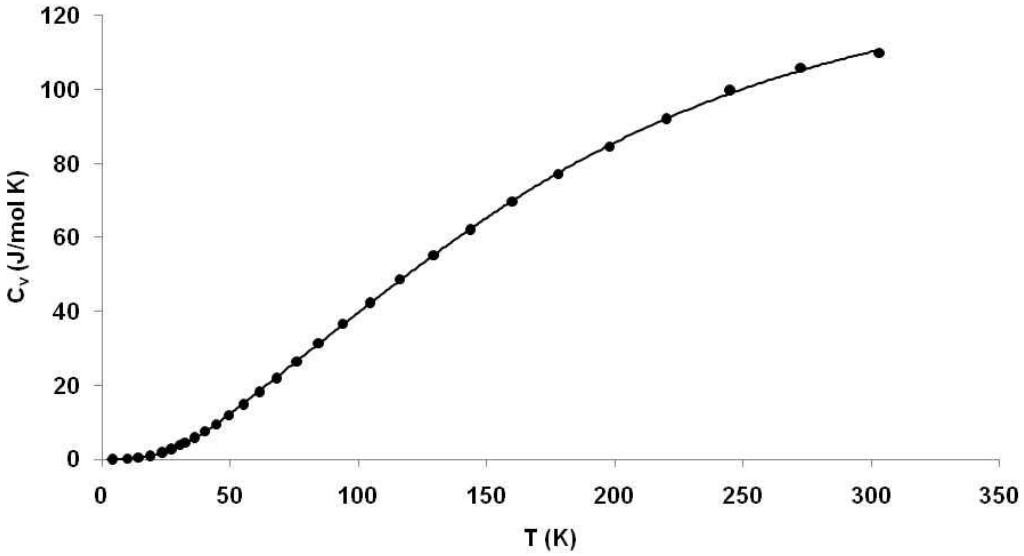

Figure 9-10: The temperature dependence of isochoric specific heat C_v (Ohgushi *et al.*, 2008) for $CaPtO_3$ PPV fitted to a double Debye model.

However, this fit to C_v is not required to tend to the classical value at high temperatures. Constraining to the classical high-temperature limit, such that Y = 1-X, gives $\theta_D^A = 199(45)$ K and $\theta_D^B = 610(6)$ K with X = 0.114(4) Y = 0.886(4) (Figure 9-11). The largest contribution to the specific heat comes from vibrational modes whose characteristic temperature is very similar to the temperature of 615(8) K obtained from fitting *V(T)*.

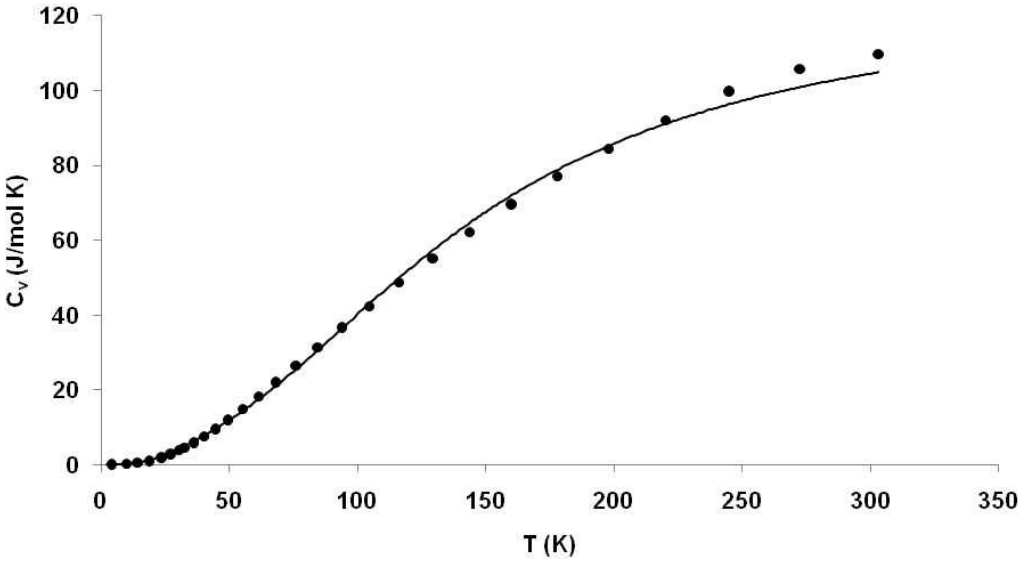

Figure 9-11: The temperature dependence of isobaric specific heat C_v (Ohgushi *et al.*, 2008) for $CaPtO_3$ PPV fitted to a double Debye model with X and Y constrained to the high-temperature classical limit (Y=1-X).

The thermodynamic Grüneisen parameter, γ, is defined as $\gamma = \alpha KV/C_V$, where the specific heat at constant volume, C_V, and that at constant pressure, C_P, are related by $C_P = C_V(1+\alpha\gamma T)$. By combining the thermal expansion measurements made using neutron diffraction with the value of K_0 for $CaPtO_3$ from the X-ray synchrotron experiment (Table 8-2) and with the specific heat measurements of Ohgushi *et al.* (2008), the value of γ was calculated as 1.16(1) at 291 K. This is in good agreement with the value of $\gamma' = 1.21(1)$ obtained from the expression $Q = V_0K_0/\gamma'$, using the data shown in Table 9-5 and the value of K_0 from Table 8-2. It is also in good agreement with the value of the thermodynamic Grüneisen parameter at 291 K obtained within the Debye approximation from the fit to the unit-cell volume (see Wood *et al.*, 2002 and Section 16.1 Appendix D):

$$\gamma = [QV_0/(Q - bU)^2]\, K_T \qquad (9.6)$$

which gives γ =1.23(3).

These values for the Grüneisen parameter are very similar to those calculated for post-perovskite $MgSiO_3$ by Tsuchiya *et al.* (2005). Using density–functional perturbation theory, they concluded that γ for post-perovskite $MgSiO_3$ lies in the range from 1.14 to

1.2 at P = 125 GPa and 300 K < T < 4000 K (i.e. at temperatures through and above the stability field of $MgSiO_3$ post-perovskite). However, although Equation 9.3 provides a reasonable estimate of both θ_D and γ for post-perovskite $CaPtO_3$, it is less successful in producing a correct value for K'_0; the value of b of 3.4(4) in Table 9-5 gives K'_0 = 7.9(8), which is somewhat larger than that determined in the X-ray synchrotron experiment described in Chapter 8 (K'_0 = 4.51(6)).

Previous work on the thermal expansion of post-perovskite $CaIrO_3$ (Lindsay-Scott *et al.*, 2007) used a modification of Equation 9.3 (Section 16.2 Appendix D) to estimate the axial incompressibilities of the material. However, later comparison with the actual axial incompressibilities - determined with a DAC by Boffa-Ballaran *et al.* (2007) - revealed that the estimated values were not correct. In $CaIrO_3$, axial thermal expansion and axial compression are not related to each other in a simple way; for example, although the c-axis of $CaIrO_3$ shortens less than the a-axis under pressure, it expands much more than the a-axis on heating. The present work shows that $CaPtO_3$ also displays behaviour of this type, but that its behaviour differs in detail from that of $CaIrO_3$. For example, in $CaPtO_3$, although the b-axis shortens most under pressure it does not expand most on heating. This point is discussed further in Section 9.4.1 below.

9.3 Crystal structure refinements of post-perovskite $CaPtO_3$

The fractional atomic coordinates and isotropic displacement parameters for post-perovskite $CaPtO_3$ obtained from the Rietveld refinements at high-pressure (at 291 K) are given in Table 9-1; the corresponding values for the measurements made as a function of temperature, at ambient pressure, are given in Table 9-6.

Temp (K)	V/V_0	Vol (Å^3)	a(Å)	b(Å)	c(Å)	Ca y	Ca Uiso	Pt Uiso	O1 y	O1 Uiso	O2 y	O2 z	O2 Uiso	µAh
Cryostat														
2	0.9967	227.173(1)	3.12366(2)	9.90717(6)	7.34081(4)	0.2512(1)	0.39(3)	0.23(2)	0.9177(1)	0.17(3)	0.6285(1)	0.0489(1)	0.41(2)	80
33	0.9967	227.174(2)	3.12362(2)	9.90730(5)	7.34083(4)	0.2515(2)	0.47(4)	0.43(3)	0.9180(2)	0.38(3)	0.6284(1)	0.0488(2)	0.54(3)	60
66	0.9968	227.189(1)	3.12368(2)	9.90746(5)	7.34104(4)	0.2515(2)	0.36(4)	0.25(2)	0.9180(2)	0.18(3)	0.6285(1)	0.0490(1)	0.40(3)	60
100	0.9970	227.234(1)	3.12383(2)	9.90821(5)	7.34163(4)	0.2513(2)	0.41(3)	0.26(2)	0.9179(2)	0.20(3)	0.6284(1)	0.0489(1)	0.40(2)	60
133	0.9973	227.304(1)	3.12406(2)	9.90935(5)	7.34249(4)	0.2514(2)	0.39(3)	0.22(2)	0.9179(2)	0.20(3)	0.6284(1)	0.0490(1)	0.38(2)	60
150	0.9975	227.352(1)	3.12424(1)	9.91004(5)	7.34310(4)	0.2515(2)	0.42(3)	0.28(2)	0.9179(1)	0.24(3)	0.6284(1)	0.0489(1)	0.40(2)	80
166	0.9977	227.399(1)	3.12439(2)	9.91072(5)	7.34378(4)	0.2512(2)	0.45(3)	0.25(2)	0.9178(2)	0.22(3)	0.6283(1)	0.0490(1)	0.42(2)	60
200	0.9982	227.517(1)	3.12483(2)	9.91251(5)	7.34520(4)	0.2512(2)	0.47(4)	0.26(2)	0.9179(2)	0.25(3)	0.6284(1)	0.0491(1)	0.41(3)	60
233	0.9988	227.645(1)	3.12530(2)	9.91439(5)	7.34682(4)	0.2515(2)	0.49(4)	0.25(2)	0.9177(2)	0.28(3)	0.6284(1)	0.0492(1)	0.42(3)	60
266	0.9994	227.789(1)	3.12587(2)	9.91650(5)	7.34858(4)	0.2510(2)	0.58(4)	0.26(2)	0.9179(2)	0.33(3)	0.6284(1)	0.0492(1)	0.44(3)	100
300	1.0001	227.949(1)	3.12649(1)	9.91885(5)	7.35054(3)	0.2512(2)	0.62(3)	0.23(2)	0.9182(2)	0.43(3)	0.6286(1)	0.0487(1)	0.50(2)	80
Furnace														
291	1.0000	227.918(2)	3.12633(2)	9.91857(6)	7.35012(4)	0.2513(3)	0.88(5)	0.40(3)	0.9181(2)	0.54(4)	0.6285(2)	0.0485(2)	0.70(3)	160
373	1.0019	228.342(2)	3.12798(2)	9.92472(6)	7.35534(5)	0.2511(3)	1.17(5)	0.48(3)	0.9184(2)	0.82(4)	0.6284(2)	0.0486(2)	0.84(3)	160
473	1.0043	228.905(2)	3.13016(2)	9.93278(7)	7.36237(5)	0.2511(3)	1.25(6)	0.34(3)	0.9192(3)	1.05(5)	0.6289(2)	0.0484(2)	0.79(4)	160
573	1.0070	229.512(2)	3.13244(2)	9.94128(7)	7.37020(5)	0.2505(3)	1.41(7)	0.39(3)	0.9195(3)	1.22(5)	0.6286(2)	0.0481(2)	0.95(4)	160
673	1.0097	230.118(2)	3.13480(2)	9.94984(7)	7.37776(5)	0.2509(3)	1.47(6)	0.46(3)	0.9198(3)	1.17(5)	0.6281(2)	0.0480(2)	1.03(4)	160
773	1.0124	230.743(2)	3.13724(2)	9.95882(7)	7.38539(5)	0.2514(3)	1.57(7)	0.66(4)	0.9199(3)	1.26(6)	0.6277(2)	0.0478(2)	1.09(4)	160
869	1.0152	231.392(2)	3.13966(2)	9.96858(6)	7.39322(5)	0.2515(3)	1.79(6)	0.78(3)	0.9200(3)	1.39(5)	0.6276(2)	0.0476(2)	1.21(4)	160

Table 9-6: Unit-cell volume, unit-cell parameters, atomic coordinates and isotropic atomic displacement parameters (Uiso) for $CaPtO_3$ as a function of temperature (60-160 µAh cumulative beam current, Rietveld refinement) at ambient pressure. Uiso values are x 10^2 Å^2. V_0 was taken as the volume at 291K. The numbers in parentheses are estimated standard uncertainties and refer to the least-significant digits.

Figure 9-12 shows the fractional coordinates both on compression at ambient temperature (solid symbols) and on cooling/heating at ambient pressure (open symbols), plotted as a function of V/V_0, to enable comparison of the behaviour of the material as either P or T is varied. V_0 is taken to be the unit-cell volume at $T = 291$ K and $P = 0$ (strictly, 0.1 MPa).

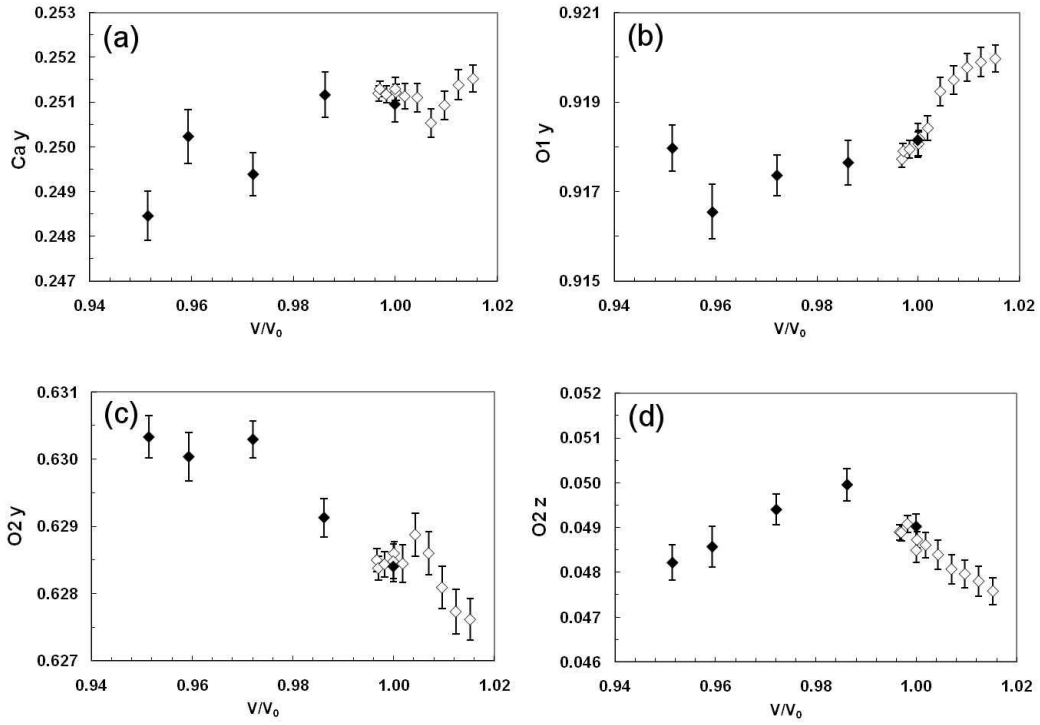

Figure 9-12: $CaPtO_3$ fractional atomic coordinates: (a) Ca y; (b) O1 y; (c) O2 y; (d) O2 z. Solid symbols are data from compression at 291 K, open symbols from cooling/heating at ambient pressure; to improve legibility, only selected data points from the sample in the cryostat (2 K, 100 K, 200 K and 300 K) have been plotted.

Data collected either in the cryostat below 291K or on compression have $V/V_0 < 1$; points for which $V/V_0 > 1$ correspond to the ambient-pressure isobar above 291 K (note that to improve legibility, in Figure 9-12 to Figure 9-15, only selected data points from the sample in the cryostat, at 2 K, 100 K, 200 K and 300 K, have been plotted). The fractional coordinates from all three experiments (i.e. pressure cell, cryostat and furnace) show good agreement for $V/V_0 = 1$ with the measured values at 291 K consistent within one estimated standard uncertainty between the compression, cryostat and furnace experiments. Although the changes in the fractional atomic

coordinates are very small (< 0.0035 in all cases), the systematic trends that can be observed in Figure 9-12 are probably meaningful.

As described in Section 1.4, the post-perovskite $CaPtO_3$ structure may be defined in terms of the four bond lengths Pt-O1, Pt-O2, Ca-O1 and Ca-O2 and the three angles Δ_1, Δ_2 and p required to define the geometry of the PtO_6 octahedron and its orientation within the unit cell.

The values of these four cation-anion distances for both the 291 K isotherm and the ambient-pressure isobar are listed in Table 9-7 and shown in Figure 9-13; a fifth Ca-O bond length (Ca-O2′) corresponding to the distance between the Ca ion and the O^{2-} ions that cap the prism faces of the CaO_8 coordination hendecahedron is included for completeness. Since only the Bragg reflections have been considered in the data analysis, the bond distances discussed here correspond to the interatomic separations in the average crystal structure, uncorrected for thermal motion.

The structural analysis spreadsheet (see Section 3.9.2) was used to calculate atomic positions, interatomic distances, angles and volumes using unit-cell parameter and atomic coordinate data from the Rietveld refinements. Errors in the unit-cell parameters and atomic coordinates were taken from the Rietveld refinements. The standard uncertainty in each interatomic distance, angle and volume was calculated by combining errors in unit-cell parameters and atomic coordinates.

V/V_0	Pressure (GPa)	Pt-O1(Å)	Pt-O2(Å)	Ca-O1(Å)	Ca-O2(Å)	Ca-O2′(Å)	Δ_1^o	Δ_2^o	p^o	V_{hen}(Å^3)	V_{oct}(Å^3)	V_{void}(Å^3)
0.9514	9.27(7)	1.987(5)	2.022(5)	2.243(5)	2.416(5)	2.464(4)	24.03(16)	15.51(13)	99.34(27)	23.535(56)	10.565(14)	20.964(45)
0.9593	7.69(9)	1.988(6)	2.030(5)	2.243(6)	2.428(5)	2.463(5)	23.85(19)	15.57(15)	99.16(31)	23.744(64)	10.669(17)	20.696(57)
0.9721	5.07(7)	1.995(5)	2.033(4)	2.262(5)	2.436(4)	2.488(4)	23.84(14)	15.92(11)	99.43(24)	24.203(51)	10.741(13)	20.460(53)
0.9862	2.38(7)	2.001(5)	2.040(4)	2.266(5)	2.457(5)	2.497(4)	23.78(16)	16.13(12)	99.54(25)	24.663(56)	10.848(14)	20.264(67)
0.9999	0.02(5)	2.008(4)	2.046(3)	2.281(4)	2.472(4)	2.504(3)	23.76(12)	15.84(9)	99.63(19)	25.082(44)	10.946(11)	20.124(57)
	Temperature (K)											
Cryostat												
0.9967	2	2.008(2)	2.047(2)	2.272(2)	2.469(2)	2.497(1)	23.95(6)	15.75(4)	99.48(9)	24.898(19)	10.949(5)	20.946(20)
0.9967	33	2.007(2)	2.046(2)	2.271(2)	2.471(2)	2.495(2)	23.88(5)	15.73(5)	99.52(12)	24.924(24)	10.938(6)	20.932(25)
0.9968	66	2.007(2)	2.047(2)	2.272(2)	2.470(2)	2.496(2)	23.87(5)	15.78(4)	99.48(10)	24.921(20)	10.945(5)	20.932(21)
0.9970	100	2.008(2)	2.046(2)	2.273(2)	2.470(2)	2.497(2)	23.90(5)	15.76(4)	99.53(10)	24.930(20)	10.940(5)	20.938(20)
0.9973	133	2.008(2)	2.046(2)	2.272(2)	2.471(2)	2.498(2)	23.90(5)	15.80(4)	99.51(10)	24.935(20)	10.947(5)	20.944(21)
0.9975	150	2.008(2)	2.047(2)	2.271(2)	2.472(2)	2.496(1)	23.90(5)	15.75(4)	99.50(9)	24.937(19)	10.950(5)	20.951(20)
0.9977	166	2.009(2)	2.046(2)	2.273(2)	2.470(2)	2.499(2)	23.94(5)	15.79(4)	99.53(10)	24.942(20)	10.950(5)	20.958(21)
0.9982	200	2.008(2)	2.047(2)	2.275(2)	2.470(2)	2.500(2)	23.89(5)	15.81(4)	99.48(10)	24.954(22)	10.962(5)	20.963(22)
0.9988	233	2.010(2)	2.047(2)	2.270(2)	2.472(2)	2.500(2)	23.96(5)	15.86(4)	99.50(10)	24.958(22)	10.970(5)	20.983(23)
0.9994	266	2.009(2)	2.048(2)	2.277(2)	2.469(2)	2.503(2)	23.90(5)	15.84(4)	99.48(10)	24.985(21)	10.975(5)	20.987(22)
1.0001	300	2.009(2)	2.049(2)	2.277(2)	2.472(2)	2.499(2)	23.83(5)	15.68(4)	99.44(9)	25.001(20)	10.983(5)	21.003(20)
Furnace												
1.0000	291	2.009(2)	2.048(2)	2.276(2)	2.474(2)	2.497(2)	23.86(7)	15.63(6)	99.50(13)	25.009(28)	10.968(7)	21.002(29)
1.0019	373	2.009(2)	2.049(2)	2.281(3)	2.474(3)	2.500(2)	23.77(7)	15.67(6)	99.50(14)	25.079(30)	10.984(7)	21.023(31)
1.0043	473	2.008(3)	2.053(3)	2.289(3)	2.475(3)	2.500(3)	23.55(9)	15.55(7)	99.34(16)	25.142(34)	11.026(8)	21.059(35)
1.0070	573	2.009(3)	2.053(3)	2.297(3)	2.477(3)	2.504(3)	23.48(9)	15.49(7)	99.47(16)	25.263(34)	11.022(8)	21.093(35)
1.0097	673	2.010(3)	2.051(3)	2.298(3)	2.484(3)	2.506(3)	23.40(8)	15.52(7)	99.68(16)	25.411(33)	11.006(8)	21.113(34)
1.0124	773	2.011(3)	2.050(3)	2.297(3)	2.491(3)	2.507(3)	23.37(9)	15.51(7)	99.83(16)	25.534(35)	11.003(9)	21.150(36)
1.0152	869	2.013(3)	2.051(2)	2.299(3)	2.496(3)	2.508(3)	23.35(9)	15.46(7)	99.89(15)	25.628(33)	11.018(8)	21.202(33)

Table 9-7: Bond lengths and bond angles calculated for $CaPtO_3$ as a function of V/V_0. In compression, V_0 was taken to be the EOS value shown in Table 9-4. On cooling/heating, V_0 was taken to be the measured value at 291 K. The numbers in parentheses are estimated standard uncertainties and refer to the least-significant digits.

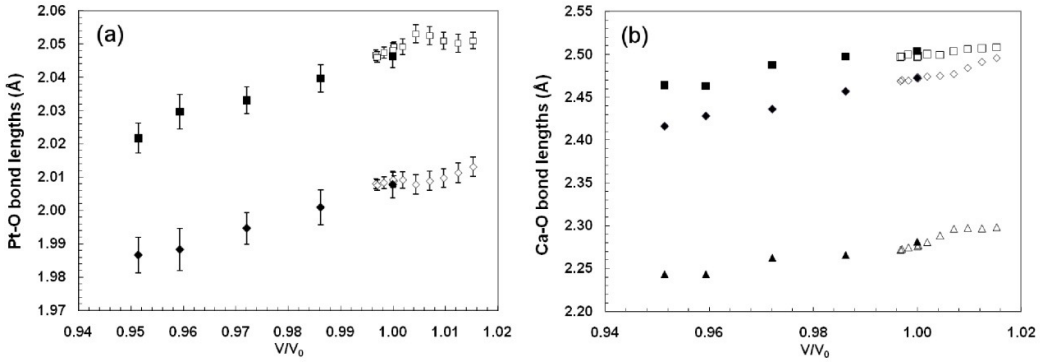

Figure 9-13: $CaPtO_3$ bond lengths: (a) Pt-O bonds: Squares – Pt-O2. Diamonds – Pt-O1. (b) Ca-O bonds: Squares – Ca-O2'. Diamonds – Ca-O2. Triangles – Ca-O1. Estimated uncertainties in the Ca-O bond distances are the same size as symbols (due to the larger vertical scale). Solid symbols are for data obtained on compression, open symbols from cooling/heating at ambient pressure. To improve legibility, only selected data points from the sample in the cryostat (2 K, 100 K, 200 K and 300 K) have been plotted.

The angles Δ_1, Δ_2 and p are listed in Table 9-7 and shown in Figure 9-14. Figure 9-15 shows the changes in the volumes of the CaO_8 coordination hendecahedron, the PtO_6 octahedron and the void space in the unit cell not occupied by hendecahedra or octahedra (numerical values are listed in Table 9-7). Finally, the seven shortest oxygen-oxygen distances are shown in Figure 9-16.

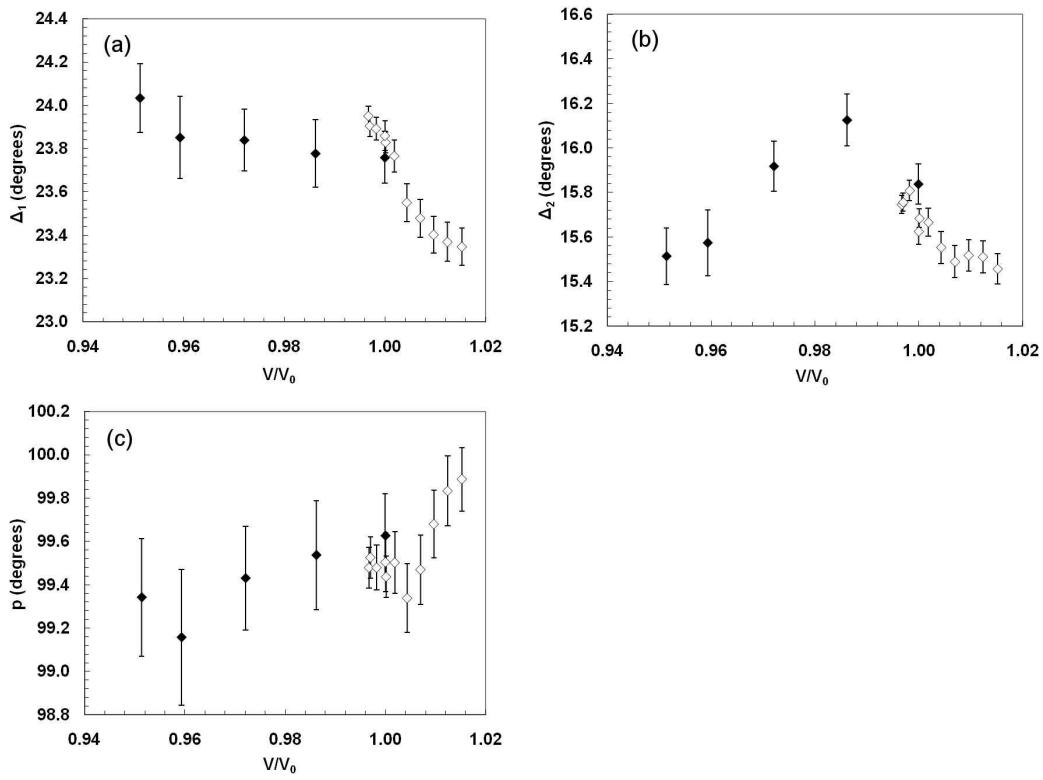

Figure 9-14: $CaPtO_3$ angles: (a) Δ_1; (b) Δ_2; (c) p. Solid symbols are for data obtained on compression, open symbols from cooling/heating at ambient pressure. To improve legibility, only selected data points from the sample in the cryostat (2K, 100K, 200K and 300K) have been plotted.

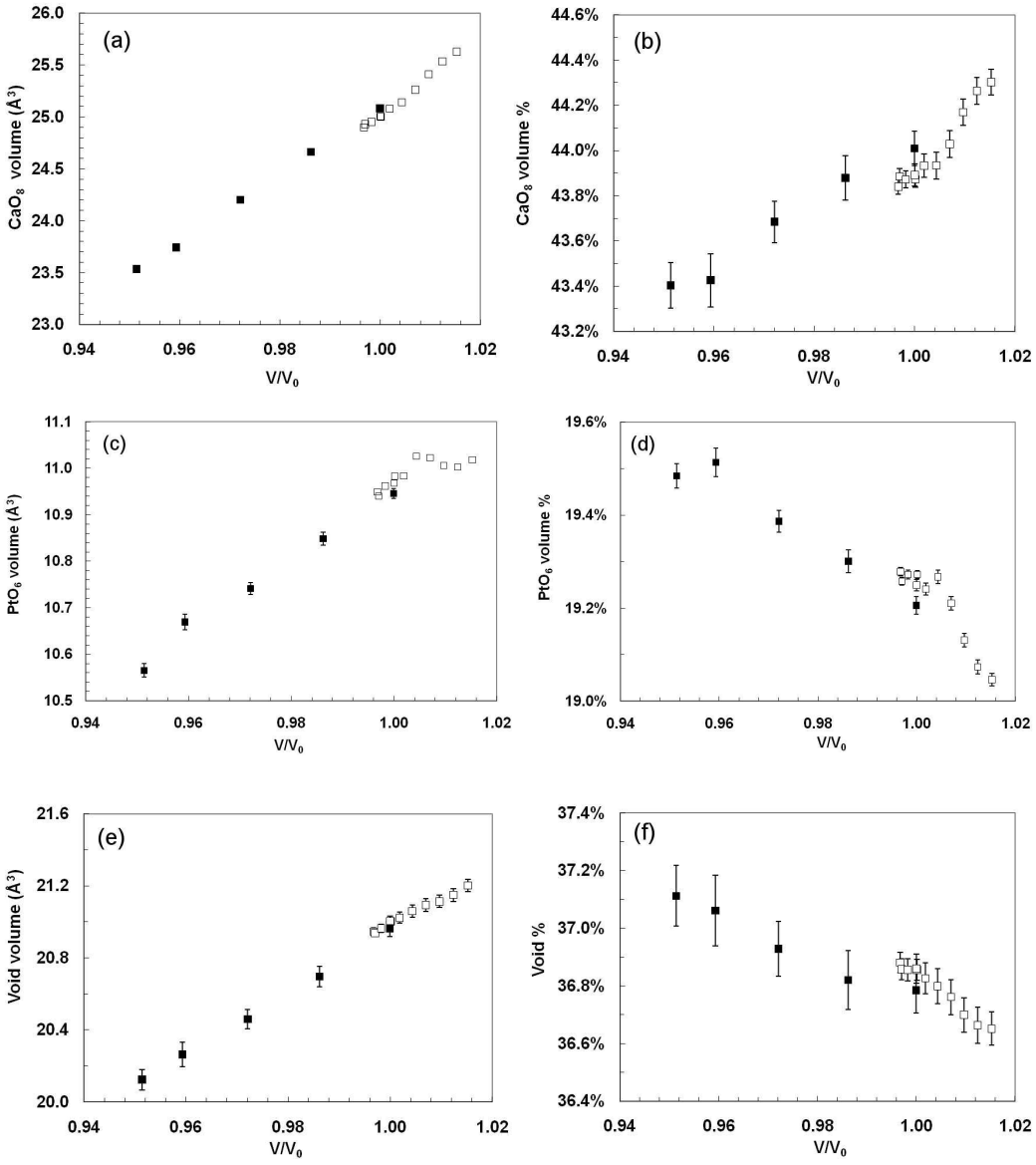

Figure 9-15: $CaPtO_3$ volumes: (a) CaO_8 hendecahedron; (b) CaO_8 hendecahedron volume as a percentage of unit-cell volume; (c) PtO_6 octahedron; (d) PtO_6 octahedron as a percentage of unit-cell volume; (e) Void volume; (f) Void volume as a percentage of unit-cell volume. Solid symbols are for data obtained on compression, open symbols from cooling/heating at ambient pressure. To improve legibility, only selected data points from the sample in the cryostat (2 K, 100 K, 200 K and 300 K) have been plotted. Where they are not indicated, estimated standard uncertainties are smaller than the symbols.

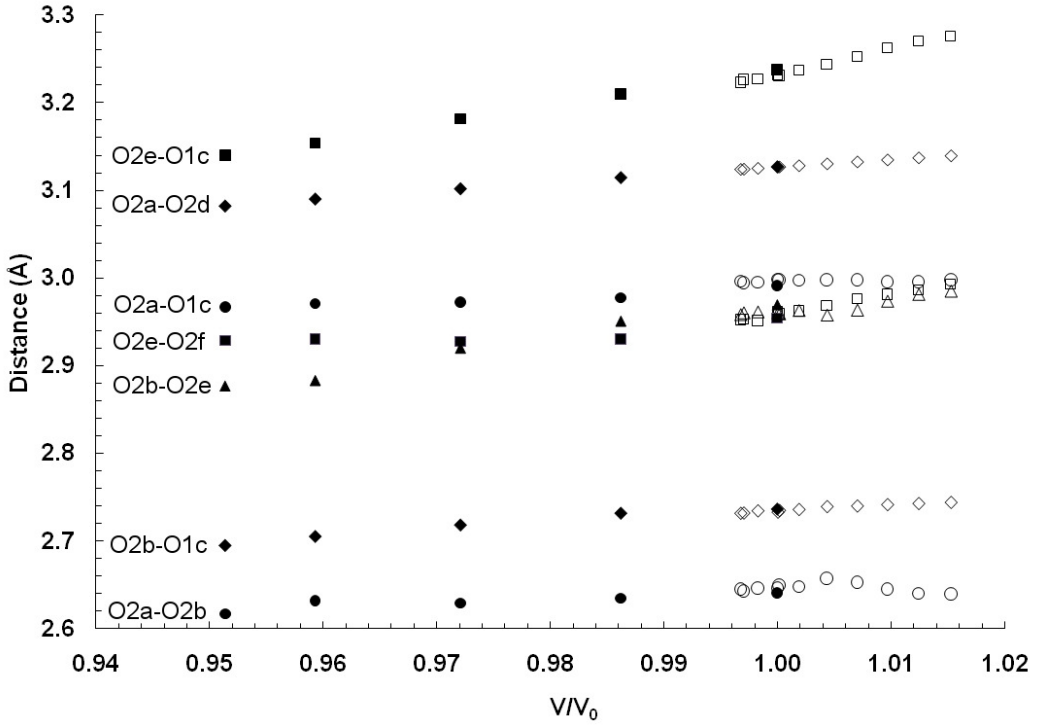

Figure 9-16: $CaPtO_3$ oxygen-oxygen distances. Solid symbols are for data obtained on compression, open symbols from cooling/heating at ambient pressure. To improve legibility, only selected data points from the sample in the cryostat (2 K, 100 K, 200 K and 300 K) have been plotted. See Figure 1-1 and Figure 1-4 for the key to the oxygen anion positions. O2a-O2b and O2a-O2d form the shorter and longer sides of the central plane of the octahedron respectively. O2b-O1c and O2a-O1c form the shorter and longer distances from the central plane O2 anions to the apical anion. O2a-O2d (equal to the cell parameter *a*) is the length of the trigonal prism component of the CaO_8 hendecahedron along [100]. O2e-O1c is the length of the two equal sides of the isosceles triangle defining the trigonal prism component of the hendecahedron, and O2e-O2f is the length of its base. O2b-O1c forms the shorter of the two sides of the hendecahedral prism cap; O2b-O2e is the longer of the two sides of the prism cap. Estimated standard uncertainties are smaller than the symbols.

The isotropic displacement parameters from the Rietveld refinements, listed in Table 9-1 and in Table 9-6, show the expected form, increasing with temperature and decreasing slightly with pressure. In general, they take the form $U_{Pt} < U_{O1} \approx U_{O2} < U_{Ca}$. However, the refined values are sensitive to both the absorption correction applied to the data and to the preferred orientation correction, showing a marked increase (~0.002 $Å^2$) at room temperature between the values determined with the sample in the cryostat

and in the furnace. For this reason they have not been interpreted in terms of the vibrational frequencies of the atoms as has been done previously for perovskites (e.g. Wood *et al.*, 2002).

Although these data were not sufficiently good to allow anisotropic atomic displacements to be used in general, the datasets collected at the three highest useable temperatures (673 K and above) were refined against such a model. The resulting displacement parameters from the refinement at 869 K are shown in Table 9-8, Figure 9-17 and Figure 9-18. The average U_{ij} values taken over the three refinements at 673 K, 773 K and 869 K are quite similar in form to those shown in the Table.

	U_{11}	U_{22}	U_{33}	U_{23}
Ca	1.74(16)	1.12(17)	2.43(17)	-
Pt	0.91(8)	0.69(9)	0.72(7)	0.03(5)
O1	2.28(14)	0.85(12)	1.06(13)	-
O2	1.78(10)	0.45(10)	1.22(9)	-0.19(6)

Table 9-8: Anisotropic atomic displacement parameters of $CaPtO_3$ at 869 K ($Å^2$ x 100). The numbers in parentheses are estimated standard uncertainties and refer to the least-significant digits.

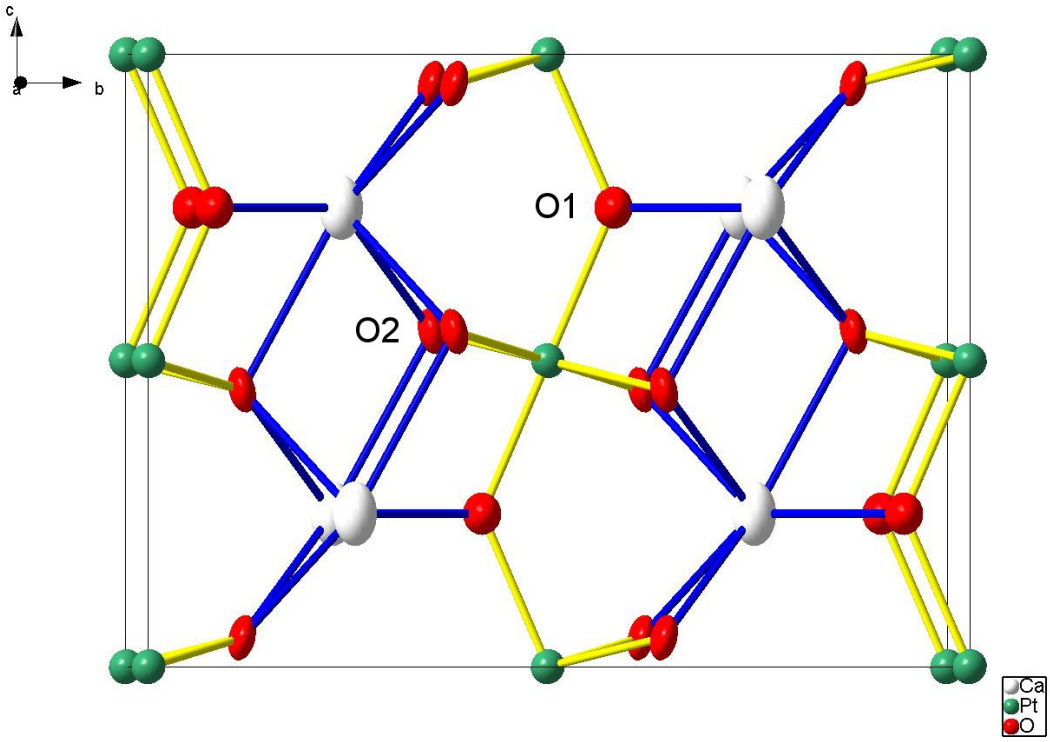

Figure 9-17: $CaPtO_3$ displacement ellipsoids at 869K drawn at the 90% level viewed along the *a*-axis.

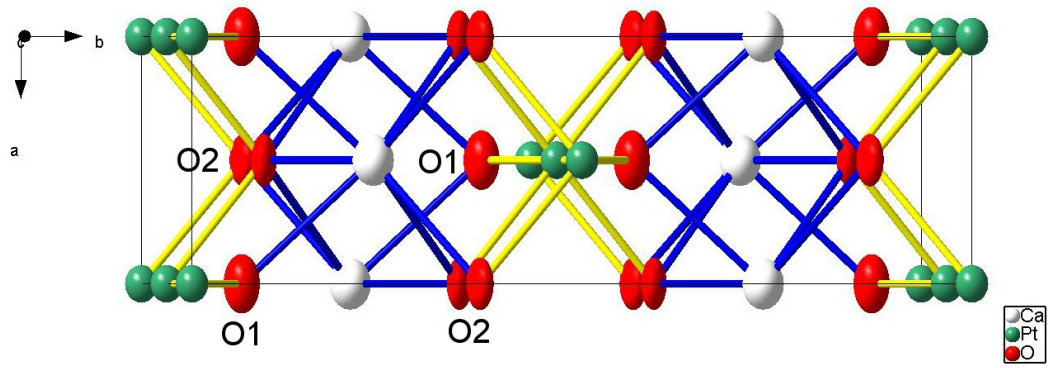

Figure 9-18: $CaPtO_3$ displacement ellipsoids at 869K drawn at the 90% level viewed along the *c*-axis.

Although the site symmetry of all four atoms allows the atomic probability density to take the form of triaxial ellipsoids, it also requires that, for Ca and O1, the principal axes of these ellipsoids must lie parallel to the unit-cell axes. For Pt and O2, the ellipsoids are allowed one degree of rotational freedom, about a line parallel to [100]. The probability ellipsoid of the O1 (apical) oxygen ion is a prolate spheroid, with the

largest component of vibration along [100], which would correspond to a buckling of the rods of PtO_6 octahedra about the shared edge "hinges". In contrast, the ellipsoids corresponding to the Ca and O2 ions are oblate spheroids, with their smallest components parallel or nearly parallel (inclined at 13°) to the *b*-axis of the unit cell. As might be expected, the ellipsoid of the Pt atom is the smallest in magnitude and the most isotropic.

There are currently no published single-crystal measurements of the anisotropic displacement parameters of any oxide post-perovskite at high-temperature. Two previous single-crystal X-ray diffraction studies of $CaIrO_3$ post-perovskite have been reported, but only at room temperature. Sugahara *et al*. (2008) found a high degree of anisotropy in the atomic displacements, a result which was disputed by Hirai *et al.* (2009) who suggested that it was possibly an artefact resulting from an inadequate absorption correction; the absorption coefficient of $CaIrO_3$, even for Mo radiation, is very high, being ~61 mm^{-1} (see Section 7.2.1). At room temperature, Hirai *et al.* (2009) found that there was no significant anisotropy in the atomic displacement parameters of any atoms. However, they did conclude that, despite its larger mass, the displacement parameters for the Ca ions were of the same magnitude as those of the O^{2-} ions. This observation is in agreement with the results shown in Table 9-8 for $CaPtO_3$.

9.4 Post-perovskite structures in compression and expansion

9.4.1 $CaPtO_3$, $CaIrO_3$ and $MgSiO_3$ – unit-cells, *P* and *T*

If a post-perovskite material is to be a "successful analogue" of post-perovskite $MgSiO_3$, its cell parameters should respond at ambient pressure and temperature to pressure and temperature in a similar way to those of post-perovskite $MgSiO_3$ at lower-mantle pressures and temperatures. However, the present work has shown that although the anisotropy of axial compression of post-perovskite $CaPtO_3$ (and that of post-perovskite $CaIrO_3$) is similar to that of post-perovskite $MgSiO_3$, the anisotropy of axial thermal expansion in post-perovskite $CaPtO_3$ differs both from that of post-perovskite $MgSiO_3$ and from that of post-perovskite $CaIrO_3$. Axial compression and expansion can be compared for $MgSiO_3$, $CaPtO_3$ and $CaIrO_3$ (and also with the bulk properties of the materials) by plotting the cubes of axial compression and expansion

ratios $(i/i_0)^3$ (where $i = a$, b or c unit-cell parameter) against V/V_0. Figure 9-19a shows such a plot for post-perovskite $MgSiO_3$ at high-pressure and temperature, obtained using EOS derived from experiment (Guignot *et al.*, 2007).

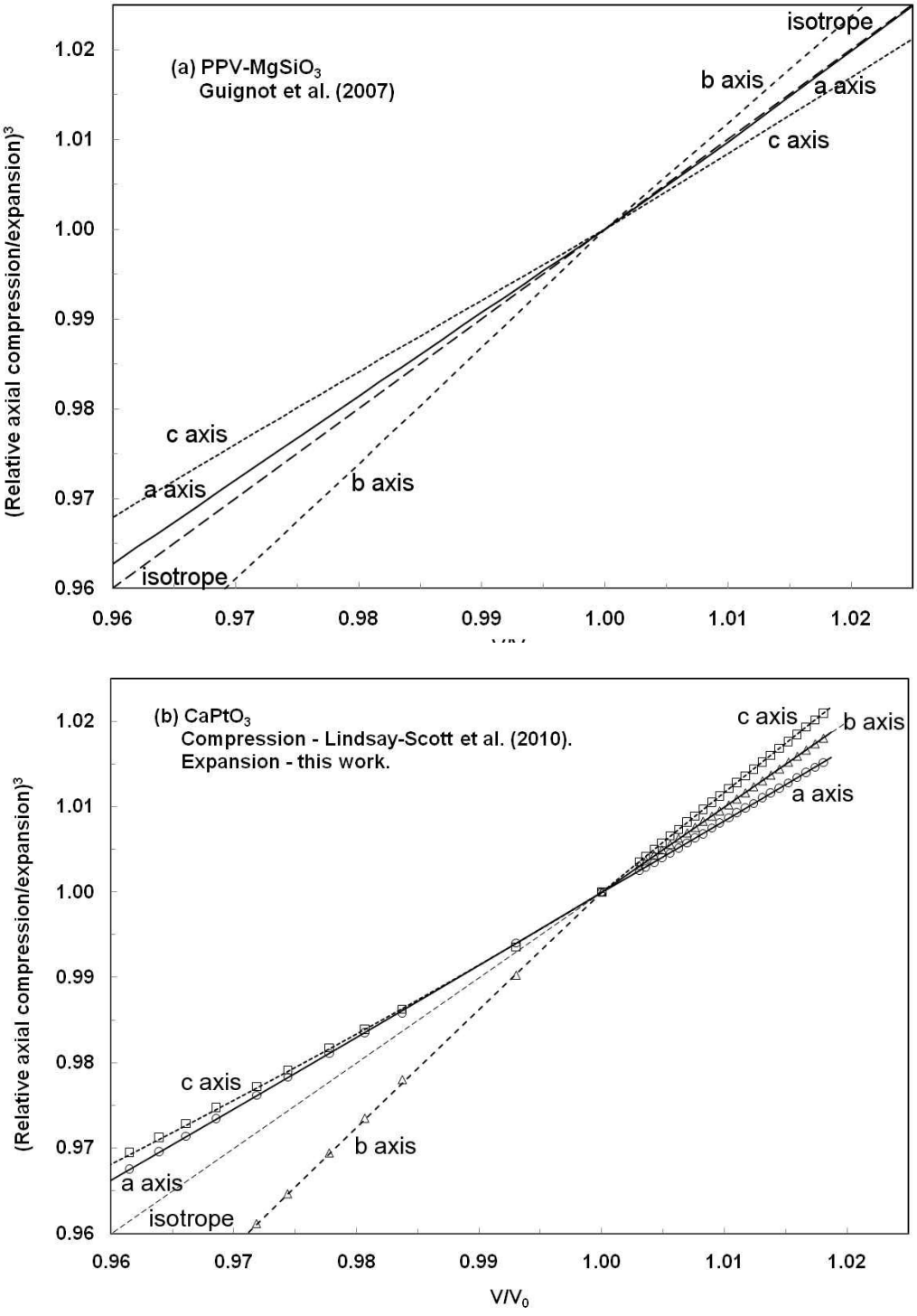

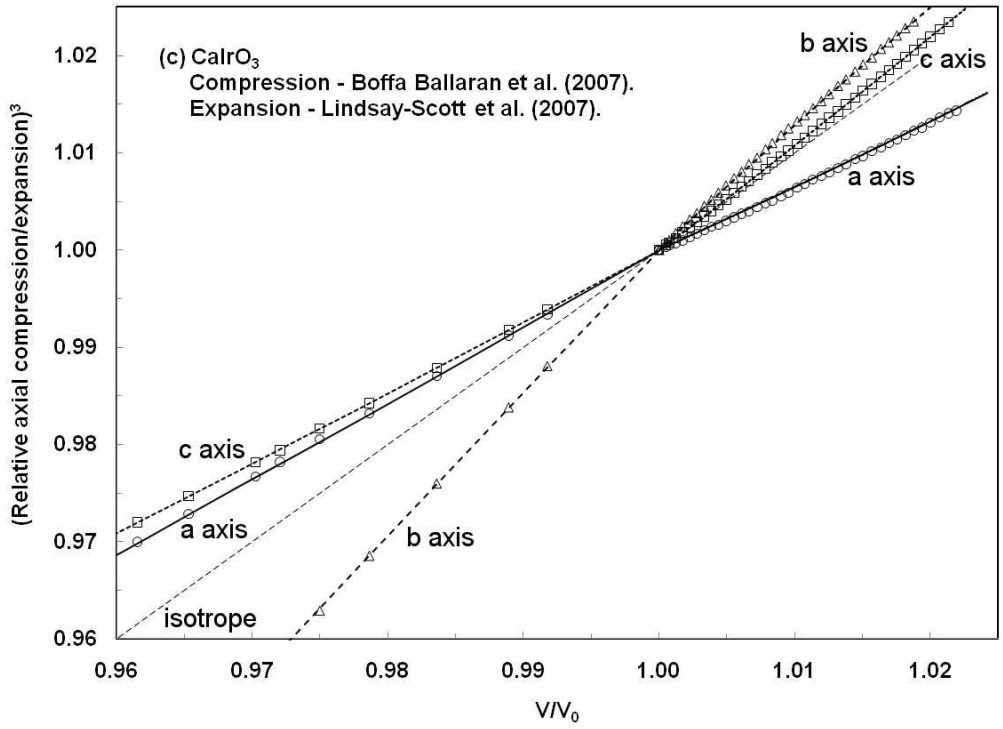

Figure 9-19: Axial expansion and compression of (a) $MgSiO_3$ (from Guignot *et al.*, 2007) (b) $CaPtO_3$ (compression: synchrotron X-ray powder diffraction (Chapter 8; expansion: this Chapter) and (c) $CaIrO_3$ (compression: Boffa Ballaran *et al.*, 2007; expansion: Lindsay-Scott *et al.*, 2007). The axial expansion and compression are shown as the ratios $(i/i_0)^3$, where $i = a$, b or c unit-cell parameters. Experimental values are shown as points in (b) and (c), with lines showing their fit to third-order Birch-Murnaghan EOSs (compression) or to thermal expansion models; the lines shown in (a) indicate values derived from EOSs. The isotrope where $(i/i_0)^3 = (V/V_0)$ is shown as a dashed line. A V_0 value of 1.0 in (b) and (c) corresponds to ambient temperature and pressure; a V_0 value of 1.0 in (a) corresponds to 137.3 GPa and 2535 K (Guignot *et al.*, 2007). Points for which $V/V_0 < 1$ correspond to compression of the material; points for which $V/V_0 > 1$ correspond to thermal expansion on heating. In (b) and (c), error bars on the experimental values are smaller than the symbols used. Note also that the results of Martin *et al.* (2007a) for post-perovskite $CaIrO_3$ are very similar to those shown in (c).

For $MgSiO_3$ the axial compression sequence $\kappa_c > \kappa_a > \kappa_b$ (where κ_i are axial incompressibilities) is the reverse of the expansion sequence $\alpha_b > \alpha_a > \alpha_c$. For post-perovskite $CaPtO_3$ (Figure 9-19b) the behaviour on compression is quite similar to that of post-perovskite $MgSiO_3$, though $CaPtO_3$ shows greater anisotropy. In particular, the behaviour of the *b*-axis of $CaPtO_3$ in expansion is almost identical to that of the unit-

cell volume, i.e. to the isotrope. However, although post-perovskite $CaPtO_3$ has the same axial compression sequence $\kappa_c > \kappa_a > \kappa_b$ as post-perovskite $MgSiO_3$, it shows a different thermal expansion sequence, with $\alpha_c > \alpha_b > \alpha_a$; the *b*-axis in $CaPtO_3$ expands much less when heated than might naively be expected from its change in length on compression, and the *c*-axis expands more.

$CaIrO_3$ (Figure 9-19c) has the same axial compression sequence as both $MgSiO_3$ and $CaPtO_3$ (though with a slightly greater anisotropy than $CaPtO_3$), but on expansion the sequence $\alpha_b > \alpha_c > \alpha_a$ is observed. This is partly explained by the greater deviation of the behaviour of the *b*-axis in $CaIrO_3$ from that of the isotrope; if the $CaIrO_3$ *b*-axis were closer to the isotrope in compression, and if its slope in expansion maintained the same angular offset to the slope in compression, then the slope of the $CaIrO_3$ *b*-axis in expansion would be nearly coincident with that of the *c*-axis.

The change of slope from compression to expansion for each axis is illustrated in Figure 9-20. A negative percentage change (on the *y*-axis of this Figure) indicates a "convex" (as viewed from the top of Figure 9-19) pair of compression-expansion lines for the *a*, *b* or *c*-axes, where an axis is less expansible than would be expected by extrapolation of its compressibility. A positive percentage change indicates the reverse. Figure 9-20 shows that the *b*-axis of each of the three post-perovskites is less expansible than expected from an extrapolation of its compressibility, and their *c*-axes are more expansible. Both $CaPtO_3$ and $CaIrO_3$ show *c*-axes which are more expansible than expected from their compressibilities.

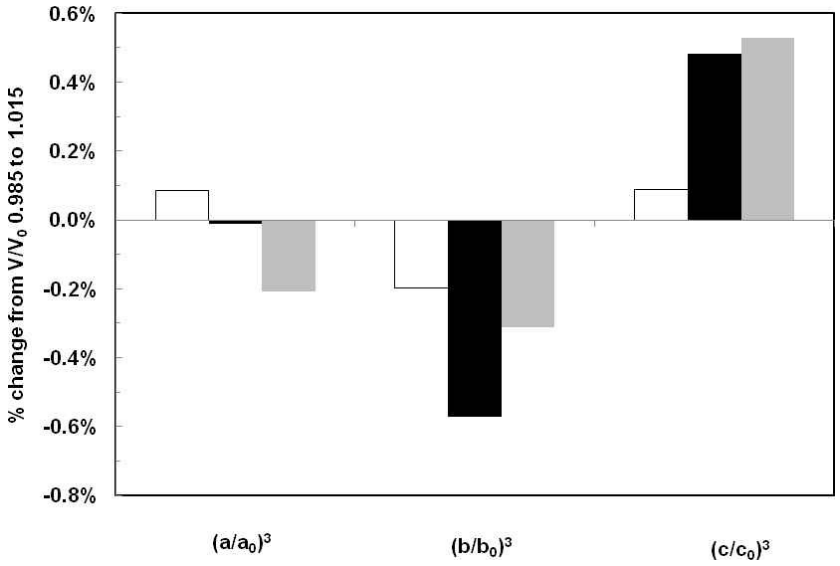

Figure 9-20: Change of slope from axial compression (V/V_0 = 0.985) to axial expansion (V/V_0 = 1.015) for post-perovskites. Open bars – $MgSiO_3$. Black bars – $CaPtO_3$. Grey bars – $CaIrO_3$. Data is taken from Figure 9-19.

However, it should be borne in mind that, since the purpose of this study is to investigate low-pressure analogue phases of $MgSiO_3$, V_0 is determined at ambient pressure and temperature from the $CaPtO_3$ and $CaIrO_3$ experiments, while for $MgSiO_3$ V_0 is calculated at 137.3 GPa and 2535 K. The effect on compressibility of the change in pressure from 0 GPa to 136 GPa will be much greater than that of the change in temperature from 298 K to 2535 K. So the change in axial behaviour shown in the $MgSiO_3$ data may be dominated by the effect of the high-pressure regime. If this is so it will not be directly comparable to the change from compression to expansion at 0 GPa in $CaPtO_3$ and $CaIrO_3$.

The changes in pressure and temperature across the D" layer between depths of 2590 km and 2890 km are predicted to be from 118 GPa to 136 GPa (Dziewonski and Anderson, 1981) and from ~2600 K to 3700–4100 K (Trønnes, 2010). The EOSs for $MgSiO_3$ post-perovskite (Guignot *et al.*, 2007) predict that an isothermal change in pressure from 118 GPa to 136 GPa will result in a change at 2535 K in V/V_0 of of 3.1%, while an isobaric change in temperature from 2600 K to 3700 K or to 4100 K will result in changes in V/V_0 of 1.4% and 2.0% respectively. So the change in volume of $MgSiO_3$ post-perovskite due to the change in temperature across the D" layer is significant compared with that due to the change in pressure. Analogue materials

should, ideally, show a response to both temperature and pressure which is similar to that of $MgSiO_3$. The differences in the axial expansion behaviours of $CaPtO_3$ and $CaIrO_3$ at 0 GPa from that of $MgSiO_3$ at high-pressure may, therefore, significantly weaken the case for the use of $CaPtO_3$ and $CaIrO_3$ as low-pressure analogues of $MgSiO_3$ at elevated temperatures.

The changes of slope from compression to expansion for the *b* and *c*-axes of $CaPtO_3$ are reflected in corresponding changes of slope for two of the inter-octahedral O-O distances shown in Figure 9-16. These two O-O distances are compared with unit-cell parameters *b* and *c* in Figure 9-21; the distance O2e-O2f forms one edge of the base of the trigonal CaO_8 prism parallel to the *c*-axis, and the distance O2b-O2e is the edge of the prism's cap sub-parallel with the *b*-axis (see Figure 1-1). The distance (O2b-O2e)′ shown in Figure 9-21b is the projection of O2b-O2e onto [010]. Ad-hoc scaling offsets are used to bring the *b* and *c*-axis measurements onto the plots.

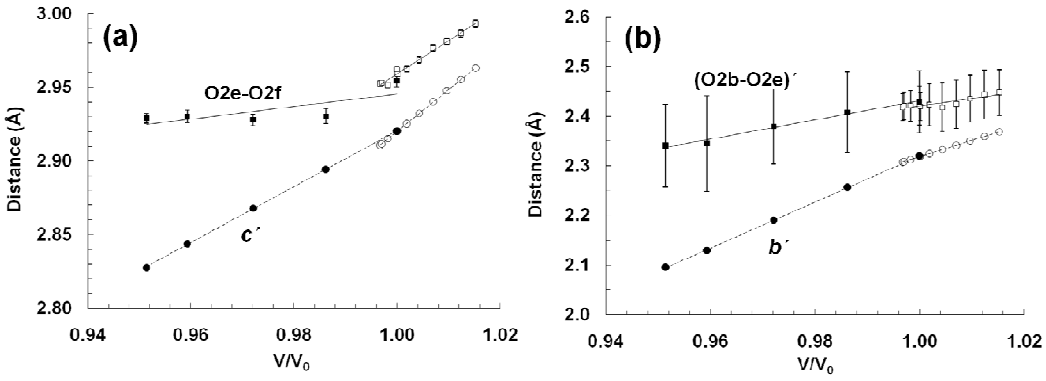

Figure 9-21: Comparison of inter-octahedral O-O distances in $CaPtO_3$ with unit-cell parameters (a) O2e-O2f and *c*´ where *c*´ = *c*-axis – 4.43 (scaling offset) (b) (O2b-O2e)´ and *b*´ where *b*´ = *b*-axis -7.12 (scaling offset). Solid lines – linear trend lines for O-O distances. Dotted lines – linear trend lines for axial distances. Error bars are smaller than symbols for (O2b-O2e)', *c*´ and *b*´.

The comparisons in Figure 9-21 show that each of the two O-O distances changes slope from compression to expansion in the same sense as its corresponding unit-cell axis. It has already been suggested that O-O repulsion between O2e and O2f may be responsible for the *c*-axis incompressibility being higher than that of the *a*-axis in $MgGeO_3$ (Kubo *et al.*, 2008; see Section 8.4.2). An increase in this repulsion with rising temperature in $CaPtO_3$ could accelerate the expansion of the *c*-axis with rising

temperature, by comparison with its compression. Conversely, it is possible that a decrease in repulsion between O2b and O2e with rising temperature could decelerate the expansion of the *b*-axis, although the trend is less marked. The changes in anisotropy of the *b* and *c*-axes between compression and expansion in $CaPtO_3$ could, therefore, be due to changing magnitudes of repulsion between O anions. From Figure 9-20, the same mechanism could apply to $CaIrO_3$. This is discussed further in Section 10.9.

9.4.2 *P* and *T* dependence of the structure of post-perovskite $CaPtO_3$

Figure 9-12 shows the variation of the atomic coordinates (listed in Table 9-1 and Table 9-6) of post-perovskite $CaPtO_3$ with V/V_0. If the values on the ambient-*P* isobar below 291 K are discounted, it can be seen that O1 *y* is the only atomic coordinate to show a monotonic change across the full range of V/V_0, i.e. as the material passes from the regime of compression to that of thermal expansion. Ca *y* shows a local minimum at 573 K, O2 *y* a local maximum at 473 K and O2 *z* a global maximum at 2.38 GPa. However, the changes in the structure are very small and so the local minimum and maximum in Ca *y* and O2 *y* may not be significant, although the trends appear to be systematic. These characteristics are reflected in the interatomic distances and geometrical parameters derived from the coordinates (as determined from the average positions of the atoms in the crystal, uncorrected for thermal motion). So the O2 *y* local maximum is associated with both the maximum in Pt-O2 bond length (Figure 9-13a) and the local minimum in the angle *p* at 473 K (Figure 9-14c). Similarly, the maximum in O2 *z* corresponds to the maximum in the Δ_2 tilt angle at 2.38 GPa (Figure 9-14b).

All Ca-O and Pt-O bond lengths are observed to decrease on compression (Figure 9-13). However, the behaviour on heating is less simple, with the Pt-O2 bond distance reaching a maximum at 473 K, after which it appears to saturate, or possibly to decline slowly; similarly, there appears to be a plateau in the Ca-O1 bond length above 573 K, though this is less obvious (Figure 9-13b). The behaviour of the average structure of $CaPtO_3$ therefore differs from that reported for $CaIrO_3$ by Martin *et al.* (2007a), in which the Ir-O2 and Ca-O1 distances were found to shorten on heating. The Δ_1 tilt of the octahedron changes little on compression but decreases on heating (Figure 9-14(a)). The Δ_2 tilt decreases from its maximum near 2.38 GPa both when compressed and

when heated (Figure 9-14b). The angle *p* decreases with compression and increases with heating (Figure 9-14c), since under pressure the shorter O2a-O2b bond is stiffer than the O2a-O2d bond (Figure 9-16), while on heating O2a-O2d increases steadily but O2a-O2b decreases above 473 K.

The volumes of both the PtO_6 octahedron and the CaO_8 hendecahedron decrease under compression and increase on heating (Figure 9-15), although the octahedral volume appears to saturate above 473 K, possibly decreasing slightly thereafter; this effect arises from the insignificant expansion of octahedral O1-O2 distances above room temperature (Figure 9-16) combined with a shortening of the Pt-O2 distance by a decrease in O2 *y* and O2 *z* (Figure 9-12c and Figure 9-12d). However, consideration of the proportion of the unit-cell volume occupied by the two different coordination octahedra reveals a difference in behaviour. The percentage volume occupied by the octahedra (Figure 9-15d) and by the void space (Figure 9-15f) falls with increasing V/V_0, while the proportion occupied by hendecahedra (Figure 9-15b) rises.

9.4.3 Crystal structure and unit cell parameters of $CaPtO_3$

In order to determine the physical origin of the difference in behaviour of the unit-cell parameters of $CaPtO_3$ shown on compression and on heating, the axial compression and expansion can be analysed in terms of Equations 1.4 – 1.6 (i.e. in terms of the four shortest cation-anion bond distances in the structure and the three angles, Δ_1, Δ_2 and *p* needed to specify the geometry and linkage of the PtO_6 octahedron). Since the changes in magnitude of all of the quantities are small, partial differentiation of Equation 1.4, for example, gives

$$da = \left(\frac{\partial a}{\partial(Pt-O2)}\right)_p d(Pt-O2) + \left(\frac{\partial a}{\partial p}\right)_{(Pt-O2)} dp \qquad (9.7)$$

$$\text{where } \left(\frac{\partial a}{\partial(Pt-O2)}\right)_p = 2\sin(p/2) \text{ and}$$

$$\left(\frac{\partial a}{\partial p}\right)_{(Pt-O2)} = (Pt-O2)\cos(p/2)$$

Similar equations can be derived for the *b*-axis and the *c*-axis (for convenience, the seven partial derivatives required for the analysis of the *b*-axis were calculated numerically).

Table 9-9 shows the relative importance of each of the contributing terms to the change in length of the unit-cell axes of $CaPtO_3$, both during compression (comparing the results from the data collected at 0.02 GPa and 9.27 GPa) and during expansion (from data collected at 291 K and 869 K). It can be seen that, despite the fact that different bonds and angles are involved, the *a*-axis and the *c*-axis show remarkable similarity in behaviour. For both *a* and *c* the dominant compression mechanism is by shortening of the Pt-O bonds; this term accounts for ~85% of the observed shortening of these axes, with only 15% of the observed shortening coming from changes in the angle (*p*) specifying the geometry of the central plane of the octahedron (for the *a*-axis) or in the angle (Δ_1) specifying the orientation of the apical oxygens of the octahedron (for the *c*-axis). On heating, however, the mechanism for expansion is clearly very different; 66% of the increase in length results from changes in angles and only 34% from expansion of the Pt-O bonds.

Understanding the origin of the behaviour observed for the *b*-axis is a little more complex, because the length of this axis depends on all 4 of the bond lengths and all 3 angles; however, some general conclusions may still be drawn. Under pressure, shortening of the *b*-axis results largely from shortening of the Ca-O bonds, especially the Ca-O2 bond; the changes in the Pt-O bonds and in the three angles (Δ_1, Δ_2 and *p*), taken individually, each produce only a small effect. These changes are reflected in the fact that the PtO_6 octahedron occupies a larger percentage of the unit-cell as pressure increases (Figure 9-15d) while the percentage occupied by the CaO_8 hendecahedron decreases (Figure 9-15b).

On heating, the expansion of the $CaPtO_3$ *b*-axis arises from expansion of the Ca-O bonds, but the angles *p* and Δ_1 now both provide a major contribution, acting in the opposite sense to the change in Ca-O bond lengths. The O1 and O2 atoms move away from the Ca atom as the Ca-O bonds expand, and this has the effect of decreasing angle Δ_1 and increasing angle *p* (Figure 9-14), although the effect of the simultaneous decrease in angle Δ_2 is to reduce angular distortion of the octahedra. These angular

changes also have the effect of increasing the *a*- and *c*-axes. In expansion the volume of the PtO_6 octahedron tends to plateau (Figure 9-15c) while the volume of the CaO_8 hendecahedron increases (Figure 9-15a).

The signs of the partial derivatives are such that lengthening of either of the Pt-O bonds or increasing the angle *p* (other quantities remaining constant) produces a shortening of the *b*-axis. In the case of Pt-O2 and *p* this arises because the increase in length of the *a*-axis that arises from an increase in either Pt-O2 or *p* must produce a decrease in the length of the *b*-axis if the Ca-O2 distance is to remain constant. A similar argument applies for Pt–O1; an increase in the length of this bond increases the length of the *c*-axis, which in turn (for a constant Ca–O2 distance) must result in the *b*-axis becoming smaller.

Post-perovskite $CaPtO_3$

Compression: from 0.02 to 9.265 GPa ($V/V_0 = 0.951$)

Expansion: from 291 to 869 K ($V/V_0 = 1.015$)

a-axis

	(i) % of calculated change in *a* due to change in Pt-O2 bond	(ii) % of calculated change in *a* due to change in angle *p*
Compression	85%	15%
Expansion	34%	66%

b-axis

	% change in *b* due to change in						
	(i) Pt-O1 bond	(ii) Pt-O2 bond	(iii) Ca-O1 bond	(iv) Ca-O2 bond	(v) angle *p*	(vi) angle Δ_1	(vii) angle Δ_2
Compression	-13%	-19%	47%	101%	-11%	-12%	6%
Expansion	-11%	-10%	125%	177%	-66%	-101%	-14%

c-axis

	(i) % of calculated change in *c* due to change in Pt-O1 bond	(ii) % of calculated change in *c* due to change in angle Δ_1
Compression	83%	17%
Expansion	33%	67%

Table 9-9: Relative importance for $CaPtO_3$ (the present work) of changes in bond distances and of changes in angles in determining the change of unit-cell parameters during compression and during expansion. Note that in this table (and in Table 9-10 and Table 9-11) in compression a positive contribution is taken as one that shortens the axis as the applied pressure is increased. For expansion, a positive contribution corresponds to a lengthening of the axis as the temperature is raised.

9.4.4 Comparison with post-perovskite $CaIrO_3$ and $MgSiO_3$

The approach described above for determining the mechanisms of the changes in unit-cell parameters under pressure and on heating may also be used to examine the differences in these mechanisms between $CaPtO_3$, $CaIrO_3$, and $MgSiO_3$.

The change in the average structure of $CaIrO_3$ post-perovskite under compression has been studied by Rietveld refinement to 9.72 GPa using neutron powder diffraction by Martin *et al.* (2007b) and on heating to 1109 K by X-ray powder diffraction by Martin *et al.* (2007a). Table 9-10 shows the contributions from the different elements of the crystal structure to the changes in length of the axes of the unit cell. The percentage of the measured change in the expansion of the *a*-axis in column (iii) of Table 9-10 is moderately sensitive (± 4 %) to the choice of high (1109 K) or low (332 K) temperature values for the angle *p* and for the length of the Ir-O2 bond used to calculate the partial derivative in Equation 9.7. A similar sensitivity occurs for the *c*-axis (± 5%) and the choice of values for the angle Δ_1 and the length of the bond Ir-O1. This effect arises because the changes in $CaIrO_3$ are large and tend to cancel each other out, unlike the changes for $CaPtO_3$ in Table 9-9 and for $MgSiO_3$ in Table 9-11.

Post-perovskite $CaIrO_3$: Table calculated using crystal structures taken from:
Compression: from 0.0 to 9.72 GPa (V/V_0 = 0.952); Martin *et al.* (2007b)
Expansion: from 332 to 1109 K (V/V_0 =1.026); Martin *et al.* (2007a)

a-axis

	(i) % of calculated change in *a* due to change in Ir-O2 bond	(ii) % of calculated change in *a* due to change in angle *p*
Compression	59%	41%
Expansion	-137%	237%

b-axis

	% change in *b* due to change in						
	(i) Ir-O1 bond	(ii) Ir-O2 bond	(iii) Ca-O1 bond	(iv) Ca-O2 bond	(v) angle *p*	(vi) angle Δ_1	(vii) angle Δ_2
Compression	-13%	-13%	49%	121%	-29%	-16%	0%
Expansion	-52%	24%	-65%	218%	-144%	116%	0%

c-axis

	(i) % of calculated change in *c* due to change in Ir-O1 bond	(ii) % of calculated change in *c* due to change in angle Δ_1
Compression	78%	22%
Expansion	199%	-99%

Table 9-10: Relative importance for $CaIrO_3$ of changes in bond distances and of changes in angles in determining the change of unit-cell parameters during compression and during expansion.

On compression, the $CaIrO_3$ structure appears to respond in a quite similar way to that of $CaPtO_3$, with the change in length of the axes produced mainly by a decrease in the Ir–O distances (for *a* and *c*) and a decrease in the Ca–O distances (for *b*). It appears,

however, that changes in the angles Δ_1, Δ_2 and p may play a larger role in this material, especially in the case of the a-axis.

On heating, the behaviour shown by $CaIrO_3$ appears to be completely different from that of $CaPtO_3$ with, for example, a contraction of the Ir-O2 bond producing a shortening of the a-axis which is then overcome by an increase in the angle p. Unlike $CaPtO_3$, the O1 atom moves towards the Ca atom, increasing angle Δ_1 and decreasing the length of the Ca-O1 bond.

However, because of the dominance of the scattering from the Ir atoms, the oxygen coordinates in the high-temperature structures of $CaIrO_3$ are very difficult to determine accurately by X-ray powder diffraction and so these results should be treated with caution. Martin *et al.* (2007a) found that both the Ca-O1 and the Ir-O2 bond lengths in the average structure of $CaIrO_3$ showed significant negative thermal expansion and that the IrO_6 octahedra decreased in volume with increasing temperature. This is similar to the plateau in the Ca-O1 bond length above 573 K, and the shrinkage in both the Pt-O2 bond length and PtO_6 octahedral volume between 473K and 773K found in the present work.

A subsequent examination of X-ray powder data from $CaIrO_3$ at high-temperature using a pair-distribution function approach (Martin, 2008) suggested that the apparent decrease in length of these bonds with temperature may be an artefact resulting from the effect of thermal motion on the average position of the atoms. Such effects would appear to be less significant for $CaPtO_3$ than for $CaIrO_3$. In this connection it is of interest to note that the MD simulations of $CaIrO_3$ and $CaPtO_3$ described in Section 4.3 produce an Ir-O2 distance computed from the average positions of the atoms that is almost temperature invariant, although the average of the instantaneous Ir-O2 distances at each simulation step increases; in contrast, the corresponding values for Pt-O2 both show a clear increase with temperature. So if in $CaIrO_3$ there is a weakening in Ir-O bonds with heating relative to Ca-O bonds, it may be more marked than for Pt-O bonds in $CaPtO_3$.

The crystal structure of post-perovskite $MgSiO_3$ has been studied as a function of pressure by Shim *et al.* (2008), but the relatively large uncertainties in the atomic coordinates (Figure 10-12) from this high-pressure X-ray diffraction DAC study makes a detailed comparison of the structural changes on compression very difficult, although the reported decrease in the angle *p* with increasing pressure is consistent with the results of the present work. Since accurate crystal structure determinations of $MgSiO_3$ are not available as a function of either pressure or temperature, Table 9-11 shows, instead, an analysis of the relationship between crystal structure and cell parameter changes in $MgSiO_3$ based on two sets of computer simulations.

Post-perovskite $MgSiO_3$: Table calculated using crystal structures taken from: *Compression:* from 136 to 178 GPa (V/V_0 = 0.946); athermal *ab initio* computer simulations using the VASP code (see Section 4.2)
Expansion: from 500 to 4000 K (V/V_0 = 1.043) at 136 GPa; *ab initio* quantum molecular dynamics computer simulations using the VASP code; Stackhouse and Brodholt (2007)(see Section 4.3)

a-axis

	(i) % of calculated change in *a* due to change in Si-O2 bond	(ii) % of calculated change in *a* due to change in angle *p*
Compression	87%	13%
Expansion	102%	-2%

b-axis

	% change in *b* due to change in						
	(i) Si-O1 bond	(ii) Si-O2 bond	(iii) Mg-O1 bond	(iv) Mg-O2 bond	(v) angle *p*	(vi) angle Δ_1	(vii) angle Δ_2
Compression	-24%	-18%	50%	96%	-9%	10%	-1%
Expansion	-23%	-27%	66%	96%	2%	-13%	-1%

c-axis

	(i) % of calculated change in *c* due to change in Si-O1 bond	(ii) % of calculated change in *c* due to change in angle Δ_1
Compression	109%	-9%
Expansion	89%	11%

Table 9-11: Relative importance for $MgSiO_3$ of changes in bond distances and of changes in angles in determining the change of unit-cell parameters during compression and during expansion.

To obtain the compression data, athermal simulations were made with VASP (Section 4.2.1); for the expansion data the molecular dynamics results of Stackhouse and Brodholt (2007) at simultaneous high-*P* and high-*T* were used (as in Section 4.3.1). Once again, the structure distorts under pressure mainly by shortening of the Si-O and Mg-O bond distances in a similar manner to that shown by $CaPtO_3$ and $CaIrO_3$. On heating, however, it seems that $MgSiO_3$ behaves differently from the two analogue compounds, with changes in bond length still dominating the expansion mechanism.

In summary, $CaPtO_3$ and $CaIrO_3$ post-perovskites have the same axial compression sequence ($\kappa_c > \kappa_a > \kappa_b$) as $MgSiO_3$ post-perovskite, but each of the three post-perovskites has a different axial expansion sequence; $CaPtO_3$ and $CaIrO_3$ are better analogues for $MgSiO_3$ in compression than when heated.

9.5 Determination of the Anderson-Grüneisen parameter of $CaPtO_3$ by neutron diffraction; an unsuccessful experiment

The intention of this experiment was to use high-pressure neutron powder diffraction collected by time-of-flight on the PEARL beamline at ISIS (see Section 9.1) to measure the Anderson-Grüneisen parameter and the high-pressure/high-temperature crystal structure of post-perovskite $CaPtO_3$.

The Anderson-Grüneisen parameter, δ, where

$$\delta = \left(\frac{\partial \ln \alpha}{\partial \ln V}\right) = -\left(\frac{1}{\alpha K}\right)\left(\frac{\partial K}{\partial T}\right) = -\left(\frac{K}{\alpha}\right)\left(\frac{\partial \alpha}{\partial P}\right) \qquad (9.8)$$

links the rate of change of the bulk incompressibility *K* with temperature ($\partial K/\partial T$) to that of the thermal expansion coefficient α with pressure ($\partial \alpha/\partial P$). The rate of change $\partial K/\partial T$ is an important geophysical parameter because the temperature difference across the D'' layer is likely to be ~1000 K. This means that the value of the incompressibility *K* for the post-perovskite phase will reduce significantly with depth as the temperature rises, leading to a reduction in seismic wave velocities. Measurements of ($\partial K/\partial T$) for post-perovskite $MgSiO_3$ have been reported (Guignot *et al.*, 2007; Komabayashi *et al.*,

2008) and its value has also been determined by computer simulation (Stackhouse *et al.*, 2005a), but the agreement between the results, -0.015, -0.0085(11) and -0.024 GPa K^{-1} respectively, is poor. After completion of this experiment, ($\partial K/\partial T$) of post-perovskite $CaIrO_3$ was reported as -0.038(11) GPa K^{-1} (Liu *et al.*, 2011).

The Anderson-Grüneisen parameter could readily be measured using X-ray diffraction, but the intended measurement using neutron diffraction was additionally expected to give changes in crystal structure with simultaneously changing pressure and temperature.

This experiment used the high-pressure high-temperature setup for the Paris-Edinburgh cell described by Wood *et al.* (2008) with an MgO pressure standard. Temperatures were measured by neutron absorption resonance radiography of a Hf foil; a check of the consistency of the pressure and temperature values could also be obtained by measuring the unit-cell parameter of Pt foils. The sample/heater assembly is shown in Figure 9-22. The central, roughly spherical, part of the gasket containing the cylindrical sample was surrounded by an outer toroidal gasket made of MgO which provided greater support at simultaneous high-pressure and high-temperature conditions (Wood *et al.*, 2008).

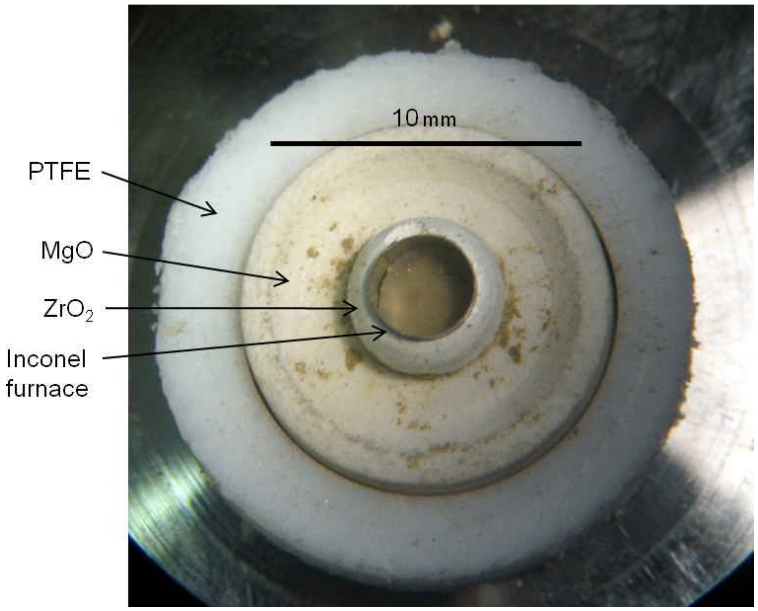

Figure 9-22: Toroidally gasketted, high-P/T sample/heater assembly used with "Los Alamos profile" WC anvils from ISIS.

To prevent the sample coming into contact with the inconel furnace, in the first experiment the sample was contained within a cylindrical quartz glass sample cell ~ 4mm long and ~ 3mm internal diameter. Similarly, the 50 μm Hf foil within the sample cell was enclosed in 12.5 μm Pt foils to prevent reduction of the $CaPtO_3$. The sample used was a mixture of 60% post-perovskite $CaPtO_3$ and 40% MgO powders. The $CaPtO_3$ sample was taken from the material prepared for previous ISIS experiments (see Chapter 9).

It was found that this setup produced a very weak diffraction pattern, and so the assembly was changed to improve the diffraction peak signal/noise ratio. The steel plugs sealing the ends of the cell were replaced by ZrO_2 plugs. The sample mixture was changed to 80% post-perovskite $CaPtO_3$ and 20% MgO. A 3.0 mm instead of 2.5 mm diameter BN incident beam collimator was used, with a Gd mask. Measurements were then taken at 3 pressure/temperature points (Table 9-12).

Oil pressure tonnes	Pressure GPa	Temperature °C (Hf)
1	0.09	Ambient
15	1.08	222
35	2.88	281

Table 9-12: Anderson-Grüneisen experiment pressure/temperature points

Additional measurements were made between the second and third data points, but were discarded because of a pressure loss and temperature instability. Measurements were interrupted by beam loss for about 50% of the experimental period. Each measurement took about 5 hours (~800 μAh of beam current), plus 1 hour for temperature/pressure stabilisation. Figure 9-23 shows the diffraction pattern collected at 1 tonne of oil pressure (0.09 GPa) at ambient temperature.

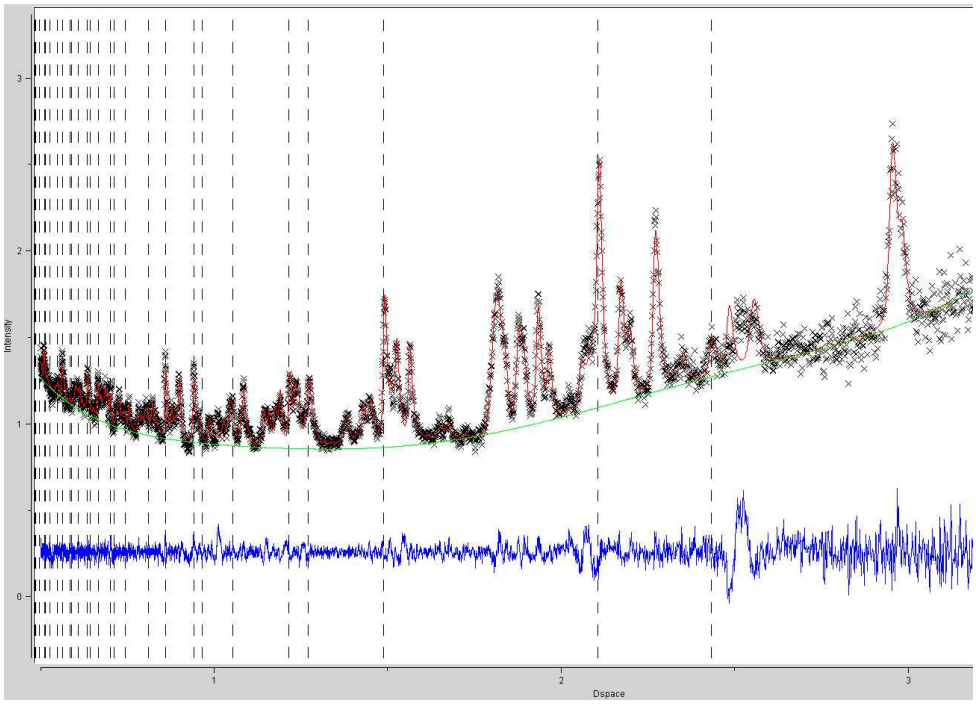

Figure 9-23: Neutron diffraction pattern at 1 tonne (0.09 GPa) and ambient temperature. Calculated MgO peak positions are shown as dashed lines. The difference curve is shown below.

The data shown in Figure 9-23 are not of good quality but might have been useable. Unfortunately, the diffraction pattern became weaker with increasing pressure and temperature, and pressure measurement became more uncertain because of the overlap of MgO peaks with other peaks; the main MgO calibration peak became unusable at 35 tonnes oil pressure (see Figure 9-24).

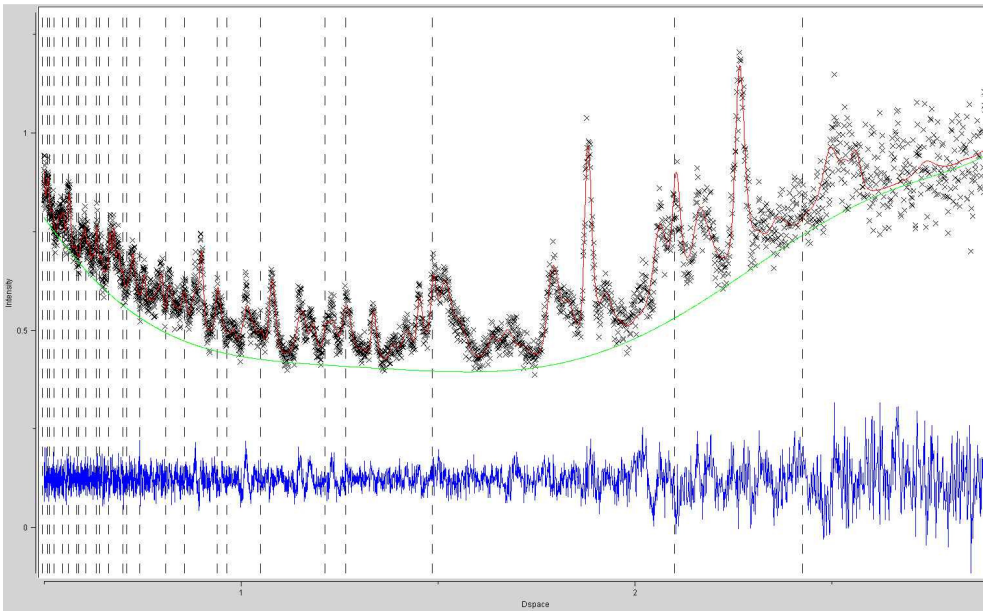

Figure 9-24: Neutron diffraction pattern at 35 tonnes (2.88 GPa) and 281°C. Calculated MgO peak positions are shown as dashed lines. The difference curve is shown below.

As there was no possibility of obtaining useful information from this experiment because of lost beam time and the weak diffraction pattern, it was decided not to proceed with higher pressure and temperature measurements. An alternative approach would be to measure the Anderson-Grüneisen parameter (but not the high-pressure/temperature crystal structure) using a DAC with X-ray diffraction at a synchrotron source such as at ESRF with temperatures up to 800°C and pressure up to 40 GPa.

9.6 Summary of neutron powder diffraction studies of $CaPtO_3$

1. The thermoelastic and structural properties of post-perovskite $CaPtO_3$ were measured to 9.27 GPa at ambient temperature and from 2 K to 973 K at ambient pressure, by time-of-flight neutron powder diffraction at ISIS. The experiment at the ESRF described in Chapter 8 used X-ray powder diffraction with synchrotron radiation to determine the bulk and axial EOSs of post-perovskite $CaPtO_3$ in compression; the experiments described in this Chapter used neutron data to determine the crystal structure as a function of pressure and temperature.
2. The equation-of-state parameters determined in the high-pressure experiment in this Chapter are consistent with those found in Chapter 8.
3. For temperatures above 300 K, the volumetric coefficient of thermal expansion, $\alpha(T)$, can be represented by $\alpha(T) = a_0 + a_1(T)$, with $a_0 = 2.37(3)\times10^{-5}$ K^{-1} and $a_1 = 5.1(5)\times10^{-9}$ K^{-2}. Axial coefficients of thermal expansion were also calculated; on heating, the *b*-axis expands at approximately the same rate as the volumetric (bulk) value divided by three, while the *c*-axis expands faster than *b*, and the *a*-axis expands more slowly.
4. $CaPtO_3$ post-perovskite has the same axial compression sequence $\kappa_c > \kappa_a > \kappa_b$ (where κ_i are axial incompressibilities) as both $MgSiO_3$ and $CaIrO_3$ post-perovskites. However, when heated, $CaPtO_3$ shows axial expansion in the form $\alpha_c > \alpha_b > \alpha_a$, a sequence which is not simply the inverse of the axial incompressibilities. In this respect $CaPtO_3$ differs from both $MgSiO_3$ (for which the sequence $\alpha_b > \alpha_a > \alpha_c$, is the same as $1/\kappa_i$) and $CaIrO_3$ (for which $\alpha_b > \alpha_c > \alpha_a$).
5. The change in volume of $MgSiO_3$ post-perovskite due to the change in temperature across the D'' layer is significant compared with that due to the change in pressure. Analogue materials should, ideally, show a response to both temperature and pressure which is similar to that of $MgSiO_3$. The differences in the axial expansion behaviours of $CaPtO_3$ and $CaIrO_3$ at 0 GPa from that of $MgSiO_3$ at high-pressure may, therefore, significantly weaken the case for the use of $CaPtO_3$ and $CaIrO_3$ as low-pressure analogues of $MgSiO_3$ at elevated temperatures.
6. The *b*-axis of each of the three post-perovskites is less expansible than expected from an extrapolation of its compressibility, and their *c*-axes are more expansible. The changes in anisotropy of the *b* and *c*-axes between compression and

expansion in $CaPtO_3$ could be due to changing magnitudes of repulsion between O anions; the same mechanism could also apply to $CaIrO_3$.

7. For the full range of temperature investigated, the unit-cell volume of $CaPtO_3$ can be fitted well by a second-order Grüneisen approximation to the zero-pressure volumetric equation of state, with the internal energy calculated via a Debye model, and parameters: $\theta_D = 615(8)$ K, $V_0 = 227.186(3)$ Å^3, $K'_0 = 7.9(8)$ and $(V_0K_0/\gamma') = 3.16(3)\times10^{-17}$ J, where θ_D is the Debye temperature, V_0 the unit-cell volume at $T = 0$ K, K'_0 the first derivative with respect to pressure of the isothermal incompressibility, K_0, and γ' is a Grüneisen parameter.
8. The specific heat curve for C_V can best be represented by a model with two Debye moments with characteristic temperatures of 295(4) K and 811(3) K, with the higher temperature mode dominant.
9. Calculations of axial Debye temperatures give 648(13) K for the *a*-axis, 574(7) K for *b* and 624(10) K for *c*.
10. By combining these measurements with previously reported heat capacity data, the thermodynamic Grüneisen parameter γ can be calculated as 1.16(1) at 291 K, which is very similar to that calculated previously for post-perovskite $MgSiO_3$.
11. The behaviour of the average structure of $CaPtO_3$ differs from that reported for $CaIrO_3$, in which the Ir-O2 and Ca-O1 distances were found to shorten on heating; the corresponding Pt-O2 and Ca-O1 distances in $CaPtO_3$ decline slowly or saturate at higher temperatures.
12. Under pressure, $CaPtO_3$, $CaIrO_3$ and $MgSiO_3$ all contract mainly by reduction in the B-X and A-X distances. On heating, $MgSiO_3$ expands (at high pressure) mainly by increases in the length of the Si-O and Mg-O bonds. In contrast, the expansion of $CaPtO_3$ (and possibly also $CaIrO_3$), at atmospheric pressure, arises more from changes in angles than from increased bond distances.
13. An experiment to determine the Anderson-Grüneisen parameter of $CaPtO_3$ by neutron diffraction was unsuccessful, due to weak diffraction patterns, overlapping peaks and lost beam time. An alternative approach would be to measure the Anderson-Grüneisen parameter (but not the high-pressure/ temperature crystal structure) using a DAC with X-ray diffraction at a synchrotron source with temperatures up to 800°C and pressure up to 40 GPa.

10 Comparison of experimental and simulation results

10.1 Introduction

The experimental measurements of $CaPtO_3$ in Chapter 9 provide an overview of the behaviour of this post-perovskite structure from compression to expansion, but they are still limited by the temperature and, in particular, the pressure reached. DFT simulation offers the prospect of being able to predict this behaviour over a wider range of pressure and temperature, for hypothetical as well as for known post-perovskite compounds. However, these predictions can only be credible if the simulation results compare well with available experimental measurements. In this Chapter I therefore compare the simulated effects of compression and expansion on the structure of a number of post-perovskites with results from experimental measurements.

The athermal simulation results are shown over their full pressure range in Chapter 4. In this Chapter I examine these results over the more restricted range of compression available from experiment, and I add the results from the simulation of expansion.

Studies reporting the 7 structural variables of post-perovskite at a range of pressures and/or temperatures have been relatively rare (see Table 1-4), and most have been subject to experimental constraints which have made it difficult to obtain an overview of the changes in post-perovskite structure from compression to expansion. It is difficult to obtain accurate measurements of the small changes in the post-perovskite structure in DAC experiments such as those on $Mg_{0.91}Fe_{0.09}SiO_3$ (Shim *et al.*, 2008) and $MgGeO_3$ (Kubo *et al.*, 2008). The study of changes in post-perovskite structure in experiments on $CaIrO_3$ has been hampered by the dominant X-ray scattering by the Ir atoms and by its very high X-ray absorption coefficient (see Section 7.2.1).

10.2 Experimental compression EOSs compared with simulation

The experimental and simulated bulk and axial compression EOS parameters for post-perovskites are shown in Table 10-1, together with the percentage differences between experiment and simulation.

	$MgSiO_3$[a]	$MgGeO_3$[b]	$CaIrO_3$[c]	$CaPtO_3$[d]	$NaMgF_3$[e]	$NaZnF_3$[f]	$NaNiF_3$[h]
Volume							
Expt. V_0 (Å^3)	162.2[g]	179.2(7)	226.38(1)	228.10(2)	223.0(1)	234(1)	224.27(2)
Sim. V_0 (Å^3)	165.8	188.6	232.2	236.7	231.8	240.2	232.6
Difference (%)	2.23	5.27	2.55	3.80	3.9	2.65	3.73
Expt. K_0 (GPa)	231.2(1)	207(5)	181(3)	168.2(8)	54(3)	56(2)	
Sim. K_0 (GPa)	232.3	179.0	168.6	156.1	60.7	65.9	64.2
Difference (%)	0.46	-13.6	-6.9	-7.2	12.5	17.6	
Expt. K'_0	4.4	4.4[i]	2.3(8)	4.51(6)	5.7(4)	4[g]	
Sim. K'_0	3.9	4.2	4.2	4.3	4.5	4.4	4.9
Difference (%)	-11.1	-4.5	75	-4.7	-21	9	
V/V_0 minimum	0.97	0.74	0.96	0.84	0.72	0.82	
***a*-axis**							
Expt. a_0 (Å)	2.68(2)	2.803(2)	3.1454(1)	3.12777(8)		3.055(4)	3.0291(2)
Sim. a_0 (Å)	2.714	2.833	3.198	3.173	3.050	3.097	3.065
Difference (%)	1.28	1.05	1.66	1.45		1.38	1.18
Expt. K_0 (GPa)	285(26)	230(4)	228(5)	195.7(8)		78(3)	
Sim. K_0 (GPa)	235.9	203.9	180.9	174.3	51.9	69.2	77.9
Difference (%)	-17	-11	-21	-11		-11	
Expt. K'_0	4[g]	4.6[i]	4(1)	6.63(8)		4[g]	
Sim. K'_0	4.4	4.7	9.2	7.2	8.9	6.9	6.4
Difference (%)	11	2	190	9		73	
***b*-axis**							
Expt. b_0 (Å)	9.35(6)	9.292(27)	9.8619(3)	9.9191(5)		10.251(7)	10.0208(6)
Sim. b_0 (Å)	9.199	9.392	9.785	9.917	10.213	10.280	10.172
Difference (%)	-1.61	1.08	-0.78	0.55		0.3	1.51
Expt. K_0 (GPa)	110(9)	161(7)	124(2)	123.3(5)		28.6(4)	
Sim. K_0 (GPa)	167.3	161.1	114.1	120.5	43.2	46.3	46.8
Difference (%)	52	0.1	-8	-2		62	
Expt. K'_0	4[g]	4.0[i]	0.9(5)	2.37(3)		4[g]	
Sim. K'_0	3.5	3.6	2.6	2.5	3.0	2.8	3.1
Difference (%)	-11	-11	190	7		-29	
***c*-axis**							
Expt. c_0 (Å)	6.53(2)	6.882(5)	7.2979(1)	7.3551(4)		7.493(8)	7.3885(4)
Sim. c_0 (Å)	6.717	6.972	7.311	7.409	7.455	7.555	7.432
Difference (%)	2.86	1.30	0.18	1.52		0.83	0.59
Expt. K_0 (GPa)	403(24)	247(3)	243(4)	192(2)		94(4)	
Sim. K_0 (GPa)	226.7	183.7	235.8	152.6	55.3	56.0	74.5
Difference (%)	-44	-26	-3	-21		-41	
Expt. K'_0	4[g]	4.7[i]	5(1)	12.2(3)		4[g]	
Sim. K'_0	5.1	5.4	9.2	14.8	14.6	15.8	11.0
Difference (%)	27	15	84	21		295	

Table 10-1: Experimental (Expt.) and simulated (Sim.) bulk and axial compression EOS parameters for post-perovskites, with the % difference (simulation-experiment) between them.

(Table 10-1 continued) Simulated values are from the present work (Table 4-1: 0 GPa and ~0 K *i.e.* athermal). A blank entry indicates that experimental data are not available. V/V_0 minimum specifies the minimum value of V/V_0 used in the experimental EOS, where V_0 is the volume at 0 GPa and V is the volume at the highest pressure. Experimental values are all calculated at 0 GPa and ambient temperature, and are taken from:

[a] Guignot *et al.* (2007)

[b] Kubo *et al.* (2006)

[c] Boffa Ballaran *et al.* (2007)

[d] the present work (Chapter 8)

[e] Hustoft *et al.* (2008)

[f] Yakovlev *et al.* (2009) – I recalculated the bulk EOS from the published data using the EOS-fit program (Angel, 2000, 2001), weighted by errors in volume, excluding the compression data points and the first decompression data point (20.44 GPa)(see Figure 10-8) because these gave larger errors.

[g] Fixed

[h] the present work (Section 6.8.3) – V, a, b and c at ambient P and T (no experimental EOS available)

[i] No error specified.

Two issues must be considered when comparing these EOS parameters; firstly, how do results from simulations in the present work compare with those from previous simulations (Section 10.2.1) ? Secondly, how do they compare with experimental results (Section 10.2.2) ?

There are three general factors which affect these comparisons. The first is the choice of DFT pseudopotential. The present work's simulations use GGA pseudopotentials, which tend to produce larger V_0 volumes and smaller K_0 bulk incompressibilities than LDA (see Section 2.1.4). This is discussed further below.

The second factor relates to temperature. The experimental EOS determines V_0, K_0 and K'_0 at ambient temperature, but the athermal simulation EOS calculates them effectively at 0 K. Experimental data for $CaPtO_3$ indicates that (assuming an ambient temperature of 300 K) the simulated V_0 is likely to be 0.34% too small, and the simulated K_0 is likely to be 6.3% too large, assuming $\partial K/\partial T = -0.038$ as for $CaIrO_3$

(Liu *et al.*, 2011). So taking this difference in temperature into account, the differences in V_0 and in unit-cell axes in Table 10-1 are (where positive) likely to be even larger than shown; similarly the differences in K_0 (where negative) are also likely to be larger.

The third factor is the range of pressures over which the volumes (and unit-cell parameters) are measured and simulated. A larger range of pressures is available in simulation than is accessible in experiments. A P-V curve may show greater curvature using data from a wider range of (simulated) pressures than from a more restricted range of (experimental) pressures, so that the incompressibility K is smaller and its rate of change with pressure K' is larger. This may also be true for the individual axes, as illustrated below for $CaIrO_3$ (Section 10.2.2). The simulated EOS parameters shown in Table 10-1 (and in Table 4-1) have been calculated over wider ranges of V/V_0 and hence of pressure than those used in experiments. The minimum value of V/V_0 used in each EOS is shown for simulation in Table 4-1 and for experiment in Table 10-1. However, rather than restricting the pressure range to that used in each experiment, results from the wider ranges are shown as they are potentially more representative of the compound over a wide pressure range.

The difference in pressure required to bring the simulated and experimental values of V_0 into alignment using a P-V EOS is about 6-7 GPa for $MgSiO_3$ and $MgGeO_3$. This has the effect of reducing the difference between simulated and experimental values of K_0 to less than 2%.

10.2.1 Comparison of simulation results from this and from previous work

There is a relatively large number of results published from DFT simulation of the bulk (rather than axial) properties of post-perovskites, using both GGA and LDA pseudopotentials.

The only published simulation of post-perovskite $CaPtO_3$ (Matar *et al*., 2008; using LDA), with V_0 = 212.14 Å^3, K_0 = 222, GPa and K'_0 = 4.59, does not compare well with experiment (see Section 8.4.1); the present work's simulated bulk EOS for $CaPtO_3$ compares better (Table 10-1).

The published simulation of post-perovskite $CaIrO_3$ (Stølen and Trønnes, 2007; using GGA), for which V_0 = 233.22 Å^3, K_0 = 164, GPa and K'_0 = 4.0, agrees marginally less well with experiment than do the results from simulation in the present work. The published simulation of post-perovskite $NaZnF_3$ (Yakovlev *et al*., 2009; LDA/GGA not specified) (V_0 = 212.28 Å^3, K_0 = 100.26 GPa, K'_0 = 4.59) does not compare well with experiment. However, the published simulation of post-perovskite $NaMgF_3$ (Umemoto *et al.* 2006; using GGA) (V_0 = 232.04 Å^3, K_0 = 60.8 GPa, K'_0 = 4.5) agrees reasonably well with experiment and gives similar results to the simulation in the present work.

A published simulation of post-perovskite $MgSiO_3$ (Oganov and Ono, 2004) used both GGA and LDA. Results from LDA (V_0 = 162.86 Å^3, K_0 = 231.93 GPa, K'_0 = 4.43) compare better with experiment than those from GGA (V_0 = 167.64 Å^3, K_0 = 199.96 GPa, K'_0 = 4.541), and compare marginally better with experiment than the present work's simulation.

A published simulation of post-perovskite $MgGeO_3$ (Kubo *et al.,* 2008) also uses both GGA and LDA. Using the pressure-volume data published in that paper with a third-order Birch-Murnaghan EOS, I calculated V_0 = 189.00 Å^3, K_0 = 176 GPa and K'_0 = 4.22 (GGA) and V_0 = 177.65 Å^3, K_0 = 207 GPa and K'_0 = 4.25 (LDA). In this case the EOS parameters from LDA simulation are closer to experimental results than those from GGA simulation in that paper or in the present work. As the Kubo *et al.* (2008) paper includes details of pressure and volume data points for both GGA and LDA simulations, it is possible to compare those unit-cell volumes from GGA and LDA

simulation and experiment with the present work's GGA-simulated unit-cell volumes (Figure 10-1). The present work's unit-cell volume trend line lies between those of the GGA and LDA volumes from Kubo *et al.* (2008). The experimental volume trend line lies between the present work's GGA and the LDA volume. Plots of the unit-cell parameters *a*, *b* and *c* show similar trends.

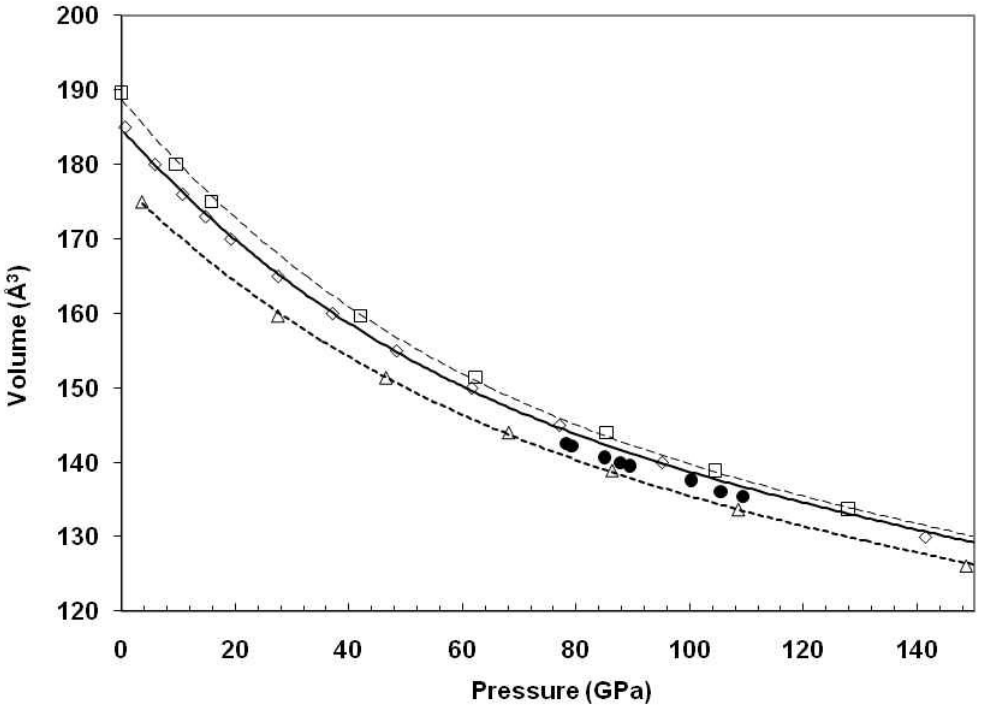

Figure 10-1: Unit-cell volume plotted against pressure for simulated and experimental data on post-perovskite $MgGeO_3$. The present work's GGA data points are shown as diamonds (solid trend line). GGA, LDA and experimental data points from Kubo *et al.* (2008) are shown as squares (dashed trend line), triangles (dotted trend line) and solid circles respectively. Error bars for experimental data points are smaller than the symbols used.

The conclusion from this comparison of bulk EOS results from the use of GGA and LDA pseudopotentials with those from experiment is that the GGA simulation results in the present work are relatively close to experimental results. Figure 10-13 shows that simulated atomic coordinates of $MgGeO_3$ from GGA and LDA are very similar. GGA is considered to produce more accurate energetic data (see Section 2.1.4).

10.2.2 Comparison of EOS simulation results with experiment

The differences between simulated results obtained in the present work and experimental results from the present work and elsewhere are shown as a percentage difference for each EOS parameter in Table 10-1. The percentage differences in V_0 are positive (*i.e.* the simulated V_0 is larger than experiment), and so are the percentage differences in unit-cell parameters (as expected from the use of GGA), with the exception of *b*-axis parameters for $MgSiO_3$ and $CaIrO_3$. The differences in K_0 are negative (the simulated K_0 is smaller than experiment) in 15 out of the 21 cases shown in Table 10-1, also as expected from the use of GGA. It is possible that the wider range of pressures of the simulations allows better modelling of the curvature of the P-V plot. A higher value of K'_0 reflects a larger increase in the value of K as pressure increases than would be expected with a smaller value of K'_0. So, for example, the effects of the values of K'_0 for the simulations of the axes of $CaIrO_3$ appearing in Table 10-1 are shown in Figure 4-4, where the *c*-axis, with $K'_0 = 9.2$ curves upwards (K'_0 for the *c*-axis being greater than that for the unit-cell volume) while the *b*-axis with $K'_0 = 2.6$ curves downwards (K_0' for the *b*-axis being less than that for the unit-cell volume). Note that the smaller experimental values of K'_0 are usually coupled with larger experimental values of K_0: the two parameters are strongly correlated, as shown in the following example.

The effect of choosing a narrower pressure range is illustrated by the simulated bulk EOS parameters for $CaIrO_3$. The experimental data points were recorded from V/V_0 from 1 to 0.96 (Boffa Ballaran *et al.*, 2007), while the simulated data points in Table 10-1 covered the range V/V_0 from 1 to 0.67. Refitting the simulated bulk EOS using only data points in the range V/V_0 from 1 to 0.92 gave a value for the bulk K'_0 of 1.7 instead of 4.2 compared with an experimental value of 2.3(8), and a value for the bulk K_0 of 199.8 instead of 168.6 GPa compared with eexperimental value of 181(3) GPa. The same result holds true for the EOSs for the *a* and *c* axes of $CaIrO_3$ obtained from simulation: refitting over the smaller pressure range raises K_0 and lowers K'_0. The simulated *b*-axis parameters change when refitted by less than 1 experimental ESD.

As a consequence of the range of values for K'_0, the axial compression sequences for post-perovskites cannot be judged solely on their K_0 values: a large value of K'_0 will rapidly increase K as pressure increases. So although K_0 for the *c*-axis of $CaPtO_3$ is

less than that for its *a*-axis (Table 10-1), the large value of K'_0 for the *c*-axis makes this axis more incompressible than the *a*-axis for V/V_0 of less than 0.95 (Figure 10-3a).

The small number of experimental axial data points available for $NaMgF_3$ (Martin *et al.*, 2006b) in compression show considerable scatter, but it is evident that $\kappa_c > \kappa_a > \kappa_b$, as in the simulation of $NaMgF_3$.

10.3 Experimental and simulated axial compression and thermal expansion

The axial compression and expansion measured by experiment for the post-perovskites $MgSiO_3$, $CaPtO_3$ and $CaIrO_3$ are described in section 9.4.1. This section compares these experimental results with those from computer simulations, using athermal multiple ***k***-point simulation for compression and MD for expansion (see Figure 10-2, Figure 10-3 and Figure 10-4).

The common key to Figure 10-2, Figure 10-3 and Figure 10-4 is:

Red diamonds – *a*-axis. Green triangles – *b*-axis. Blue squares – *c*-axis. Solid data points – experiment. Open data points – simulation. Solid lines – *a*-axis. Longer dashed lines – isotrope. Shorter dashed lines – *b*-axis. Dotted lines – *c*-axis. Black lines – simulation trend lines. Coloured lines – experimental data EOSs. Error bars for $CaPtO_3$ and $CaIrO_3$ are smaller than the symbols used.

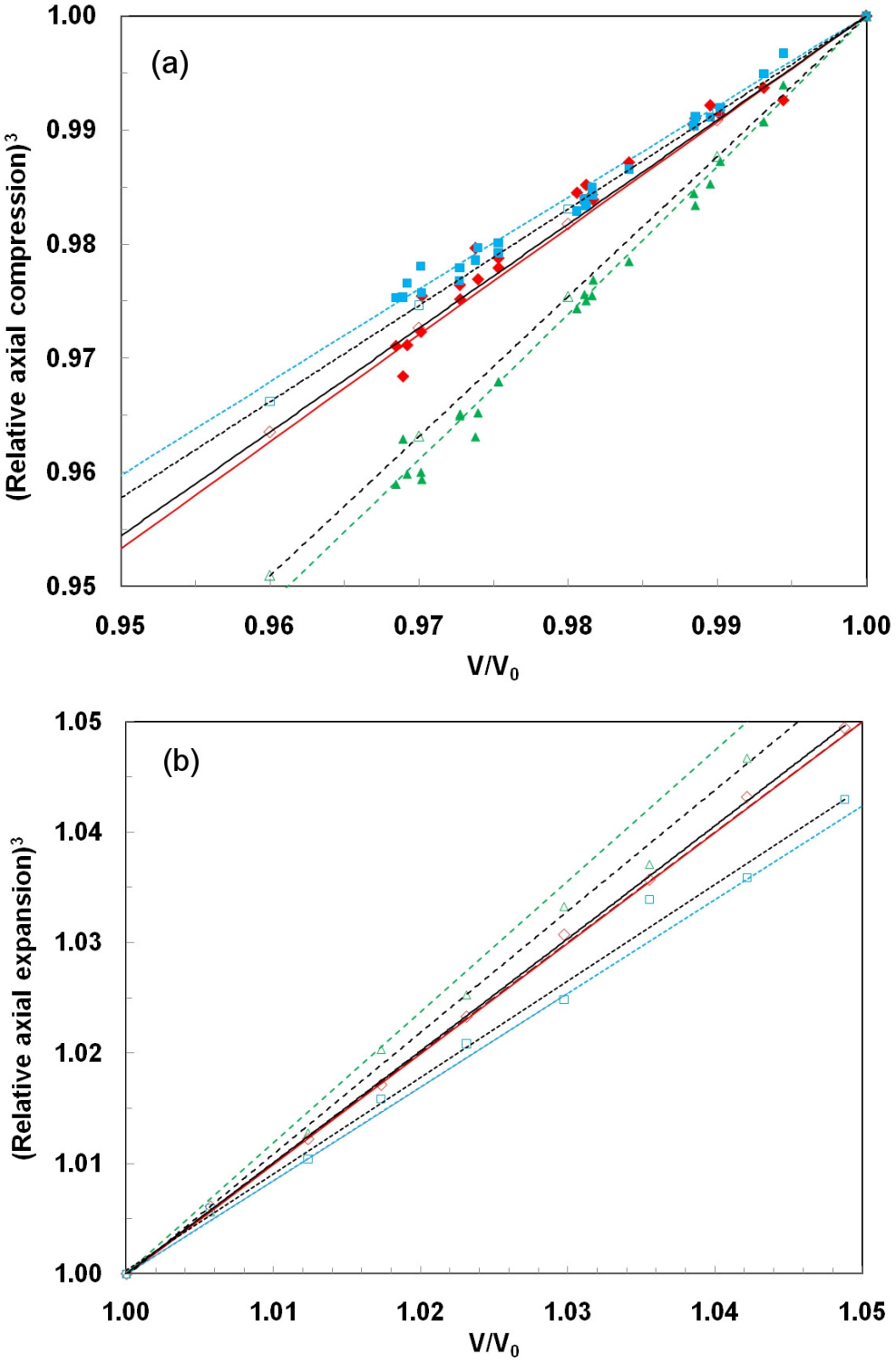

Figure 10-2: Experimental and simulated relative axial compression and expansion for post-perovskite $MgSiO_3$. Experimental EOSs are from Guignot *et al*. (2007), relative to V_0 at 137.3 GPa and 2535K. (a) Compression – athermal simulation with multiple ***k***-points (the present work). (b) Expansion – MD simulation data by Stackhouse and Brodholt (2007). All $MgSiO_3$ simulation is relative to V_0 at 136 GPa and 0 K. Errors are not available for $MgSiO_3$ experimental data points in compression or for its MD simulation in expansion.

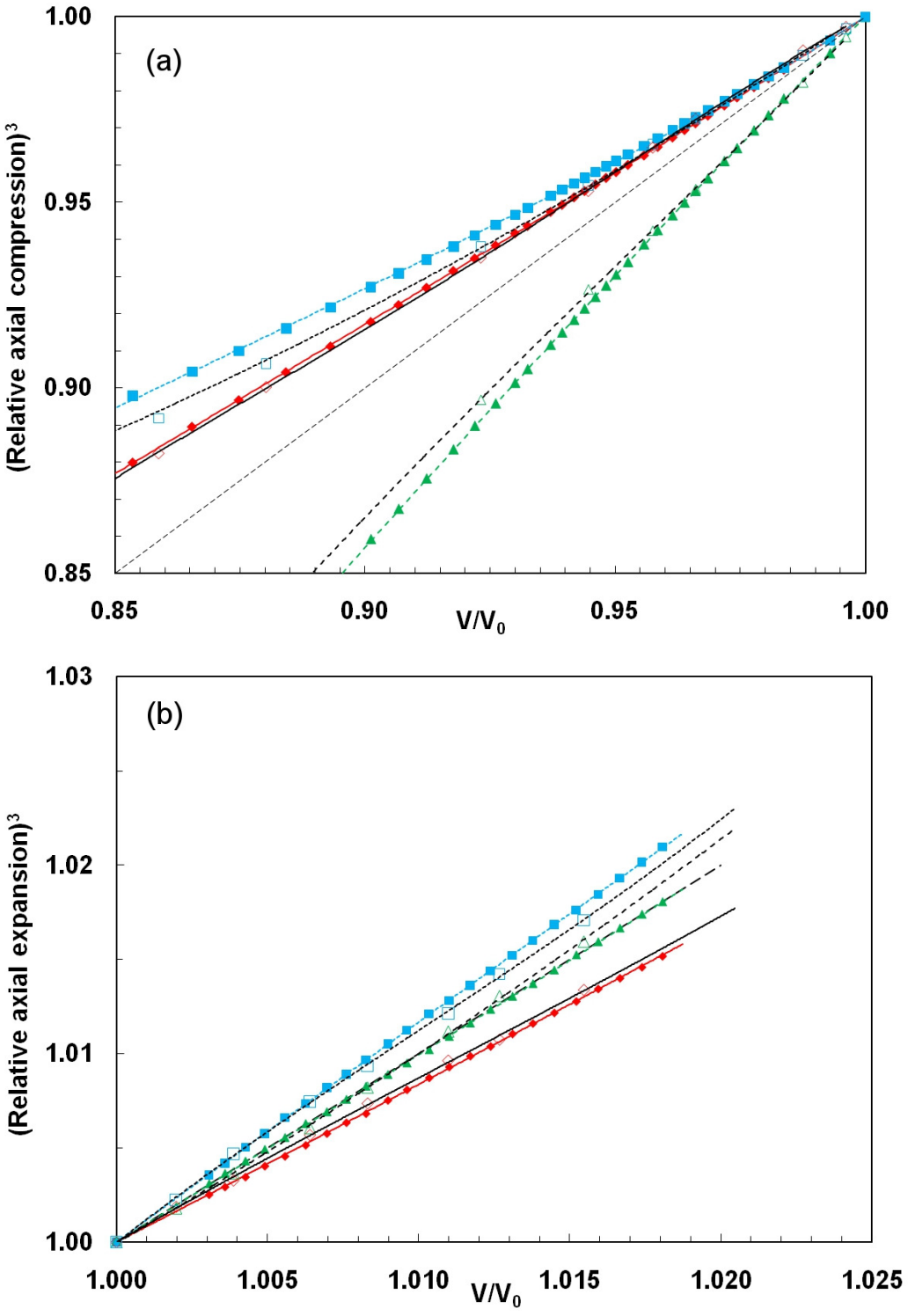

Figure 10-3: Experimental and simulated relative axial compression and expansion for post-perovskite $CaPtO_3$. Simulation results are from the present work. (a) Compression – experimental data from Chapter 8 (b) Expansion – experimental data from Section 9.2. The x-axis is scaled for comparison with Figure 10-4b ($CaIrO_3$).

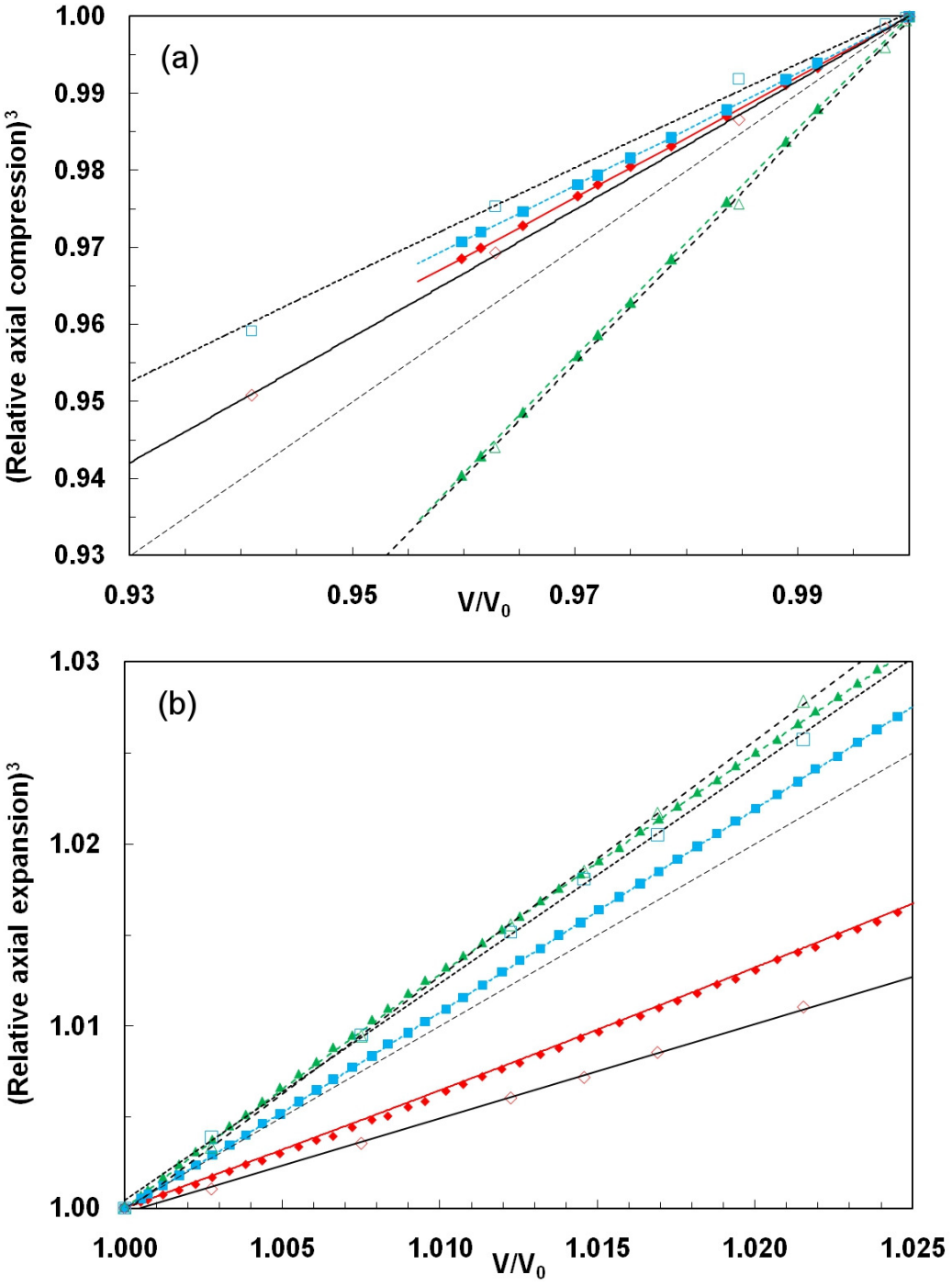

Figure 10-4: Experimental and simulated relative axial compression and expansion for post-perovskite $CaIrO_3$. Simulation results are from the present work. (a) Compression – experimental data from Boffa Ballaran *et al.* (2007) (b) Expansion – experimental data from Lindsay-Scott *et al.* (2007).

Inspection of Figure 10-2, Figure 10-3 and Figure 10-4 shows that the simulated axial compression and expansion sequences (*i.e.* the relative sizes of κ_a, κ_b and κ_c and the

relative sizes of α_a, α_b and α_c) correspond with the experimental sequences for each of these 3 post-perovskites, suggesting that simulation results for $MgSiO_3$ post-perovskite are likely to be reliable (but see Section 10.4.1).

The *c*-axes of simulated and experimental $CaPtO_3$ both show significant curvature in compression, consistent with their relatively high values of K'_0. The simulated *b* and *c*-axes of $CaPtO_3$ and $MgSiO_3$ show less anisotropy that the experimental data, in compression and during expansion. The simulated axial expansion matches the experimental expansion better in $CaPtO_3$ than in $CaIrO_3$.

10.4 Experimental and simulated unit-cell parameters and volume

10.4.1 $CaPtO_3$ and $CaIrO_3$

The ABX_3 post-perovskite structure is defined by 7 variables: the 3 unit-cell axes *a*, *b* and *c*, and the 4 atomic coordinates A *y*, X1 *y*, X2 *y* and X2 *z*. Simulation and experimental results for the 3 unit-cell axes and for the unit-cell volume (their product) of the post-perovskite $CaPtO_3$ are shown in Figure 10-5, and for $CaIrO_3$ in Figure 10-6. The simulated compression is shown using results from both multiple ***k***-point and gamma point simulation (see Section 3.8). The gamma point data in compression is calculated using the same Brillouin-zone sampling as the MD simulation of expansion, while the multiple ***k***-point simulation uses a denser sampling: the gamma point data therefore gives a better indication of the trend of the MD data extrapolated from expansion to compression. The gamma point data in compression illustrates how much of the difference between multiple ***k***-point simulation and MD simulation at $V/V_0 = 1$ may be due to their different Brillouin zone sampling.

The comparisons in Figure 10-5 and Figure 10-6 show that for the $CaPtO_3$ and $CaIrO_3$ post-perovskites the simulated unit-cell axes and volumes are in general larger than those from experiment, as expected for GGA simulation. The exception is the *c*-axis in expansion, where the MD simulation data points are smaller than those from experiment. Here the simulated values of the O1 *y* atomic coordinates are significantly smaller than the experimental values (Figure 10-9b), which will produce a larger angle Δ_1 (Figure 10-15(a)) and smaller values of *c*; however the simulated Pt-O1 bond

lengths are slightly larger than the experimental ones (Figure 10-14a), which has the opposite effect.

These differences between the experimental and MD simulated *c*-axis lead to the simulated unit cell shapes of $CaPtO_3$ and $CaIrO_3$ (the ratio *c*/*a*) differing in expansion from those from experiment. However, the large gaps between the multiple ***k***-point data and the gamma point data for the *c*-axis in compression in $CaPtO_3$ (Figure 10-5c) and in $CaIrO_3$ (Figure 10-6c) suggest that the reduced Brillouin-zone sampling density of the MD simulations may result in inaccurate simulation of the *c*-axis in expansion in these analogues. Alternatively the use of a supercell larger than 60 atoms should also improve accuracy by reducing the size of the Brillouin zone.

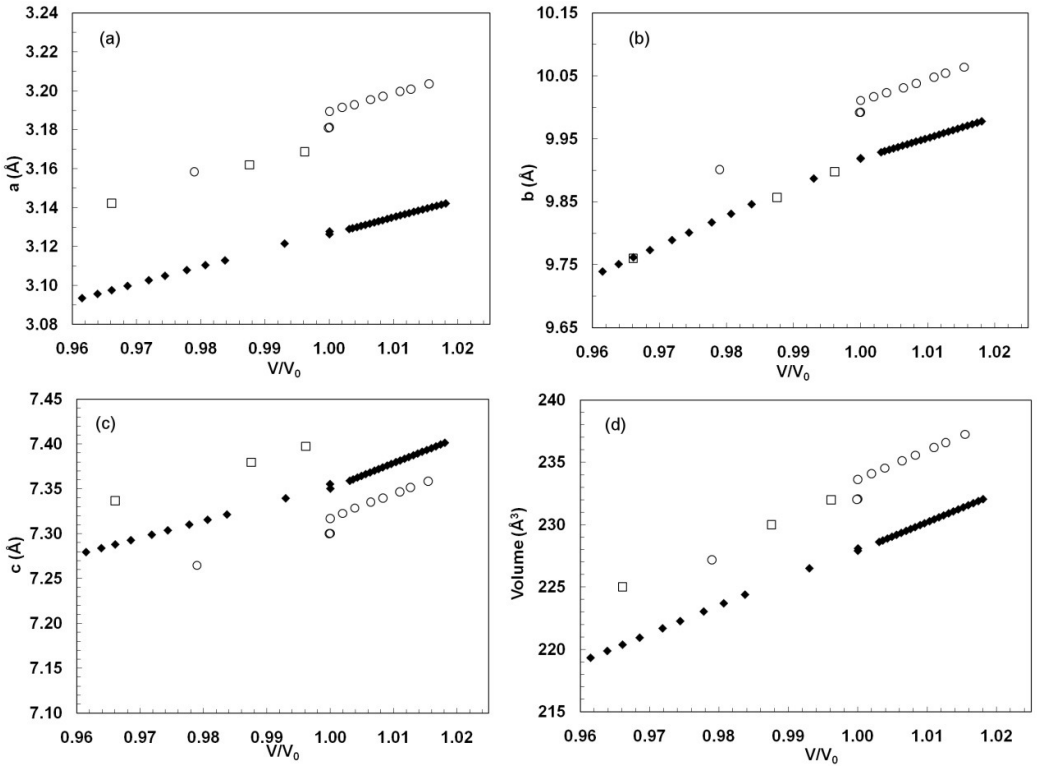

Figure 10-5: Experimental and simulated unit-cell parameters and volume of post-perovskite $CaPtO_3$ (a) *a*-axis (b) *b*-axis (c) *c*-axis (d) volume. Solid diamonds – experiment (the present work). Open circles – MD (expansion) or gamma point athermal (compression) simulation. Open squares – multiple ***k***-point athermal simulation. Error bars for MD are smaller than the symbols used. Data sources – as for Figure 10-3.

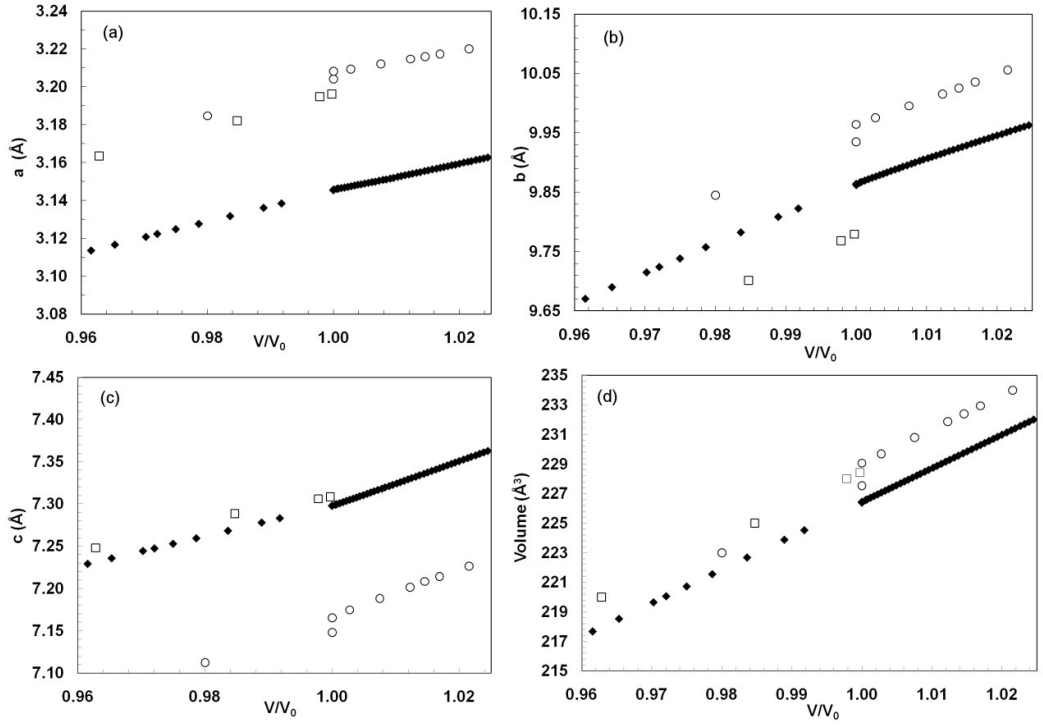

Figure 10-6: Experimental and simulated unit-cell parameters and volume of post-perovskite $CaIrO_3$ (a) *a*-axis (b) *b*-axis (c) *c*-axis (d) volume. Solid diamonds – experiment. Open circles – MD (expansion) or gamma point athermal (compression) simulation. Open squares – multiple ***k***-point athermal simulation. Error bars for MD are smaller than the symbols used. Data sources – as for Figure 10-4.

10.4.2 $MgSiO_3$

For $MgSiO_3$ (Figure 10-7), the isothermal experimental unit-cell parameter data in compression were obtained between 111.1 and 132.4 GPa at 300K (Guignot *et al*., 2007). The multiple ***k***-point simulation values for compression were adjusted to a starting pressure of 111.1 GPa using the isothermal EOS. The isobaric MD simulation values for expansion were modelled at a pressure of 136 GPa (Stackhouse and Brodholt, 2007): Figure 10-7 also shows these values adjusted to 111.1 GPa using the experimental isothermal EOS (Guignot *et al*., 2007). When adjusted to 111.1 GPa, the simulated unit-cell dimensions and volume are higher than the experimental values, as expected for GGA. The simulated *c*-axis values for expansion show the largest discrepancies from the experimental values. However, these MD simulated *c*-axis values are too large, while those for $CaPtO_3$ and $CaIrO_3$ are too small (see previous Section).

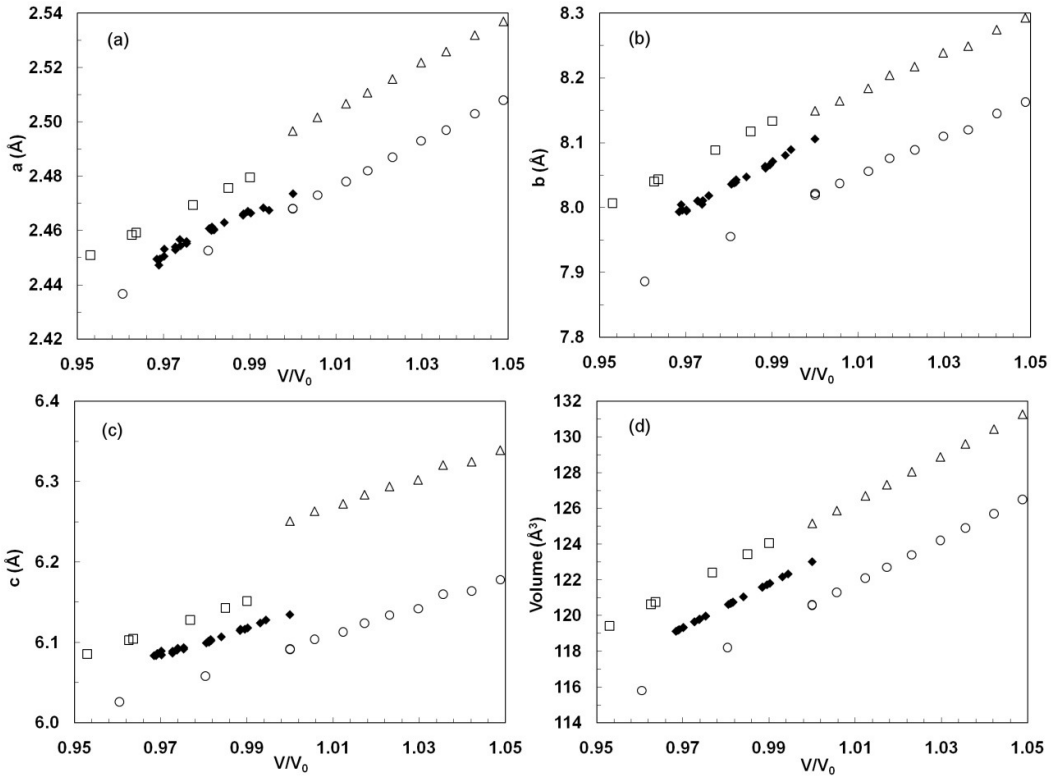

Figure 10-7: Experimental and simulated unit-cell parameters and volume of post-perovskite $MgSiO_3$ (a) *a*-axis (b) *b*-axis (c) *c*-axis (d) volume. Solid diamonds – experiment, relative to V_0 at 111.1 GPa and 300 K (Guignot *et al*., 2007). Open circles – MD (expansion)(Stackhouse and Brodholt, 2007) or gamma point athermal (compression)(the present work) simulation, relative to V_0 at 136 GPa and 0 K. Open triangles – the same MD results relative to V_0 at 111.1 GPa and 0K. Open squares – multiple ***k***-point athermal simulation (the present work), relative to V_0 at 111.1 GPa and 0 K. Isobaric expansion data are not available from experiment, and errors are not available for MD simulations of $MgSiO_3$.

10.4.3 $NaMgF_3$, $NaZnF_3$ and $NaNiF_3$

MD simulations have not been performed for these post-perovskite fluorides; the simulated and experimental unit-cell axes and unit-cell volumes under compression of post-perovskite $NaZnF_3$, $NaMgF_3$ and $NaNiF_3$ are shown in Figure 10-8. The $NaZnF_3$ simulations were made over a range of volumes, corresponding to the experiment of Yakovlev *et al.* (2009). For $NaNiF_3$ and $NaMgF_3$ the simulations were made at a single volume, corresponding to the experimental results at ambient pressure. Experimental unit-cell values were measured for $NaZnF_3$ and for $NaNiF_3$ but not for $NaMgF_3$.

The simulated fluoride unit-cell parameters and volumes are, as in the case of the oxides, larger than the experimental results, as expected from simulation using GGA pseudopotentials (see also Table 10-1). The differences between simulated and experimental values are similar in $NaMgF_3$ and $NaNiF_3$ to those of $NaZnF_3$.

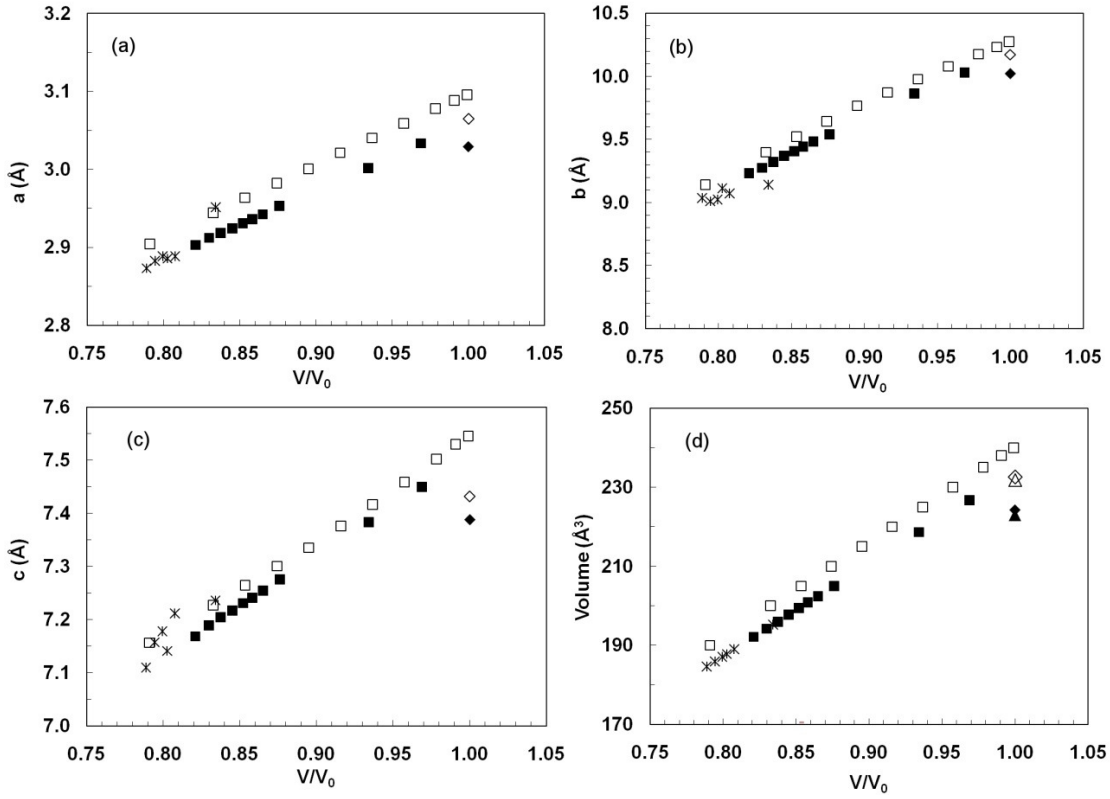

Figure 10-8: Experimental and simulated unit-cell parameters and volume of post-perovskite fluorides (a) *a*-axis (b) *b*-axis (c) *c*-axis (d) volume. Solid data points – experiment. Open data points – multiple ***k***-point simulation (the present work). Squares and asterisks – $NaZnF_3$ (experiment – Yakovlev *et al*., 2009)). Squares are decompression data points used in the present work to calculate EOS parameters. Asterisks are compression data points, including the highest pressure decompression data point. Triangle – $NaMgF_3$ (experiment - only volume was reported, not unit-cell parameters – Hustoft *et al.,* 2008). Diamonds – $NaNiF_3$ (experiment – the present work). Experimental error bars are smaller than the symbols used.

10.5 Experimental and simulated atomic coordinates

10.5.1 $CaPtO_3$ and $CaIrO_3$

The experimental and simulated atomic coordinates of post-perovskite $CaPtO_3$ and $CaIrO_3$ are shown in Figure 10-9 and Figure 10-10. The experimental data for expansion of $CaIrO_3$ from X-ray diffraction in Figure 10-10 shows a considerable degree of scatter, so the plots show the linear fits from Martin *et al*. (2007a) to these atomic coordinates ±1 standard uncertainty.

For $CaPtO_3$ and $CaIrO_3$ the multiple $\boldsymbol{k}$-point simulated atomic coordinates show approximately the same magnitude and sense of change with pressure as the experimental data, with the exception of the O2 z coordinates for $CaPtO_3$. The simulation is less accurate in expansion. The sense of change with increasing temperature in the O2 z coordinates of both $CaPtO_3$ and $CaIrO_3$ is the opposite to that of the experimental data. As already noted (Section 10.4.1), the simulated $CaPtO_3$ O1 y coordinate values are considerably smaller than the experimental values. However, the senses of change on expansion of the simulated O1 y coordinate values for both $CaPtO_3$ and $CaIrO_3$ do reflect the experimental results: the Δ_1 angle decreases with increasing temperature in $CaPtO_3$, while the opposite is true of $CaIrO_3$.

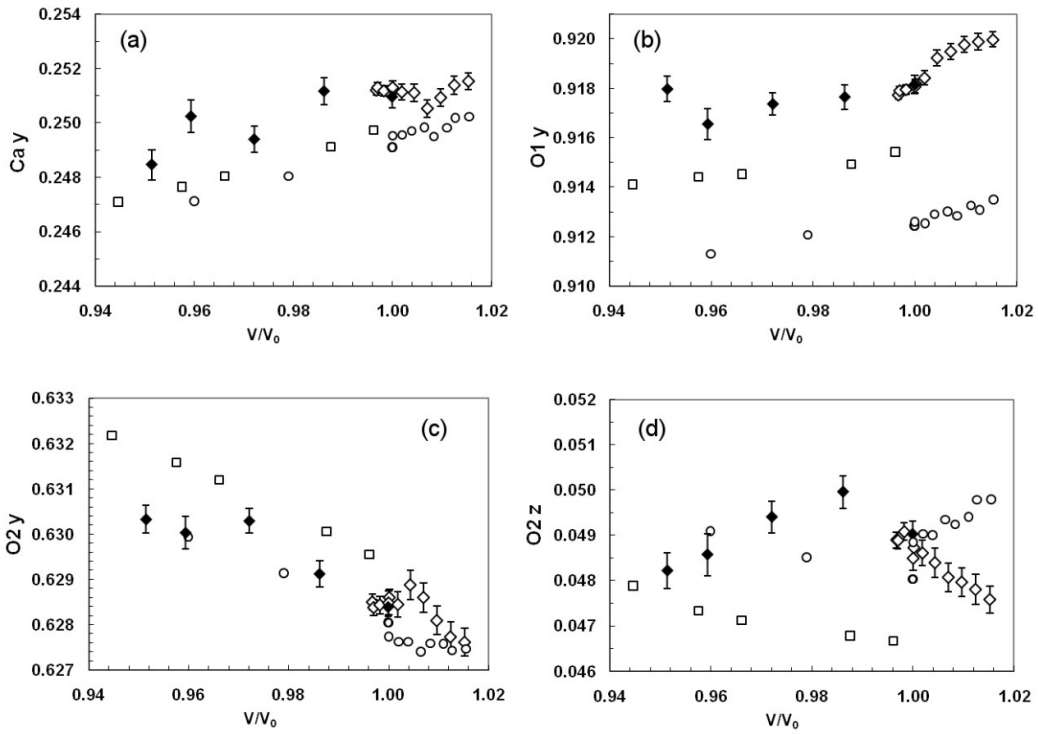

Figure 10-9: Experimental and simulated atomic coordinates of post-perovskite $CaPtO_3$ (a) Ca *y* (b) O1 *y* (c) O2 *y* (d) O2 *z*. Diamonds – Experimental data points (Solid – compression. Open – expansion). Open circles – MD (expansion) and gamma point athermal (compression) simulation. Open squares – multiple ***k***-point —athermal simulation. Error bars for MD are smaller than the symbols used. All data is from the present work.

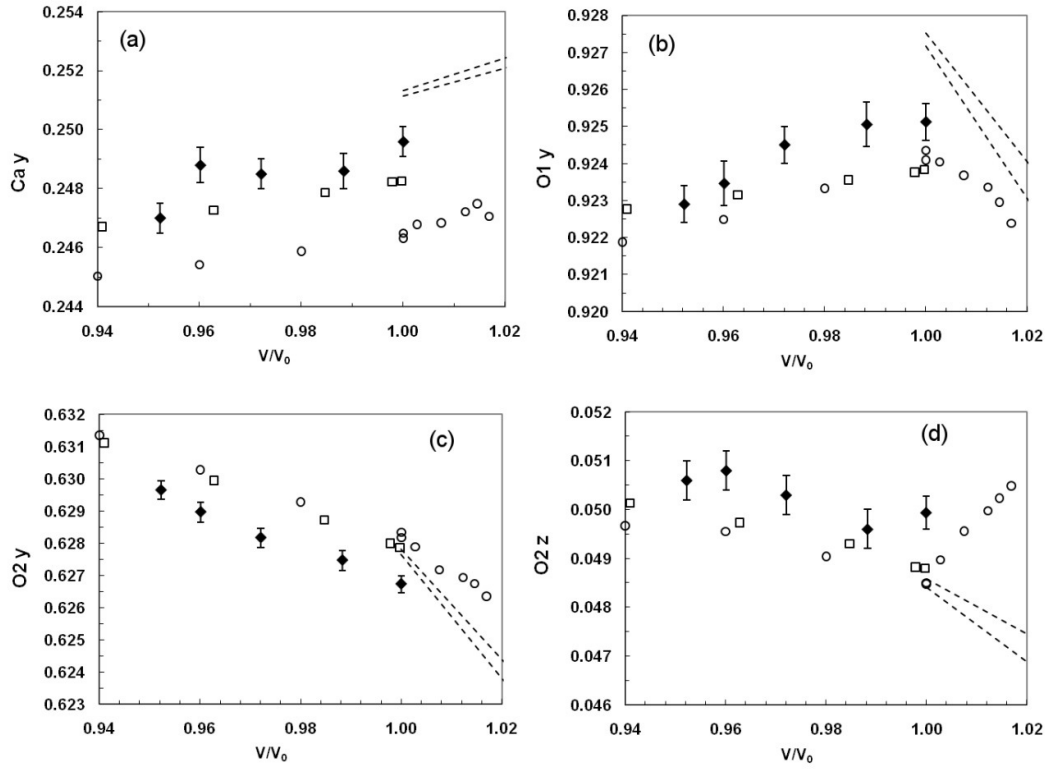

Figure 10-10: Experimental and simulated atomic coordinates of post-perovskite $CaIrO_3$ (a) Ca *y* (b) O1 *y* (c) O2 *y* (d) O2 *z*. Diamonds – Experimental data points (compression)(Martin *et al*., 2007b). Open circles – MD (expansion) and gamma point athermal (compression) simulation (the present work). Open squares – multiple ***k***-point athermal simulation (the present work). Error bars for MD are smaller than the symbols used. Dashed lines – linear fits to expansion atomic coordinates ±1 ESD (Martin *et al*., 2007a).

10.5.2 $MgSiO_3$

The simulated atomic coordinates for compression and expansion for $MgSiO_3$ are shown in Figure 10-11. The increase in the O1 *y* coordinate with expansion is analagous to the corresponding increase in $CaPtO_3$. However, the MD and gamma point simulations of the O2 *z* coordinate display significant scatter.

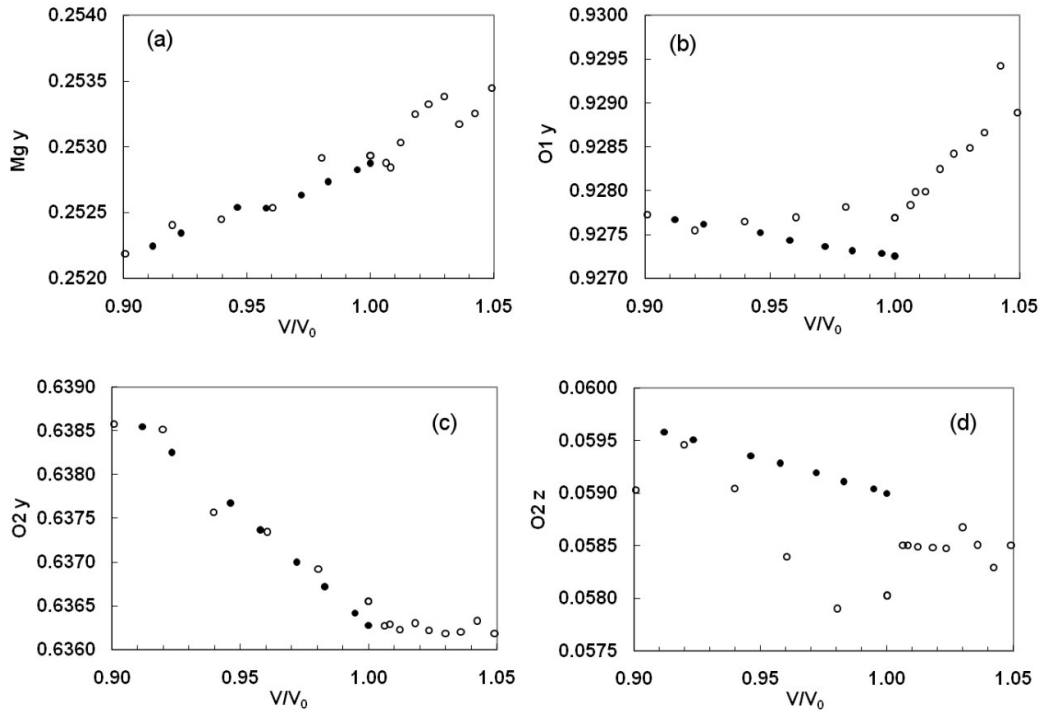

Figure 10-11: Simulated atomic coordinates of post-perovskite $MgSiO_3$ (a) Mg *y* (b) O1 *y* (c) O2 *y* (d) O2 *z*. Solid circles (compression) – multiple ***k***-point athermal simulation (the present work). Open circles – (expansion) MD simulation (Stackhouse and Brodholt, 2007), (compression) gamma point athermal simulation (the present work). All $MgSiO_3$ simulation is relative to V_0 at 136 GPa and 0 K.

Figure 10-12 compares these simulations with the only relevant experimental atomic coordinate data available, which are for $Mg_{0.91}Fe_{0.09}SiO_3$ between 114 and 126 GPa at 300 K (Shim *et al*., 2008)(none are available at one pressure over a range of temperatures). The range and errors in the experimental atomic coordinates using X-ray powder diffraction in a DAC are much larger than any change in the simulations,

and probably reflect the difficulties of the experiment rather than real changes in the crystal structure.

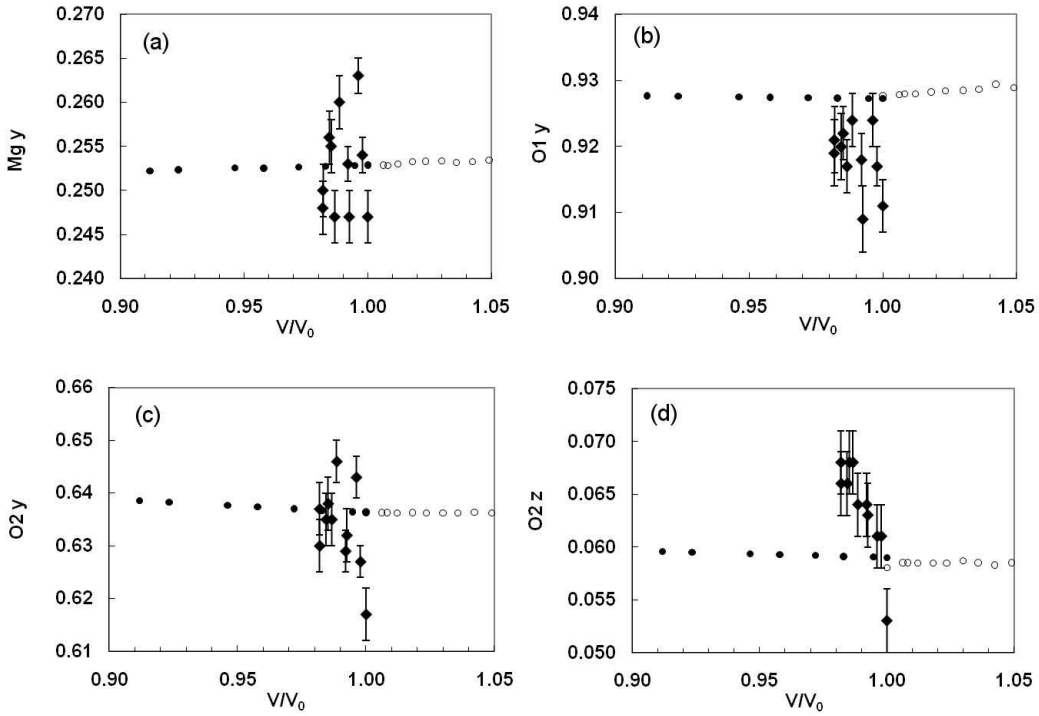

Figure 10-12: Experimental and **s**imulated atomic coordinates of post-perovskite $MgSiO_3$ (a) Mg *y* (b) O1 *y* (c) O2 *y* (d) O2 *z*. Legend as for Figure 10-11 plus solid diamonds – experimental data for $Mg_{0.91}Fe_{0.09}SiO_3$ between 114 and 126 GPa at 300 K (Shim *et al*., 2008)(V_0 at 114 GPa).

10.5.3 $MgGeO_3$

The simulated (GGA and LDA) atomic coordinates of post-perovskite $MgGeO_3$ in compression are shown in Figure 10-13. The correspondence between the different simulations is much better than between simulation and experiment; there is significant scatter in the experimental data, due to the difficulty of obtaining accurate structural measurements using X-ray powder diffraction in a DAC.

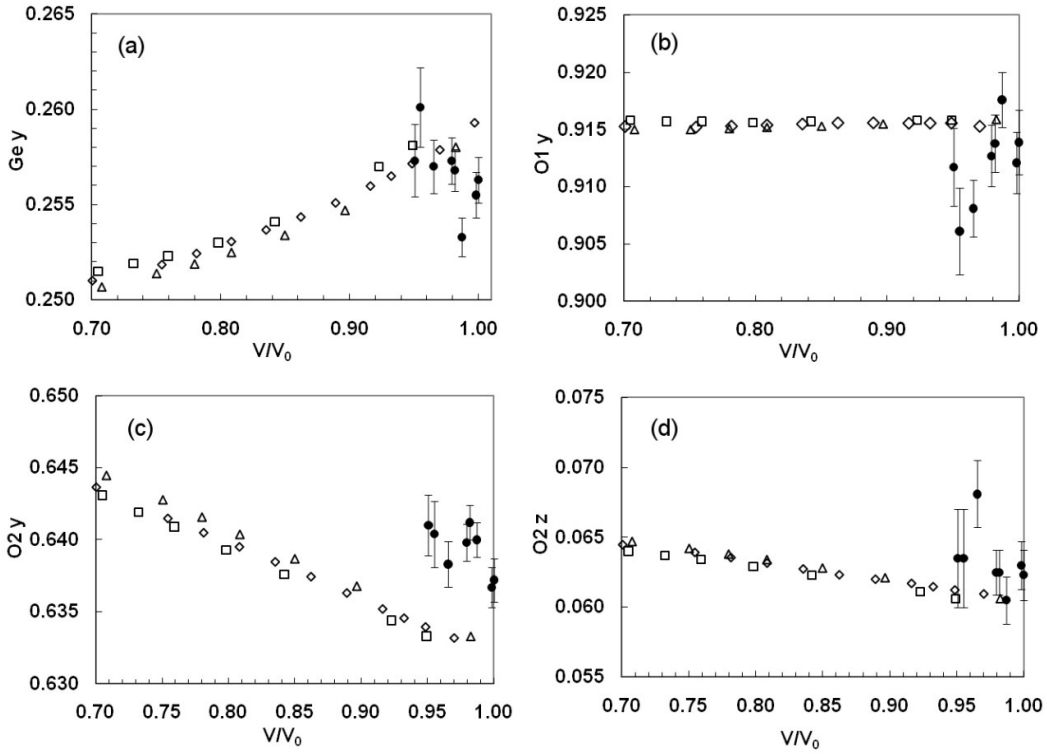

Figure 10-13: Atomic coordinates of post-perovskite $MgGeO_3$. The present work's GGA simulations are shown as diamonds. GGA, LDA and experimental values from Kubo *et al.* (2008) are shown as squares, triangles and solid circles respectively. Experimental data were collected at ambient temperature. All simulations are athermal (~0 K). Error bars are shown for experimental data points.

10.6 Experimental and simulated bond lengths, angles and distortion

The changes with pressure and with temperature in unit-cell parameters and in atomic coordinates combine to produce changes in the 4 bond lengths and 3 angles which are characteristic of the post-perovskite structure. The ways in which these bond lengths and angles vary in $CaPtO_3$ are shown in Figure 10-14 and Figure 10-15 as an example, since the experimental data for this compound in expansion are more accurate than those for $CaIrO_3$. Simulated bond lengths appear to be larger than those measured in experiment, as expected from the use of GGA.

Simulation and experiment agree on the sense of change of angle Δ_1 on expansion, although as noted in Section 10.5.1 the discrepancy in the simulated O1 y coordinate in expansion leads to an over-large simulated value of Δ_1. The divergence of the simulated O2 z coordinate from experiment leads to differences between experimental and simulated angles Δ_2 and p.

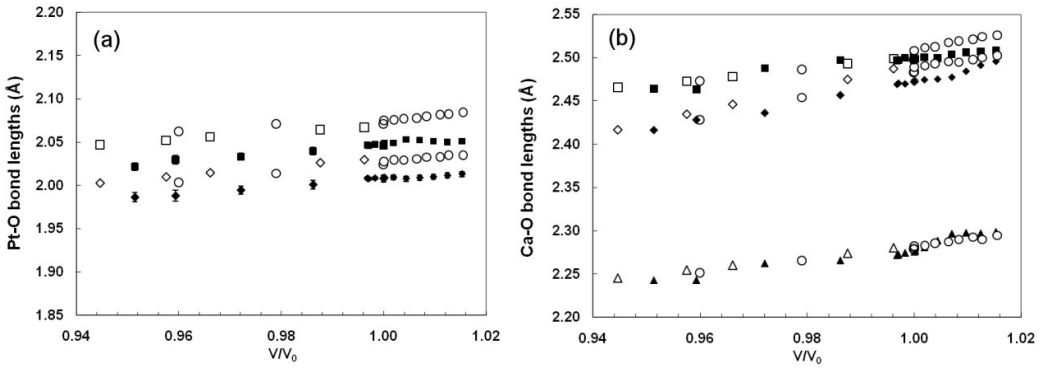

Figure 10-14: Experimental and simulated bond lengths of post-perovskite $CaPtO_3$. (a) Pt-O1 (diamonds) and Pt-O2 (squares) bond lengths (b) Ca-O1 (triangles), Ca-O2 (diamonds) and Ca-O2' (squares) bond lengths. Solid points – experiment. Open points – simulation (circles for MD and athermal gamma point simulation: squares, diamonds or triangles for multiple $\boldsymbol{k}$-point athermal simulation). Error bars for MD are smaller than the symbols used. All values are from the present work.

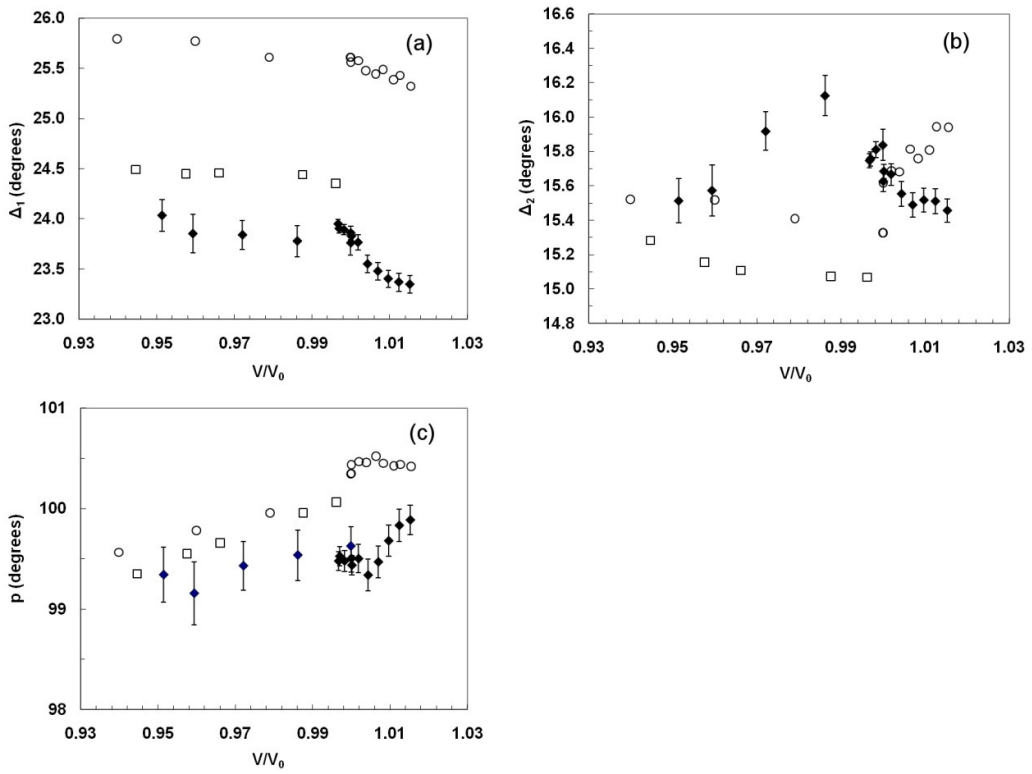

Figure 10-15: Experimental and simulated angles within the structure of post-perovskite $CaPtO_3$. (a) Angle Δ_1 (b) Angle Δ_2 (c) Angle p. Solid data points – experiment. Open data points – simulation (circles for MD and athermal gamma point simulation, squares for multiple $\boldsymbol{k}$-point athermal simulation). Error bars for MD are smaller than the symbols used. All values are from the present work.

Simulated compression of post-perovskites leads in general to a decreasing angle Δ_1 as pressure increases (Figure 4-11a). Angle Δ_1 is also found to decrease with increasing pressure in simulated post-perovskite $Mg_{1-x}Fe_xSiO_3$ (Caracas and Cohen, 2008), and in experimental data on post-perovskite $Mg_{0.9}Fe_{0.1}SiO_3$ and $Mg_{0.85}Fe_{0.15}Al_{0.15}Si_{0.85}O_3$ (Nishio-Hamane *et al.,* 2009). A decrease in octahedral tilt as pressure increases is also found in the corner-linked ABX_3 perovskite structure when the octahedron is less compressible than the cation polyhedron (Zhao *et al.,* 2006). However, experimental data for $CaPtO_3$ appear to show an increasing Δ_1 up to 9.27 GPa ($V/V_0 = 0.95$)(Figure 10-15a), although the changes observed might be considered not to be significant. This is shown together with simulated values over a wider pressure range in Figure 10-16. A higher pressure experiment would be required to ascertain whether angle Δ_1 decreased in $CaPtO_3$ at higher pressures.

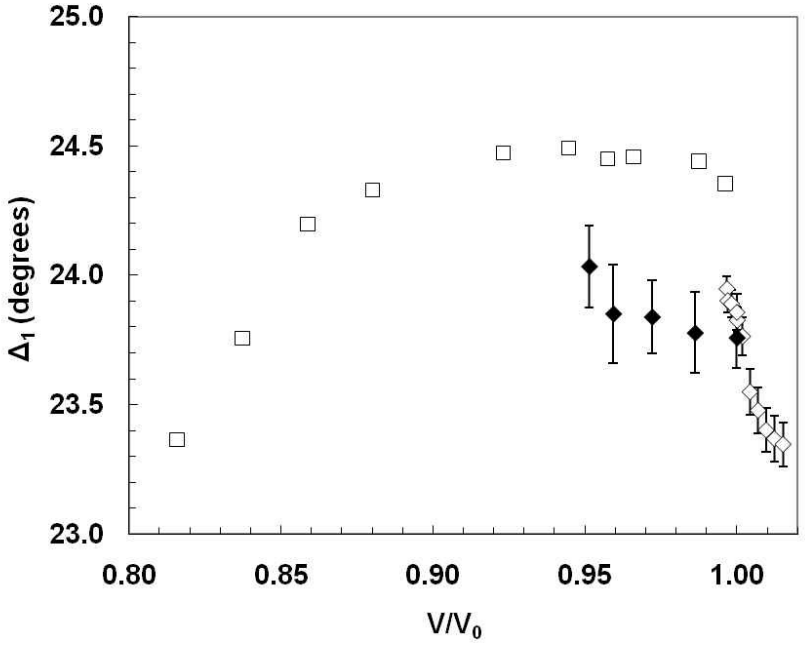

Figure 10-16: Simulated and experimental angle Δ_1 for $CaPtO_3$. Solid diamonds – experiment in compression. Open diamonds – experiment in expansion. Open squares – multiple ***k***-point athermal simulation. All values are from the present work.

Figure 10-17 shows how the volumes of the octahedra and hendecahedra in $CaPtO_3$ vary with changes with pressure and with temperature. The discrepancy on expansion between the simulated and experimental values of O2 z leads to the divergence of the simulated octahedron volume from the experimental one.

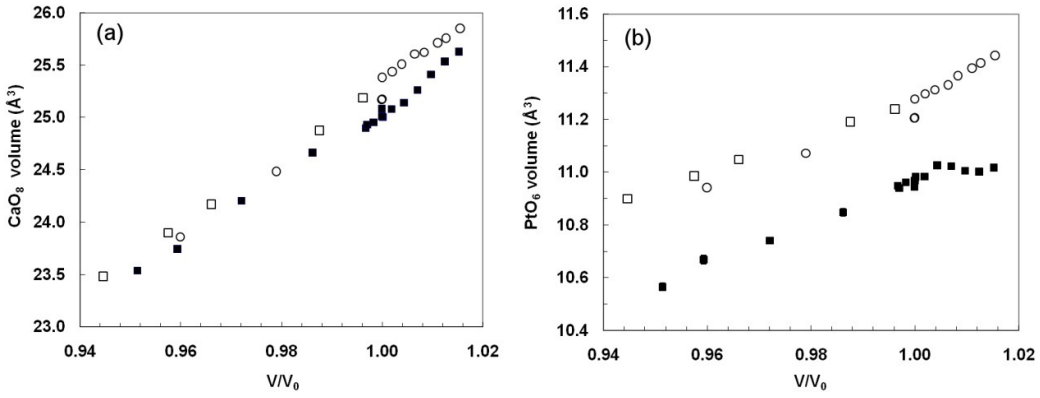

Figure 10-17: Experimental and simulated octahedral volumes of post-perovskite $CaPtO_3$. (a) CaO_8 hendecahedron volume (b) PtO_6 octahedron volume. Solid data points – experiment. Open data points – simulation (circles for MD and athermal gamma point simulation, squares for multiple ***k***-point athermal simulation). Error bars for MD are smaller than the symbols used. All values are from the present work.

As discussed in Section 4.2.4, octahedral distortion may be measured using the bond length ratio B-X1/B-X2 and the octahedral angular variance. Experimental results for $CaPtO_3$ do not show clear trends in these measures on compression, but do show a decrease in Pt-O1/Pt-O2 distortion and an increase in octahedral angular distortion above 473 K (Figure 10-18) as O2 *y* decreases and the angle *p* increases (see Section 9.4.2). The simulated and experimental measures of octahedral distortion shown in Figure 10-18 reflect the differences between changes in simulated and experimental Pt-O bond lengths in Figure 10-14a, and between changes in angles in Figure 10-15. The simulated angle *p* does not increase with increasing temperature as the experimental values do, and the difference between the simulated angles Δ_1 and Δ_2 decreases with increasing temperature. Both of these effects tend to decrease the simulated octahedral angular distortion with increasing temperature, which is the reverse of the experimental trend.

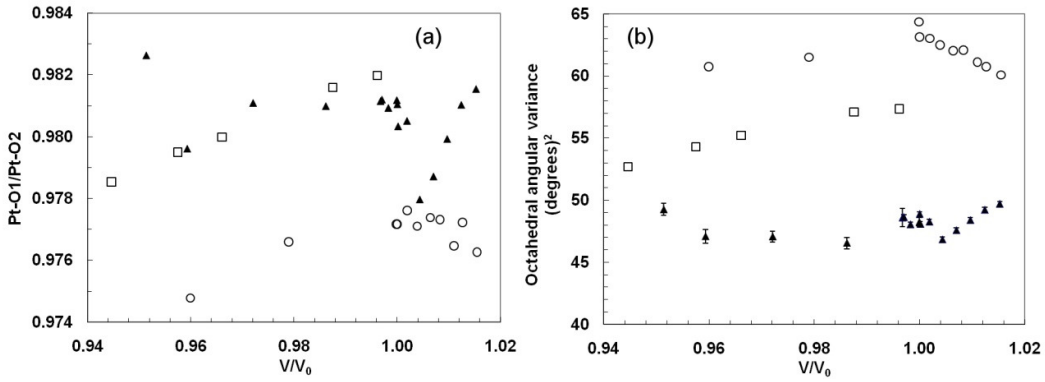

Figure 10-18: Experimental and simulated octahedral distortion in $CaPtO_3$ (a) bond length ratio Pt-O1/Pt-O2 (b) octahedral angular variance. Solid data points – experiment. Open data points – simulation (circles for MD and athermal gamma point simulation, squares for multiple ***k***-point athermal simulation). Error bars for MD are smaller than the symbols used. All values are from the present work.

The difficulty of obtaining accurate structural parameters for post-perovskite compounds at high-pressure in a DAC already shown in Figure 10-12 is illustrated further by the scatter of the measurements made of the angle Δ_1 for $Mg_{0.91}Fe_{0.09}SiO_3$ at 300 K (Shim *et al*., 2008) and for $MgSiO_3$ (Murakami *et al.*, 2004)(Figure 10-19). This Figure also shows the trend line and some data points obtained from athermal multiple ***k***-point simulation.

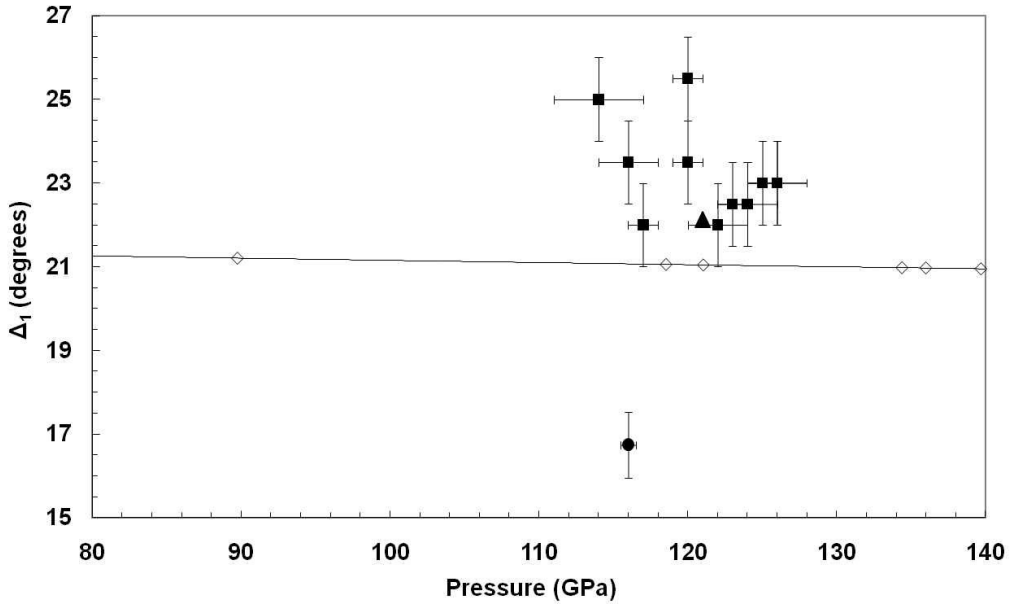

Figure 10-19: Post-perovskite $MgSiO_3$ experimental Δ_1 octahedral tilt. Solid squares: $Mg_{0.91}Fe_{0.09}SiO_3$ between 114 and 126 GPa at 300 K (Shim *et al.*, 2008). Solid circle: $MgSiO_3$ at room temperature (Ono *et al.*, 2006b). Solid triangle: $MgSiO_3$ (Murakami *et al.*, 2004)(no ESDs available). Open diamonds and trend line: athermal multiple ***k***-point simulation (the present work).

10.7 Experimental and simulated anisotropic atomic displacements

The anisotropy of atomic displacements due to thermal motion in the $CaPtO_3$ experiment is described in Section 9.3. This section describes atomic displacements derived from MD simulation of $MgSiO_3$ (Stackhouse and Brodholt, 2007), $CaPtO_3$ and $CaIrO_3$ (both the present work), and compares the simulated $CaPtO_3$ results with experiment.

Figure 10-20 shows the atomic densities of the BO_6 octahedra in $MgSiO_3$, $CaPtO_3$ and $CaIrO_3$ at 4000 K, 869 K and 900 K respectively. The atoms shown are the 7 atoms of the central octahedron in the central of the three 20 atom cells in the 60 atom (3 x 1 x 1) supercell, summed over all time steps for a single MD simulation, and viewed along the *a*-axis. Each point represents the position of an atom during one time step. The atomic displacements appear to be less anisotropic in the 6000 time step MD simulation of post-perovskite $MgSiO_3$ at 4000 K than in the 4000 time step MD simulations of post-perovskite $CaPtO_3$ at 869 K and of post-perovskite $CaIrO_3$ at 900 K.

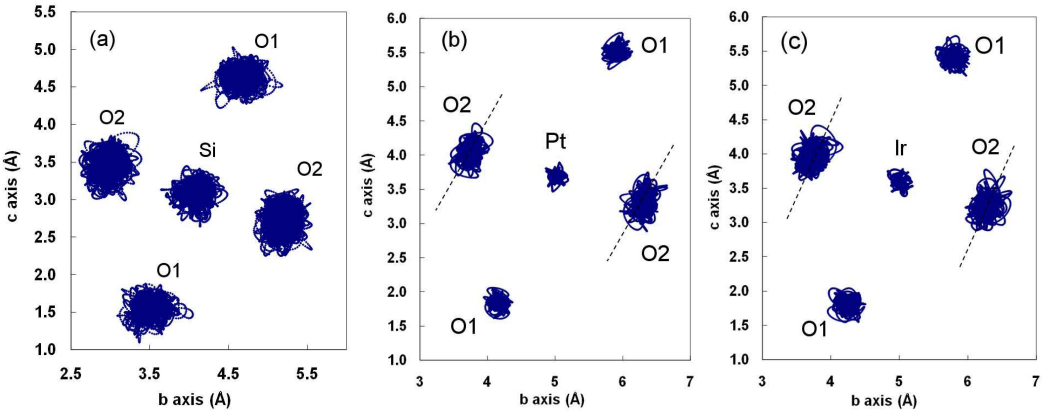

Figure 10-20: Total density of atomic positions in the post-perovskite octahedron viewed along the *a*-axis for (a) $MgSiO_3$ at 4000 K (Stackhouse and Brodholt, 2007)(b) $CaPtO_3$ at 869 K (b) $CaIrO_3$ at 900 K. Dashed lines indicate estimated axes of probability ellipsoids.

The following three Figures show the coordinates produced by the same MD simulations as in Figure 10-20 but now for all of the atoms in each supercell, summed over all time steps, and shown using plots contoured by atomic density.

Figure 10-21a shows that the Mg atomic probability density contours in post-perovskite $MgSiO_3$ are slightly lengthened (by comparison with a sphere) along [001], and the O1 contours are flattened in the same direction. The O2 contours are flattened so that the axis of the atomic density probability ellipsoid is inclined approximately along [031] as indicated in the Figure. Figure 10-21b shows no lengthening of the O1, O2 or Mg atom contours along either [100] or [010]. The superimposition of atoms viewed along the *b*-axis makes that a less useful view. These observations are consistent with the post-perovskite site symmetry described in the experimental observation of $CaPtO_3$ in Section 9.3.

The simulated anisotropy of displacement of the Mg atom differs from that of the experimental Ca atom in $CaPtO_3$ (see Figure 9-17 and Figure 9-18) because the simulated Mg atomic probability density forms a prolate ("cigar") spheroid with the largest component of vibration along [001], whereas that of the Ca atom forms an oblate ("smartie" or "M&M") spheroid with its smallest component parallel to [010]. The anisotropies of the O1 and O2 atoms in simulated $MgSiO_3$ also differ from those of O1 and O2 in experimental observation of $CaPtO_3$. The atomic probability density of O1 in the simulated $MgSiO_3$ appears to form an oblate spheroid with its smallest component of vibration along [001], whereas in the $CaPtO_3$ experiment it forms a prolate spheroid with its largest component of vibration along the [100]. The atomic probability density of O2 in simulated $MgSiO_3$ appears to form a prolate spheroid with its largest component inclined to [001], whereas in the $CaPtO_3$ experiment it forms an oblate spheroid with its smallest component of vibration sub-parallel to [010].

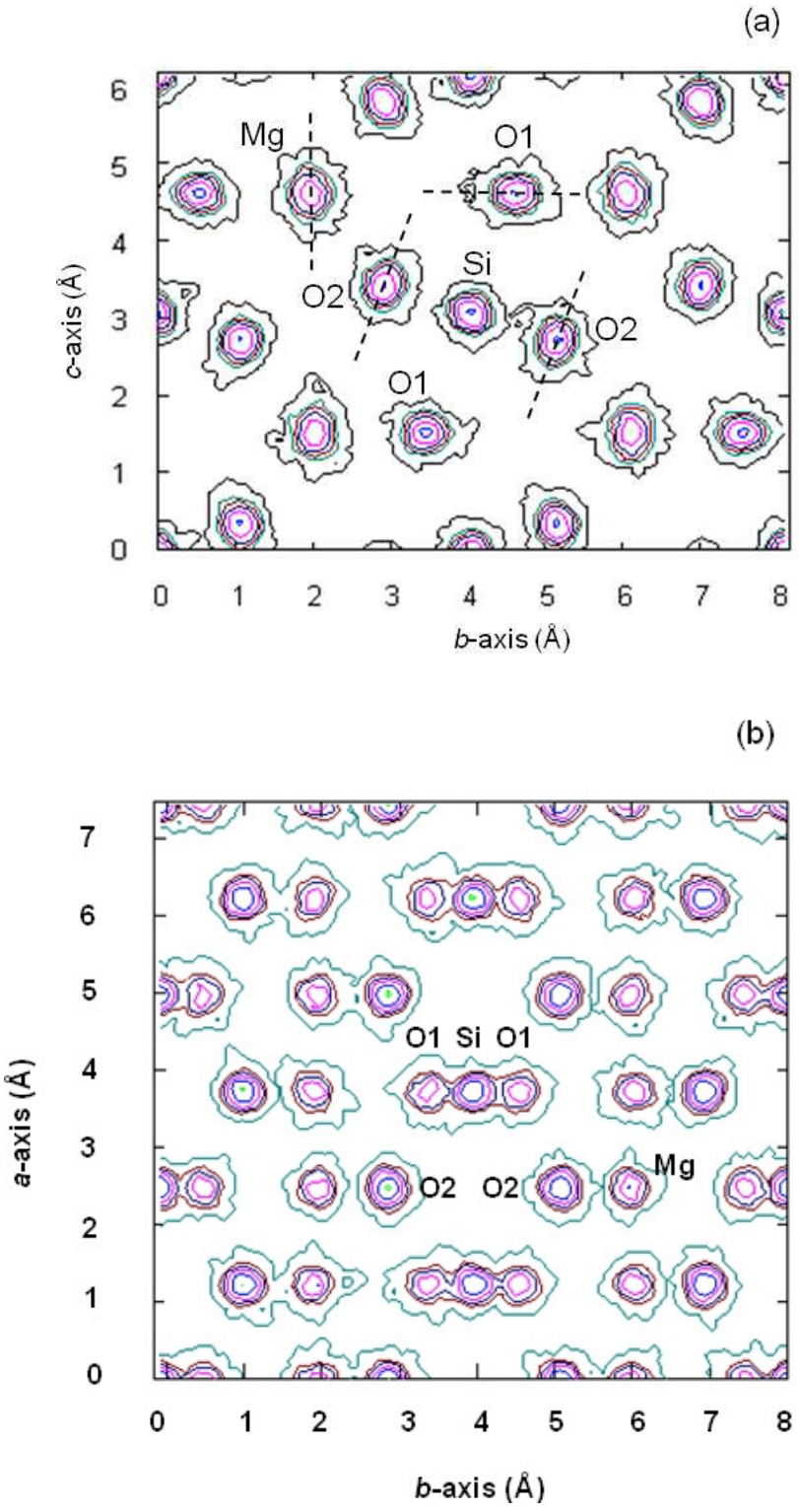

Figure 10-21: Density of atomic positions in the post-perovskite unit-cell of $MgSiO_3$ at 4000 K from MD simulation (a) viewed along the *a*-axis (b) viewed along the *c*-axis. Contour levels of atomic densities are at 1, 50,100,200,400,800 and 1000. Dashed lines indicate estimated axes of probability ellipsoids.

Figure 10-22a shows that the Ca atomic probability density contours in simulated post-perovskite $CaPtO_3$ lengthened along [001], and the O2 contours flattened so that the axis of the atomic probability density ellipsoid is inclined approximately along [031]. Figure 10-22b shows the O1 atom contours slightly elongated along [100], but the Ca and O2 contours are sub-circular in this view. This elongation of the O1 atom atomic probability density ellipsoid is consistent with the O1 experimental anisotropy described in Section 9.3. The simulated atomic probability density of the Ca atom appears to form a prolate spheroid with the largest component of vibration along [001], rather than the oblate spheroid observed in experiment: vibration along [100] is reduced in the simulation. Similarly the simulated O2 atom does not appear to vibrate as much along [100], whereas the experimental O2 does.

Figure 10-23 shows experimental nuclear scattering length density maps for post-perovskite $CaPtO_3$ at 869 K. The corresponding anisotropic atomic displacement parameters are listed in Table 9-8 and their effects are shown in Figure 9-17 and Figure 9-18. The anisotropic displacement of O2 atoms along [001] appears in Figure 10-23a, but the extent to which this displacement may be inclined either side of [001] in (100) to match either the experimental "anti-clockwise" displacement illustrated in Figure 9-17 or the simulated "clockwise" displacement illustrated in Figure 10-22a is not clear. The anisotropic displacement of O1 and Ca atoms along [100] shown in Figure 9-18 also appears in Figure 10-23b.

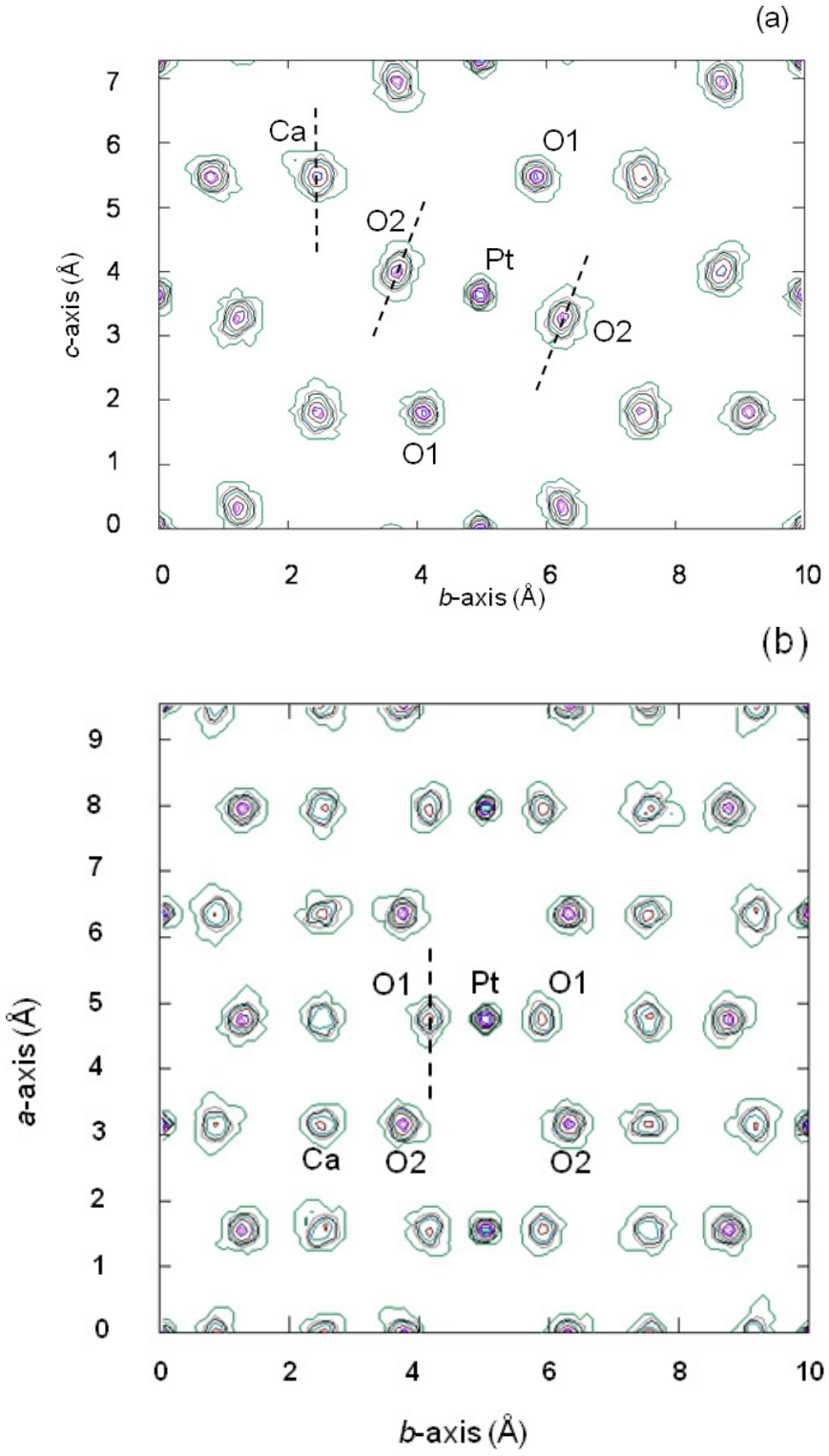

Figure 10-22: Density of atomic positions in the post-perovskite unit-cell of $CaPtO_3$ at 869 K from MD simulation (a) viewed along the *a*-axis (b) viewed along the *c*-axis. Contour levels of atomic densities are as in Figure 10-21. Dashed lines indicate estimated axes of probability ellipsoids.

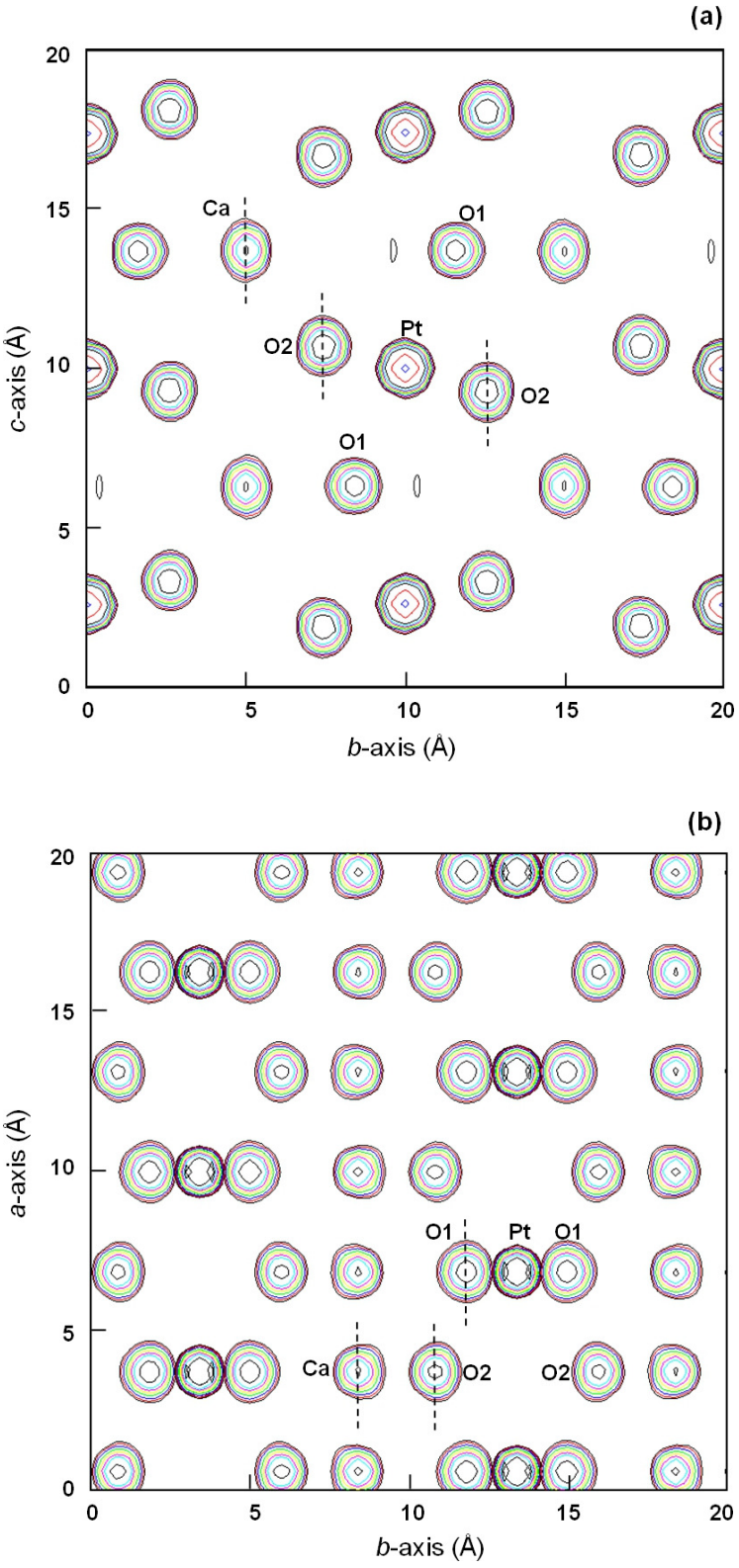

Figure 10-23: Nuclear scattering length density maps from neutron powder diffraction of post-perovskite $CaPtO_3$ at 869 K (see Section 9.2): (a) viewed along the *a*-axis, from a superposition of sections at (0 0 0) and (0.5 0 0) (b) viewed along the *c*-axis, from a superposition of sections at (0 0 0.25), (0 0 0.47), (0 0 0.53) and (0 0 0.75).

Figure 10-24a shows that the Ca atomic probability density ellipsoid in simulated post-perovskite $CaIrO_3$ is lengthened along [001], with the axis of the O2 atom ellipsoid inclined approximately along [031]. These features are similar to those of Ca and O2 in simulated $CaPtO_3$ and to those of Mg and O2 in simulated $MgSiO_3$. Figure 10-24b shows that the ellipsoid of the simulated $CaIrO_3$ O1 atom is a prolate spheroid with the largest component of vibration along [100], as in simulated $CaPtO_3$ but unlike simulated $MgSiO_3$. The ellipsoid of the simulated $CaIrO_3$ O1 atom is a prolate spheroid, and that of the O2 atom is an oblate spheroid with its smallest component of vibration sub-parallel to [100]. Caveats regarding experimental measurements of anisotropic atomic displacement are discussed in Section 9.3.

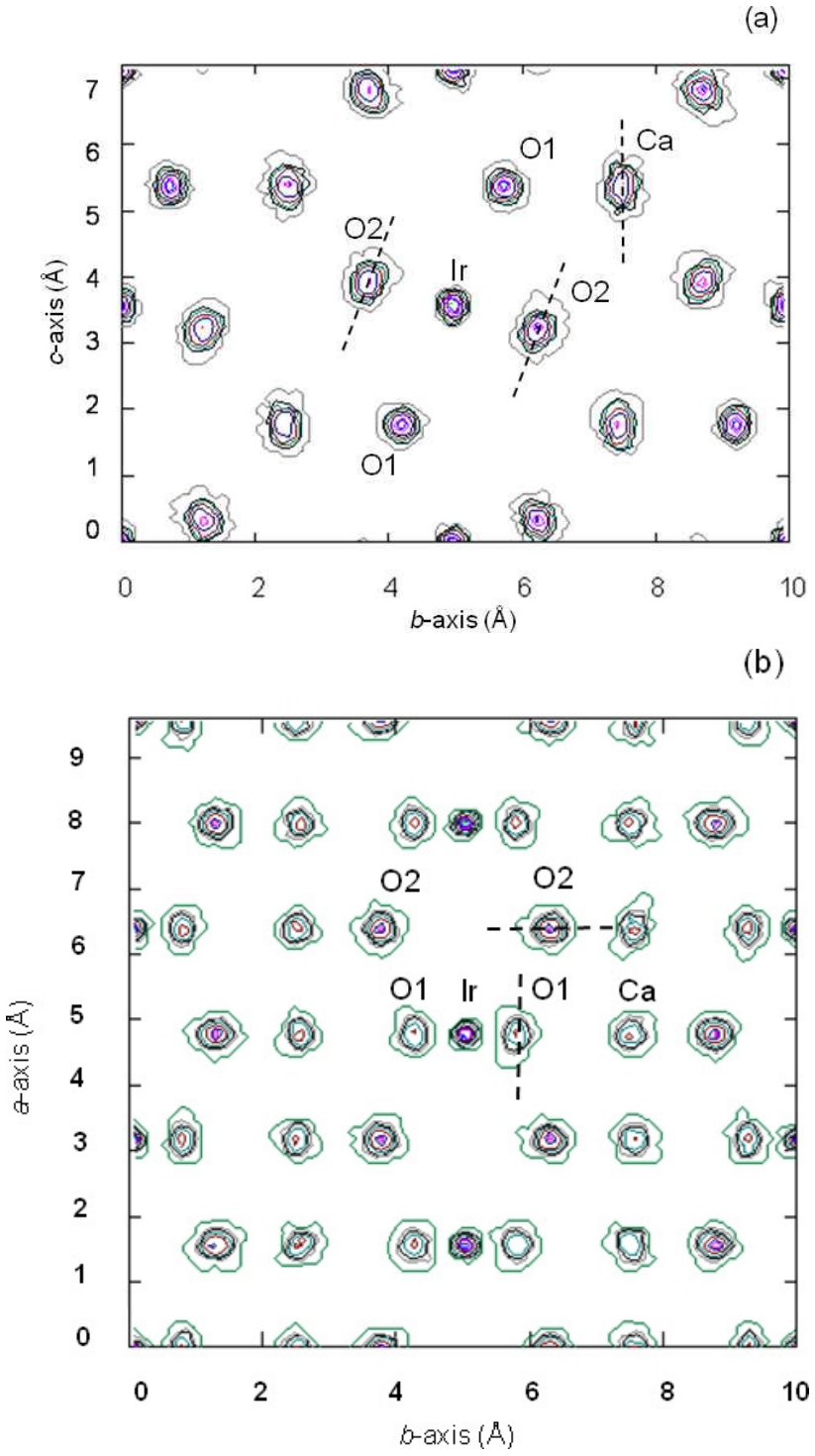

Figure 10-24: Density of atomic positions in the post-perovskite unit-cell of $CaIrO_3$ at 900 K from MD simulation (a) viewed along the *a*-axis (b) viewed along the *c*-axis. Contour levels of atomic densities are as in Figure 10-21. Dashed lines indicate estimated axes of probability ellipsoids.

10.8 Relative importance of bond lengths and angles in determining unit-cell dimensions

The relative importance of bond lengths and angles in determining post-perovskite cell sizes in compression and in expansion is examined in Section 9.4.3 using experimental results for $CaPtO_3$ and $CaIrO_3$, with data from simulation of $MgSiO_3$. This section compares these results with those from simulation of the oxides $CaPtO_3$ and $CaIrO_3$ and of the fluorides $NaMgF_3$, $NaZnF_3$ and $NaNiF_3$. The experimental measurements of the $MgGeO_3$ structure are too scattered to yield meaningful results (see atomic coordinates in Figure 10-13).

The comparison of the relative importance of the simulated and experimental values of bond lengths and angles for the cell parameters, in compression and in expansion, of post-perovskite $CaPtO_3$ and $CaIrO_3$ is shown in Table 10-2. The simulated and experimental results between which the largest discrepancies occur are italicized. It is evident that the simulated values approximate to the experimental values in compression, but not in expansion. The reason for this in the case of $CaPtO_3$ lies in the discrepancies between the rates of change of the simulated and experimental bond lengths and angles on thermal expansion (see Figure 10-14 and Figure 10-15). In the case of $CaIrO_3$ the discrepancy between simulation and experiment probably also reflects the problems associated with experimental determination of the oxygen coordinates from X-ray powder diffraction.

Post-perovskite $CaPtO_3$ and $CaIrO_3$

Experimental data as in Table 9-9 and Table 9-10.

Compression data from athermal multiple ***k***-point simulation (the present work).

***a*-axis**		*V/V₀*	(i) % of calculated change in *a* due to change in B-O2 bond	(ii) % of calculated change in *a* due to change in angle *p*
Compression				
$CaPtO_3$	Simulated	0.957	66%	34%
	Experiment	0.951	85%	15%
$CaIrO_3$	Simulated	0.952	68%	32%
	Experiment	0.952	59%	41%
Expansion				
$CaPtO_3$	Simulated	1.013	*100%*	*0%*
	Experiment	1.015	*34%*	*66%*
$CaIrO_3$	Simulated	1.019	*35%*	*65%*
	Experiment	1.026	*-137%*	*237%*

***b*-axis**		% change in *b* due to change in						
		(i) B-O1 bond	(ii) B-O2 bond	(iii) Ca-O1 bond	(iv) Ca-O2 bond	(v) angle *p*	(vi) angle Δ_1	(vii) angle Δ_2
Compression								
$CaPtO_3$	Simulated	-17%	-16%	40%	123%	-38%	-3%	0%
	Experiment	-13%	-19%	47%	101%	-11%	-12%	6%
$CaIrO_3$	Simulated	-15%	-15%	49%	106%	-19%	2%	-6%
	Experiment	-13%	-13%	49%	121%	-29%	-16%	0%
Expansion								
$CaPtO_3$	Simulated	-22%	-32%	*50%*	*104%*	*0%*	*-31%*	*31%*
	Experiment	-11%	-10%	*125%*	*177%*	*-66%*	*-101%*	*-14%*
$CaIrO_3$	Simulated	-42%	*-5%*	*-28%*	*97%*	*-32%*	*67%*	*44%*
	Experiment	-52%	*24%*	*-65%*	*218%*	*-144%*	*116%*	*0%*

***c*-axis**		(i) % of calculated change in *c* due to change in B-O1 bond	(ii) % of calculated change in *c* due to change in angle Δ_1
Compression			
$CaPtO_3$	Simulated	93%	7%
	Experiment	83%	15%
$CaIrO_3$	Simulated	103%	-3%
	Experiment	78%	22%
Expansion			
$CaPtO_3$	Simulated	*77%*	*23%*
	Experiment	*33%*	*67%*
$CaIrO_3$	Simulated	*155%*	*-55%*
	Experiment	*199%*	*-99%*

Table 10-2: Comparison of experimental and simulated results showing the relative importance for $CaPtO_3$ and $CaIrO_3$ of changes in atomic coordinates and angles in determining the change of unit-cell parameters during compression and during thermal expansion. The simulated and experimental results between which the largest discrepancies occur are italicized. The compression/expansion factors V/V_0 shown apply throughout.

At the time of writing there are no data published (as far as I am aware) on the changes in atomic coordinates of post-perovskite fluorides in compression or expansion. The results of my simulation of the compression of post-perovskite fluorides $NaMgF_3$, $NaZnF_3$ and $NaNiF_3$ are described in Chapter 4. Table 10-3 shows the relative importance for fluoride post-perovskites of changes in atomic coordinates and angles in determining the change of unit-cell parameters during compression as predicted by these simulations.

The relative importance in compression of the changes in bond lengths and in angles for the simulated fluoride *a*-axes is similar to that found in experimental data for post-perovskite $CaPtO_3$ and $CaIrO_3$ (Table 10-2). The decrease in angle Δ_1 with increasing compression of fluorides (see Figure 4-11a), which is the opposite of that measured experimentally in the present work over a smaller pressure range for $CaPtO_3$, determines its negative effect on the *c*-axes of the fluorides. However, a similar effect may be expected in $CaPtO_3$ if its experimental results at V/V_0 below 0.90 follow the trend of the simulated Δ_1 shown in Figure 10-16. This decrease in angle Δ_1 with increasing compression of fluorides also explains why its effect on the *b*-axis is the reverse of that found in $CaPtO_3$.

Post-perovskite $NaMgF_3$, $NaZnF_3$ and $NaNiF_3$

Compression data from athermal multiple ***k***-point simulation (the present work).

$NaMgF_3$ – 52.2 GPa, $V/V_0 = 0.69$

$NaZnF_3$ – 48.8 GPa, $V/V_0 = 0.71$

$NaNiF_3$ – 50.8 GPa, $V/V_0 = 0.72$

a-axis

	(i) % of calculated change in *a* due to change in B-F2 bond	(ii) % of calculated change in *a* due to change in angle *p*	See note A
$NaMgF_3$	84%	16%	101%
$NaZnF_3$	80%	20%	101%
$NaNiF_3$	76%	24%	101%

b-axis

	% change in *b* due to change in							
	(i) B-F1 bond	(ii) B-F2 bond	(iii) A-F1 bond	(iv) A-F2 bond	(v) angle *p*	(vi) angle Δ_1	(vii) angle Δ_2	See note B
$NaMgF_3$	-12%	-11%	38%	80%	-4%	22%	-3%	109%
$NaZnF_3$	-12%	-10%	37%	73%	-12%	15%	-1%	91%
$NaNiF_3$	-13%	-11%	42%	80%	-17%	8%	0%	89%

c-axis

	(i) % of calculated change in *c* due to change in B-F1 bond	(ii) % of calculated change in *c* due to change in angle Δ_1	See note A
$NaMgF_3$	127%	-27%	96%
$NaZnF_3$	149%	-49%	93%
$NaNiF_3$	122%	-22%	97%

Table 10-3: Simulated data regarding the relative importance for fluoride post-perovskites of changes in atomic coordinates and angles in determining the change of unit-cell parameters during compression.

A - % of total simulated change in *a* accounted for by sum of columns (i) and (ii)
B - % of total simulated change in *b* accounted for by sum of columns (i) – (vii)

Note that these percentages may differ from 100% due to the assumption of linearity in the partial derivative.

10.9 Discussion

The majority of the differences in Table 10-1 between simulated and experimental EOS parameters for the post-perovskites are consistent with the expected effect of using the GGA approximation. Differences between simulated and experimental values of K_0 and K'_0 may also be due to simulation of a wider pressure range than that used in experiments, with correlation of K_0 and K'_0. The simulation in compression of post-perovskite $MgGeO_3$ in the present work using GGA pseudopotentials gave results consistent with published simulations which used GGA and LDA pseudopotentials.

The simulated axial compression and expansion sequences corresponded with those from experiment for the three post-perovskites whose expansion was simulated in the present work. However, the axial ratios simulated for $CaPtO_3$ and $CaIrO_3$ in expansion were slightly different from experiment. For example in $CaIrO_3$ at ambient pressure and 300 K the simulated *a*-axis was 2.0% larger than experiment and the *c*-axis was 1.8% smaller, rather than all axes being larger as would be expected from using GGA pseudopotentials. Inaccurate simulation of the expansion of the *c*-axis may be related to the reduced Brillouin-zone sampling density used in MD (and in gamma point) simulation, which is required to achieve feasible MD simulation run times. The use of a larger supercell for MD simulation should increase accuracy, at greater cost in computer processing time.

The simulated volume and axes of $MgSiO_3$ in expansion and in compression at high-temperature and at high-pressure were larger than experiment (as expected), although this may be due to the effect of high-pressure overriding that of high-temperature. The simulated volumes and axes of $MgGeO_3$ and $NaZnF_3$ in compression were also larger than experiment, as expected.

The sense of changes of the simulated atomic coordinates of $CaPtO_3$ and $CaIrO_3$ with changing pressure and temperature corresponded with experiment in compression and in expansion, except for the O2 *z* coordinates. This inaccuracy in simulated O2 *z* coordinates made the sense of changes of simulated angles Δ_2 and *p* and the octahedral distortion differ from experiment. It also adversely affected the accuracy of the simulation of the relative importance on thermal expansion of changes in bond lengths and angles for the unit-cell parameters of $CaPtO_3$ and $CaIrO_3$.

The relative importance, in compression, of the changes in bond lengths and angles for the changes in the axes of simulated $CaPtO_3$ and $CaIrO_3$ was consistent with experimental results. The three simulated fluoride post-perovskites showed similar behaviour in this respect to these two oxide analogues.

It is difficult to draw conclusions regarding the accuracy, compared with experiment, of the simulated structures of $MgSiO_3$ and $MgGeO_3$, because of the large scatter of experimental data points which is inherent in the use of the DAC at high-pressure.

The simulation of the anisotropy of atomic displacements at high-temperature in $CaPtO_3$ predicted some but not all of the features measured by experiment. The simulated displacements of Ca and O2 atoms form prolate spheroids rather than the oblate spheroids found in experiment. The simulated atomic displacements of $CaIrO_3$ were very similar to those of simulated $CaPtO_3$, except for those of the O2 atom. The most significant difference in the high-pressure simulation of the atomic displacements of $MgSiO_3$ from those of these two analogues at 0 GPa was that the largest amplitude of vibration of the O1 atom of $MgSiO_3$ was directed along the *b*-axis rather than the *a*-axis.

One striking difference in the changes in experimental crystal structures with increasing temperature between $CaPtO_3$ and $CaIrO_3$ was in the sense of change of atomic coordinate O1 *y* and hence angle Δ_1. O1 *y* decreased with heating in $CaIrO_3$, while it increased in $CaPtO_3$ (Figure 10-9b, Figure 10-10b): this led to movement in the opposite sense of angle Δ_1 (Figure 10-15a). However, caveats apply to the accuracy of $CaIrO_3$ atomic coordinates measured using X-ray diffraction.

The only fundamental difference between $CaPtO_3$ and $CaIrO_3$ which is likely to affect their structure and their thermoelastic behaviour is the electronic configuration of their B atoms Pt ($5d^9\ 6s^1$) and Ir ($5d^7\ 6s^2$), and of their cations Pt^{4+} ($t_{2g}^6 e_g^0$) and Ir^{4+} ($t_{2g}^5\ e_g^0$). The t_{2g}^6 configuration of the Pt^{4+} cation means that each of the d_{xy}, d_{yz} and d_{xz} orbitals is filled by 2 electrons (Figure 4-17). In the t_{2g}^5 configuration of the Ir^{4+} cation, the lower energy d_{xy} orbital is filled by 2 electrons, and the 3 remaining t_{2g} electrons are distributed between the d_{yz} and d_{xz} orbitals. As this is the only difference between

$CaPtO_3$ and $CaIrO_3$ outside their nuclei, it is likely to be responsible for any difference in the direction of change of O1 *y* with heating. The delocalisation of electrons with increasing temperature (Fei *et al.*, 1994) or pressure (Keppler *et al.*, 2007; Loa *et al.*, 2001) may differ between $CaPtO_3$ and $CaIrO_3$, because of their different electronic configurations. These different electronic configurations may lead to differences in the rates at which their bonds become more ionic or more covalent with increasing temperature or pressure. Differences in bonding between $CaPtO_3$ and $CaIrO_3$ might also be caused by differences in the effects of pressure on the spatial orientation of occupied *d*-orbitals (Loa *et al.*, 2007). In ABO_3 perovskites where B is a transition element, the B-O π-bonding strength is affected by the energy, spatial extent and filling of the *d*-orbitals of B atoms (Woodward, 1997b).

The bonds whose changing strength may influence the change in O1 *y* are Pt-O1 and Ca-O1. The decrease with heating of angle Δ_1 in $CaPtO_3$ could be caused by a strengthening of Pt-O1 bonds and/or a weakening of Ca-O1 bonds, moving the O1 anion either towards the Pt cations or away from the Ca cations or both. The lower electron density along the *c*-axis in Ir^{4+} as a result of having 3 electrons in the d_{yz} and d_{xz} orbitals (rather than the 4 electrons of Pt^{4+}) could lead to the Ir-O1 bonds weakening faster with increasing temperature than the Ca-O1 bonds, resulting in an increase in angle Δ_1. The relatively larger Ir-O1 instantaneous bond length expansivity (see Section 4.3.2) may also reduce O1-O2 repulsion in $CaIrO_3$ as temperature increases, allowing angle Δ_1 to increase.

Changes in the ionicity/covalency of the bonds due to compression or heating may change the effective charge on anions and on cations, and so change the repulsion between pairs of anions (such as O2e-O2f along the *c*-axis) and between pairs of cations (such as Ir-Ir along the *a*-axis). The position of the O1 anion may be influenced by its repulsion by the nearest O2 anions: the angle Δ_2 decreases with increasing temperature in $CaPtO_3$ (Figure 10-15b), but the distances O2b-O1c and O2a-O1c do not increase significantly (Figure 9-16), implying that the O2 anions maintain their distance from O1.

In simulated post-perovskite $MgHAlO_3$, the *c*-axis is the most compressible (Table 4-1); the presence of the H^+ cation between the O2e and O2f anions (Figure 4-1) may

cause this by reducing O2-O2 repulsion. O2e-O2f repulsion as a driver for *c*-axis expansion is consistent with the observed change in compressibility of the O2e-O2f distance between compression and expansion (Figure 9-21). An increase in the ionicity of B-O bonds caused by an increase in temperature would increase the charge on the O anions and the repulsion between them. This could result in a decrease in angle Δ_1 and the faster expansion of the *c*-axis than the *a*-axis seen in $CaPtO_3$ and in $CaIrO_3$ (Figure 9-20). The fact that this increase in c-axis expansion on heating is not observed in the $MgSiO_3$ experiment (Figure 9-19a) may be because the heating took place at high-pressure, where the ionicity of the Si-O bonds did not increase as much as that of the Ir-O and Pt-O bonds at ambient pressure. Alternatively there may be less electron transfer in $MgSiO_3$ than in $CaPtO_3$ or $CaIrO_3$.

Differences between the ways in which Si ($3s^2$ $3p^2$) and the *d*-orbital transition elements Pt and Ir bond with O ($2s^2$ $2p^6$) are also likely to contribute to differences between the axial anisotropy of $MgSiO_3$ and that of $CaPtO_3$ and $CaIrO_3$. Again, these differences are likely to change with compression or heating.

It would be interesting to know how post-perovskite $NaZnF_3$ and $NaCoF_3$ differ in their axial anisotropies; the electronic configuration of Co ($3d^7$ $4s^2$) is likely to give a cationic electronic configuration Co^{2+} ($t_{2g}^5 e_g^2$)(high-spin), compared with Zn ($3d^{10}$ $4s^2$) and Zn^{2+} ($t_{2g}^6 e_g^4$). The incomplete Co^{2+} electronic configuration may lead (by analogy with $CaIrO_3$) to greater anisotropy on compression in $NaCoF_3$ and higher B-F1/B-F2 distortion than found in $NaZnF_3$. The higher compressibility of fluoride post-perovskites compared with oxides means that a V/V_0 of 0.75 should be attainable for $NaZnF_3$ (as an example of fluoride post-perovskites) at 40 GPa using a DAC in an X-ray synchrotron, or 0.89 using a Paris-Edinburgh cell at 10 GPa at ISIS. A wider range of V/V_0 should give a better range of axial and structural data. It will also be useful to model the stabilization pressure of post-perovskite $NaCoF_3$ for comparison with data reported in Dobson *et al.* (2011): this will provide additional data for Figure 5-4.

11 Conclusions and further work

In this Chapter I summarise the conclusions from previous Chapters. References to Figures, Tables and previous work are given in those Chapters.

11.1 Simulation of post-perovskites

My simulations showed that the ABO_3 oxide post-perovskites are much less compressible than the fluoride post-perovskites. Oxide post-perovskites with main group rather than transition group B atoms are the least compressible. A less compressible AX_8 hendecahedron is associated with greater BX_6 octahedral distortion. A smaller X-B electronegativity difference is associated with stronger, more covalent octahedral bonding. The structural behaviours of $MgGeO_3$ and $NaMgF_3$ are the most similar of the post-perovskite analogues to that of $MgSiO_3$. However, at ambient conditions, post-perovskite $MgGeO_3$ is not stable, and post-perovskite $NaMgF_3$ is metastable.

Post-perovskite $CaIrO_3$ is more anisotropic than $CaPtO_3$, and both are more anisotropic than $MgSiO_3$ or $MgGeO_3$. Fluoride post-perovskites are more anisotropic at the same V/V_0 than $MgSiO_3$ or $MgGeO_3$ but less anisotropic than $CaIrO_3$ or $CaPtO_3$. The athermal simulations suggest that fluoride post-perovskites which are stable at ambient pressure and temperature such as $NaNiF_3$ and $NaCoF_3$ may provide better analogues for $MgSiO_3$ post-perovskite than oxides which are stable at ambient conditions such as $CaIrO_3$ and $CaPtO_3$.

11.2 The perovskite to post-perovskite phase transition

I developed an empirical approach to predict whether an oxide post-perovskite phase is likely to occur, and the stabilisation pressure required for it to do so. A low stabilisation pressure is necessary for synthesis of larger volumes of post-perovskites. This approach is based on a simple combination of ionic radii and electronegativities, constrained by the octahedral tilt angle and tolerance factor in the perovskite phase, using experimental data.

Only seven currently unreported $A^{2+}B^{4+}O_3$ compounds identified using this empirical approach as candidates for this phase transition fall within the required ranges of

tolerance factor and octahedral tilt angle. It therefore seems likely that few new $A^{2+}B^{4+}O_3$ post-perovskites remain to be discovered. New $A^{3+}B^{3+}O_3$ post-perovskites may be more numerous, but none of the candidate compounds are predicted to transform within the pressure range accessible with a large-volume multi-anvil press. The application of this empirical approach to $A^{+}B^{5+}O_3$ post-perovskites following the recent report of $NaIrO_3$ post-perovskite indicates that it may be possible to synthesise other new $A^{+}B^{5+}O_3$ post-perovskites at pressures accessible in a multi-anvil press.

More data are required to define any similar relationship between stabilisation pressure, ionic radii and electronegativities for fluoride post-perovskites. If a linear relationship between these parameters does exist for the fluorides, the equation of the line must be different from that for the oxides.

The limited simulation data available indicates that it is possible that once the minimum octahedral angular distortion is reached in candidate perovskites, a further increase in pressure will result in transformation to the post-perovskite structure (provided that the *t*-factor $t = \frac{1}{\sqrt{2}}\left(\frac{r_A + r_O}{r_B + r_O}\right)$ and octahedral tilt angle are favourable) because the post-perovskite structure has a lower energy than an increasingly distorted perovskite structure.

11.3 Synthesis and analysis of post-perovskites

In the present work I decided to synthesise single crystals of post-perovskite $CaIrO_3$ and polycrystalline post-perovskite $CaPtO_3$, as discussed in Section 6.1. My analysis of $CaIrO_3$ single crystals using X-ray diffraction and by examining the geometry of single crystals in a scanning electron microscope confirmed that the *a*-axis is parallel to the longest axis of the crystal, as previously reported.

Post-perovskite $CaPtO_3$ was found to be metastable in air for periods of less than 2 hours at 850 °C, but dissociation occurred at lower temperatures when heated for a longer time in a sealed evacuated container. The comparison of the transition temperatures between Pt oxides with those between Ir oxides showed that the Pt oxides dissociated in air at temperatures 300–500 °C lower than their Ir counterparts, consistent with the Pt-PtO buffer system being more oxidising than the Ir-IrO system.

The empirical approach described in Section 11.2 indicated that it might be feasible to synthesise further post-perovskite fluorides in a multi-anvil press, in addition to those already reported ($NaMgF_3$ and $NaZnF_3$). I synthesised post-perovskite $NaNiF_3$, and my supervisor Professor D.P. Dobson synthesised post-perovskite $NaCoF_3$.

11.4 Thermoelastic properties of $CaPtO_3$ at high-*P* and high-*T*

High-pressure (to 40 GPa) X-ray synchrotron powder diffraction at ESRF showed that the bulk and axial equations of state for compression of post-perovskite $CaPtO_3$ are similar to those of $CaIrO_3$. Post-perovskite $CaPtO_3$ has a slightly larger unit-cell volume and lower value of K_0 than post-perovskite $CaIrO_3$. The compression of $CaPtO_3$ is strongly anisotropic (although less so than $CaIrO_3$), being greatest for the *b*-axis (the direction perpendicular to the sheets of PtO_6 octahedra and Ca-ion interlayers) and smallest for the *c*-axis (along the chains of apex-linked PtO_6 octahedra).

High-pressure (to 9.7 GPa) neutron powder diffraction at ISIS at ambient temperature produced bulk and axial equations of state for compression of post-perovskite $CaPtO_3$ which were consistent with (but less precise than) those obtained from the (higher-pressure) synchrotron X-ray powder diffraction. The ISIS experiment also measured atomic positions and hence crystal structure changes with increasing pressure.

The low incompressibility of the *b*-axis relative to that of the *c*-axis in both $CaPtO_3$ and $CaIrO_3$ is similar in magnitude to that reported for $MgSiO_3$, at pressures and temperatures comparable to those expected in the D'' region of the Earth's mantle. However, much worse agreement is found with the axial incompressibility ratios for $Mg_{0.6}Fe_{0.4}SiO_3$ at 140 GPa and ambient temperature. The larger axial anisotropy in $CaIrO_3$ compared with $CaPtO_3$ may be due to distortion of the IrO_6 octahedra in $CaIrO_3$, caused by the Jahn-Teller effect; the absence of this effect in $CaPtO_3$ may indicate that it is therefore a somewhat better low pressure analogue for post-perovskite $MgSiO_3$.

Low (to 2 K) and high-temperature (to 973 K) neutron powder diffraction at ambient pressure produced bulk and axial thermal expansion coefficients for post-perovskite $CaPtO_3$, as well as changes in atomic positions and crystal structure with increasing

temperature. The Debye temperatures obtained by fitting the three axes and the volume were quite similar, with the sequence for the three axes being $\theta_{Db} < \theta_{Dc} \approx \theta_{Da}$ (compare with $\kappa_b < \kappa_a < \kappa_c$: in fact $\kappa_a \approx \kappa_c$). The value of the thermodynamic Grüneisen parameter γ was calculated as 1.16(1) at 291 K, which is very similar to that calculated for post-perovskite $MgSiO_3$.

The probability ellipsoid of the O1 (apical) oxygen ion in post-perovskite $CaPtO_3$ at 869 K was a prolate spheroid, with the largest component of vibration along [100], which corresponds to a buckling of the rods of PtO_6 octahedra about the shared edge "hinges".

For post-perovskite $MgSiO_3$ the axial compression sequence $\kappa_c > \kappa_a > \kappa_b$ is the reverse of the expansion sequence $\alpha_b > \alpha_a > \alpha_c$. For post-perovskite $CaPtO_3$ the behaviour in compression was quite similar to that of post-perovskite $MgSiO_3$. However, $CaPtO_3$ showed a different thermal expansion sequence from $MgSiO_3$, with $\alpha_c > \alpha_b > \alpha_a$. $CaIrO_3$ has the same axial compression sequence as both $MgSiO_3$ and $CaPtO_3$, but on expansion the sequence $\alpha_b > \alpha_c > \alpha_a$ is observed. This is different from both $MgSiO_3$ and from $CaPtO_3$. The changes in anisotropy of the *b* and *c*-axes between compression and expansion in both $CaPtO_3$ and $CaIrO_3$ could be due to changing magnitudes of repulsion between O anions.

The axial behaviour of $MgSiO_3$ in expansion at high-pressure may be dominated by the effect of its high-pressure regime. If this is so it will not be directly comparable to the change in $CaPtO_3$ and $CaIrO_3$ from compression to expansion at 0 GPa.

11.5 Changes in the crystal structure of post-perovskite $CaIrO_3$ and $CaPtO_3$

All Ca-O and Pt-O bond lengths are observed to decrease on compression. However, the shortening on heating of Pt-O2 bond lengths in the average structure of $CaPtO_3$ was not as significant as that reported for Ir-O2 bonds in $CaIrO_3$. The percentage volume occupied by the PtO_6 octahedra and by the void space fell with increasing V/V_0, while the proportion occupied by CaO_8 hendecahedra rose.

For the *a* and *c* axes the dominant compression mechanism was by shortening of the Pt-O bond. On heating, however, most of the increase in length resulted from changes in angles between Pt-O bonds rather than from expansion of Pt-O bonds. Under pressure, shortening of the *b*-axis resulted largely from shortening of the Ca-O bonds, especially the Ca-O2 bonds. On heating, the expansion of the *b*-axis arose from expansion of the Ca-O bonds, but the changes in the angles *p* and Δ_1 both provided a major contribution, acting in the opposite sense to the change in Ca-O bond lengths

On compression, the $CaIrO_3$ structure appears to respond in a quite similar way to that of $CaPtO_3$. On heating, the behaviour shown by $CaIrO_3$ appears to be completely different from that of $CaPtO_3$ with, for example, a contraction of the Ir-O2 bond producing a shortening of the *a*-axis which is then overcome by an increase in the angle *p*. Unlike $CaPtO_3$, the O1 atom moves towards the Ca atom, increasing angle Δ_1. However, because of the dominance of the scattering from the Ir atoms, the oxygen coordinates in the high-temperature structures of $CaIrO_3$ are very difficult to determine accurately by X-ray powder diffraction and so these results from previous work should be treated with caution. The MD simulations of $CaIrO_3$ and $CaPtO_3$ in the present work showed that if in $CaIrO_3$ there is a weakening in Ir-O bonds with heating relative to Ca-O bonds, it may be more marked than for Pt-O bonds in $CaPtO_3$. In computer simulations of $MgSiO_3$, the structure distorts under pressure mainly by shortening of the Si-O and Mg-O bond distances in a similar manner to that shown by $CaPtO_3$ and $CaIrO_3$. On heating at high-pressure, however, it seems that $MgSiO_3$ behaves differently from the two analogue compounds, with changes in bond length rather than angle dominating the expansion mechanism.

11.6 Comparison of results from simulation with those from experiment

The majority of the differences found between simulated and experimental EOS parameters for the post-perovskites in compression were consistent with the expected effect of using the GGA approximation. Differences between simulated and experimental values of K_0 and K'_0 may have been due to simulation of a wider pressure range than that used in experiments.

The simulated axial compression and expansion sequences corresponded with those from experiment for the three post-perovskites whose expansion was simulated in the present work ($MgSiO_3$, $CaPtO_3$ and $CaIrO_3$). However, the axial ratios simulated for $CaPtO_3$ and $CaIrO_3$ in expansion were slightly different from experiment. Inaccurate simulation of the expansion of the *c*-axis may be related both to the reduced Brillouin-zone sampling density used in MD (and in gamma point) simulation, and to the use of a 60 atom supercell, which is required to achieve feasible MD simulation run times.

The sense of changes of the simulated atomic coordinates of $CaPtO_3$ and $CaIrO_3$ with changing pressure and temperature corresponded with experiment in compression and in expansion, except for the O2 *z* coordinates. This inaccuracy in simulated O2 *z* coordinates made the sense of changes of simulated angles Δ_2 and *p* and the octahedral distortion differ from experiment. It also adversely affected the accuracy of the simulation of the relative importance for thermal expansion of changes in bond lengths and angles for the unit-cell parameters of $CaPtO_3$ and $CaIrO_3$. The simulated atomic coordinates of $MgSiO_3$ and $MgGeO_3$ could not be compared with experiment because of the degree of scattering and errors in experimental results obtained using DACs.

The relative importance in compression of the changes in bond lengths and angles for the changes in the axes of simulated $CaPtO_3$ and $CaIrO_3$ was consistent with experimental results. The three simulated fluoride post-perovskites showed similar behaviour in this respect to these two oxide analogues.

One striking difference with increasing temperature between the experimentally determined crystal structures of $CaPtO_3$ and $CaIrO_3$ was in the sense of change of atomic coordinate O1 *y* and hence angle Δ_1. O1 *y* decreased with heating in $CaIrO_3$, while it increased in $CaPtO_3$: this led to movement in the opposite sense of angle Δ_1.

However, caveats apply to the accuracy of $CaIrO_3$ atomic coordinates from previous work measured using X-ray diffraction.

The only fundamental difference between $CaPtO_3$ and $CaIrO_3$ which is likely to affect their structure and their thermoelastic behaviour is the electronic configuration of their B atoms Pt ($5d^9\ 6s^1$) and Ir ($5d^7\ 6s^2$), and of their cations Pt^{4+} ($t_{2g}^6 e_g^0$) and Ir^{4+} ($t_{2g}^5\ e_g^0$). As this is the only difference between $CaPtO_3$ and $CaIrO_3$ outside their nuclei, it is likely to be responsible for the difference in the direction of change of O1 *y* with heating. The delocalisation of electrons with increasing temperature or pressure may differ between $CaPtO_3$ and $CaIrO_3$, because of their different electronic configurations, as may the rates at which bonds become more ionic or covalent with increasing temperature or pressure. The changing strength of bonds may influence the decrease with heating of angle Δ_1 in $CaPtO_3$ and the increase in angle Δ_1 in $CaIrO_3$. Changes in the ionicity/covalency of the bonds due to compression or heating may change the effective charge on anions and on cations, and so change the repulsion between pairs of anions (such as O2e-O2f along the *c*-axis) and between pairs of cations (such as Ir-Ir along the *a*-axis).

In the simulation in the present work of the hypothetical post-perovskite $MgHAlO_3$, the *c*-axis was the most compressible; the presence of the H^+ cation between the O2e and O2f anions may have caused this by reducing O2-O2 repulsion. O2e-O2f repulsion as a driver for *c*-axis expansion is consistent with the observed change in compressibility of the O2e-O2f distance between compression and expansion. An increase in the ionicity of B-O bonds caused by an increase in temperature would increase the charge on the O anions and the repulsion between them. This could result in a decrease in angle Δ_1, and the faster expansion of the *c*-axis relative to the *a*-axis seen in $CaPtO_3$ and in $CaIrO_3$. The fact that this increase in c-axis expansion on heating is not observed experimentally in $MgSiO_3$ may be because the heating took place at high-pressure, where the ionicity of the Si-O bonds did not increase as much as that of the Ir-O and Pt-O bonds at ambient pressure. Alternatively there may be less electron transfer in $MgSiO_3$ than in $CaPtO_3$ or $CaIrO_3$.

Differences between the ways in which Si ($3s^2\ 3p^2$) and the *d*-orbital transition elements Pt and Ir bond with O ($2s^2\ 2p^6$) are also likely to contribute to differences

between the axial anisotropy of $MgSiO_3$ and that of $CaPtO_3$ and $CaIrO_3$. Again, these differences are likely to change with compression or heating.

The simulated EOSs and unit-cell values for fluoride post-perovskites show reasonable agreement with experimental data where these are available (bulk EOS for $NaMgF_3$ and $NaZnF_3$; axial EOS for $NaZnF_3$; unit-cell data for $NaZnF_3$ and $NaNiF_3$). There have been no reports of experimental measurements of the changes in atomic coordinates with changing pressure (or temperature) of any fluoride post-perovskite for comparison with simulated values.

11.7 Summary of conclusions

1. $CaPtO_3$ and $CaIrO_3$ post-perovskites have the same axial compression sequence ($\kappa_c > \kappa_a > \kappa_b$) as $MgSiO_3$ post-perovskite, but each of the three post-perovskites has a different axial expansion sequence: $CaPtO_3$ and $CaIrO_3$ are much better analogues for $MgSiO_3$ in compression than when heated. The change in volume of $MgSiO_3$ post-perovskite due to the change in temperature across the D'' layer is likely to be similar to that due to the change in pressure. This means that the differences in the axial expansion behaviours of $CaPtO_3$ and $CaIrO_3$ at 0 GPa from that of $MgSiO_3$ at high-pressure may be significant, and so the case for the use of $CaPtO_3$ and $CaIrO_3$ as low-pressure analogues of $MgSiO_3$ at elevated temperatures is substantially weakened.
2. Athermal simulations suggest that fluoride post-perovskites which are stable at ambient pressure and temperature - and which can be synthesised within the pressure range accessible with a large-volume multi-anvil press - such as $NaNiF_3$ may provide better analogues for $MgSiO_3$ post-perovskite than $CaIrO_3$ or $CaPtO_3$.
3. Changes in the axial behavior of a post-perovskite between compression and expansion may be due to changes in bond covalency on compression or on heating, changing the effective charge on and repulsion between pairs of anions.
4. It seems likely that few new $A^{2+}B^{4+}O_3$ post-perovskites remain to be discovered. New $A^{3+}B^{3+}O_3$ post-perovskites may be more numerous, but none of the candidate compounds are predicted to transform within the pressure range accessible with a large-volume multi-anvil press. It may however be possible to synthesise new $A^{+}B^{5+}O_3$ post-perovskites at pressures accessible in a multi-anvil press.
5. It is possible that once the octahedral angular distortion in a space group 62 perovskite has decreased to a minimum with increasing pressure, a further increase in pressure will result in transformation to the post-perovskite structure, provided that the *t*-factor and octahedral tilt angle are favourable.

11.8 Further work

There are three main areas for further experiments and simulation:

1. Identification and examination of additional post-perovskite analogues
2. Investigation of factors influencing the perovskite to post-perovskite transition
3. Further investigation of $CaPtO_3$.

11.8.1 Identification and examination of additional post-perovskite analogues

Thermoelastic and structural properties of fluoride post-perovskites

My computer simulation studies reported in Chapter 4 included three fluorides. These were $NaMgF_3$ and $NaZnF_3$ - both of which had been reported as occurring as post-perovskites (Liu *et al*., 2005; Yakovlev *et al*., 2009) - and $NaNiF_3$. Both $NaNiF_3$ and $NaCoF_3$ have since been shown also to occur in a post-perovskite phase (Section 6.8.3; Dobson *et al*., 2011). Low-pressure ABF_3 fluoride post-perovskites have several advantages over other low-pressure post-perovskite analogues. Their atomic mass ratios are more similar to that of $MgSiO_3$, since they have B atoms from the first transition element period (e.g. Ni) rather than the second (e.g. Rh) or third (e.g. Ir). It is therefore easier to measure atomic coordinates using X-ray diffraction. Their octahedral distortion is also more similar to that of $MgSiO_3$ (see Figure 4-13) than that of $CaPtO_3$ or $CaIrO_3$.

The perovskite and post-perovskite phases of $NaCoF_3$ could be simulated using *ab initio* methods in order to predict the pressure of its transition between these phases. Its thermoelastic properties could also be investigated in this way to predict its behaviour at high-pressure and high-temperature, and these results compared with results from simulation of $NaNiF_3$ and $NaZnF_3$ in order to assess the role of the B element in the thermoelastic behaviour of ABF_3 post-perovskite fluorides. The results would be useful for prioritising experimental examination of these analogues. The thermoelastic properties of suitable fluoride post-perovskites could then be determined experimentally in order to establish the suitability of these compounds as low-pressure analogues for post-perovskite $MgSiO_3$. An NERC grant application is in preparation to further this work.

Thermoelastic and structural properties of post-perovskites which have B cations with 4d valence electrons

The 4d valence electron orbital post-perovskites $CaRhO_3$ (Shirako *et al.,* 2009; Yamaura *et al*., 2009; Matar *et* al., 2010; Wang *et al.*, 2011) and $CaRuO_3$ (Kojitani *et al.,* 2007; Zhong *et al*., 2010; Shirako *et al*., 2011) have been synthesised and their structures examined at ambient conditions, but no high-pressure or high-temperature studies of their thermoelastic properties have been reported. It would be interesting to analyse their thermoelastic properties using *ab initio* simulation, and also to simulate their perovskite to post-perovskite transitions. This would help to establish how the difference between 5d and 4d valence electron orbitals may be expected to influence post-perovskite properties and the transition between perovskite and post-perovskite phases.

Identification and investigation of post-perovskites with pentavalent B cations

The perovskite to post-perovskite transitions of $NaIrO_3$, $NaPtO_3$, $NaRhO_3$ and other potential $A^{+}B^{5+}O_3$ compounds could be simulated using *ab initio* methods, including determination of the perovskite octahedral tilt angle Φ. This could include mixed-valence solid solutions such as $(Na,Ca)IrO_3$. This may help to identify constraints on post-perovskite formation related to *t*-factors and octahedral tilt angles. The thermoelastic properties of suitable candidates could then be simulated to predict their behaviour at high-pressure and high-temperature. As for the fluorides, these results would be useful for prioritising the synthesis (in addition to the recently reported $NaIrO_3$: Bremholm *et al*., 2011) and experimental examination of such analogues, in order to establish their suitability as low-pressure analogues for post-perovskite $MgSiO_3$.

11.8.2 Factors influencing the transition from perovskite to post-perovskite

Octahedral tilts and the transition to the post-perovskite phase

My supervisor Dr. I.G. Wood has proposed an experiment at ISIS to determine compression mechanisms in $BaCeO_3$ and $SrPbO_3$ perovskites at high-pressure, in order to understand their perovskite to post-perovskite transitions. A high-pressure neutron diffraction study of $SrCeO_3$ perovskite has shown that its dominant compression mechanism is by bond shortening instead of by the expected tilting of the CeO_6 octahedra. The empirical approach described in Chapter 5 of the present work suggests that $BaCeO_3$ and $SrPbO_3$ perovskites should change to the post-perovskite structure at very low pressure; however, their octahedral tilt angles may be too small. If, like $SrCeO_3$, their dominant compression mechanism is by bond shortening, then this may preclude their transition to the post-perovskite structure at higher pressures. This experiment will examine the evolution of their crystal structure at high-pressure.
A preliminary *ab initio* simulation of $BaCeO_3$ perovskite (Ammann, 2011) predicts that the relative change in its unit-cell volume to 10 GPa is almost entirely accounted for by bond shortening rather than by a changing octahedral tilt angle (Figure 11-1).

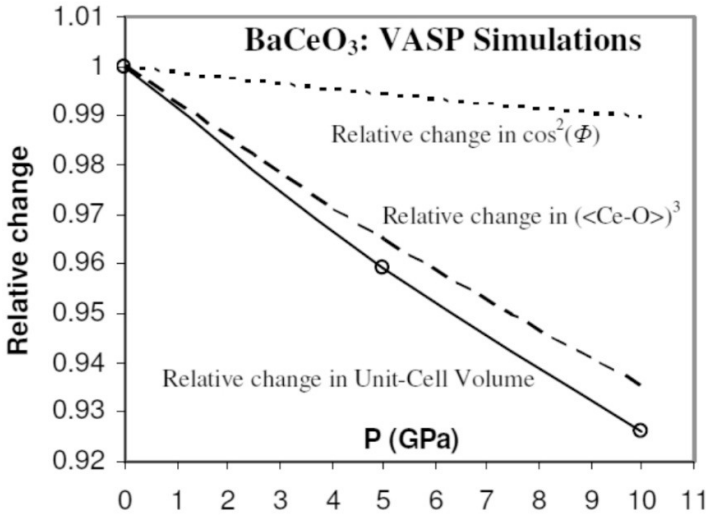

Figure 11-1: Relative change in the cube of the mean Ce-O bond length and in the square of the cosine of the octahedral tilt angle Φ (see Equation 5.4) compared with the relative change in the unit-cell volume of $BaCeO_3$ perovskite in compression. Assuming regular octahedra, the unit-cell volume is $V = 32\ (<\text{Ce-O}>)^3 \cos^2 \Phi$; more than 86% of the change in volume is from bond shortening. Open circles are simulated cell volumes. The solid line shows the volume calculated using this equation. Dashed and dotted lines show the relative changes in $(<\text{Ce-O}>)^3$ and $\cos^2 \Phi$ (Ammann, 2011)

It would be useful to investigate further structural change with increasing pressure in $BaCeO_3$ and $SrPbO_3$ perovskites using athermal *ab initio* simulation, both for comparison with experiment and to establish whether minima in octahedral angular distortion may be used to predict transition pressures from these perovskite to post-perovskite phases. A relatively invariant octahedral angular distortion in $BaCeO_3$ and $SrPbO_3$ perovskites, as shown in the present work for simulated $CaSiO_3$ perovskite (Section 5.12), would imply that this phase transition will not take place.

Section 5.9 describes the ABO_3 compounds which I consider most likely to transform to post-perovskites (Table 5-4). $SrPrO_3$ perovskite (Hinatsu *et al*., 1997) is the compound predicted to transform at the lowest pressure. *Ab initio* simulation could be used to investigate the dominant compression mechanism of $SrPrO_3$ perovskite, as described above for $SrCeO_3$. Pr is adjacent to Ce in the Periodic Table, although Pr^{4+} has a smaller radius than Ce^{4+}. If the compression of $SrPrO_3$ perovskite is predominantly by bond shortening instead of by tilting of the octahedra, a successful synthesis of its post-perovskite phase may be less likely.

Octahedral angular distortion and the transition to the post-perovskite phase

The work proposed in the previous section could be extended to investigate the relationship between octahedral angular distortion in perovskites and the transition pressures from perovskite to post-perovskite phases (see Section 5.12). This could be done by using athermal *ab initio* simulation of further perovskites whose transition pressure is known experimentally, such as $CaSnO_3$, $CaRhO_3$ and $MnGeO_3$, so as to determine whether this approach is validated by the additional data. Other perovskites such as $CaReO_3$ and $SrIrO_3$ which are known not to form post-perovskites below experimentally determined pressures (see caption to Table 5-2) could also be simulated to see whether they display similar behaviour to $CaSiO_3$ in their octahedral angular distortion (see Figure 5-5a). Transition pressures from perovskite to post-perovskite could also be simulated (see Section 4.4.3). This approach could be employed for the perovskites which have been identified as candidates for transition to post-perovskites (see Table 5-4 and Table 5-6).

11.8.3 Further investigation of $CaPtO_3$

Simulation of $CaPtO_3$ perovskite

Inaguma *et al.* (2008) stated their intention to synthesize the perovskite phase of $CaPtO_3$, but the result has not been reported. A previous athermal *ab initio* simulation of the perovskite and post-perovskite phases of $CaPtO_3$ (Matar *et al.*, 2008) has been the subject of caveats (see Section 8.4.1). It would be useful to repeat and extend this simulation in order to model the perovskite to post-perovskite transition in this compound, and so indicate whether it may be possible to synthesise the perovskite phase.

Experimental determination of the bulk and axial thermal equations of state for $CaPtO_3$ at simultaneous high-P and T

Liu *et al.* (2011) determined the temperature derivative of the bulk incompressibility $\partial K/\partial T$ of post-perovskite $CaIrO_3$ using X-ray powder diffraction but did not report results for the unit-cell axes. An attempt to make similar measurements for $CaPtO_3$ by neutron powder diffraction during the present study was not successful (Section 9.5). However, these volumetric and axial equations of state could readily be determined for post-perovskite $CaPtO_3$ using synchrotron X-ray powder diffraction. This would help to assess its suitability as an analogue for post-perovskite $MgSiO_3$ at high-temperature; it is possible that the post-perovskite $CaPtO_3$ axial expansion sequence $\alpha_c > \alpha_b > \alpha_a$ may be modified at high-pressure due to changes with increasing pressure in the relative magnitudes of the axial expansibilities α_i as expressed in

$$\left(\frac{\partial \alpha_i}{\partial P}\right)_V = \frac{1}{K_{Ti}^2}\left(\frac{\partial K_{Ti}}{\partial T}\right)_P \qquad (11.1)$$

This experiment would also enable comparison with $CaIrO_3$, and might develop a better understanding of the role of the B element when ABO_3 post-perovskites are heated which can also be applied to ABF_3 post-perovskites.

12 References

Akber-Knutson, S., Steinle-Neumann, G. and Asimow, P.D. (2005) Effect of Al on the sharpness of the $MgSiO_3$ perovskite to post-perovskite phase transition. *Geophysical Research Letters*, **32**, L14303

Alfè, D. and Gillan, M. (2007) *Ab initio* statistical mechanics of surface adsorption and desorption. I. H_2O on MgO (001) at low coverage. *Journal of Chemical Physics*, **127**, 114709

Allen, L.C. (1989) Electronegativity is the average one-electron energy of the valence-shell electrons in ground-state free atoms. *Journal of the American Chemical Society*, **111**, 9003-9014

Allred, A.L. (1961) Electronegativity values from thermochemical data. *Journal of Inorganic and Nuclear Chemistry*, **17**, 215-221

Allred, A.L. and Rochow, E.G. (1958) A scale of electronegativity based on electrostatic force. *Journal of Inorganic and Nuclear Chemistry*, **5**, 264-268

Ammann, M.W., Brodholt, J.P., Wookey, J. and Dobson, D.P. (2010) First-principles constraints on diffusion in lower-mantle minerals and a weak D" layer. *Nature*, **465**, doi:10.1038/nature09052

Ammann, M.W. (2011) Personal communication

Andersen, H.C. (1980) Molecular dynamics simulations at constant pressure and/or temperature. *Journal of Chemical Physics,* **72**(4), 2384

Angel, R.J., Zhao, J. and Ross, N.L. (2005) General rules for predicting phase transitions in perovskites due to octahedral tilting. *Physical Review Letters*, **95**, 025503

Angel, R.J., Bujak, M., Zhao, J., Diego Gatta, G. and Jacobsen, S.D. (2007) Effective hydrostatic limits of pressure media for high-pressure crystallographic studies. *J. Appl. Cryst.,* **40**, 26-32

Angel, R. J. (2000) Equations of State. In: R. M. Hazen and R. T. Downs (Editors), *Reviews in Mineralogy and Geochemistry*, **41**, Mineral. Soc. Am. Washington, USA

Angel, R. J. (2001) EOS-FIT V5.2. Computer program. Crystallography Laboratory, Department of Geological Sciences, Virginia Tech, Blacksburg, Virginia, USA

Ardit, M., Cruciani, G., Dondi, M., Merlini, M. and Bouvier, P. (2010) Elastic properties of perovskite $YCrO_3$ up to 60 GPa. *Physical Review B*, **82**, 064109

Avdeev, M., Caspi, E.N. and Yakovlev, S. (2007) On the polyhedral volume ratios V_A/V_B in perovskites ABX_3. *Acta Cryst. B*, **63**, 363-372

Babel, D., Rüdorff, W. and Tschöpp, R. (1966) Erdalkaliiridium(IV)-oxide: Struktur von Dicalcium-iridium(IV)-oxid, Ca_2IrO_4. *Zeitschrift fur anorganische und allgemeine Chemie*, **347**, 282-288

Bergner, D. and Kohlhaas, R. (1973) Neue Verbindugen vom $Na_xPt_3O_4$-Strukturtyp. Z. *Anorg. Allg. Chem.* **401**, 15-20

Birch, F. (1978) Finite strain isotherm and velocities for single crystal NaCl at high pressures and 300 degrees K. *J. Geophys. Res.*, **83**, 1257–1268

Blöchl, P.E. (1994) Projector augmented-wave method. *Phys.Rev.B*, **50**, 17953–17979

Boffa Ballaran, T., Trønnes, R.G. and Frost, D.J. (2007) Equations of state of $CaIrO_3$ perovskite and post-perovskite phases. *Am. Mineral.*, **92**, 1760-1763

Bremholm, M., Dutton, S.E., Stephens, P.W. and Cava, R.J. (2011) $NaIrO_3$ – a pentavalent post-perovskite. *Journal of Solid State Chemistry*, **184**, 601-607

Brodholt, J.P. and Refson, K. (2000) An ab initio study of hydrogen in forsterite and a possible mechanism for hydrolytic weakening. *Journal of Geophysical Research,* **108**, B8, 18977-18982

Burdett, J.K., Price, G.D.P. and Price, S.L. (1981) Factors influencing solid-state structure – an analysis using pseudopotential radii structural maps. *Physical Review B*, **24**, **6**, 2903-2912

Bushmeleva, S.N., Pomjakushin, V.Yu., Pomjakushina, E.V., Sheptyakov, D.V. and Balagurov, A.M. (2006) Evidence for the band ferromagnetism in $SrRuO_3$ from neutron diffraction. *Journal of Magnetism and Magnetic Materials*, **305**, 491-496

Caglioti, G., Paoletti, A. and Ricci, F.P. (1958) Choice of collimators for a crystal spectrometer for neutron diffraction. *Nucl. Instrum. Methods*, **3**, 223-228

Cahen, D., Ibers, J.A. and Mueller, M.H. (1974) Platinum bronzes II Crystal structure of $CaPt_2O_4$ and $Cd_{0.3}Pt_3O_4$. *Inorganic Chemistry*, **13**, 1, 110-115

Cai,Y., Wei, Y., Ming, X., Du, F., Meng, X., Wang, C. and Chen, G. (2011) Prediction of the phase transition from ferromagnetic perovskite to non-magnetic post-perovskite in $SrRuO_3$: a first-principles study. *Solid State Communications*, **151**, 798-801

de la Calle, C., Alonso, J.A., Garcia-Hernández, M., and Pomjakushin, V. (2006) Neutron diffraction study and magnetotransport properties of stoichiometric $CaMoO_3$ perovskite prepared by a soft-chemistry route. *Journal of Solid State Chemistry*, **179**, 1636-1641

Caracas, R. and Cohen, R.E. (2008) Ferrous iron in post-perovskite from first-principles calculations. *Physics of the Earth and Planetary Interiors*, **168**, 147-152

Carpenter, M.A., Becerro, A.I. and Seifert, F. (2001) Strain analysis of phase transitions in $(Ca,Sr)TiO_3$ perovskites. *American Mineralogist*, **86**, 348-363

Carpenter, M.A., Howard, C.J., Knight, K.S. and Zhang, Z. (2006) Structural relationships and a phase diagram for $(Ca,Sr)TiO_3$ perovskites. *J. Phys.: Condens. Matter*, **18**, 10725-10749

Carpenter, M.A. and Howard, C.J. (2009) Symmetery rules and strain/order parameter relationships for coupling between octahedral tilting and cooperative Jahn-Teller transitions in ABX_3 perovskites. I. Theory. *Acta Crystallographica*, **B65**, 134-146

Catalli, K., Shim, S-H. and Prakapenka, V. (2009) Thickness and Clapeyron slope of the post-perovskite boundary. *Nature*, **462**, 782-785

Ceperley D. M. and Alder B. J. (1980) Ground-state of the electron-gas by a stochastic method. *Phys. Rev. Lett.* **45**, 569-569

Cheng, J.-G., Zhou, J.-S. and Goodenough, J.B. (2010) Stress-induced perovskite to post-perovskite transition in $CaIrO_3$ at room temperature. *Physical Review B* **82**, 132103

Cheng, J.-G., Zhou, J.-S., Goodenough, J.B., Sui, Y., Ren, Y. and Suchomel, M.R. (2011) High-pressure synthesis and physical properties of perovskite and post-perovskite $Ca_{1-x}Sr_xIrO_3$. *Physical Review B*, **83**, 064401

Claridge, J.B., Layland, R.C. and zur Loye, H-C. (1997) Ca4PtO6. *Acta. Cryst.*, **C53**, 1740-1741

Cooper, M.J. (1963) Dispersion corrections for X-ray scattering of atoms for Ag *Kα* and Co *Kα* radiation. *Acta Cryst*. **16**, 1067-1069

Côté, A.S (2008) Personal communication

Demazeau, G., Jung, D.Y., Largeteau, A., Cros, C. and Choy, J.H. (1997) High oxygen pressures and the stabilization of the highest oxidation states of transition elements. *Journal of Alloys and Compounds*, **262-263**, 191-193

Dewaele, A., Loubeyre, P. and Mezouar, M. (2004) Equations of state of six metals above 94 GPa. *Phys. Rev. B* **70**, 094112

Dijksma F.J.J, Vente J.F., Frikee E. and Ijdo D.J.W. (1993) The structure of a calcium-deficient hexagonal calcium iridium oxide compound. *Materials Research Bulletin*, **28(11)**, 1145-1151

Dobson. D.P., Crichton, W.A., Bouvier, P., Vočadlo, L. and Wood, I.G. (2003) The equation of state of CsCl-structured FeSi to 40 GPa: Implications for silicon in the Earth's core. *Geophysical Research Letters*, **30**, 1, 1014, doi:10.1029/2002GL016228

Dobson, D. and Jacobsen, S. (2004) The flux growth of magnesium silicate perovskite single crystals. *American Mineralogist*, **89**, 807-811

Dobson, D.P., Hunt, S.A., Lindsay-Scott, A. and Wood, I.G. (2011) Towards better analogues for $MgSiO_3$ post-perovskite: $NaCoF_3$ and $NaNiF_3$, two new recoverable fluoride post-perovskites. *Phys. Earth Planet. Inter.*, **189**, 171-175

Dudarev, S.L., Botton, G.A., Savrasov, S.Y., Humphreys, C.J and Sutton, A.P. (1998) Electron-energy-loss spectra and structural stability of nickel oxide: An LSDA+U study. *Phys. Rev. B*, **57(3)**, 1505-1509

Dziewonski, A.M. and Anderson, D.L. (1981) Preliminary reference Earth model. *Physics of the Earth and Planetary Interiors*, **25**, 297-356

Ehrenberg, H., Fuess, H., Hesse, S., Zimerman, J., von Seggern, H. and Knapp, M. (2007) Structures of $CsEuBr_3$ and its degradation product $Cs_2EuBr_5.10H_2O$. *Acta Cryst. B*, **63**, 201-204

Epstein, A., Makovsky, J., Melamud, M. and Shaked, H. (1968) Magnetic structure of $NaNiF_3$. *Phys. Rev.*, **174(2)**, 560-561

Fang, C-M., and Ahuja, A. (2006) Structures and stability of ABO_3 orthorhombic perovskites at the Earth's mantle conditions from first-principles theory. *Physics of the Earth and Planetary Interiors*, **157**, 1-7

Fei, Y. (1995) AGU Reference Shelf 2: Mineral Physics and Crystallography – A Handbook of Physical Constants, edited by T.J. Ahrens, pp 29-44. AGU, Washington, USA

Fei, Y., Virgo, D., Myse, B., Wang, Y., Mao, H.K. (1994) Temperature-dependent electron delocalization in $(Mg,Fe)SiO_3$ perovskite. *American Mineralogist*, **79**, 826-837

Feng, L.M., Jiang, L.Q., Zhu, M., Liu, H.B., Zhou, X. and Li, C.H. (2008) Formability of ABO_3 cubic perovskites. *Journal of Physics and Chemistry of Solids*, **69**, 967-974

Fletcher, D.A., McMeeking, R.F., and Parkin, D. (1996) The United Kingdom Chemical Database Service. *Journal of Chemical Information and Computer Sciences*, **36**, 746-749

Fortes, A.D. (2004) Computational and experimental studies of solids in the ammonia-water system. Ph.D Thesis UCL, University of London, UK

Fortes, A.D., Wood, I.G. and Knight, K.S. (2006) Neutron powder diffraction studies of sulphuric acid hydrates. I. The structure of sulphuric acid hemitriskaidekahydrate $D_2SO_4{\cdot}6½D_2O$. *J. Chem. Phys.* **125**, 144510

Fortes, A.D., Wood, I.G., Alfredsson, M., Vočadlo, L., Knight, K.S., Marshall, W.G., Tucker, M.G. and Fernandez-Alonso, F. (2007) The high-pressure phase diagram of ammonia dihydrate. *High Pressure Research*. **27**, 2, 201–212

Fortes, A.D., Wood, I.G., Vočadlo, L., Chapon, L., Knight, K. and Smith, R.I. (2008) Neutron powder diffraction studies of sulphuric acid hydrates. II. The structure, thermal expansion, incompressibility, and polymorphism of sulphuric acid tetrahydrate ($D_2SO_4{\cdot}4D_2O$). *J. Chem. Phys.* **128**, 054506

Fu, W.T. and Ijdo, D.J.W. (1995) A comparative study on the structure of $APbO_3$ (A=Ba,Sr). *Solid State Communications*, **95**, 581-585

Fujino, K., Nishio-Hamane, D., Suzuki, K., Izumi, H., Seto, Y., and Nagai, T. (2009) Stability of the perovskite structure and the possibility of transition to the post-perovskite structure in $CaSiO_3$, $FeSiO_3$, $MnSiO_3$ and $CoSiO_3$. *Physics of the Earth and Planetary Interiors*, **177**, 147-151

Garcia-Jaca, J., Larramendi, J.I.R., Insausti, M., Arriortua M.I., and Rojo, T. (1995) Synthesis, Crystal Structure and Transport Properties of a new non-stoichiometric $CaVO_{3-\delta}$ phase. *Journal of Materials Chemistry*, **5**, 1995-1999

Giacovazzo, C. (1992) The diffraction of X-rays by crystals (p.200). In: *IUCr texts on crystallography (2): Fundamentals of crystallography. Ed: Giacovazzo, C.* International Union of Crystallography, Oxford University Press, Oxford, UK

Giaquinta, D.M. and zur Loye, H-C. (1994) Structural predictions in the ABO_3 phase diagram. *Chemical Materials*, **6**, 365-372

Gillan, M.J., Alfè, D., Brodholt, J., Vočadlo., L. and Price, G.D. (2006) First-principles modeling of Earth and planetary materials at high pressures and temperatures. *Reports on Progress in Physics*, **69**, 2365-2441

Gillet, P., Guyot, F., Price, G.D., Tournerie, B., and Le Cleach A. (1993) Phase changes and thermodynamic properties of $CaTiO_3$. Spectroscopic data, vibrational modelling and some insights on the properties of $MgSiO_3$ perovskite. *Physics and Chemistry of Minerals*, **20**, 159-170

Glazer, A.M. (1972) The classification of tilted octahedra in perovskites. *Acta Cryst. B*, **28**, 3384-3392

Glerup M., Knight K.S., and Willy Poulsen, F. (2005) High temperature structural phase transitions in $SrSnO_3$ perovskite. *Materials Research Bulletin*, **40**, 507-520

Goldschmidt, V.M. (1926). Die Gesetze der Krystallochemie. *Naturwissenschaften*, **14**, 477–485

Goodenough, J.B. (1998) Jahn-Teller phenomena in solids. *Annu. Rev. Mater. Sci.*, **28**, 1-27

Goodenough, J.B. (2004) Electronic and ionic transport properties and other physical aspects of perovskites. *Reports on Progress in Physics*, **67**, 1915-1993

Green, J.C. (2003) Bonding in Molecules II undergraduate lecture course. University of Oxford Department of Chemistry, Oxford, UK

Green, M.A., Prassides, K., Day, P., and Neumann, D.A. (2000) Structure of the n = 2 and n = ∞ member of the Ruddlesden-Popper series, $Sr_{n+1}Sn_nO_{3n+1}$. International *Journal of Inorganic Materials*, **2**, 35-41

Guennou, M., Bouvier, P., Krikler, B., Kreisel, J., Haumont, R. and Garbarino, G. (2010) High-pressure investigation of $CaTiO_3$ up to 60 GPa using x-ray diffraction and Raman spectroscopy. *Physical Review B*, **82**, 134101

Guignot, N., Andrault, D., Morard, G., Bolfan-Casanova, N. and Mezouar, M. (2007) Thermoelastic properties of post-perovskite phase $MgSiO_3$ determined experimentally at core-mantle boundary P-T conditions. *Earth and Planetary Science Letters*, **256**, 162-168

Guinier, A. (1963) X-ray diffraction in crystals, imperfect crystals, and amorphous bodies. W.H. Freeman and Company, San Franciso, U.S.A.

Hafner, J., Kresse. K., Eichler, A., Lorenz, R., Hirschl, R., Marsman, M. (2010) VASP workshops. Faculty of Physics, Universität Wien, Austria http://cms.mpi.univie.ac.at/vasp-workshop/slides/documentation.htm

Hammersley, A.P., Svensson, S.O., Thompson, A., Graafsma, H., Kvick, A. and Moy, J. P. (1995) Calibration and correction of distortion in two dimensional detector systems, *Rev. Sci. Instrum.*, **66**, 2729–2733

Harris, P., Larsen, S. and Lebech, B. (1992) A single crystal neutron diffraction study of $KMnCl_3$, its twinning and magnetic structure. *J. Phys. Chem. Solids*, **53**, 1021-1025

Hazen, R.M. and Finger, L.W. (1979) Polyhedral tilting: a common type of pure displacive phase transition and its relationship to analcite at high pressure. *Phase Transitions*, **1**, 1-22

Hester, J.R., Howard, C.J., Kennedy, B.J., and Macquart, R. (2002) High-temperature structural studies of $SrPbO_3$ and $BaPbO_3$. *Australian Journal of Chemistry*, **55**, 543-545

Hinatsu, Y., Itoh, M. and Edelstein, N. (1997) Structure and magnetic properties of tetravalent praseodymium perovskite $SrPrO_3$. *Journal of Solid State Chemistry*, **132**, 337-341

Hirai, S., Welch, M.D., Aguado, F. and Redfern, S.A.T. (2009) The crystal structure of $CaIrO_3$ post-perovskite revisited. *Zeit. Krist.*, **224**, 345-350

Hirai, S., Sanehira, T., Nishiyama, N., Irifune, T., Klemme, S., Bromiley, G. and Attfield, J.P. (2011) Tuning of structure, morphology and magnetism in postperovskite oxide solid solutions. *Chem. Mater.*, **23**, 114-121

Hirate, H., Sawai, H., Saito, Y., Yukawa, H. and Morinaga, M. (2010) Unusual energy balance between atoms in postperovskite $MgSiO_3$. *J. Am. Ceram. Soc.*, **93**, 3449-3454

Hirose K. and Fujita Y. (2005) Clapeyron slope of the post-perovskite phase transition in $CaIrO_3$. *Geophysical Research Letters*, **32**, L13313, doi:10.1029/2005GL023219

Hirose, K., Kawamura, K., Ohishi, Y., Tateno, S., and Sata, N. (2005) Stability and equation of state of $MgGeO_3$ post-perovskite phase. *American Mineralogist*, **90**, 262–265

Hohenberg P. and Kohn W. (1964) Inhomogeneous electron gas. *Phys. Rev*. **136**, 864-871

Hohnstedt, C. and Meyer, G. (1993) Metallothermische Reduktion des Tribromids und -iodids von Dysprosium mit Alkalimetallen. *Zeitschrift für anorganische und allgemeine Chemie*, **619**, 1374-1378

Holmes, N.C., Moriarty, J.A., Gathers, G.R. and Nellis, W.J. (1989) The equation of state of platinum to 660 GPa (6.6 Mbar). *J. Appl. Phys*. **66**, 2962-2967

Howard, C.J. and Carpenter, M.A. (2010) Octahedral tilting in cation-ordered Jahn-Teller distorted perovskites – a group-theoretical analysis. *Acta Crystallographica*, **B66**, 40-50

Howard, C.J. and Stokes, H.T. (1998) Group-theoretical analysis of octahedral tilting in perovskites. *Acta Cryst. B*, **54**, 782-789

Hunt, S.A., Weidner, D.J., Li, L., Wang, L., Walte, N.P., Brodholt, J.P., and Dobson, D.P. (2009) Weakening of calcium iridate during its transformation from perovskite to post-perovskite. *Nature Geoscience*, **2**, 11, 794-797 doi: 10.1038/NGEO663

Hustoft, J., Catalli, K., Shim, S-H., Kubo, A., Prakapenka, V.B., and Kunz, M. (2008) Equation of state of $NaMgF_3$ postperovskite: implication for the seismic velocity changes in the D" region. *Geophysical Research Letters*, **35**, L10309

Ibberson, R. M., David, W. I. F. & Knight, K. S. (1992) Report RAL-92-031, Rutherford Appleton Laboratory, Didcot, Oxfordshire, UK

Inaguma, Y., Hasumi, K., Yoshida, M., Ohba, T. and Katsumata, T. (2008). High-pressure synthesis, structure, and characterization of a post-perovskite $CaPtO_3$ with $CaIrO_3$-type structure. *Inorganic Chemistry*, **47**, 1868-1870

ISIS Annual Report (1996). Report RAL-TR-96-050, pp. 61–62. Rutherford Appleton Laboratory, Didcot, Oxfordshire, UK

ISIS Neutron training course (2010) Chapter 1 : Neutron diffraction. http://www.isis.stfc.ac.uk/learning/neutron-training-course/downloads/general/neutron-training-course---manual10674.pdf

Istomin, S.Ya., Svensson, G., D'yachenko, O.G., Holm, W., and Antipov, E.V. (1998) Perovskite-Type $Ca_{1-x}Sr_xNbO_3$ ($0 \leq x \leq 1$) Phases: A Synthesis, Structure and Electron Microscopy Study. *Journal of Solid State Chemistry*, **141**, 514 – 521

Ito, K., Tezuka, K., and Hinatsu, Y. (2001) Preparation, magnetic susceptibility, and specific heat on interlanthanide perovskites ABO_3 (A = La-Nd, B=Dy-Lu). *Journal of Solid State Chemistry*, **157**, 173-179

Ito, E., Fukui, H., Katsura, T., Yamazaki, D., Yoshino, T., Aizawa, Y., Kubo, A., Yokoshi, S., Kawabe, K., Zhai, S., Shatzkiy, A., Okube, M., Nozawa, A., and Funakoshi, K.-I. (2009). Determination of high-pressure phase equilibria of Fe_2O_3 using the Kawai-type apparatus equipped with sintered diamond anvils. *American Mineralogist*, **94**, 205-209

Jacobsen, S.D., Holl, C. M., Adams, K.A., Fischer, R.A., Martin, E.S., Bina, C.R., Lin, J.-F., Prakapenka, V.B., Kubo, A. and Dera, R. (2008) Compression of single-crystal magnesium oxide to 118 GPa and a ruby pressure gauge for helium pressure media. *Am. Mineral.*, **93**, 1823-1828

Jahn, H. and Teller, E. (1937) Stability of Polyatomic Molecules in Degenerate Electronic States. I. Orbital Degeneracy. *Proceedings of the Royal Society of London. Series A, Mathematical and Physical Sciences (1934-1990)* **161** (905): 220–235 doi:10.1098/rspa.1937.0142

Karki, B.B., Stixrude, L., Wentzcovitch, R.M. (2001) High-pressure elastic properties of major materials of Earth's mantle from first principles. *Review of Geophysics,* **39**, 4, 507-534

Kennedy, B.J., Howard, C.J., and Chakoumakos, B.C. (1999) High-temperature phase transitions in $SrHfO_3$. *Physics Review B*, **60**, 2972 – 2975

Keppler, H., Kantor, I. and Dubrovinsky, L.S. (2007) Optical absorption spectra of ferropericlase to 84 GPa. *American Mineralogist*, **92**, 433-436

Kim, S.-J., Lemaux, S., Demazeau, G., Kim, J.-Y., and Choy, J.-H. (2001) $LaPdO_3$: the first Pd^{III} oxide with the perovskite structure. *Journal of the American Chemical Society*, **123**, 10413-10414

Knee, C.S., Magrasó, A., Norby, T., and Smith, R.I. (2009) Structural transitions and conductivity of $BaPrO_3$ and $BaPr_{0.9}Y_{0.1}O_{3-\delta}$. *Journal of Materials Chemistry*, **19**, 3238-3247

Knight, K.S. (1994) Structural Phase transitions in $BaCeO_3$. *Solid State Ionics*, **74**, 109-117

Knight, K.S. (2009) Parameterisation of the crystal structures of centrosymmetric zone-boundary-tilted perovskites: an analysis in terms of symmetry-adapted basis-vectors of the cubic aristotype phase. *Canadian Mineralogist*, **47**, 381-400

Knight, K.S. and Bonanos, N. (1995) The crystal structures of some doped and undoped alkaline earth cerate perovskites. *Materials Research Bulletin*, **30**, 347-356

Knight, K.S., Marshall, W.G., Bonanos, N., and Francis D.J. (2005) Pressure dependence of the crystal structure of $SrCeO_3$ perovskite. *Journal of Alloys and Compounds*, **394**, 131-137

Knight, K.S. and Price, G.D. (2008) Powder neutron-diffraction studies of clinopyroxenes. I. The crystal structure and thermoelastic properties of jadeite between 1.5 and 270 K. *Canadian Mineralogist*, **46**, 1593-1622

Kohn W. and Sham L. J. (1965) Self-consistent equations including exchange and correlation effects. *Phys. Rev.* **140**, 1133

Kojitani, H., Shirako, Y., and Akaogi, M. (2007) post-perovskite phase transition in $CaRuO_3$. *Physics of the Earth and Planetary Interiors*, **165**, 127-134

Komabayashi, T., Hirose, K., Sugimura, E., Sata, N., Ohishi, Y., and Dubrovinsky, L.S. (2008) Simultaneous volume measurements of post-perovskite and perovskite in $MgSiO_3$ and their thermal equations of state. *Earth and Planetary Science Letters*, **265**, 515-524

Kresse, G. and Furthmüller, J. (1996) Efficiency of ab-initio total energy calculations for metals and semiconductors using a plane-wave basis set. *Comput. Mater. Sci.*, **6**, 15-50

Kresse,G. and Joubert, J. (1999) From ultrasoft pseudopotentials to the projector augmented wavemethod. *Phys.Rev.B*, **59**, 1758–1775

Kresse, K., Marsman, M. and Furthmüller, J. (2010) VASP Guide. Faculty of Physics, Universität Wien, Austria http://cms.mpi.univie.ac.at/vasp/vasp/vasp.html

Kubo, A., Kiefer, B., Shen, G., Prakapenka, V.B., Cava, R.J. and Duffy, T.S. (2006) Stability and equation of state of the post-perovskite phase in $MgGeO_3$ to 2 Mbar. *Geophysical Research Letters*, 33, L12S12

Kubo, A., Kiefer, B., Shim, S-H., Shen, G., Prakapenka, V.B., and Duffy, T.S. (2008) Rietveld structure refinement of $MgGeO_3$ post-perovskite phase to 1 Mbar. *American Mineralogist*, **93**, 965-976

Larson, A.C. and Von Dreele, R. B. (1994) General Structure Analysis System (GSAS). Los Alamos National Laboratory Report LAUR 86-748

Le Bail, A., Duroy, H. and Fourquet, J.L. (1988). Ab initio structure determination of $LiSbWO_6$ by X-ray powder diffraction. *Mat. Res. Bull.*, **23**, 447-452

Levin, I., Amos, T.G., Bell, S.M., Farber, L., Vanderah, T.A., Roth, R.S., and Toby, B.H. (2003) Phase Equilibria, crystal structures, and dielectric anomaly in the $BaZrO_3$-$CaZrO_3$ system. *Journal of Solid State Chemistry*, **175**, 170-181

Li, K. and Xue, D. (2006) Estimation of electronegativity values of elements in different valence states. *Journal of Physical Chemistry A*, **110**, 11332-11337

Li, J., Zhou, X., Zhu, W., Li, J. and Jing, F. (2007) A shock-induced phase transformation in a $LiTaO_3$ crystal. *Journal of Applied Physics*, **102**, 083503

Li,L., Weidner, D.J., Brodholt, J., Alfè, D., Price, G.D., Caracas, R. and Wentzcovitch, R. (2006) Phase stability of $CaSiO_3$ perovskite at high pressure and temperature: insights from ab initio molecular dynamics. *Phys. Earth Planet. Inter.*, **155**, 260-268

Li, C., Lu, C., Ding, W., Feng, L., Gao, Y. and Guo, Z. (2008) Formability of ABX_3 (X = F, Cl, Br, I) halide perovskites. *Acta Cryst. B*, **64**, 702-707

Liang, L., Wencong, L., and Nianyi C. (2004) On the criteria of formation and lattice distortion of perovskite-type complex oxides. *Journal of Physics and Chemistry of Solids*, **65**, 855-860

Lindsay-Scott, A., Wood, I.G. and Dobson, D. (2007) Thermal expansion of $CaIrO_3$ determined by X-ray powder diffraction. *Phys. Earth Planet. Inter.*, **162**, 140-148

Lindsay-Scott, A., Wood, I.G., Dobson, D., Vočadlo, L., Brodholt, J.P., Crichton, W., Hanfland, M. and Taniguchi, T. (2010) The isothermal equation of state of $CaIrO_3$ post-perovskite to 40 GPa. *Phys. Earth Planet. Inter.*, **182**, 113-118

Lindsay-Scott, A., Wood, I.G., Dobson, D., Vočadlo, L., Brodholt, J.P., Knight, K.S., Tucker, M.G. and Taniguchi, T. (2011) Thermoelastic properties and crystal structure of $CaPtO_3$ post-perovskite from 0–9 GPa and from 2–973 K. *J. Appl. Cryst.,* **44**, 999-1016

Liu, H.-Z., Chen, J., Hu, J., Martin, C.D., Weidner, D.J., Häusermann, D. and Mao, H.-K. (2005) Octahedral tilting evolution and phase transition in orthorhombic $NaMgF_3$ perovskite under pressure. *Geophysical Research Letters*, **32**, L04304, doi:10.1029/2004GL022068

Liu, Z., Sun, X., Zhang, C., Tian, L. and Guo, Y. (2010) Thermodynamic properties of $MgSiO_3$ post-perovskite. *Modern Physics Letters B*, **24/3**, 315-324

Liu, W., Whitaker, M.L., Liu, Q., Wang, L., Nishiyama, N., Wang, Y., Kubo, A., Duffy, T.S. and Li, B. (2011) Thermal equation of state of $CaIrO_3$ post-perovskite. *Phy. Chem. Minerals,* **38**, 407-417

Loa, I., Adler, P., Grzechnik, A., Syassen, K., Schwarz, U., Hanfland, M., Rozenberg, G.Kh,. Gorodetsky, P., Pasternak, M.P. (2001) Pressure-Induced Quenching of the Jahn-Teller Distortion and Insulator-to-Metal Transition in $LaMnO_3$. *Physical Review Letters*, **87**, 12, 125501

Loa, I., Wang, X., Syassen, K., Roth, H., Lorenz, T., Hanfland, H. and Mathis, Y.-L. (2007) Crystal structure and the Mott-Hubbard gap in $YTiO_3$ at high pressure. *J. Phys.: Condens. Matter*, **19**, 406223, 1-8

Loridant, S. and Lucazeau, G. (1999) High-Pressure Raman study of the perovskite $BaCeO_3$. *Journal of Raman Spectroscopy*, **30**, 485-492

Lufaso, M.W. and Woodward, P.M. (2004) Jahn-Teller distortions, cation ordering and octahedral tilting in perovskites. *Acta Crystallographica*, **B60**, 10-20

Macquart, R.B., Smith, M.D., and zur Loye, H.-C. (2006) Crystal growth and single-crystal structures of $RERhO_3$ (RE = La, Pr, Nd, Sm, Eu, Tb) orthorhodites from a K_2CO_3 flux. *Crystal Growth and Design*, **6**, 1361-1365

MANTID (2008) ISIS gears up for a data deluge. *Scientific Computing World*, 29 January 2008, http://www.scientific-computing.com/news/news_story.php?news_id=327

MANTID (2010) MANTID project web site. http://www.mantidproject.org

Mansuetto, M.F., Keane, P.M. and Ibers, J.A. (1992) Synthesis, structure and conductivity of the new group IV chalcogenides, $KCuZrQ_3$ (Q = S, Se, Te). *J. Solid State Chemistry,* **101**, 257-264

Mao, H.K., Bell, P.M., Shaner, J.W. and Steinberg, D.J. (1978) Specific volume measurements of Cu, Mo, Pd, and Ag and calibration of the ruby R_1 fluorescence pressure gauge from 0.06 to 1 Mbar. *J. Appl. Phys.*, **49(6)**, 3276-3283

Mao, H.-K., Xu, J. and Bell, P.M. (1986) Calibration of the ruby pressure gauge to 800 Kbar under quasi-hydrostatic conditions. *J. Geophys. Res.*, **91**, 4673–4676

Mao, H.-K., Hemley, R.J., Wu, Y., Jephcoat, A.P., Finger, L.W., Zha, C.S. and Bassett, W.A. (1988) High-pressure phase diagram and equation of state of solid helium from single-crystal X-ray diffraction to 23.3 GPa. *Phys. Rev. Lett.*, **60**, 2649-2652

Mao, W.L., Meng, Y. and Mao, H.-K. (2010) Elastic anisotropy of ferromagnesian post-perovskite in Earth's D" layer. *Phys. Earth Planet. Inter.*, **180**, 203-208

Marshall, W.G. and Francis, D.J. (2002) Attainment of near-hydrostatic compression conditions using the Paris-Edinburgh cell. *J. Appl. Cryst.* **35**, 122-125

Martin, C.D., Crichton, W.A., Liu, H., Prakapenka, V., Chen, J. and Parise, J. (2006a) Rietveld structure refinement of perovskite and post-perovskite phases of $NaMgF_3$ (Neighborite) at high pressures. *American Mineralogist,* **91**, 1703-1706

Martin, C.D., Crichton, W.A., Liu, H., Prakapenka, V., Chen, J. and Parise, J. (2006b) Phase transitions and compressibility of $NaMgF_3$ (Neighborite) in perovskite- and post-perovskite-related structures. *Geophysical Research Letters*, **33**, L11305

Martin, C.D., Chapman, K.W., Chupas, P.J., Prakapenka, V., Lee P.L., Shastri, S.D. and Parise, J.B. (2007a) Compression, thermal expansion, structure and instability of $CaIrO_3$, the structure model of $MgSiO_3$ post-perovskite. *Am. Mineral.*, **92**, 1048-1053

Martin, C.D., Smith, R.I., Marshall, W.G. and Parise, J.B. (2007b) High-pressure structure and bonding in $CaIrO_3$: The structure model of $MgSiO_3$ post-perovskite investigated with time-of-flight neutron powder diffraction. *Am. Mineral.*, **92**, 1912-1918

Martin, C.D. (2008) The local post-perovskite structure and its temperature dependence: atom-pair distances in $CaIrO_3$ revealed through analysis of the total X-ray scattering at high temperatures. *J. Appl. Cryst.*, **41**, 776-783

Martin, C.D. and Parise, J.B. (2008) Structure constraints and instability leading to the post-perovskite phase transition of $MgSiO_3$. *Earth and Planetary Science Letters*, **265**, 630-640

Matar, S.F., Demazeau, G. and Largeteau, A. (2008) Ab initio investigation of perovskite and post-perovskite $CaPtO_3$. *Chem. Phys.*, **352**, 92-96

Matar, S.F., Demazeau, G. and Largeteau, A. (2010) DFT study of electronic and magnetic structure of perovskite and post-perovskite $CaRhO_3$. *Solid State Sciences*, **12**, 373-378

Mazin, I.I., Khomskii, D.I., Lengsdorf, R., Alonso, J.A., Marshall, W.G., Ibberson, R.M., Podlesnyak, A., Martinez-Lope, M.J. and Abd-Elmeguid, M.M. (2007) Charge ordering as alternative to Jahn-Teller distortion. *Physical Review Letters,* **98**, 176406

McCormack, R. (2011) Ph.D. thesis, University College London, U.K.

McCormack, R., Dobson, D.P., Heidelbach, F., Beard, A., Ammann, M.W. and Brodholt, J.P. (2010) Single-crystal Ir-Pr interdiffusion in $CaIrO_3$ post-perovskite. *Annual Report* 2010, Bayerisches Forschungsinstitut für Experimentelle Geochemie und Geophsik, Universität Bayreuth, Germany

McCormack, R., Dobson, D.P., Walte, N.P., Miyajima, N., Taniguchi, T. and Wood, I.W. (2011) The development of shape- and crystallographic-preferred orientation in $CaPtO_3$ post-perovskite deformed in pure shear. *American Mineralogist*, **96**, 1630-1635

McDaniel C.L. and Schneider S.J. (1972) Phase relations in the CaO-IrO_2-Ir system in air. *J. Solid State Chemistry*, **4**, 275-280

Miyajima, N., Ohgushi, K., Ichihara, M. and Yagi, T. (2006) Crystal morphology and dislocation microstructures of $CaIrO_3$: a TEM study of an analogue of the $MgSiO_3$ post-perovskite phase. *Geophysical Research Letters*, **33**, L12302, doi:10.1029/2005GL025001

Mizoguchi, H., Woodward, P.M., Byeon, S-H., and Parise, J.B. (2004a) Polymorphism in NaSbO3: structure and bonding in metal oxides. *Journal of the American Chemical Society*, **126**, 3175-3184

Mizoguchi, H., Eng, H.W., and Woodward, P.M. (2004b) Probing the electronic structures of ternary perovskite and pyrochlore oxides containing Sn^{4+} or Sb^{5+}. *Inorganic Chemistry*, **43**, 1667-1680

Monkhorst. H. J., and J. D. Pack (1976) Special points for Brillouin-zone integrations. *Phys. Rev. B* **13(12)**, 5188-5192

Mooser, E. and Pearson, W.B. (1959) On the crystal chemistry of normal valence compounds. *Acta Cryst.*, **12**, 1015-1022

Muller, O. and Roy, R. (1974) The major ternary structural families. Springer, Berlin

Murakami, M., Hirose, K., Kawamora, K., Sata, N. and Ohishi, Y. (2004) Post Perovskite Phase Transition in $MgSiO_3$. *Science*, **304**, 855-858

Nishio-Hamane, D. and Yagi, T. (2009) Equations of state for postperovskite phases in the $MgSiO_3$-$FeSiO_3$-$FeAlO_3$ system. *Physics of the Earth and Planetary Interiors*, **175**, 145-150

Nishio-Hamane, D., Yagi, T., Ohshiro, M., Niwa, K., Okada, T. and Seto, Y. (2010) Decomposition of perovskite $FeTiO_3$ into wüstite $Fe_{1-x}Ti_{0.5x}O$ and orthorhombic $FeTi_3O_7$ at high pressure. *Physical Review B*, **82**, 092103

Niwa, K., Yagi, T. and Ohgushi, K. (2010) Elasticity of $CaIrO_3$ with perovskite and post-perovskite structure. *Phys. Chem. Minerals*, doi 10.1007/s00269-010-0378-z

Nosé, S. (1984) A unified formulation of the constant temperature molecular dynamics methods. *J. Chem. Phys*. **81**, 511-519

Oganov, A.R., Brodholt, J.P. and Price, G.D. (2002) Ab initio theory of phase transitions and thermoeleasticity of minerals. In: *EMU Notes in Mineralogy, Vol. 4 (2002): Energy Modelling in Minerals. Ed.: Gramaccioli, C.M.* European Mineralogical Union, Wien, Austria

Oganov, A.R. and Ono S. (2004) Theoretical and Experimental Evidence for a post-perovskite Phase of $MgSiO_3$ in Earth's D" layer. *Nature*, **430**, 445-448.

Oganov, A.R. and Ono, S. (2005) The high-pressure phase of alumina and implications for Earth's D'' layer. *Proceedings of the National Academy of Sciences*, **102 (31)**, 10828-10831

Oganov, A.R., Martonak, R., Laio, A., Raiteri, P. and Parrinello, M. (2005) Anisotropy of Earth's D'' layer and stacking faults in the $MgSiO_3$ post-perovskite phase. *Nature*, **438**, 1142-1144

Ohgushi, K., Gotou, H., Yagi, T., Kiuchi, Y., Sakai, F. and Ueda, Y. (2006) Metal-insulator transition in $Ca_{1-x}Na_xIrO_3$ with post-perovskite structure. Physical Review B, **74**, 241104(R)

Ohgushi, K., Matsushita, Y., Miyajima, N., Katsuya, Y., Tanaka, M., Izumi, F., Gotou, H., Ueda, Y. and Yagi, T. (2008) $CaPtO_3$ as a novel post-perovskite oxide. *Phys. Chem. Minerals*, **35**, 189-195

Okada, T., Tagi, T. and Nishio-Hamane, D. (2011) High-pressure phase behavior of $MnTiO_3$: decomposition of perovskite into MnO and $MnTi_2O_5$. *Phys. Chem. Minerals*, **38**, 251-258

O'Keeffe, M. and Hyde, B.G. (1977) Some structures topologically related to cubic perovskite ($E2_1$), ReO_3 ($D0_9$) and Cu_3Au ($L1_2$). *Acta Crystallographica*, **B33**, 3802-3813

Ono, S., Oganov, A.R., Koyama, T., and Shimuzu, H. (2006a) Stability and compressibility of the high-pressure phases of Al_2O_3 up to 200 GPa: implications for the electrical conductivity of the base of the lower mantle. *Earth and Planetary Science Letters*, **246**, 326-355

Ono, S., Kikegawa, T. and Ohishi, Y. (2006b) Equation of state of $CaIrO_3$-type $MgSiO_3$ up to 144 GPa. *American Mineralogist*, **91**, 475-478

Ono, S. and Ohishi, Y. (2005) In situ X-ray observation of phase transtransition in Fe_2O_3 at high pressures and high temperatures. *Journal of Physics and Chemistry of Solids*, **66**, 1714-1720

Pauling, L. (1960) The nature of the chemical bond. Cornell University Press, New York, USA. ISBN 0801403332

Payne, M.C., Teter, M.P., Allan, D.C., Arias, T.A. and Joannopoulos, J.D. (1992) Iterative minimization techniques for *ab initio* total-energy calculations: Molecular dynamics and conjugate gradients. *Reviews of Modern Physics*, **64**, 4, 1045-1097

Perdew, J.P., Burke, K. and Ernzerhof, M, (1996) Generalized gradient approximation made simple *Phys. Rev. Lett.* **77,** 3865–8

Piermarini, G.J., Block, S., Barnett, J.D. and Forman, R.A. (1975) Calibration of the pressure dependence of the R_1 ruby fluorescence line to 195 kbar. *J. Appl. Phys.*, **46(6)**, 2774-2780

Poirier J-P. (2000) Introduction to the physics of the Earth's interior (2^{nd} ed.), Cambridge University Press, Cambridge, UK

Price, G.D.P., Price, S.L. and Burdett, J.K. (1982) The factors influencing cation site-preferences in spinels – a new Mendelyevian approach. *Phys. Chem. Minerals*, **8**, 69-76

Putnis, A. (1992) Introduction to mineral sciences. Cambridge University Press, Cambridge, UK

Rodi F. and Babel D. (1965) Erdalkaliiridium (IV)-oxide: Kristallstruktur von $CaIrO_3$. Z. Anorg. Allg. Chem., **336**, 17-23

Ross, N.L. and Hazen, R.M. (1989) Single crystal X-ray diffraction study of $MgSiO_3$ perovskite from 77 to 400 K. *Phys. Chem. Minerals*, **16**, 415-420

Santillan, J., Shim, S.-H., Shen, G., and Prakapenka, V.B. (2006) High-pressure phase transition in Mn2O3: application for the crystal structure and preferred orientation of the $CaIrO_3$ type. *Geophysical Research Letters*, **33**, L15307, doi:10.1029/2006GL026423

Sasaki, S., Prewitt, C.T., and Bass, J.D. (1987) Orthorhombic perovskite $CaTiO_3$ and $CdTiO_3$: Structure and space group. *Acta Crystallographica,* **C43**, 1668-1674

Schilling, G., Kunert, C., Schleid, T. and Meyer, G. (1992) Metallothermische Reduktion der Tribromide und -iodide von Thulium und Ytterbium rnit Alkalimetallen. *Zeitschrift für anorganische und allgemeine Chemie*, **618**, 7-12

Schneider, B.W., Liu, W., and Baosheng L. (2008) Searching for post-perovskite transition in $CaSnO_3$ at high pressure: an ultrasonic velocity study to 18 GPa. *High Press Research,* **28**, 397-404

Scholten, M. and Dronskowski, R. (1996) $InCaBr_3$, an electron absorbent layered material containing univalent indium. *Comptes Rendus de l'Academie des Sciences Serie II Fascicule B-Mecanique Physique Chimie Astronomie*, **322**, 699-706

Sears, V.F. (1992) Neutron scattering lengths and cross Sections. *Neutron News*, **3**, 3, 26-37

Shannon, R.D. (1976) Revised effective ionic radii and systematic studies of interatomic distances in halides and chalcogenides. *Acta Crystallographica*, **A32**, 751–767

Shim, S-H., Catalli, K., Hustoft, J., Kubo, A., Prakapenka, V.B., Caldwell, W.A., and Kunz, M. (2008) Crystal structure and thermoelastic properties of $(Mg_{0.91}Fe_{0.09})SiO_3$ postperovskite up to 135 GPa and 2,700K. *Proceedings of the National Academy of Sciences of the United States of America*, **105**, 7383-7386

Shim, S-H., Bengtson, A., Morgan, D., Sturhahn, W., Catalli, K., Zhao, J., Lerche, M., and Prakapenka, V. (2009) Electronic and magnetic structures of the postperovskite-type Fe_2O_3 and implications for planetary magnetic records and deep interiors. *Proceedings of the National Academy of Sciences of the United States of America*, **106**, 5508-5512

Shirako, Y., Kojitani, H., Akaogi, M., Yamaura, K., and Takayama-Muromachi, E. (2009). High-pressure phase transitions of $CaRhO_3$ perovskite. *Physics and Chemistry of Minerals*, **36**, 455-462

Shirako, Y., Satsukawa, H., Wang, X.X., Li, J.J., Guo, Y.F., Arai, M., Yamaura, K., Yoshida, M., Kojitani, H., Katsumata, T., Inaguma, Y., Hiraki, K., Takahashi, T. and Akaogi, M. (2011) Integer spin-chain antiferromagnetism of the 4*d* oxide $CaRuO_3$ with post-perovskite structure. *Physical Review B*, **83**, 174411

Stackhouse, S., Brodholt, J.P., Wookey, J., Kendall, J-M. and Price, G.D. (2005a) The effect of temperature on the seismic anisotropy of the perovskite and post-perovskite polymorphs of $MgSiO_3$. *Earth and Planetary Science Letters,* **230**, 1-10

Stackhouse, S., Brodholt, J.P., and Price, G.D. (2005b) High temperature elastic anisotropy of the perovskite and postperovskite polymorphs of Al_2O_3. *Geophysical Research letters,* **32**, L13305

Stackhouse, S. and Brodholt, J.P. (2007) The high-temperature elasticity of $MgSiO_3$ post-perovskite. In: *Post-perovskite: the last mantle phase transition. Ed: Hirose, K., Brodholt, J.P., Lay, T. and Yuen, D. Geophysical monograph 174*. American Geophysical Union, Washington DC, USA

Stackhouse, S. (2009) Personal communication

Stackhouse, S., Stixrude, L. and Karki, B.B. (2010) Determination of the high-pressure properties of fayalite from first-principles calculations. *Earth and Planetary Science Letters*, **289**, 449-456

Stixrude, L., Lithgow-Bertelloni, C., Kiefer, B. and Fumagalli, P. (2007) Phase

stability and shear softening in $CaSiO_3$ perovskite at high pressure. *Physical Review B*, **75**, 024108

Stølen, S. and Trønnes, R.G. (2007) The perovskite to post-perovskite transition in $CaIrO_3$: Clapeyron slope and changes in bulk and shear moduli by density functional theory. *Physics of the Earth and Planetary Interiors*, **164**, 50-62

Street, J.N., Wood, I.G., Knight, K.S. and Price, G.D. (1997) The influence of thermal vibrations on the average structure of $NaMgF_3$ perovskite: a combined molecular dynamics and neutron diffraction study. *J. Phys. Condens. Matter,* **9**, L647-L655

Sugahara, M., Yoshiasa, A., Yoneda, A., Hashimoto T., Sakai, S., Okube, M., Nakatsuka, A. and Ohtaka, O. (2008) Single-crystal X-ray diffraction study of $CaIrO_3$. *Am. Mineral.*, **93**, 1148-1152

Tateno S., Hirose K., Sata N. and Ohishi Y. (2006) High-pressure behaviour of $MnGeO_3$ and $CdGeO_3$ perovskites and the post-perovskite phase transition. *Phys. Chem. Miner.*, **32**, 721-725

Tateno, S., Hirose, K., Sata, N., and Ohishi, Y. (2009) Determination of post-perovskite phase transition boundary up to 4400 K and implications for thermal structure in D" layer. *Earth and Planetary Science Letters*, **277**, 130-136

Tateno S., Hirose K., Sata N., and Ohishi Y. (2010) Structural distortion of $CaSnO_3$ perovskite under pressure and the quenchable post-perovskite phase as a low-pressure analogue to $MgSiO_3$. *Physics of the Earth and Planetary Interiors*, **181**, 54-59

Tezuka, K., Hinatsu, Y., Shimojo, Y., and Morii, Y. (1998) Study on the crystal and magnetic structures of $SrTbO_3$ and $BaTbO_3$ by powder neutron diffraction. Journal of Physics: Condensed Matter, 10, 11703-11712

Thompson, P. and Wood, I.G. (1983) X-ray Rietveld refinement using Debye-Scherrer geometry. *J. Appl. Cryst.*, **16**, 458-472

Thundathil, M.A., Jones, C.Y., Snyder, G.J., and Haile, S.M. (2005) Nonstoichiometry, structure, and electrical properties of "$SrPrO_3$". *Chemistry of Materials*, **17**, 5146-5154

Toby B.H. (2001) EXPGUI, a graphical user interface for GSAS. *J. Appl. Cryst.*, **34**, 210-221

Toby, B. (2006) LeBail intensity extraction. Argonne National Laboratory APS, http://www.aps.anl.gov/Xray_Science_Division/Powder_Diffraction_Crystallography/lebail.html

Trønnes, R.G. (2010) Structure, mineralogy and dynamics of the lowermost mantle. *Miner. Petrol.*, **99**, 243-261

Tschauner, O., Kiefer, B., Liu, H., Sinogeikin, S., Somayazulu, M. and Luo, S-N. (2008) Possible structural polymorphism in Al-bearing magnesiumsilicate post-perovskite. *American Mineralogist*, **93**, 533-539

Tsuchiya, T., Tshuchiya, J., Umemoto, K. and Wentzcovitch, R.M. (2004) Phase transition in $MgSiO_3$ perovskite in the earth's lower mantle. *Earth and Planetary Science Letters*, **224**, 241-248

Tsuchiya J., Tsuchiya T. and Wentzcovitch R. M. (2005) Vibrational and thermodynamic properties of $MgSiO_3$ postperovskite. *J. Geophys. Res.* **110**, B02204, doi:10.1029/2004/B003409

Tsuchiya, T. and Tsuchiya, J. (2006) New high-pressure phase relations in $CaSnO_3$. *American Mineralogist*, **91**, 1879-1887

Tsuchiya, T. and Tsuchiya, J. (2007a) High-pressure-high-temperature phase relations of $MgGeO_3$: first principles calculations. *Physical Review B*, **76**, Article No 092105

Tsuchiya, T. and Tsuchiya, J (2007b) Structure and elasticity of Cmcm $CaIrO_3$ and their pressure dependencies: Ab initio calculations. *Physical Review B*, **76**, Article No 144119

Umemoto, K., Wentzcovitch, R.M., Weidner, D.J., and Parise, J.B. (2006) $NaMgF_3$: A low-pressure analog of $MgSiO_3$. *Geophysical Research Letters*, **33**, L15304

Vočadlo, L. and Dobson, D. (1999) The Earth's deep interior: advances in theory and experiment. *Phil. Trans. R. Soc. Lond.* A, **357**, 3335–3357

Vočadlo, L., Knight, K.S., Price, G.D. and Wood, I.G. (2002) Thermal expansion and crystal structure of FeSi between 4 and 1173 K determined by time-of-flight neutron powder diffraction. *Phys. Chem. Minerals,* **29**: 132-139

Walker, D. (1991) Lubrication, gasketing, and precision in multianvil experiments. *American Mineralogist*, **76**, 1092-1100

Wallace, D.C. (1998) Thermodynamics of crystals, Dover, New York, USA

Walte, N., Heidelbach, F., Miyajima, N., Frost, D., Rubie, D., and Dobson, D.P. (2009) Transformation textures in post-perovskite: Understanding mantle flow in the D'' layer of the Earth. *Geophysical Research Letters*, **36**, L04302, doi:10.1029/2008GL036840

Wang, Y. and Perdew, J.P. (1991) Correlation hole of the spin-polarized electron gas, with exact small-vector and high-density scaling. *Phys. Rev. B, Condens. Matter*, **44**, 13, 298-13,307

Wang, X.X., Guo, Y.F., Shirako, Y., Akaogi, M., Yamaura, K. and Takayama-Muromachi, E. (2011) Thermal evolution of the crystal structure of the correlated 4*d* post-perovskite $CaRhO_3$. *PhysicaC*, 10.1016/j.physc.2011.05.048

Wilson, N.C. and Russo, S.P. (2009) Hybrid density functional theory of the high-pressure polymorphs of α-Fe_2O_3 hematite. *Physical Review B*, **79**, 094113

Wood, I.G. (1977) Ph.D. Thesis, University of London, U.K.

Wood, I.G. (2006) Personal communication

Wood, I.G., Knight, K.S., Price, G.D. and Stuart, J.D. (2002) Thermal expansion and atomic displacement parameters of cubic $KMgF_3$ perovskite determined by high-resolution neutron powder diffraction. *J. Appl. Cryst.*, **35**, 291-295

Wood, I.G., Vočadlo, L., Dobson, D.P., Price, G. D., Fortes, A.D., Cooper, F.J., Neale, J.W., Walker, A.M., Marshall, W.G., Tucker, M.G., Francis, D.J., Stone, H.J. and McCammon, C.A. (2008) Thermoelastic properties of magnesiowüstite, $(Mg_{1-x}Fe_x)O$: determination of the Anderson–Grüneisen parameter by time-of-flight neutron powder diffraction at simultaneous high pressures and temperatures. *Journal of Applied Crystallography*, **41**, 886-896

Woodward, P.M. (1997a) Octahedral tilting in perovskites. I. Geometrical considerations. *Acta Crystallographica*, **B53**, 32-43

Woodward, P.M. (1997b) Octahedral tilting in perovskites. II. Structure stabilising forces. *Acta Crystallographica*, **B53**, 44-66

Wu, Z. and Cohen, R.E. (2006) More accurate generalized gradient approximation for solids. *Physical Review B*, **73**, 235116

Wu, X., Dong, Y., Qin, S., Abbas, M., and Wu, Z. (2005) First-principles study of the pressure-induced phase transition in $CaTiO_3$. *Solid State Communications*, **136**, 416-420

Wu, X., Steinle-Neumann, G., Narygina, O., McCammon, C., Prakapenka, V., Swamy, V. and Dubrovinsky, L. (2009) High-pressure behaviour of perovskite: $FeTiO_3$ dissociation into $(Fe_{1-\delta},Ti_\delta)O$ and $Fe_{1+\delta}Ti_{2-\delta}O_5$. *Physical Review Letters*, **103**, 065503

Yagi, T. (1994) Structures and properties of perovskite-type compounds synthesized under very high pressures. In: *Proceedings of the NIRIM international symposium on advanced materials '94. Ed: Kamo, M., Kanda, H., Matsui, Y. and Sekine, T.* National Institute for Research in Inorganic Materials, Tsukuba, Japan

Yakovlev, S., Avdeev, M., and Mezouar, M. (2009) High-pressure structural behaviour and equation of state of $NaZnF_3$. *Journal of Solid State Chemistry*, **182**, 1545-1549

Yakovlev, S., Avdeev, M. Sterer, E., Greenberg, Y. and Mezouar, M. (2009a) High-pressure structural behaviour and equation of state of $NaZnF_3$ (vol 182, pg 1545, 2009). J*ournal of Solid State Chemistry*, **182**, 2946-2946

Yamaura, K., Shirako, Y., Kojitani, H., Arai, M., Young, D.P., Akaogi, M., Nakashima, M., Katsumata, T., Inaguma, Y. and Takayama-Muromachi, E. (2009) Synthesis and magnetic and charge-transport properties of the correlated 4d post-perovskite $CaRhO_3$. *J. Am Chem. Soc.*, **131**, 2722-2726

Yamazaki, D., Ito, E., Katsura, T., Yoshino, T., Zhai, S., Fukui, H., Shatskiy, A., Guo, X., Shan, S., Okuchi, T., Tange, Y., Higo, Y. and Funakoshi, K. (2011) Phase boundary between perovskite and post-perovskite structures in $MnGeO_3$ determined by

in situ X-ray diffraction measurements using sintered diamond anvils. *American Mineralogist*, **96**, 89-92

Yang, Y. and Ibers, J.A. (1999) Synthesis and characterization of a series of quaternary chalcogenides Ba*LnMQ*$_3$ (*Ln* = rare earth, *M* = coinage metal, *Q* = Se or Te). *J. Solid State Chemistry*, **147**, 366-371

Yashima, M. and Ali, R. (2009) Structural phase transition and octahedral tilting in the calcium titanate perovskite $CaTiO_3$. *Solid State Ionics*, **180**, 120-126

Ye, C., Yang, J., Yao, L. and Chen, N. (2002). Regularities of formation and lattice distortion of perovskite-type compounds. *Chinese Science Bulletin*, **6**, 458-460

Young, R.A. (1995) The Rietveld method. *IUCr monographs on crystallography (5).* International Union of Crystallography, Oxford Science Publications, Oxford, UK

Yusa, H., Akaogi, M., Sata, N., Kojitani, H., Yamamoto, R., and Ohishi, Y. (2006) High-pressure transformations of ilmenite to perovskite, and lithium niobate to perovskite in zinc germanate. *Physics and Chemistry of Minerals*, **33**, 217-226
Zhao, Y., Weidner, D.J., Parise, J.B. and Cox D.E. (1993a) Thermal expansion and structural distortion of perovskite – data for $NaMgF_3$ perovskite. Part I. *Physics of the Earth and Planetary Interiors*, **76**, 1-16

Zhao, Y., Weidner, D.J., Parise, J.B. and Cox D.E. (1993b) Critical phenomena and phase transition in perovskite – data for $NaMgF_3$ perovskite. Part II. *Physics of the Earth and Planetary Interiors*, **76**, 17-34

Zhao J., Ross N.L., Angel R.J. (2006) Estimation of polyhedral compressibilities and structural evolution of $GdFeO_3$-type perovskites at high pressures. *Acta Cryst*. **B62**, 431-439

Zhong, G., Li, Y., Liu, Z. and Zeng, Z. (2010) Ground state properties of perovskite and post-perovskite $CaRuO_3$: ferromagnetism reduction. *Solid State Sciences*, **12**, 2003-2009

Zhou, J.-S. and Goodenough, J.B. (1996) Heterogeneous electronic structure in $CaVO_3$. *Physical Review B*, **54**, 13393-13397

13 Appendix A – INCAR file parameters

1. Structural parameters

ISIF: ISIF=4 specifies that the unit-cell parameters and atomic coordinates are relaxed within a fixed volume.

ISYM: Symmetry is switched on (default ISYM=2).

2. Ionic relaxation parameters

IBRION: IBRION=2 specifies that a conjugate-gradient algorithm is used to relax the ions into their instantaneous groundstate. In this method, the search directions for this step are conjugated to previous search directions (Hafner *et al.*, 2010: Ionic optimisation).

MAXMIX: MAXMIX controls the maximum number of steps in the charge mixing, and is set to 50.

NSW: The maximum number of ionic steps NSW is set to 50.

3. Electronic wavefunction parameters

EDIFF: The EDIFF parameter specifies the allowed error in total energy when calculating the electronic groundstate.

ENCUT: The POTCAR file specifies a default energy cut-off ENMAX for the plane wave basis set for each element (see Section 2.1.6). For a multi-element compound the maximum value is used. This maximum is overridden by the ENCUT value specified in the INCAR file.

ENAUG: EAUG in POTCAR specifies the default kinetic energy cut-off for augmentation charges for each element, and the maximum value is overridden by the

ENAUG energy specified in INCAR. Augmentation charges are defined as the charge density difference between the all-electron wave function and the pseudopotential wave function (Kresse and Joubert, 1999).

Energy convergence tests varying the EDIFF, ENCUT, ENAUG and ***k***-points parameters are described in Section 3.4.

ISPIN: ISPIN determines whether spin-polarised calculations are made. Spin-polarised calculations approximately double the processor time required. Spin-polarised calculations require the initial magnetic moment of each atom type to be specified (e.g. 1 for Ir^{4+}, 2 for Ni^{2+}). In the case of post-perovskite $CaIrO_3$, the net simulated magnetic moment calculated by VASP (parameter MAGMOM) in the (Z = 4) unit-cell is zero. I used spin-polarisation for athermal multiple ***k***-point simulation of post-perovskite $CaIrO_3$ but not for its MD and gamma point simulation, in order to limit the run times required for the MD simulation. I found that neglecting spin-polarisation during gamma point simulation (see Section 3.8) of post-perovskite $CaIrO_3$ resulted in a mean difference of 0.02% in the unit-cell parameters and of 0.05% in the 4 atomic coordinates (Ca y, O1*y*, O2*y* and O2*z*) which define the ABX_3 post-perovskite structure (see Section 1.4). $CaIrO_3$ post-perovskite changes from paramagnetic to antiferromagnetic below 115 K (Ohgushi *et al*., 2006).

For $NaNiF_3$ perovskite and post-perovskite, the net simulated magnetic moment calculated by VASP with spin-polarisation in the (Z = 4) unit-cell was 8.0 μ_B (Bohr magnetons, or half-units of $\hbar$), corresponding to a spin of 2.0 for each Ni^{2+} ion. This is consistent with the perovskite being weakly ferromagnetic (Epstein *et al.*, 1968). Using spin-polarisation when simulating post-perovskite $NaNiF_3$ resulted in an internal energy E_0 of the unit-cell at 0 GPa which was 2.9 eV (3.2%) lower than that with no spin-polarisation. The mean differences between spin and no spin simulations at the same volume were 3.1% in the unit-cell parameters and 2.2% in the 4 atomic coordinates. I therefore specified spin-polarisation for athermal simulation of $NaNiF_3$ perovskite and post-perovskite.

NELM: NELM is the maximum number of electronic (self consistency) iterations, set to 20 – this value is not usually reached after the first ionic relaxation.

NELMIN: NELMIN is the minimum number of electronic iterations, set to 4.

ISMEAR: ISMEAR is set to -5, specifying that wavefunction partial occupancies are calculated using the tetrahedron method with Blöchl corrections, recommended for the calculation of the total energy in bulk materials (Kresse *et al.*, 2010). This was validated by checking for energy convergence when selecting the number of ***k***-points (see Section 3.4)(Hafner *et al.*, 2010: Sampling the Brillouin zone).

IALGO: IALGO=48 specifies that the wavefunctions are optimized using RMM-DIIS iterative matrix diagonalization, and this value proved robust. It is also the only value for this parameter which supports parallelised calculations over electronic wavebands, as used in the present work. Real space projection of the pseudopotentials was used throughout to avoid high frequency aliasing errors.

4. Computational efficiency parameters

NPAR: NPAR controls the degree of parallelisation (and data distribution) over wavebands, and was set to the square root of the number of HECToR cores (mppwidth) used (NPAR=16 for 128 cores).

NSIM: NSIM controls the number of wavebands optimised simultaneously, and was set to 4.

The optimum settings for NPAR and NSIM for VASP athermal and MD simulations were evolved empirically. This involved tradeoffs between the resources (number of processor nodes) requested, VASP's relative efficiency in making use of larger numbers of processors, and the queue length of jobs requesting that number of processors. These tradeoffs differ between HECToR's phase 2a (4 cores/node) and phase 2b (24 cores/node). The NPAR parameter was also important for the more computer-intensive MD runs.

Other INCAR parameters were left at their default values.

All VASP runs in the present work used the HECToR UK national high-performance computing service. I used VASP version 4.6.28 with multiple $\boldsymbol{k}$ points for athermal (0 K) simulations, and the gamma-point only version for MD and gamma-point athermal simulations (see Section 3.8).

14 Appendix B – Simulation convergence tests

Table 13.1 shows the convergence limit (energy difference per atom) for the static simulations as the ENCUT and ENAUG parameters are increased, after convergence has been achieved by adjusting first the ***k***-points and then the ENCUT parameter.

Post-perovskite	**Change in energy in meV/atom**
$MgSiO_3$	0.05
$MgGeO_3$	0.56
$CaPtO_3$	1.38
$CaIrO_3$	0.60
$NaMgF_3$	0.56
$NaZnF_3$	0.46
$NaNiF_3$	0.56
Perovskite	
$MgSiO_3$	0.09
$MgGeO_3$	0.06
$CaSiO_3$	0.11
$NaMgF_3$	0.72
$NaZnF_3$	0.85
$NaNiF_3$	0.87

Table 14-1: Energy convergence for an ENCUT/ENAUG change from 800/800 eV to 900/1000 eV, except for $MgGeO_3$ perovskite 800/800 eV to 800/1000 eV.

The convergence data for the simulated post-perovskites is plotted in Figure 3-1 and in Figure 14-1 to Figure 14-6. In these Figures the following key applies:

- 333 to 955: number of ***k***-points. Numbers of irreducible *k*-points are 8 (333 and 444), 27 (555 and 666) and 45 (955)
- nnn/mmm: values in eV of ENCUT (nnn) and ENAUG (mmm).

Figure 14-7 to Figure 14-12 show energy convergence data for simulated perovskites: $MgSiO_3$, $MgGeO_3$, $CaSiO_3$, $NaMgF_3$, $NaZnF_3$ and $NaNiF_3$.

Note that Figure 4-3 and Figure 4-10 show relatively smooth simulated changes of unit-cell parameters and atomic coordinates over a wider range of pressure. This indicates that, while some simulated parameters may be less convergent, their simulated rates and directions of change with pressure may still be usefully studied.

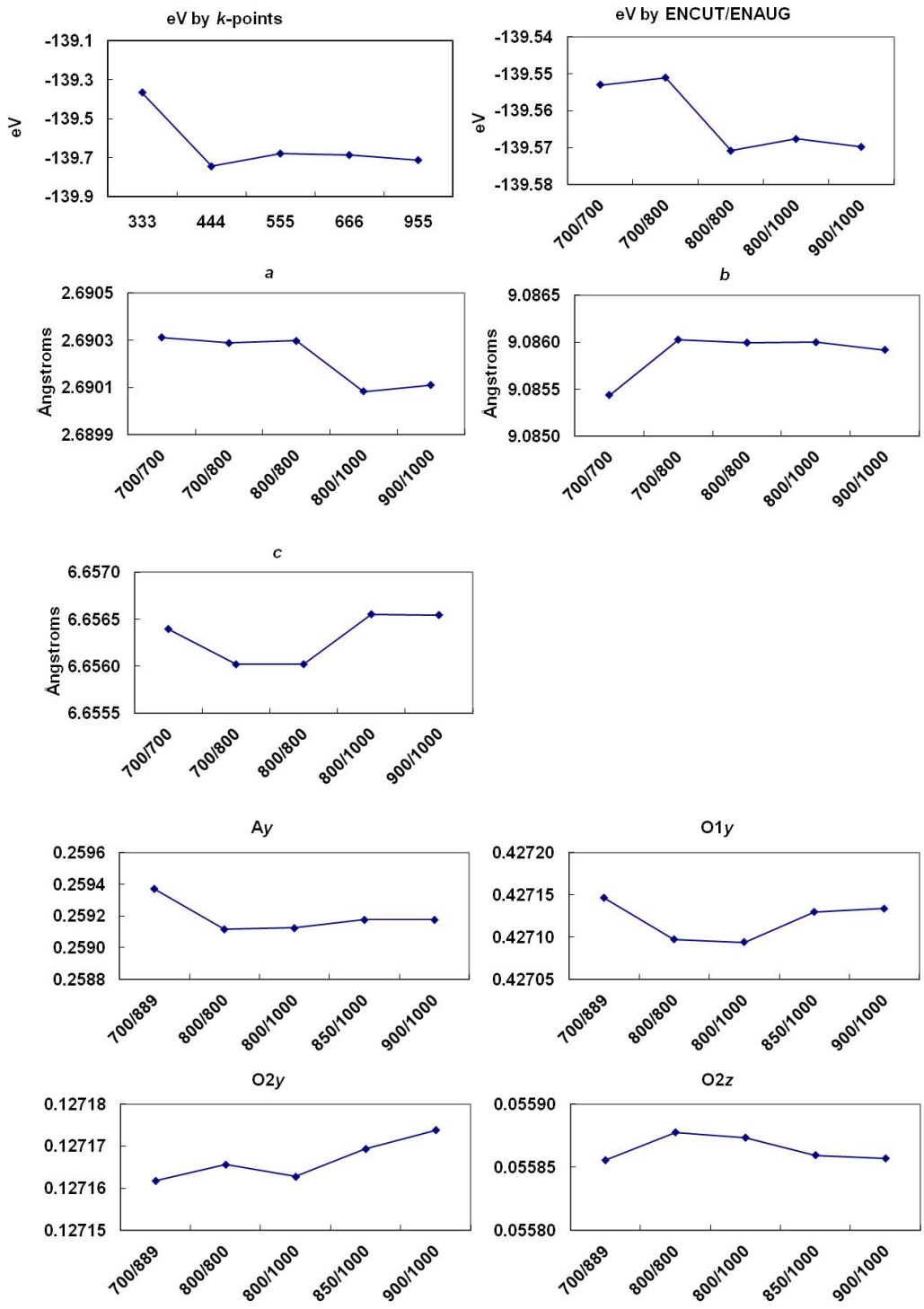

Figure 14-1: Post-perovskite $MgSiO_3$: Convergence of structural parameters.

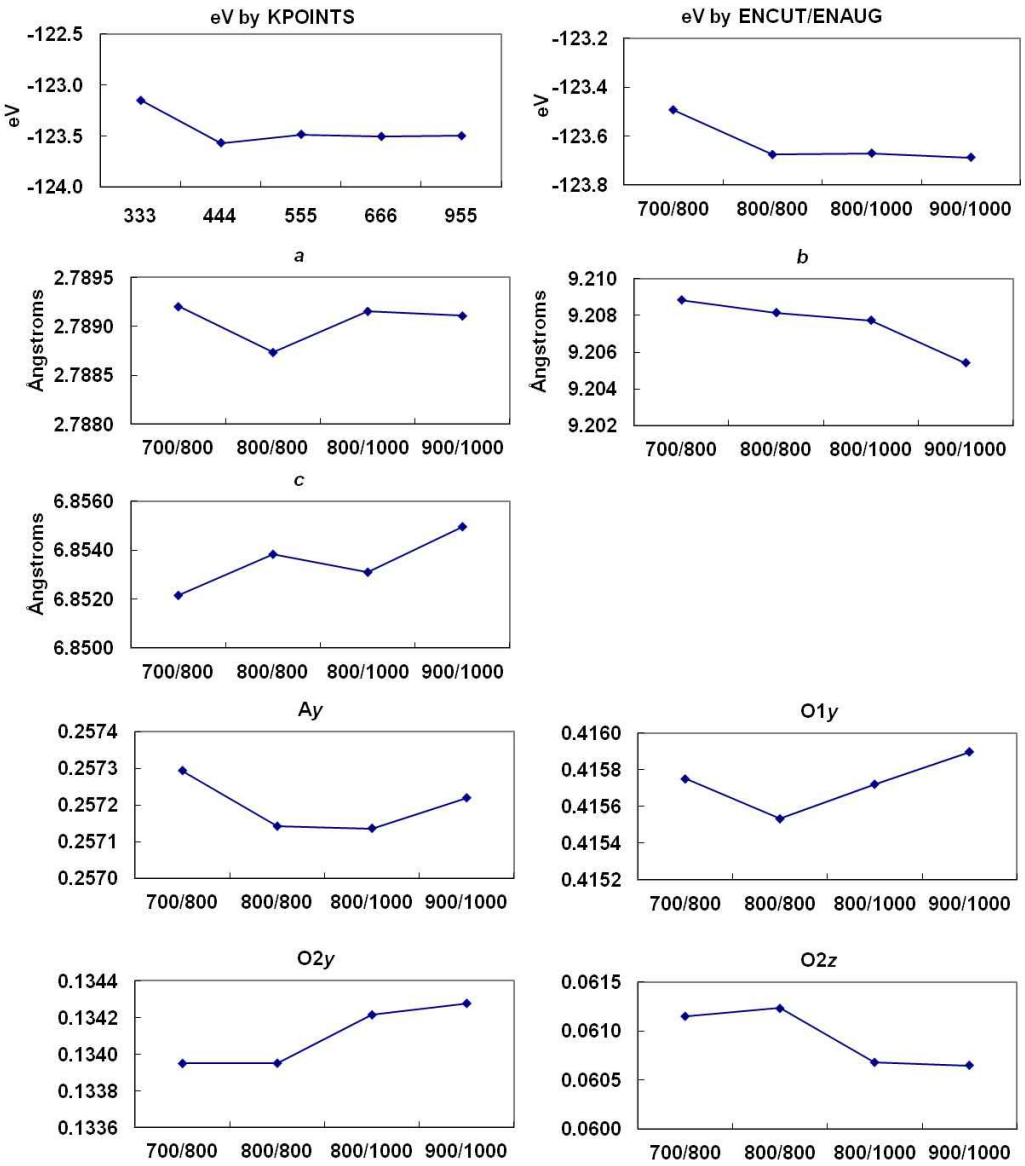

Figure 14-2: Post-perovskite $MgGeO_3$: Convergence of structural parameters.

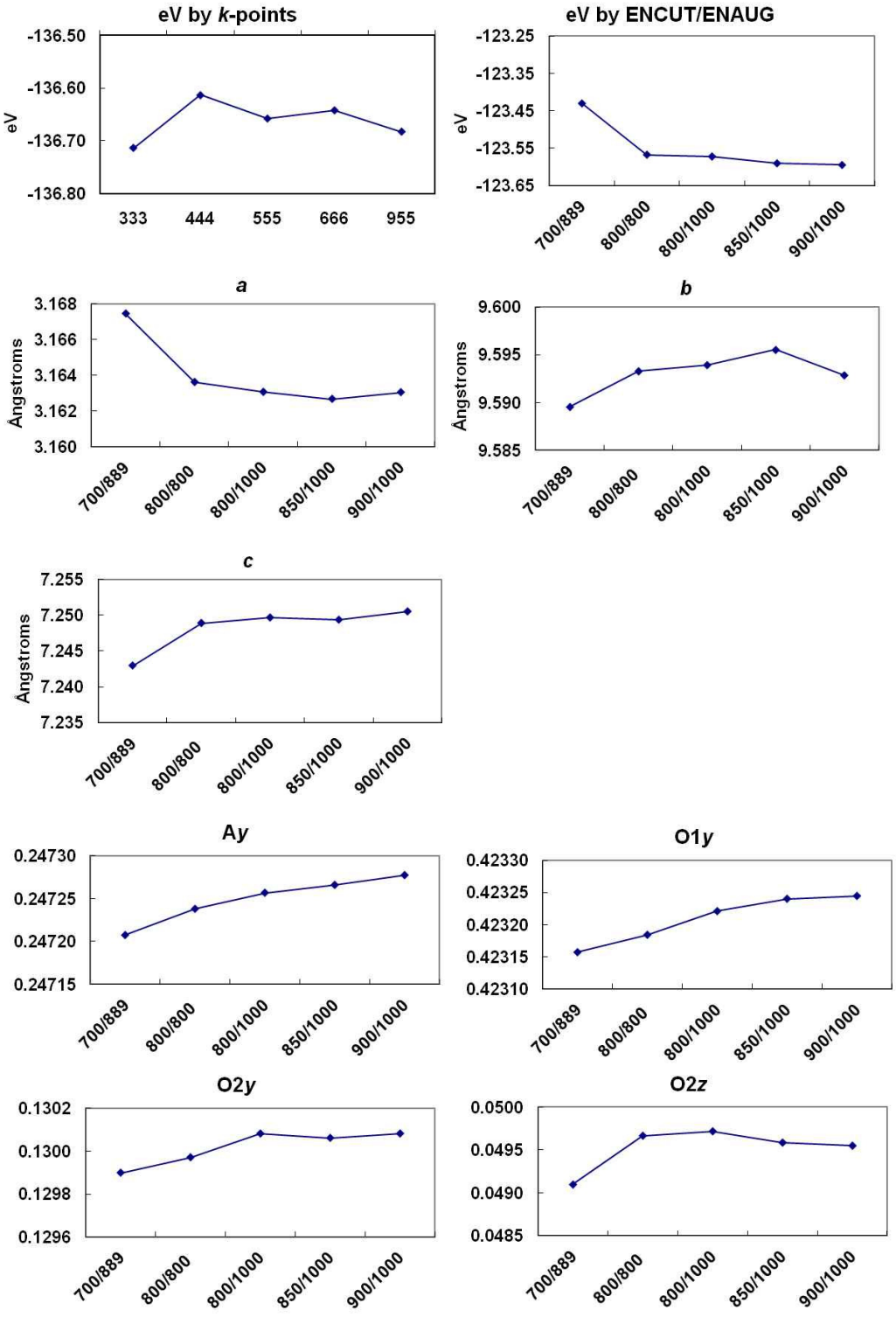

Figure 14-3: Post-perovskite $CaIrO_3$: Convergence of structural parameters.

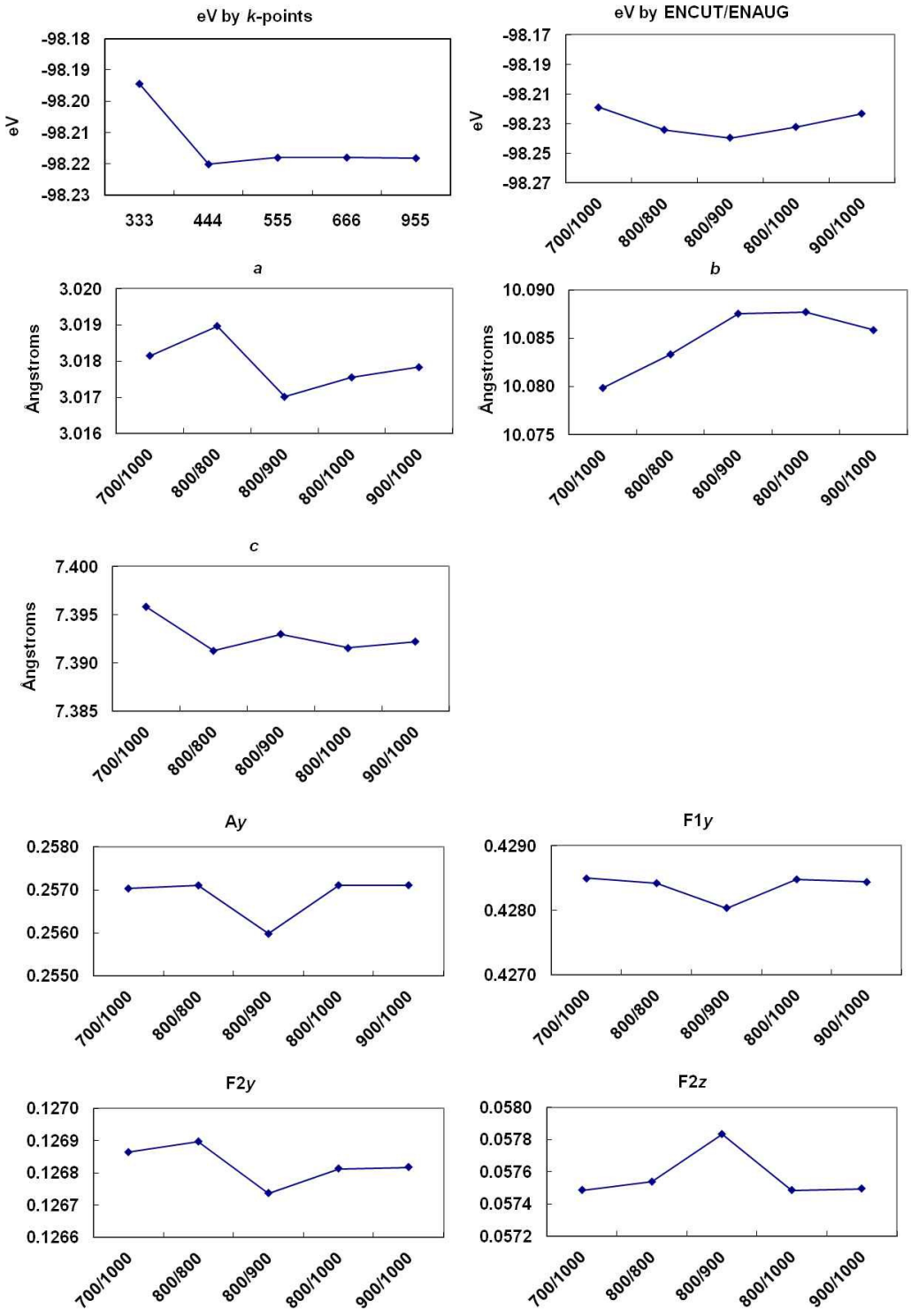

Figure 14-4: Post-perovskite $NaMgF_3$: Convergence of structural parameters.

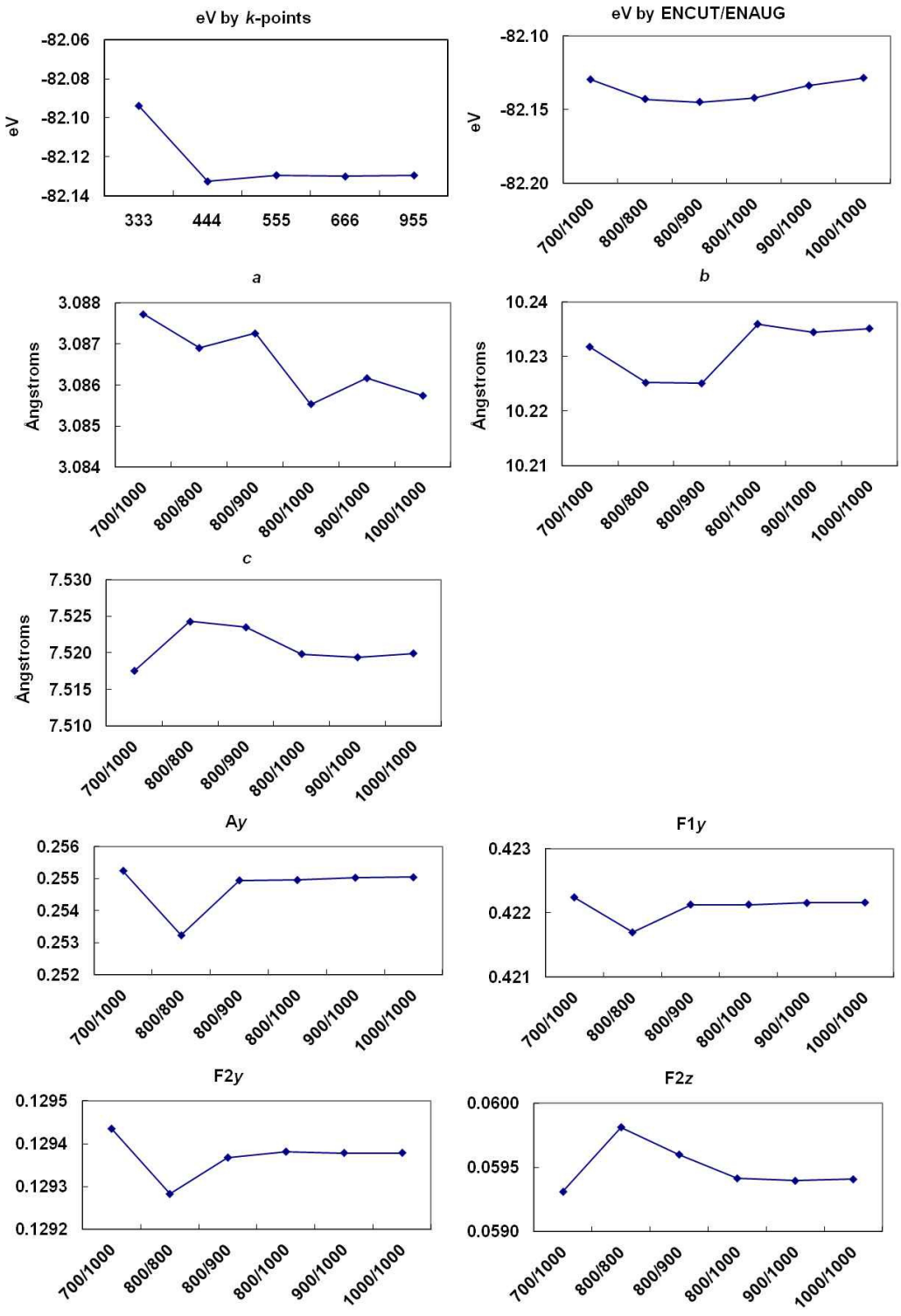

Figure 14-5: Post-perovskite $NaZnF_3$: Convergence of structural parameters.

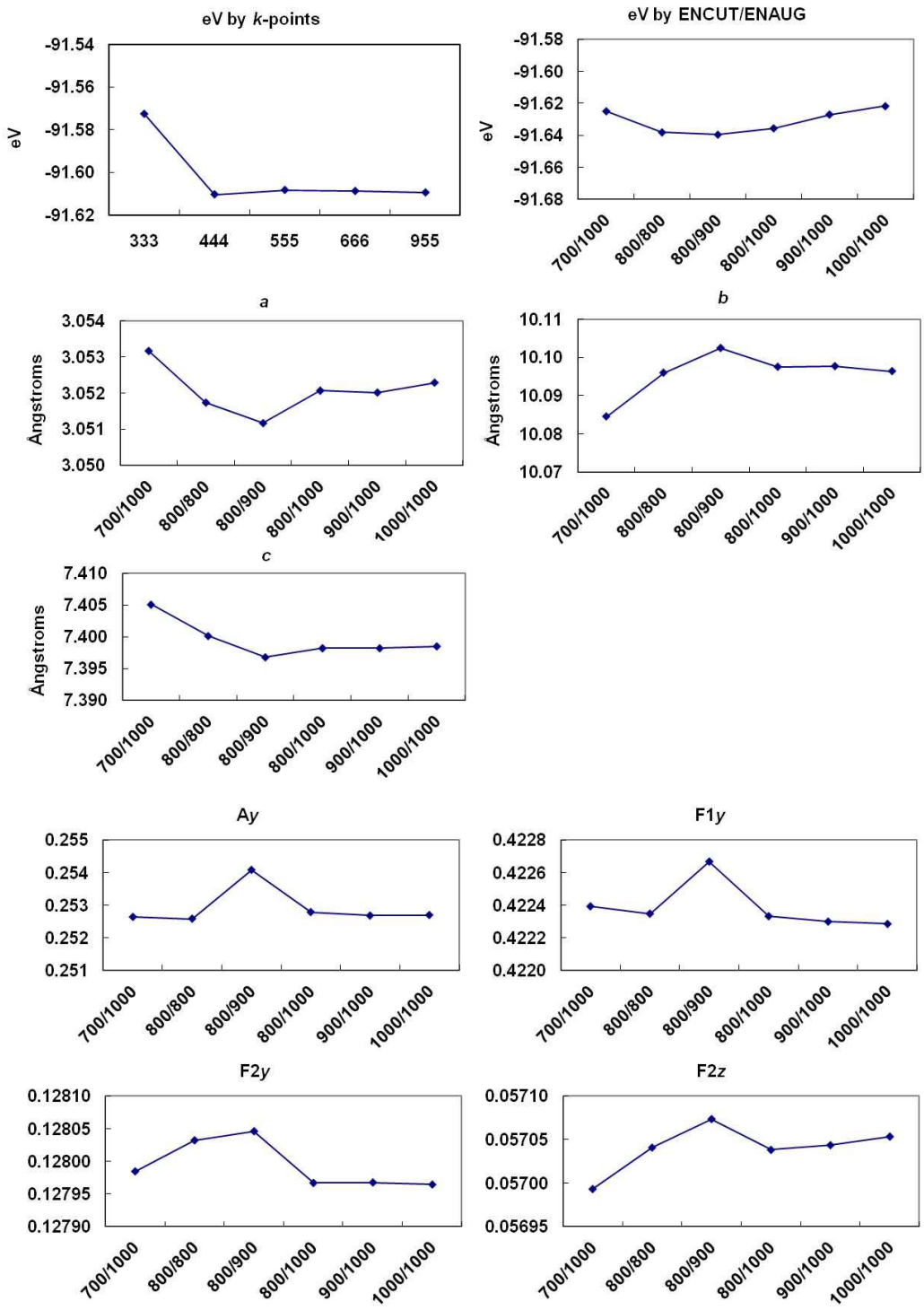

Figure 14-6: Post-perovskite $NaNiF_3$: Convergence of structural parameters.

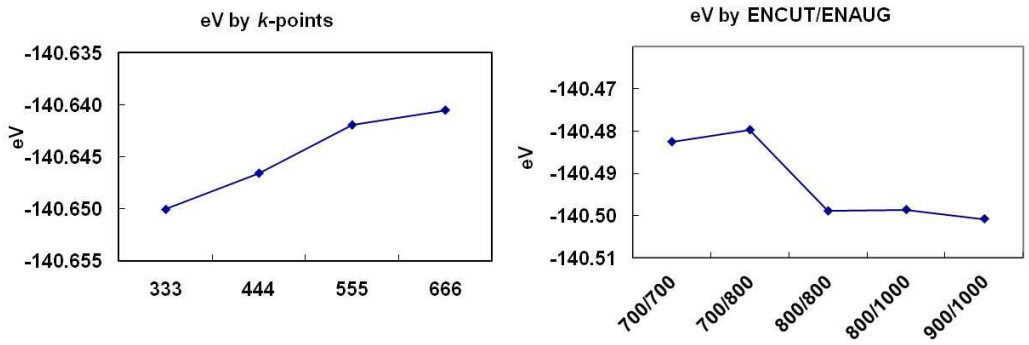

Figure 14-7: Perovskite $MgSiO_3$: Energetic convergence.

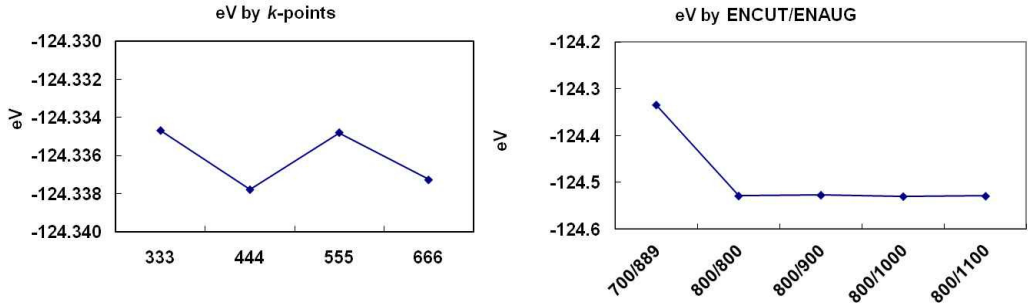

Figure 14-8: Perovskite $MgGeO_3$: Energetic convergence.

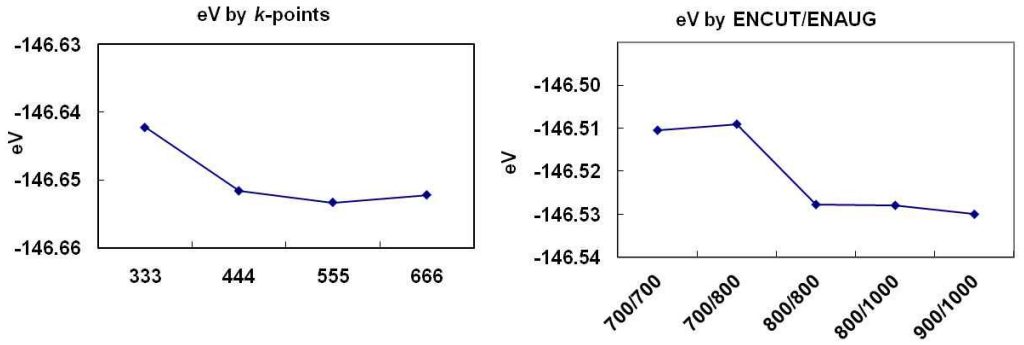

Figure 14-9: Perovskite $CaSiO_3$: Energetic convergence.

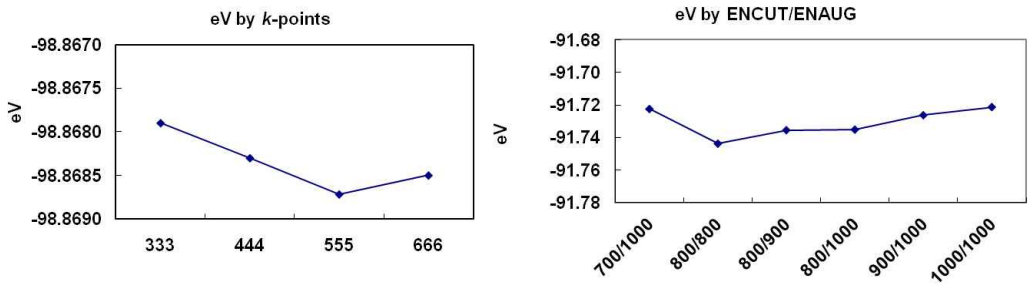

Figure 14-10: Perovskite $NaMgF_3$: Energetic convergence.

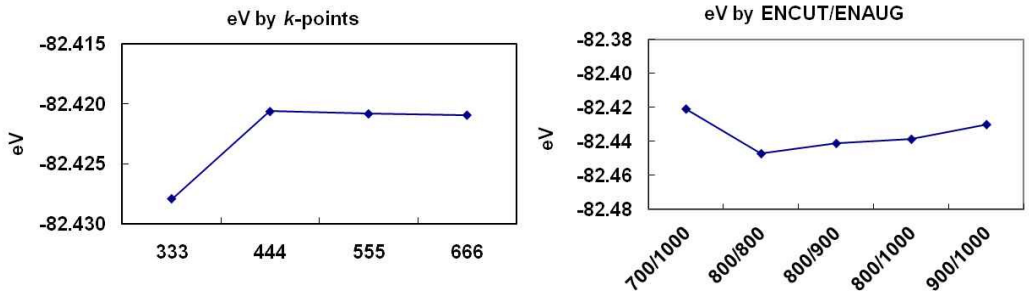

Figure 14-11: Perovskite $NaZnF_3$: Energetic convergence.

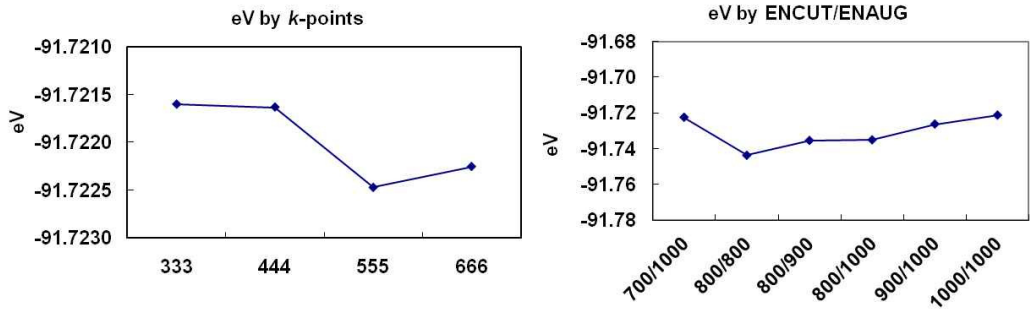

Figure 14-12: Perovskite $NaNiF_3$: Energetic convergence.

15 Appendix C - Calcium deficiencies in hexagonal Ca_2IrO_4

In the synthesis experiments described in Section 6.4.1, single crystals of hexagonal Ca_2IrO_4 ($P\bar{6}2m$)(Babel *et al.*, 1966) were produced instead of the intended single-crystal post-perovskite $CaIrO_3$. These crystals occurred in two different habits; as tabular plates (up to 180 μm across) and as acicular needles (up to 2.5mm long, 50-150 μm wide). The plates were also produced in previous work (Lindsay-Scott *et al.*, 2007) by heating polycrystalline post-perovskite $CaIrO_3$ with a $CaCl_2$ flux at ambient pressure for 3 days at 950 °C, cooling to 750 °C over 4 days and then quenching to room temperature.

Two slightly different structures have been reported for Ca_2IrO_4, both based on isolated chains of IrO_6 octahedra linked by shared edges, running parallel to the *c*-axis (Table 15-1 and Figure 15-1). In both structures Ca atoms occupy the 2*d* and 3*g* positions, Ir occupies the 3*f* and O the 3*j* (twice) and 6*j* sites (see Table 15-2). Babel *et al.* (1966) reported needle-like crystals where three Ca sites including the 1*a* sites were fully occupied. In the structure reported by Dijksma *et al.* (1993) a Ca deficiency was observed with the Ca 1 site vacant; unfortunately in this case the growth conditions of their crystals were not fully reported.

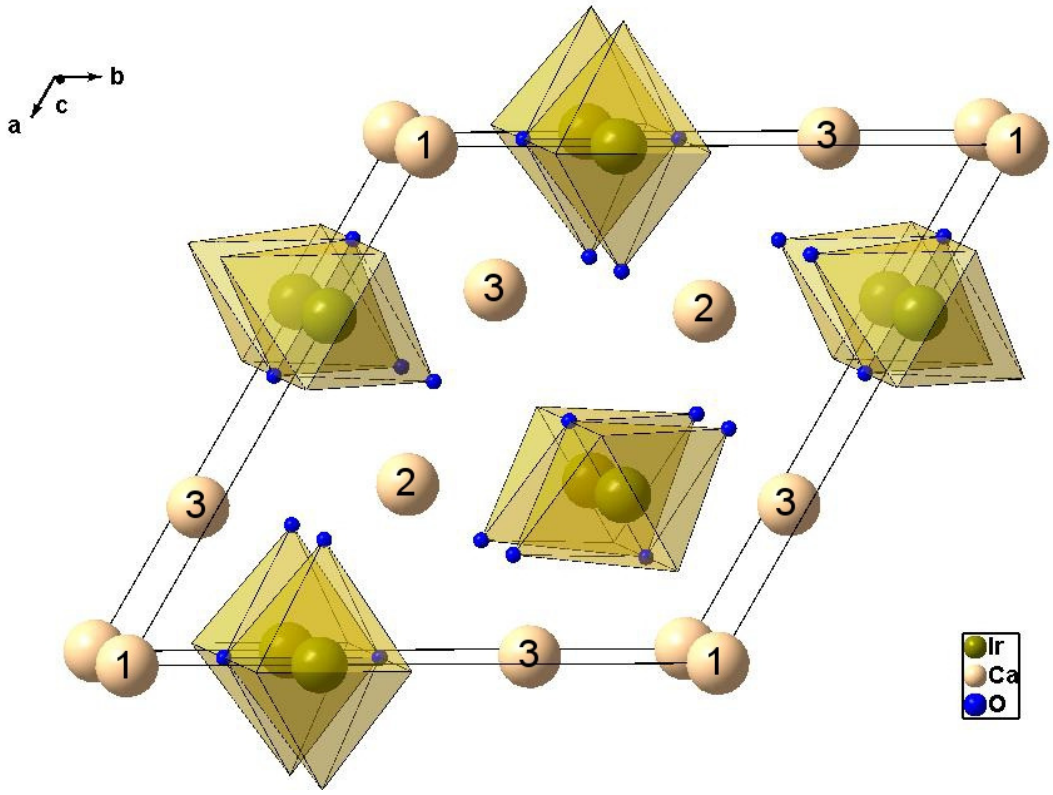

Figure 15-1: Crystal structure of Ca_2IrO_4 ($P\bar{6}2m$)(Babel *et al.*, 1966) looking at an angle of 10° to the *c*-axis. Ca sites are labelled 1 (z = 0), 2 and 3 (z = 0.5)(see Table 15-2).

X-ray powder diffraction analysis and refinement of the needles and platy crystals in the present work using GSAS showed that the unit-cell parameters and the occupancy of the Ca 1 site (normalised to the second site)(see Figure 15-1) differed significantly between the two samples (Table 15-1).

	Plates	Needles	Dijksma *et al.*	Babel *et al.*
Cell parameters (Å)				
a,b	9.41652(8)	9.4773(2)	9.4235(3)	9.42
c	3.19563(4)	3.1698(1)	3.1945(2)	3.19
Site occupancy				
Ca 1 (1*a*)	-0.06(4)	0.54(6)	0.0	1
Ca 2	1.00(6)	1.00(9)	1.00	1
Ca 3	0.85(5)	0.96(8)	0.912(15)	1
Ca 4 (1b)	0.65(6)			
x in Ca_x	5.1(1)	5.4(1)	4.74(5)	6
Atomic coordinates				
Ir *x*	0.3345(4)	0.3290(4)	0.3300(4)	0.3258
Ca3 3*g* *x*	0.726(2)	0.699(1)	0.7123(7)	0.7087
O1 3*g* *x*	0.161(4)	0.207(5)	0.1958(6)	0.1913
O2 3*g* *x*	0.440(3)	0.468(5)	0.4602(6)	0.4549
O3 6*j* *x*	0.442(3)	0.466(4)	0.4407(6)	0.4531
O3 6*j* *y*	0.233(3)	0.244(2)	0.2381(4)	0.2420

Table 15-1: Cell parameters and Ca occupancy in $Ca_xIr_3O_{12}$

The total number of Ca atom sites in the Babel *et al.* (1966) Z = 3 unit-cell is 6: Ca1, two Ca2 and three Ca3. The coordination of Ca1 is 6, of Ca2 is 9, and of Ca3 is 7. In the platy sample a further fourth Ca site at the 1*b* position at (*x*, 0, 0.5) was found to be occupied rather than the Ca1 site. The sites are shown in Table 15-2.

Atom	Site	Coordinates
Ca1	1*a*	(0, 0, 0)
Ca2	2*d*	(0.33, 0.67, 0.5)
Ca3	3*g*	(*x*, 0, 0.5)
Ca4	1*b*	(0, 0, 0.5)
Ir	3*f*	(*x,* 0, 0)
O1	3*g*	(*x*, 0, 0.5)
O2	3*g*	(*x*, 0, 0.5)
O3	6*j*	(*x*, *y*, 0)

Table 15-2: Site occupancy in Ca_2IrO_4

Examination of the two types of crystal in the electron probe showed that the needle sample (unlike the platy sample) contained Na contamination, likely to originate from

the Na_2CO_3 flux used in that synthesis. This could account for the occupancy of some of the "Ca sites" observed in the needle sample in X-ray powder diffraction.

GSAS refinements of the platy and needle samples were used to produce Fourier maps of observed electron density (Figure 15-2). The Ir ions dominated the (*x,y,*0) maps (a) and (c), and the Ca ions dominated the (*x,y,*0.5) maps (b) and (d).

The Ca1 ion appeared in the 1*a* site at (0,0,0) in the needle sample (a) as in Babel *et al.* (1966), but not in the platy sample, where instead the 1*b* site at (0,0,0.5) was occupied, forming a hexagonal ring of Ca atoms at $z = 0.5$. Dijksma *et al.* (1993) report a vacancy in the 1*a* site but no occupancy of the 1*b* site. The smallest Ca-O distance reported by GSAS in the platy sample was 1.52 Å compared with 2.40 Å in the needle sample; the position of the Ca1 atom in the platy crystals appeared to be too close to the O atoms. This suggests that this structure is unlikely, and that the $P\bar{6}2m$ structure assumed for the platy sample is incorrect. Further investigation of the platy and needle samples by single-crystal methods is required to resolve the structure.

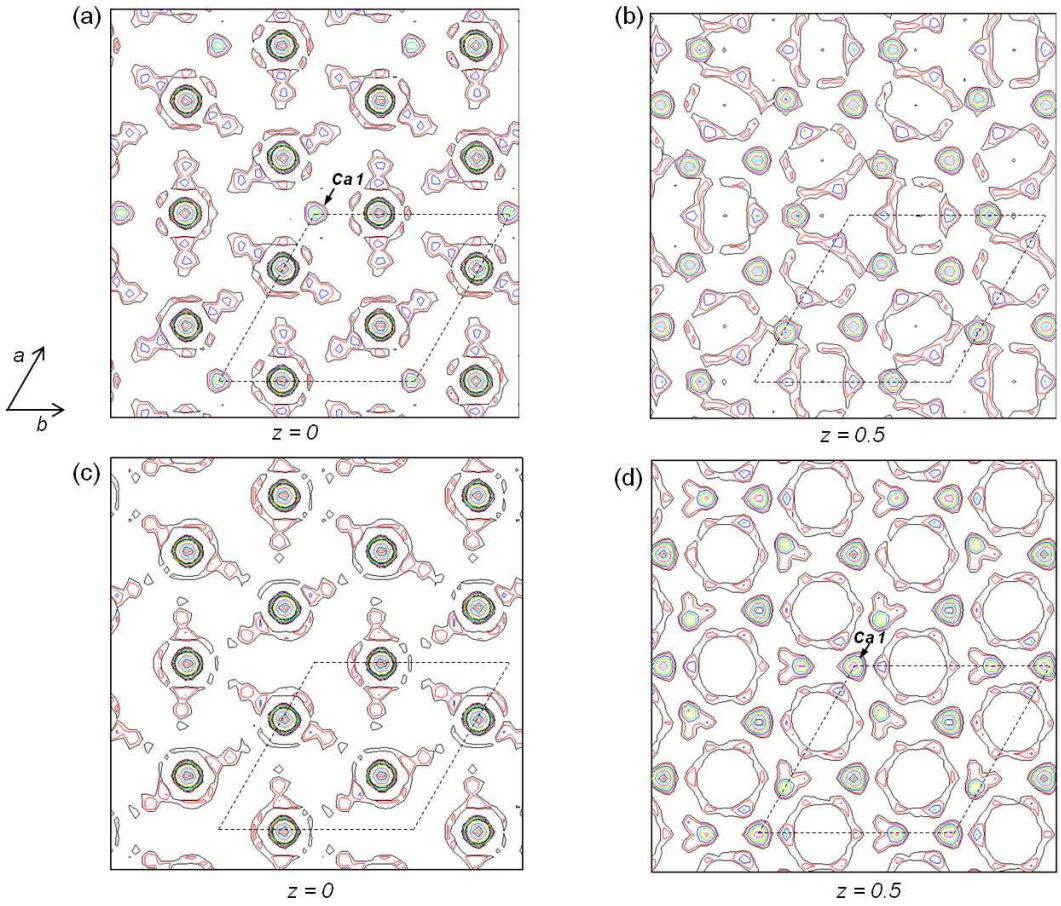

Figure 15-2: Fourier maps of observed electron density in Ca_xIrO_4 viewed along the *c*-axis. (a) Needles at (*x*,*y*,0) (b) Needles at (*x*,*y*,0.5) (c) Plates at (*x*,*y*,0) (d) Plates at (*x*,*y*,0.5). Dashed lines mark a unit-cell (Needles – XU467. Plates – XU454).

16 Appendix D – Grüneisen approximation for thermal pressure

16.1 Volumetric approximation

The Grüneisen parameter γ measures the variation of pressure with internal energy at constant volume (see e.g. Wallace, 1998), and so is a measure of the "thermal pressure" as temperature increases:

$$\gamma = \alpha V K_T / C_V \tag{16.1}$$

The volumetric thermal expansion coefficient α at temperature T and volume V for the zero-pressure EOS is defined as:

$$\alpha_0(T) = (V - V_0)/V_0 \tag{16.2}$$

where V_0 is V at $T = 0$ K and $P = 0$ GPa. The Helmholtz free energy is defined as:

$$F(V,T) = F_0(V) + F_T(V,T) \tag{16.3}$$

where $F_T = 0$ at $T = 0$ K. At equilibrium:

$$P = -(\partial F/\partial V)_T = -(dF_0/dV) - (\partial F_T/\partial V)_T \tag{16.4}$$

so that multiplying by V gives:

$$PV + V(dF_0/dV) = \gamma' U \tag{16.5}$$

where U is the internal energy and:

$$\gamma' = (V/U)(\partial F_T/\partial V)_T \tag{16.6}$$

γ' is approximately constant with respect to temperature, so that γ' = γ (Wallace, 1998). Then at $P = 0$ GPa Equation 16.5 becomes:

$$\gamma' U = V(dF_0/dV) \tag{16.7}$$

which can be expanded as a series:

$$\gamma' U = [V(dF_0/dV)]_0 - (V - V_0)[(dF_0/dV) + V(d^2F_0/dV^2)]_0 + \tfrac{1}{2}(V - V_0)^2[2(d^2F_0/dV^2) + V(d^3F_0/dV^3)]_0 + \ldots \quad (16.8)$$

where $[\ ]_0$ indicates evaluation at V_0. At $T = 0$ K, $F_T = 0$ so the final term in Equation 16.4 is also zero and from Equation 16.4 :

$$(dF_0/dV) = -P \quad (16.9)$$

Differentiating Equation 16.9 by volume gives (at $T = 0$ K):

$$(d^2F_0/dV^2) = K_0/V \quad (16.10)$$

and:

$$(d^3F_0/dV^3) = -(K_0/V^2)(1 + K_0') \quad (16.11)$$

Substituting Equations 16.10 and 16.11 into Equation 16.8 for $P = 0$ gives:

$$\gamma' U = a_0 V_0 K_0 + \tfrac{1}{2} a_0^2 V_0 K_0 (1 - K_0') + \ldots \quad (16.12)$$

Inverting Equation 16.12 for a_0,

$$a_0 = \gamma' U / V_0 K_0 + \ldots \quad (16.13)$$

Substituting a_0 from Equation 16.13 for a_0^2 in Equation 16.12:

$$\gamma' U = a_0 V_0 K_0 [1 + \tfrac{1}{2}(\gamma' U / V_0 K_0)(1 - K_0')] + \ldots \quad (16.14)$$

Then solving for a_0:

$$a_0 = U/(Q - bU + \cdots) \quad (16.15)$$

where

$$Q = V_0 K_0 / \gamma' \qquad b = \tfrac{1}{2}(K_0' - 1) \quad (16.16)$$

Then using Equation 16.2, the second order Grüneisen approximation is that:

$$V(T) = V_0\, U/(Q - bU) + V_0 \tag{16.17}$$

as in Equation 9.3. Differentiating this equation by T gives:

$$(dV/dT) = V_0((dU/dT)/(Q - bU)) + V_0 U(b(dU/dT)/(Q - bU)^2) \tag{16.18}$$

$$(dV/dT) = V_0 Q(dU/dT)/(Q - bU)^2 \tag{16.19}$$

Then since $\alpha = (1/V)\ dV/dT$ (Equation 9.5) and $C_V = dU/dT$:

$$\alpha V = V_0 Q C_V/(Q - bU)^2 \tag{16.20}$$

Substituting for γ from Equation 16.1, we obtain Equation 9.6:

$$\gamma = K_T V_0 Q/(Q - bU)^2 \tag{16.21}$$

16.2 Axial approximation

The approach used to derive the volumetric Grüneisen approximation described above has been applied to the unit-cell axes rather than the volume of an orthorhombic crystal (Wood, 2006; Lindsay-Scott *et al.*, 2007). Then the second-order approximation for the behaviour of the *a*-axis is:

$$a(T) = a_0\, U/(Q_A - b_A U) + a_0 \tag{16.22}$$

where $Q_A = \kappa_{a0} V_0 / \gamma'$ and $b_A = [\kappa'_{a0} - 2(\kappa_{a0}/\kappa_{b0}) - 2(\kappa_{a0}/\kappa_{c0}) - 1] / 2$; the subscript "A" indicates axial rather than volumetric expansion. The value of the *a*-axis at $T = 0$ K is a_0, the axial incompressibility at $T = 0$ K is κ_{a0} , and its first derivative with respect to pressure at $T = 0$ K is κ'_{a0} . Similar expressions apply to the *b* and *c*-axes.